

Structure, Lattice Dynamics, and Guest Vibrations of Methane and Xenon Hydrate

Dissertation
zur Erlangung des Doktorgrades
der Mathematisch-Naturwissenschaftlichen Fakultät
der Christian-Albrechts-Universität
zu Kiel

vorgelegt von
Julian Baumert

Kiel

2003

Referent: Prof. Dr. W. Press
Korreferent: Prof. Dr. O. Magnussen u. Prof. Dr. M.R. Johnson (ILL)
Tag der mündlichen Prüfung: 16.2.2004
Zum Druck genehmigt: Kiel, den 16.2.2004

Prof. Dr. W. Depmeier

Dekan

Abstract

Structure, Lattice Dynamics, and Guest Vibrations of Methane and Xenon Hydrate

Clathrate hydrates are inclusion compounds, in which small guest atoms or molecules are trapped in cages formed by an ice-like host lattice of water molecules. In recent years large deposits of methane hydrate have been found on the oceanic sea floors, leading to a considerable interest in the physical properties of gas hydrates.

In the present work the results from elastic and inelastic neutron scattering experiments, inelastic x-ray scattering experiments and lattice dynamical calculations are presented for methane and xenon hydrate. The structure of methane hydrate under geological conditions was determined in a high resolution neutron diffraction experiment. The crystallographic parameters of both the guest molecules and the host lattice have thus been obtained for a fully deuterated methane hydrate sample. The inelastic neutron scattering (INS) experiments focused on the translational vibrations of the guest molecules and atoms inside the cages and on the density of states of the host lattice. The powder averaged dispersion curves were determined for both methane and xenon hydrate as well as recently discovered high pressure structures of methane hydrate in inelastic x-ray scattering (IXS) experiments.

The results from the diffraction experiment show that deviations from ideal bond angles and bond lengths of the water molecules lead to strong cage deformations at geological conditions. The methane guest molecules were found to perform large amplitude motions, probing the potential surfaces of the cages thoroughly. The large amplitude thermal vibrations of the guest and host molecules are probably responsible for considerable deviations from harmonic and isotropic models that are valid at low temperatures and pressures.

A coupling between the guest and host vibrations could be confirmed in the INS experiments of methane and xenon hydrate. The experimental densities of states of the host lattice displayed excitations at energy positions corresponding to the guest vibrations. The IXS experiments provided insight into the coupling mechanism, providing experimental evidence for an avoided crossing between the localized guest modes and the acoustic host lattice phonons. On the basis of lattice dynamical calculations the experimental findings could be reproduced, showing that the avoided crossing promotes an extensive mixing of the guest and host modes. It is concluded that the mixing of the modes promotes collective guest modes as well as water molecule vibrations at the frequency of the guest modes.

As the energy of the guest modes increase with increasing temperature, the guest-host potential is thought to be dominated by the repulsive part of the guest-host interaction. The repulsive interaction was found to have a strong influence on the elastic properties of the high pressure phases of methane hydrate that were obtained from IXS experiments.

Kurzfassung

Structure, Lattice Dynamics, and Guest Vibrations of Methane and Xenon Hydrate

Gashydrate sind Einschlussverbindungen, bei denen kleine Gastmoleküle oder Gastatome in Käfigen eingeschlossen sind, die aus einem eisähnlichen Netzwerk aus Wassermolekülen bestehen. Durch den Fund grosser natürlicher Vorkommen an Methanhydrat hat sich das Interesse an den physikalischen Eigenschaften der Clathrate vervielfacht.

Im Rahmen dieser Arbeit wurde die Struktur von Methanhydrat unter geologischen Bedingungen mit elastischer Neutronenstreuung untersucht. Mit Hilfe einer vollständig deuterierten Methanhydratprobe konnten die kristallographischen Parameter der Gast- und Gittermoleküle bestimmt werden. Die Dynamik von sowohl Xenon- als auch Methanhydrate war Gegenstand inelastischer Neutronenstreu- (INS) und inelastischer Röntgenstreuexperimente (IXS). Dabei stand die Untersuchung der Translationsbewegungen der Gäste, der Zustandsdichte des Gitters und der pulvergemittelten Dispersionskurven im Vordergrund. Die inelastischen Streuexperimente wurden von theoretischen Modellrechnungen begleitet. Ausserdem wurden die elastischen Eigenschaften von neuentdeckten Hochdruckstrukturen von Methanhydrat mit inelastischer Röntgenstreuung bestimmt.

Die Diffraktionsmessungen unter geologischen Bedingungen zeigten, dass es zu Käfigverformungen verglichen mit den Ergebnissen bei tiefen Temperaturen kommt. Die thermischen Bewegungen der Methanmoleküle können ebenfalls nicht mehr von den harmonischen und isotropen Modellen beschreiben werden, die bei tiefen Temperaturen gültig sind.

Die Existenz einer Kopplung zwischen den Gast- und Gitterschwingungen konnte in den INS Experimenten an Xenon- und Methanhydrate nachgewiesen werden. Die experimentelle Zustandsdichte des Hydratgitters wies Anregungen bei Frequenzen auf, die denen der Gastschwingungen entsprachen. Mit Hilfe der IXS Experimente konnten zusätzlich die Dispersionskurven bestimmt werden, die Hinweise auf eine "vermiedene Kreuzung" zwischen den optischen Gastmoden und den akustischen Gittermoden ergaben. Eine theoretische Analyse der Gitterdynamik von Methan- und Xenonhydrat zeigte, dass die Wechselwirkung zwischen den Gast- und Gittermoden zu einer Mischung der Moden führt. Die Beobachtung von kollektiven Gastmoden in den IXS Spektren und von gekoppelten Moden in den INS Spektren konnte auf diesen Effekt zurückgeführt werden.

Die Beobachtung, dass die Energie der Gastschwingungen mit der Temperatur ansteigt, deutet darauf hin, dass dem repulsiven Anteil des Gast-Gitter Potentials eine wichtige Rolle zukommt. Die Ergebnisse der IXS Messungen an den Hochdruckstrukturen von Methanhydrat zeigten, dass die abstoßende Wechselwirkung zwischen den Gast- und Gittermolekülen einen maßgeblichen Einfluss auf die elastischen Eigenschaften dieser Hydrate hatte.

Contents

1	Introduction	1
2	Clathrate Hydrates – Physical Properties	5
2.1	Hydrate Crystal Structures	5
2.1.1	Structure Type I	6
2.1.2	Structure Type II	8
2.1.3	Structure H	10
2.1.4	High Pressure Gas Hydrates	12
2.2	Physical Properties of Gas Hydrates	13
2.3	Formation of Gas Hydrates	15
2.3.1	Thermodynamics and Pore Potentials	16
2.3.2	Stability and Pressure–Temperature Diagrams	19
2.4	Natural Methane Hydrate	20
3	Lattice Dynamics Calculations	25
3.1	Force Constants and Dynamical Matrix	25
3.2	Density of States – DOS	28
3.3	Phenomenological Models for a Clathrate Hydrate	30
3.3.1	Central Harmonic Forces and Rigid Cages	31
3.3.2	Lattice Dynamical Clathrate Model	39
4	Theory of Neutron and X–ray Scattering	43
4.1	Neutron Scattering	43
4.1.1	Scattering Cross Sections	43
4.1.2	Coherent Scattering	46
4.1.3	Incoherent Scattering	50
4.2	Inelastic x–ray Scattering	52
5	Experimental Details	55
5.1	Time–of–Flight Spectrometers FOCUS and IN6	55
5.2	Diffractometer D2B	57
5.3	Inelastic Scattering Beamline ID28	58
5.4	Sample Handling and Sample Environments	59

5.4.1	Ambient Pressure Sample Cell	60
5.4.2	High Pressure Sample Cells	61
6	Methane Hydrate – Results and Discussion	65
6.1	Structure of Methane Hydrate under Geological Conditions	65
6.1.1	Structure Refinement	66
6.1.2	Results and Discussion	71
6.1.3	Summary and Conclusions	80
6.2	Dynamics of Methane Hydrate	81
6.2.1	Neutron Spectroscopy	82
6.2.2	X-ray Spectroscopy	94
6.2.3	Lattice Dynamical Calculations	99
6.2.4	Discussion and Summary	107
6.3	Elastic Properties of High Pressure Methane Hydrates	108
6.3.1	Methane Hydrate MH-II	109
6.3.2	Methane Hydrate MH-III	116
6.3.3	Discussion and Conclusions	121
7	Xenon Hydrate – Results and Discussion	125
7.1	Neutron Spectroscopy	125
7.2	X-ray Spectroscopy	128
7.3	Lattice Dynamical Calculations	130
7.4	Discussion and Summary	136
8	Conclusions – Summary and Outlook	139
	Bibliography	143
	Eidesstattliche Erklärung	153
	Lebenslauf	155
	Acknowledgments	157

Chapter 1

Introduction

Clathrate hydrates are inclusion compounds, in which guest molecules or atoms are trapped in cages formed by an ice-like host network of water molecules. Gas hydrates have attracted a considerable interest in recent years, as large deposits of natural gas hydrates, e.g. methane hydrate, have been discovered in sediments on the ocean sea floors and in arctic permafrost areas. The estimated amount of gas contained in natural gas hydrates exceeds the conventional deposits of fossil fuels by a factor of two. The deposits are therefore considered as potentially important future energy resources. The interest in the gas hydrates is, however, not limited to the economic importance of the natural gas, but it also includes the possible implications of the stored amounts of methane gas on the global climate, as methane is known to be an important green house gas.

Natural gas hydrates were first documented by *Sir Humphrey Davy* in 1811 [33]. Over the next 150 years the goal of the research on gas hydrates was to identify possible hydrate forming gases and to determine the composition and the physical properties of hydrates. To form a hydrate from gas and water, a moderate pressure and a low water temperature are necessary. Such conditions lead to the formation of methane hydrate at water depths greater than 400 m. Already in the 1930's, natural gas hydrates were found to cause blockages in gas pipelines. Today, most common clathrate hydrates occur in one of the following three crystal structures: cubic structure type I, cubic structure type II, or hexagonal structure type H. Structure type I and II were determined in the 1940's by *v. Stackelberg* and *Müller* [133–137], whereas the structure type H was only discovered in 1987 by *Ripmeester* et. al. [111]. The structure of methane hydrate was identified by *Davidson* et.al. in 1984 [31].

The growing interest in hydrates and the geological importance of methane hydrate have led to a demand for a precise knowledge and understanding of the physical properties of gas hydrates. Many characteristics like the formation or decomposition process, the velocity of sound and the thermal conductivity are linked to a microscopic understanding of the structure and dynamics of the clathrate hydrates. It was possible to determine the structure with x-ray scattering and the dynamics of the guest molecules was the subject of NMR experiments. Overviews of the results from these surveys have been published in a series of reviews [30, 66]. Most of the investigations, however, focused on hydrates with

relatively large guest molecules like ethylene oxide or tetrahydrofuran. These hydrates were easy to synthesize and large single crystals could be grown for the experiments, but the interpretation of the results was difficult due to the complicated geometry of the guest molecules. The difficulty to obtain precise experimental results on gas hydrates has led a more theoretical approach. In the 1980's *Tse* and co-workers started to study the dynamics of hydrates with molecular dynamics simulations. Here, small spherical guest atoms and molecules were of interest as they could be easily modeled. These hydrates, however, are more difficult to synthesize and commonly exist as powders only. A particular effort is needed to grow even very small single crystals of a few μm^3 .

For the investigation of the structural and lattice dynamical properties of these hydrate powder samples, neutron scattering provides important information. Due to the isotope dependence, neutron scattering can be used to investigate both the structure (deuterated samples) and the single particle dynamics (protonated samples). The information that inelastic neutron scattering can provide on the lattice dynamics of powder samples, however, is limited. In inelastic neutron scattering the momentum transfer is related to the initial and final energies of the neutron in such a way that only very small energy transfers are accessible at small momentum transfers. Here, inelastic x-ray scattering is able to overcome this limitation, as the momentum transfer is independent of the energy transfer. Inelastic x-ray scattering has thus the capability of determining the collective dynamics of powder samples. Additionally, the high intensity x-ray beams of third generation synchrotron sources allow to investigate very small samples, i.e. high pressure sample environments can be used. In the present work a combination of inelastic neutron and inelastic x-ray scattering is therefore used to study the dynamics of methane and xenon hydrate, complemented by the study of the structure of methane hydrate under geological conditions by neutron diffraction.

Precise crystallographic parameters of both the ice-like framework and the encaged methane molecules have been reported recently in a low temperature, high resolution neutron diffraction study of methane hydrate at ambient pressure [43]. Under geological conditions the details of the cage fillings are of interest both as a function of guest species and gas pressure [21, 69]. However, large thermal vibrations render the determination of the cage occupancies difficult. Thus a precise knowledge of the structure of methane hydrate at high temperatures and high pressures seemed desirable. On the basis of the low temperature study the structure of methane hydrate under geological conditions present at natural deposits in the oceans at a water depth of ~ 1000 m ($T=4^\circ\text{C}$, $p=100$ bar) is therefore investigated.

The influence of the guest molecule vibrations on the host network is also of interest. In 1981 *Ross et. al.* discovered that the thermal conductivity of gas hydrates is unusually low and displays a temperature dependence similar to that of glasses despite the crystalline character of the hydrate [113]. The opportunity to study glass-like phenomena in crystalline materials led to several theoretical studies [143, 144]. As a result, a coupling between the guest and host vibrations acting as a scattering mechanism for

the heat carrying lattice vibrations was proposed as an explanation for the phenomenon. Recently, this coupling could be confirmed experimentally in the case of xenon hydrate [151]. For natural gas hydrates the low thermal conductivity may also play an important role for the modeling and prediction of the stability of hydrates on the continental margins in shallow arctic waters as the temperature evolution and the energy transport may be altered within the marine hydrate layers. As the low thermal conductivity was recently discovered in isostructural semiconductor clathrates as well, experimental and theoretical results may also have important implications for the use of clathrate structures in the design of high-efficiency thermoelectric materials [98]. A central point of this study is therefore to investigate the lattice dynamics of methane and xenon hydrate in detail, to possibly find experimental evidence for a connection between the guest-host coupling and the unusual thermal conductivity.

Regarding the weak van der Waals interaction between the guest molecules or atoms and the hydrate lattice such a coupling was initially unexpected. The large “effective” force constants are thought mainly to arise from the repulsive part of the potential energy surface, which is predominantly probed by the excursions of the guests from their equilibrium positions. The hydrophobic interaction between the guest molecules or atoms and the water molecules of the host lattice is thought to grow more important with increasing pressure. Recently, at higher pressure, two new structures of methane hydrate have been discovered [88]. These new structures are likely to be determined by the repulsive part of the gas-water interaction, which is relevant to problems in biology [58] and for a more fundamental understanding of the water potentials [91]. The newly discovered high-pressure phases thus provide an experimental access to unexplored regions of the hydrophobic gas-water interaction. Therefore high pressure experiments are performed to determine the lattice dynamical and elastic properties of these high pressure structures.

The present work is organized as follows: At first the physical properties of gas hydrates will be introduced. The three common crystal structures are presented along with their physical properties. An overview of the newly discovered high pressure hydrates and of natural methane hydrate is given and the theory of hydrate formation is discussed (Chapter 2). In the following the theory of lattice dynamics is introduced in order to be able to link the theory to experimentally accessible quantities. The development of both a very simplified and a more realistic lattice dynamical model for clathrate hydrates will be emphasized (Chapter 3). The theory of neutron scattering and inelastic x-ray scattering will be presented in Chapter 4. Here, the theoretical expressions that are needed to analyze the neutron experiments and x-ray experiments, will be given. Chapter 5 focuses on the description of the experimental setups and of the sample handling. The measurements and the experimental results for methane hydrate are presented in Chapter 6. First the results of the diffraction experiments are presented, and then those of the lattice dynamics. The lattice dynamics concentrates on the guest-host coupling in methane hydrate structure type I, which is investigated with a combination of inelastic neutron scattering and inelastic x-ray scattering experiments, accompanied by lattice dynami-

cal calculations. The dynamics of xenon hydrate is described in Chapter 7. The results from inelastic neutron and inelastic x-ray experiments are again compared with lattice dynamical calculations. The results of will be summarized and concluded in Chapter 8.

Chapter 2

Clathrate Hydrates – Physical Properties

The purpose of this chapter is to review the fundamental physical properties of clathrate hydrates. In the first section the different crystallographic structures of gas hydrates will be introduced. In the second section some of the basic physical properties of hydrates will be presented and compared to the properties of hexagonal ice. The last part of this chapter will focus on the formation of gas hydrates.

2.1 Hydrate Crystal Structures

Hydrates formed by natural gases were first reported by *Sir Humphrey Davy* in 1811 [33], when he found that chlorine gas – water mixtures freeze more readily than pure water. Only in the late 1940's and early 1950's *von Stackelberg* and co-workers could identify two hydrate structures, when they summarized the results of two decades of x-ray hydrate crystal diffraction experiments [133–137]. The hydrate crystal structures that were determined are two cubic structures, known as structure type I and structure type II. Both crystallographic structures were studied in more detail by *McMullan* and *Jeffrey* [65, 66]. These studies showed that structure I and II hydrates are inclusion compounds where small guest molecules or atoms are trapped in cages formed by a network of hydrogen bonded water molecules, thus the name clathrates – from the Latin “clathratus”, “to encage”.

In 1987 the hexagonal hydrate structure H was discovered by *Ripmeester* and co-workers [111]. Its detailed crystallographic structure was determined only recently by a single crystal diffraction study [152]. Structure H requires both a small and larger guest molecule to form and thus allows molecules, too large to fit in any of the structure I or II cavities, to form hydrates.

Even though the detailed shape of the cavities is different for the three hydrate structures, there are similarities and the topology of the network of water molecules is the same: the hydrogen bonds between the water molecules lead to a tetrahedral coordination. The water molecules are connected to four next neighbor molecules through the

hydrogen bonds. From these building blocks the host network of the hydrate structures is formed, consisting of a packing of polyhedra. The three structure types differ in the number and geometry of these polyhedra in the unit cell. Similar structures may be formed by other tetrahedrally coordinated elements. In the presence of alkali atoms Si or Ge are found to form structure type I and II clathrates [29] and clathrasils are formed by SiO_2 molecules [40]. An important property, which is shared between the clathrate hydrates and many ice phases, is the proton disorder of the water molecule network.

In order to stabilize the hydrate structures a guest molecule or atom is needed. The attractive interactions between the water molecules forming the cavities lead to an inward directed force, rendering empty hydrates unstable. The repulsive interaction between the guest molecule or atom and the surrounding water molecules is therefore thought to stabilize the structure and to be an important factor for hydrate formation. Guest molecules, for example, do not contain a strong hydrogen bond group or a number of weaker hydrogen bond groups [66]. Therefore two interactions seem to play the dominant role in clathrate hydrates, the hydrogen bonds between the water molecules forming the cavities and the van der Waals interaction between the guest molecule or atom and the surrounding water molecules.

A large variety of at least 120 guest species is known to be suitable to form hydrates [30]. The size of the guests reaches from small rare gas atoms, e.g. krypton, argon, with van der Waals diameters of about 4 Å to larger molecules like cyclooctane with van der Waals diameters of up to 9 Å. The size of the guest molecule or atom determines the size of the cavity, which can be stabilized. Asymmetric cages may furthermore require an asymmetric guest in order to be stable. The type of guest atom or molecule is therefore a deciding factor for the type of hydrate structure that is formed.

2.1.1 Structure Type I

The structure type I is a cubic structure with the space group $\text{Pm}\bar{3}\text{n}$ and a lattice constant of about 12 Å (Figure 2.2). The first detailed crystallographic study was performed on ethylene oxide hydrate [94]. The hydrate structure I is found to be formed by two of the polyhedra shown in Figure 2.1. The 12-sided cavity has twelve pentagonal faces (5^{12}) and is a pentagonal dodecahedron. The 14-sided cavity is a tetrakaidecahedron consisting of 12 pentagonal and 2 hexagonal faces ($5^{12}6^2$). Both of the cavities follow the *Euler* theorem, where the number of faces (F) plus the vertices (V) is equal to the edges (E) plus 2 ($F + V = E + 2$).

The pentagonal dodecahedron or small cage is a building unit common to all of three hydrate structures. It is almost spherical with an average cavity radius of about 3.95 Å. The small cages are situated on the corners and in the middle of the unit cell, their centers have cubic site symmetry ($m\bar{3}$) (Table 2.1). The small cavities are connected through their vertices, leading to somewhat larger, oblate spaces between them. These spaces are the large ellipsoidal $5^{12}6^2$ cages, which are centered on points with tetragonal $\bar{4}2\text{m}$ site symmetry. The average cavity radius of the large cage is 4.33 Å. It can thus

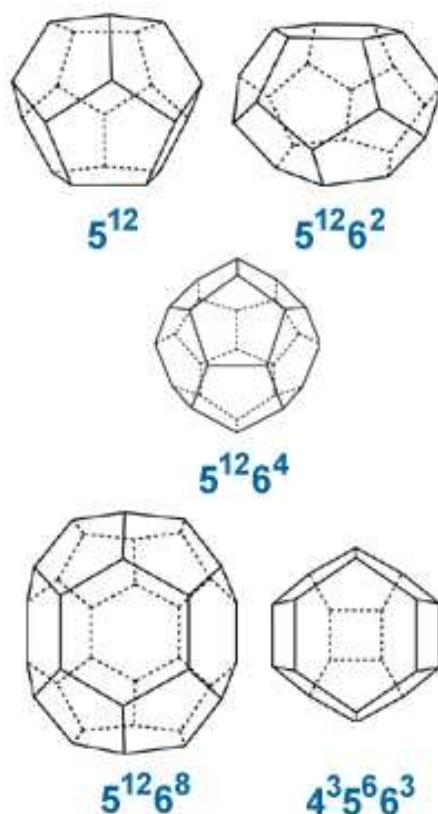


Figure 2.1: The five different cages present in the three common gas hydrate structures. Hydrate structure I is formed by the 5^{12} and the $5^{12}6^2$ cages, structure II by the 5^{12} and the $5^{12}6^4$ cages, and structure H by the 5^{12} , the $5^{12}6^8$, and $4^35^66^3$ cages.

be occupied by molecules with a diameter of up to 6 Å. The hydrate structure type I is therefore formed by guest molecules with an average van der Waals diameter of 4.2 Å to ~6 Å (e.g. CH₄, Xe, H₂S, or C₂H₆).

The proton disorder of the host network leads to a statistic disorder, which is averaged in scattering experiments. A structural analysis thus gives results on the averaged crystal structure, e.g. leading to an occupancy of 0.5 for the protons. Therefore symmetries are always related to the averaged structure and not to the local realization of a single cavity or unit cell.

The ideal guest/water ratio is 8 G·46 H₂O for molecules which can occupy both the small and the large cages. In general the ratio is given by 2 X·6 Y·46 H₂O, with X and Y referring to the molecules in the small and large cages, respectively. As guest molecules rather occupy the larger cages, the hydrate compounds are most of the time non-stoichiometric. Especially for larger guest molecules the occupation of the small cages is avoided due to energetic reasons. Typical occupancies of the large cages are greater than 95%, whereas the small cages are usually occupied to 50%. The non-stoichiometry depends on the size ratio of the guest and the cavity and increases as the ratio approaches

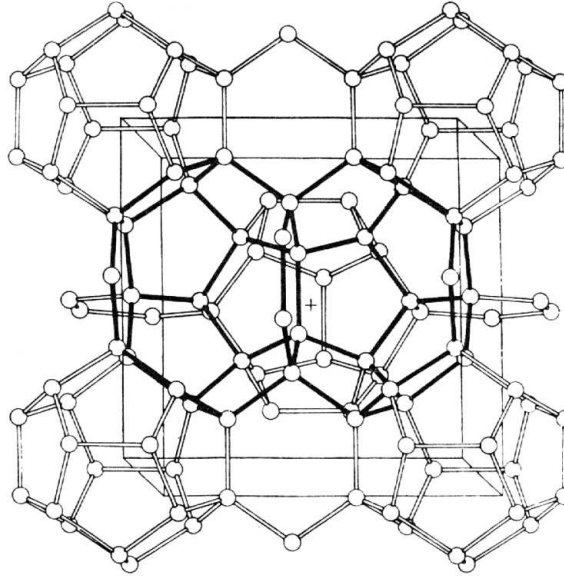


Figure 2.2: The unit cell of the cubic hydrate crystal structure I [94]. The small 5^{12} cages can be seen at the corners and in the center of the unit cell. The large $5^{12}6^2$ cages (bold) are located on the faces of the unit cell.

unity. It also depends on the gas pressure during hydrate formation: higher gas pressures lead to higher occupancies. However, the hydrate structure can be stable with only a fraction of the cavities filled. In the case of ethane hydrate, where the structure is mostly stabilized by the filling of the large cages, only 6% of the small cages are occupied [153]. One of the few exceptions is methane hydrate, where nearly all the cages are occupied by a methane molecule [43].

2.1.2 Structure Type II

The structure type II is again a cubic structure with the space group $Fd\bar{3}m$ and a lattice constant of about 17 \AA . The hydrate structure type II was deduced from a single crystal x-ray study of tetrahydrofuran/hydrogen sulfide hydrate [92]. It consists of a network of small (5^{12}) cages, connected through face-sharing in three dimensions. The voids between the cavities form the large ($5^{12}6^4$) cages that are connected again through face-sharing of the hexagons (Figure 2.3). The unit cell of structure II thus contains 16 pentagonal

	Structure I		Structure II		Structure H		
Crystal System	Cubic		Cubic		Hexagonal		
Space Group	Pm3n		Fd3m		P6/mmm		
Approx. Lattice Parameters [\AA]	a=12		a=17		a=12 c=10		
No. of Water Molecules per Unit Cell	46		136		34		
Cavity	Small	Large	Small	Large	Small	Medium	Large
Geometry	5^{12}	$5^{12}6^2$	5^{12}	$5^{12}6^4$	5^{12}	$4^35^66^3$	$5^{12}6^8$
No. of Cavities	2	6	16	8	3	2	1
Site Symmetry	m3	$\bar{4}2m$	$\bar{3}m$	$\bar{4}3m$	mmm	$\bar{6}2m$	6/mm
Average Cage Radius [\AA]	3.95	4.33	3.91	4.73	3.91	4.06	5.71

Table 2.1: Hydrate crystal structures and cage geometries for structure type I, II, and H hydrates (values after [129]).

dodecahedra and eight hexakaidecahedra that form a diamond lattice. In this structure type the small cavities occupy lattice points with cubic $\bar{3}m$ site symmetry whereas the large cavities are centered on positions with cubic $\bar{4}3m$ site symmetry.

The hexakaidecahedra ($5^{12}6^4$) consist of 12 pentagonal and four hexagonal faces (Figure 2.1). As each hexagon is surrounded by pentagonal faces, there are no hexagons sharing an edge. The $5^{12}6^4$ cavity follows the *Euler* theorem like the dodecahedra and the tetrakaidecahedra. With an average inner radius of 5.74 \AA the hexakaidecahedra are bigger than the $5^{12}6^2$ cages of structure type I (Table 2.1). Due to the symmetrical arrangement of the hexagonal faces, they are also the most spherical of all the cavities of the three common hydrate structures and can host molecules with a diameter as large as $d \sim 6.6 \text{\AA}$.

The ideal stoichiometry of a structure type II hydrate is given by $16 X \cdot 8 Y \cdot 136 H_2O$. As the large cage in structure II can contain bigger molecules as any of the cages in structure I, it was thought for a long time that structure II is only formed with guest molecules too large to fit in any of the cavities of structure I, such as propane or iso-butane. Both of these molecules occupy only the large cavity, leading to an ideal guest/water ratio of $8 Y \cdot 136 H_2O$. Later, *Davidson et al.* [31] showed that molecules too small to stabilize either of the $5^{12}6^2$ or $5^{12}6^4$ cavities could form structure II hydrates as the fraction of small 5^{12} cages in the unit cell is larger as for structure I. Therefore molecules or atoms with a diameter smaller than 4.2 \AA (e.g. N_2 , Ar, Kr) form structure II as well. Recently, both experimental and theoretical evidence has been presented that more than one guest

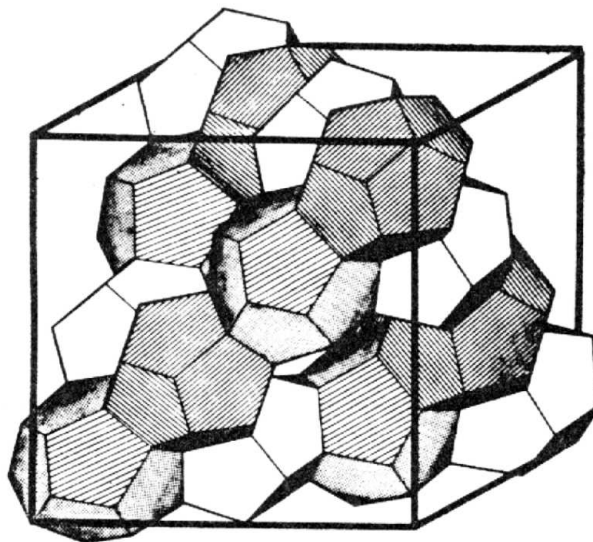


Figure 2.3: A schematic drawing of the unit cell of the cubic hydrate crystal structure II [92].

molecule or atom may be encaged in the large cavity of structure II [75, 63]. The smallest molecules with diameters less than 3 \AA , i.e. Helium or Hydrogen, are not large enough to stabilize the small 5^{12} cage and therefore do not form simple cage-like hydrate structures. These atoms were rather found to be included in the channels of ice structures.

2.1.3 Structure H

The structure type H is a hexagonal structure with the space group $P6/mmm$. The lattice constants are about $a=12 \text{ \AA}$ and $c=10 \text{ \AA}$ (Figure 2.4). The exact crystallographic structure was determined by a single crystal diffraction experiment on 2,2-dimethylpentane \cdot 5(Xe, H₂S) \cdot 34 H₂O hydrate [152]. It is formed by three different types of cages: three pentagonal dodecahedra (5^{12}), one 20-sided cavity, the icosahedron ($5^{12}6^8$), consisting of 12 pentagonal and 8 hexagonal faces, and two 12-sided irregular dodecahedra ($4^35^66^3$) (Figure 2.1). The latter cavity has the unusual property of following the *Euler* theorem without having 12 pentagonal faces. Additionally it contains square faces as found in silica compounds. The structure H is found to be iso-structural with clathrasil dodecasil-1H [40], subse-

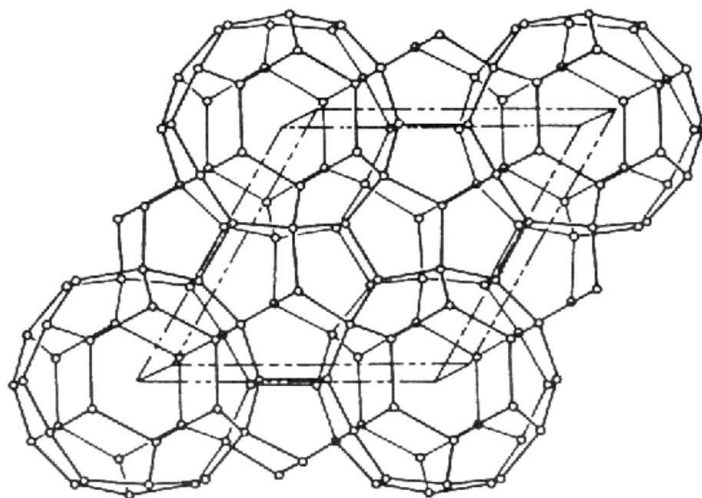


Figure 2.4: The unit cell of the hexagonal hydrate structure H [129].

quently allowing for new possible hydrate structures and guest species [111, 152].

The large $5^{12}6^8$ cages are situated on the edges of the c -axis, centered on sites with the $6/mmm$ site symmetry. The axes of the large cages perpendicular and parallel to the c -axis have an approximate length of 6.84 \AA and 8.85 \AA , respectively [152]. They are therefore the largest of the hydrate cages, able to encage guest molecules as large as cyclooctane. The centers of the small 5^{12} and $4^3 5^6 6^3$ cages are situated on sites with mmm and $\bar{6}2m$ symmetry, respectively. It is worth noting that both the $4^3 5^6 6^3$ and the $5^{12}6^8$ cavities are highly strained and significantly less spherical when connected in a structure H model compared to the free-standing cages shown in Figure 2.1.

Simple hydrates, containing only one guest species, do not form structure H. It is only formed with the help of small molecules (“help gas”) that fill the two small cages and large molecules fitting in the large cages. So the simplest stoichiometry would be $5 X \cdot 1 Y \cdot 34 H_2O$, and in general the guest/water ratio is given by $3 X \cdot 1 Y \cdot 2 Z \cdot 34 H_2O$, with Z referring to the $4^3 5^6 6^3$ cavities. The shape of the guest molecule seems to play an important role in structure H formation, e.g. by simple size considerations methyl butanes would fit well into the large cage of structure H but yet they are too spherical to stabilize the cavity and thus do not form hydrates [112]. As both structure I and II hydrates, the structure H hydrates can be found in nature, natural samples could be recovered in the Gulf of Mexico [116].

2.1.4 High Pressure Gas Hydrates

Clathrate hydrates forming one of the three common hydrate structures require mostly moderate pressures of a few hundred bar in order to be stable. It was thought until recently that the clathrates would dissociate at high pressures above about 10 kbar, e.g. methane hydrate was thought to dissociate into a high pressure phase of ice and solid methane [51].

It is however known that new gas hydrates form at higher pressures. Helium- and hydrogen-water systems do not form hydrates at moderate pressures but it was found that at higher pressures of a few thousand bar they would adopt structures related to ice-II and ice-I_c [154, 86]. The helium and hydrogen molecules are located in channels within the water network, which resembles that of the related ice phase. In contrast to the common hydrate structures where the guest molecules are located in cages whose diameter is much larger than the channels connecting them, the diameter of the channels in helium and hydrogen hydrate does not vary significantly. These structures are widely referred to as “filled-ices”. Hydrogen-ice has a hexagonal unit cell with the rhombohedral space group $R\bar{3}$ and lattice constants of about $a=12.7 \text{ \AA}$ and $c=5.9 \text{ \AA}$ at pressures between 7.5 kbar and 30 kbar. Above 23 kbar a second hydrogen hydrate structure was found that has a cubic unit cell of space group $Fd\bar{3}m$ with a lattice constant of about $a=6.4 \text{ \AA}$. The helium hydrate is found to have a hexagonal unit cell ($a \simeq 12.9 \text{ \AA}$ and $c \simeq 6.2 \text{ \AA}$) with the rhombohedral space group $R\bar{3}$. With the recent discovery of a structural transition of methane hydrate from a cage clathrate to a “filled-ice” at about 19 kbar, these structures seem to be a way to keep gas hydrates stable even under very high pressures [87]. The filled-ice structure of methane hydrate (MH-III) is related to ice-I_h, where the methane molecules are situated in the channels along the c -axis (Figure 2.5). It is found to have a body-centered orthorhombic unit cell, with unit cell dimensions of about $a=4.7 \text{ \AA}$, $b=8.1 \text{ \AA}$, and $c=7.8 \text{ \AA}$ and the space group $Imcm$.

Additionally, a second high-pressure structure of methane hydrate was found to be stable between 9 kbar and 19 kbar [23, 121]. It could be identified with a hexagonal unit cell with $a \simeq 11.8 \text{ \AA}$ and $c \simeq 9.9 \text{ \AA}$. The structure has yet to be solved, but it seems related to structure H, where two or more methane molecules would stabilize the large $5^{12}6^8$ cage [52, 88]. Cage-like high pressure hydrate structures have also been proposed for other guest molecules [53, 37], although these structures are still under discussion. However, the existing data suggest that the details of the high pressure structures depend strongly on the guest species and that they are likely to be determined by the repulsive gas-water potentials. Already hydrogen, helium, and methane form a diversity of clathrates and filled-ice structures that depend not only on the guest molecules or atom but also on the pressure. These new hydrate structures therefore open new possibilities to study hydrophobic interactions in detail.

The high pressure structures seem as well to be important for the understanding of processes on Earth and the outer solar system. They can occur in deep lying sediment layers or in permafrost regions, where pressures of a few kilobar may be reached. Methane

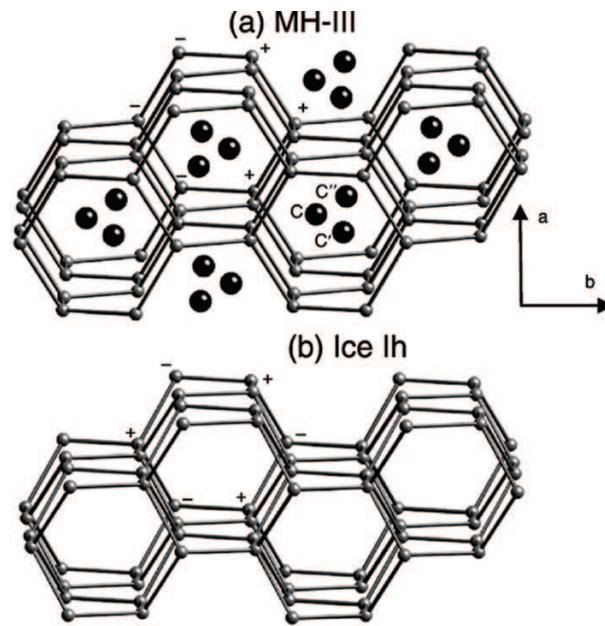


Figure 2.5: The structures of (a) “filled-ice” methane hydrate (MH-III) and (b) regular Ice I_h are shown projected parallel to the c -axis. The methane molecules can be seen in the channels of the water network of MH-III (a) [87].

hydrate is also thought to be the dominant methane-containing phase on Titan, Saturn’s largest moon [88]. These newly found structures suggest that further gas-water systems may be present under high pressure and may help to understand the nature of gas-water potentials.

2.2 Physical Properties of Gas Hydrates

All three low pressure hydrate structures consist at least to 85% of hydrogen bonded water molecules. Due to the non-stoichiometric nature of the hydrate structures the actual percentage of water in these structures is even higher. With such a high water content it is useful to consider some properties of hydrates as a variation from those of ice. This first approximation is supported by the hydrogen bond length and the O-O-O bond angles, which for both structure type I and II differ only very little from the bond length and tetrahedral angles in ice I_h [30]. The contribution of the guest molecules is, however, neglected in this approach.

Elastic properties could in some cases be estimated on the basis of the crystal structure of the hydrate itself. Properties like the sound velocity were based on estimations that the value for clathrate hydrates should be similar to that of ice [158]. Overall, it can be stated that there is a lack of precise experimental data for the elastic properties of gas hydrates. Only very recently precise elastic constants, the bulk modulus, and acoustic sound velocities of methane hydrate could be determined in a Brillouin light scattering

Property	Ice I_h	Structure I	Structure II
H ₂ O Reorientation Time at 273 K [μ sec]	21	~ 10	~ 21
H ₂ O Diffusion Jump Time at 273 K [μ sec]	2.7	>200	>200
Bulk Modulus [GPa]	8.8 (273 K) [39]	8.0 (296 K) [122]	—
Long. Sound Velocity [km/s]	3.8 (273 K)	3.7 (296 K) [122]	3.6 (273 K)
Therm. Expansion at 200 K [K^{-1}]	$56 \cdot 10^{-6}$	$77 \cdot 10^{-6}$	$52 \cdot 10^{-6}$
Therm. Conductivity at 263 K [W/(m·K)]	2.23	0.49	0.51

Table 2.2: Comparison of physical properties of ice I_h , structure I and structure II hydrates extrapolated to atmospheric pressure (Unless indicated, values after [129]). For structure II most of the values were estimated from the structure itself.

experiment [122]. These values are especially important to the field of natural gas hydrate research, as they play a role in hydrate detection and mechanical stability for instance.

Some dynamic properties of gas hydrates could, however, not be approximated by the properties of hexagonal ice. The motions of the water molecules in the host lattice were found to differ from that of ice I_h in nuclear magnetic resonance (NMR) experiments [32]. The water molecules are found to reorient 20 times faster than they diffuse in contrast to ice I_h , where the molecules diffuse ten times faster than they reorient. Overall the diffusion of water molecules in hydrates is two orders of magnitude slower than in regular ice (Table 2.2). The diffusive motion of the water molecules was also found to disappear for temperatures below 50 K, so the hydrate lattice becomes rigid at these temperatures.

The linear thermal expansion of clathrate hydrates has been determined by x-ray and neutron diffraction [146, 43]. For hydrate structure I it was found to be substantially larger than that of regular ice I_h . In the case of structure II hydrates the thermal expansion differed at low temperatures and approached the value of ice with increasing temperature. The relatively large thermal expansivity of the gas hydrates is thought to be attributed to an anharmonicity of the water lattice caused by encaged guest molecules.

Another intriguing property of gas hydrates is their thermal conductivity. *Stoll* and *Bryan* measured for the first time the thermal conductivity Λ of a gas hydrate (propane hydrate) and found it to be a factor five smaller (0.5 W/Km) than in ice I_h at $T=263$ K [140]. Even more surprisingly, the thermal conductivity is proportional to the temperature, similar to the behavior in glassy solids [113]. Since the discovery of this phenomenon, the thermal conductivity of several hydrate compounds has been measured [28, 49] and found to behave in a similar way. Very recently an effort was made to measure the temperature dependence of the thermal conductivity of tetrahydrofuran (Figure 2.6) and methane hydrate over a large range of temperatures. In order to explain the unusual thermal conductivity at least two different qualitative models have been proposed: (i)

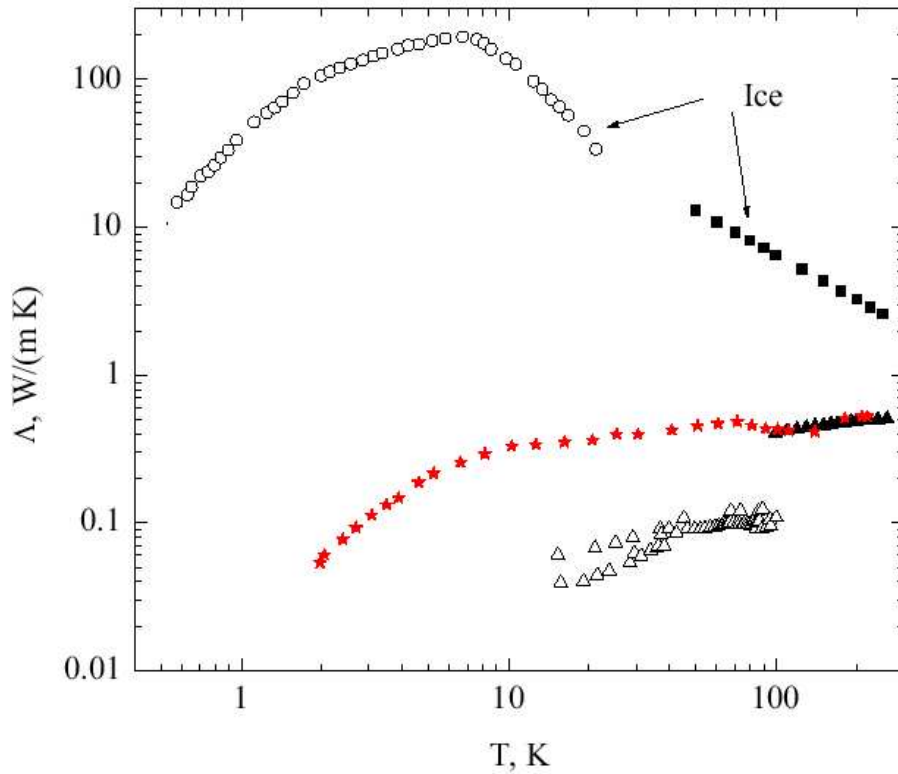


Figure 2.6: The thermal conductivity of tetrahydrofuran as measured by *Krivchikov et. al.* [73] (★) and of different gas hydrates from previous experiments (Δ, \blacktriangle) [147, 4], compared with the thermal conductivity of ice I_h (\circ, \blacksquare) [128, 70].

the large unit cell is leading to a limited phonon free path [35], and (ii) a coupling between low frequency vibrations of the guest and host molecules leads to effective phonon scattering [147]. In iso-structural Ge clathrates (alkali doped) the same behavior of the thermal conductivity was observed recently [25]. It was found to scale with the number of atoms n in the unit cell as $\Lambda \sim 1/n^{2/3}$ [36], reducing the thermal conductivity Λ considerably. In addition to the large unit cell and open framework structure, there are also guest atoms/molecules trapped inside the cages of the host structure, suggesting a further reduction of the thermal conductivity and possibly explaining its glass-like temperature dependence due to an interaction of the guests with the host network.

2.3 Formation of Gas Hydrates

In order to be able to make predictions on the formation conditions and thermodynamic phase equilibria a connection between the macroscopic properties and the microscopic structure and properties has to be found. Through the diffraction and spectroscopic experiments knowledge of the structural and molecular properties of the cavities and of

the encaged guest molecules was gained. On the basis of the crystallographic structure and the non-stoichiometry of hydrates, a statistical description of hydrates could be made. *van der Waals* and *Platteeuw* [155] developed a statistical thermodynamic model that treats the cages as adsorption sites that can be occupied by guest molecules. The model was developed on the basis of four basic assumptions:

- The free energy of the lattice is independent of the occupation of the cages. Under this premise the host lattice does not distort in the presence of guest molecules.
- Each cavity contains only one guest molecule and guest molecules do not diffuse.
- The energy of the guest molecules is independent of the number and types of molecules present.
- Classical statistics are valid.

With this model it is thus possible to predict hydrate equilibria and to describe hydrate composition as a function of pressure and temperature.

2.3.1 Thermodynamics and Pore Potentials

To statistically describe a simple hydrate, the starting point is a canonical partition function, which can be written as the product of a partition function of the empty clathrate lattice and of a partition function of the guest molecules [129]:

$$Q = \exp\left(-\frac{F^0}{kT}\right) \prod_i \left[\frac{(\nu_i N_w)!}{(\nu_i N_w - N_{M_i})! N_{M_i}!} q_{M_i}^{N_{M_i}} \right], \quad (2.1)$$

where F^0 is the free energy of the empty hydrate lattice, N_w is the number of water molecules, ν_i the number of cavities of type i per water molecule, and N_{M_i} is the number of molecules in the cavity of type i . q_{M_i} are the partition functions of the molecules inside the i -th cavity.

The grand canonical partition function Θ is then obtained from the canonical partition function Q by the transformation

$$\Theta = \sum_N Q e^{\mu N/kT}, \quad (2.2)$$

where μ is the chemical potential. As the chemical potential μ is related to the activity λ by

$$\lambda = e^{\mu/kT}, \quad (2.3)$$

equations (2.2) and (2.3) can be combined to give the grand canonical partition function

$$\Theta = \exp\left(-\frac{F^0}{kT}\right) \sum_{N_{M_i}} \prod_i \left[\frac{(\nu_i N_w)!}{(\nu_i N_w - N_{M_i})! N_{M_i}!} (q_{M_i} \lambda_{M_i})^{N_{M_i}} \right]. \quad (2.4)$$

The sum in equation (2.4) can be simplified using the multinomial theorem. The final partition function is then a product of terms for each cavity type:

$$\Theta = \exp\left(-\frac{F_0}{kT}\right) \prod_i (1 + q_{M_i} \lambda_M)^{\nu_i N_w}. \quad (2.5)$$

The thermodynamic potential can now be obtained from

$$d(kT \ln \Theta) = SdT + PdV + kTN_M d(\ln \lambda_M) - \mu_w dN_w, \quad (2.6)$$

where N_M is the number of engaged molecules M with activity λ_M , and μ_w is the chemical potential of the water molecules in the host lattice. Thus all of the macroscopic thermodynamic properties may be derived from equation (2.5). The total number of engaged molecules M in cavity for instance is given by

$$N_M = \sum_i N_{M_i} = \lambda_M (\partial \ln \Theta / \partial \lambda_M)_{T,V,N_w} = \sum_i \frac{\nu_i N_w q_{M_i} \lambda_M}{1 + q_{M_i} \lambda_M}. \quad (2.7)$$

The occupancy of a cage type i , which is given by the number of molecules M in this type of cavity divided by the number of cavities $\nu_i N_w$, can be calculated with the help of equation (2.7):

$$y_{M_i} = N_{M_i} / (\nu_i N_w) = \frac{q_{M_i} \lambda_M}{1 + q_{M_i} \lambda_M}. \quad (2.8)$$

In order to have a more direct access to an important quantity like the cage occupancy of a hydrate, it is suitable to express the activity λ_M and the molecular partition function q_{M_i} through a quantity more readily accessible to experiments. They may be taken into account through a constant

$$C_{M_i} = \frac{q_{M_i} \lambda_M}{P_M}, \quad (2.9)$$

and thus the occupancy of a cage becomes a function of the partial pressure P_M and can be written in the form of a Langmuir-isotherm:

$$y_{M_i} = \frac{C_{M_i} P_M}{1 + C_{M_i} P_M}, \quad (2.10)$$

accordingly C_{M_i} is called Langmuir-constant of a gas hydrate. The stability and the phase diagram of gas hydrates may be obtained with the help of the chemical potential of the water inside the hydrate that can now be expressed as a function of the fractional cage occupation. The chemical potential is given by

$$\begin{aligned} \mu_w &= -kT (\partial \ln \Theta / \partial N_w)_{T,V,\lambda_M} \\ &= \mu_w^0 - kT \sum_i \nu_i \ln(1 + q_{M_i} \lambda_M) = \mu_w^0 + kT \sum_i \nu_i \ln(1 - y_{M_i}), \end{aligned} \quad (2.11)$$

where μ_w^0 is the chemical potential of the empty clathrate lattice. Equation (2.11) shows that with increased filling of the cages the chemical potential is lowered and the hydrate

becomes thermodynamically more stable. Therefore with the help of equations (2.10) and (2.11) (p,T) phase equilibria and hydrate compositions can be calculated at a constant pressure and temperature.

The Langmuir constant can be related to experimental variables if the potential energy of the guest molecules inside the cavities is known. The *spherical cell approximation* introduced by *van der Waals* and *Platteeuw* can describe the intermolecular potentials by a pair potential and thus it is possible to calculate the Langmuir constant C_M from the guest host interactions. In order to be applicable, two restrictive assumptions have to be made:

- Rotational and translational energies of the guest molecules are the same as in an ideal gas.
- The potential energy of the guest molecules can be described by the spherical symmetric potential $\omega(r)$ proposed by *Lennard–Jones* and *Devonshire* [81, 82].

A 12-6 Lennard–Jones potential was used originally to calculate the guest–host interaction in hydrates. The pair potential is a function of the distance between two particles and is given by:

$$V(r) = \begin{matrix} \infty & \text{for} & r \leq 2a \end{matrix} \quad (2.12)$$

$$V(r) = 4\epsilon \left[\left(\frac{\sigma}{r-2a} \right)^{12} - \left(\frac{\sigma}{r-2a} \right)^6 \right] \quad \text{for} \quad r > 2a \quad (2.13)$$

where σ , a , and ϵ are the cores distance, the core radius, and the maximum attractive potential, respectively. These potential parameters are unique to every guest molecule. In the *spherical cell approximation* the pair potentials of the guest and each water molecule are then averaged over all the water molecules in the cavity walls, thus yielding the cell potential $\omega(r)$ that is only depending on the distance r of the guest molecule from the cage center:

$$\omega(r) = 2z\epsilon \left[\frac{\sigma^{12}}{R^{11}r} \left(\delta^{10} + \frac{a}{R}\delta^{11} \right) - \frac{\sigma^6}{R^5r} \left(\delta^4 + \frac{a}{R}\delta^5 \right) \right], \quad (2.14)$$

with R the mean free cavity radius, z the number of water molecules in the cage wall and

$$\delta^N = \frac{1}{N} \left[\left(1 - \frac{r}{R} - \frac{a}{R} \right)^{-N} - \left(1 + \frac{r}{R} - \frac{a}{R} \right)^{-N} \right]. \quad (2.15)$$

The parameters for the z and R do not change with the guest molecules as it was assumed that there would not be any cage distortions due to the enclathration of the guest molecules. From the cage potential an expression for the partition function of the guest molecules can be found, and thus the Langmuir constant can be expressed in terms of the particle potential within the cavity:

$$C_{M_i} = \frac{4\pi}{kT} \int_0^R e^{\left(-\frac{\omega(r)}{kT}\right)} r^2 dr. \quad (2.16)$$

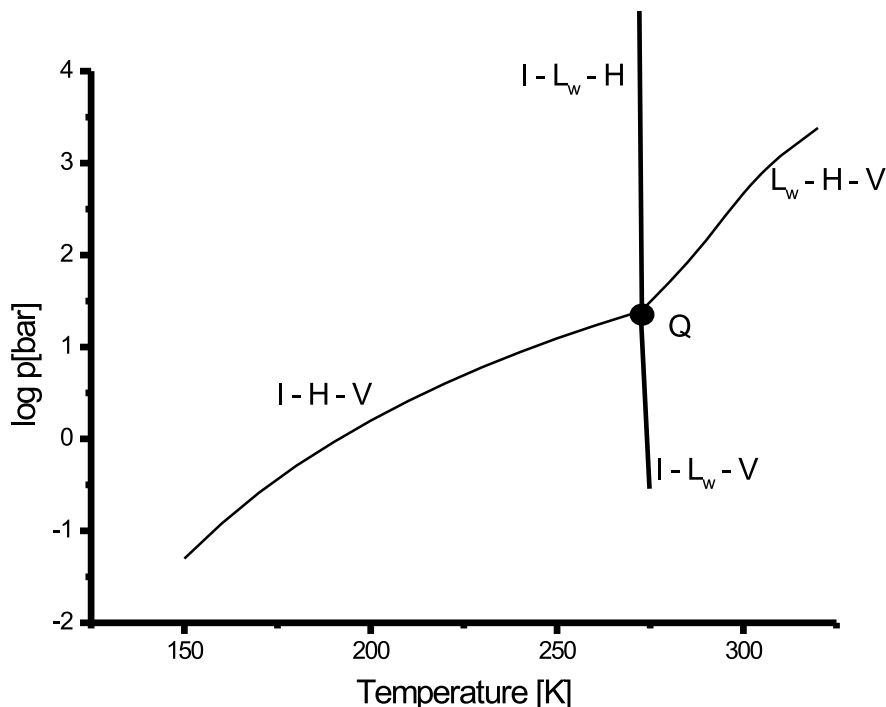


Figure 2.7: Theoretical (p,T) phase diagram of methane gas and water/ice. Methane hydrate is stable at low temperatures and high pressures above the L_w -H-V and the I-H-V three-phase lines that mark the coexistence of liquid water (L_w), hydrate (H), vapor (V) and Ice (I), hydrate, vapor, respectively.

The Langmuir constant may then be determined from a set of experimentally fitted potential parameters. Generally they are determined from equilibrium temperature–pressure data or dissociation pressure data. The advantage of this method is that from the knowledge of formation data for simple hydrates, mixtures of those guest components can be easily predicted.

2.3.2 Stability and Pressure–Temperature Diagrams

The original statistical thermodynamic model for hydrate equilibria was generalized by *Parrish* and *Prausnitz* [100] in order to predict hydrate dissociation pressures. The method was further simplified by introducing a set of reference properties for each hydrate structure [54]. This methodology is now widely used in computer programs for thermodynamic and equilibrium calculations of gas hydrates [129].

The phase equilibria of clathrate hydrates differ widely from those of regular ice I_h . In Figure 2.7 the pressure–temperature (p,T) phase–diagram for methane and water is shown as predicted by the program of *Sloan* et. al. In the pressure and temperature region that is considered here, the methane has to be taken into account in its gas phase only. The phases present in the diagram are therefore ice (I), liquid water (L_w), hydrate (H), and vapor (V). An area is a region of co–existence of two phases, a line of three, and

a point of all four phases. The quadruple point Q is found at a temperature of around 273 K, which is similar for all hydrate formers, whereas the quadruple pressure varies substantially with the guest molecule. From the quadruple point the four three-phase lines start. The L_w -H-V and the I-H-V lines mark the stability limit of methane hydrate, that can only exist above these two lines. The I- L_w -H line rises almost vertically from the quadruple point, due to the low compressibility of the three phases. The I- L_w -V line is connecting the quadruple point Q with the triple point of water.

Of special interest for natural gas hydrate systems is the L_w -H-V line. It displays the stability limits of e.g. marine hydrate deposits: at pressures and temperatures above the line water and hydrate are stable beneath it water and gas. As the water temperature found in the deep ocean is about 4°C, it can be seen from the diagram that under the presence of free methane gas, methane hydrate will form below depths of about 400 m. Phase diagrams are also important to the natural gas industry. As both solid hydrates and ice cause flow problems in pipelines, the temperature has to be kept above the ice point to the right of the I- L_w -V line and the pressure below the L_w -H-V line.

2.4 Natural Methane Hydrate

Methane hydrate is stable at low temperatures and moderate pressures only. From the phase diagram (Figure 2.8) it can be estimated that methane hydrate would occur in nature in two regions: (i) permafrost regions where it would form at low temperatures form ice (continental hydrates) and (ii) deep sea sediments where the water temperature and the hydrostatic pressure correspond to the stability conditions (oceanic hydrates). In both cases the stability zone is limited by the geothermal gradient leading to increasing temperatures in the sediment with increasing depth. In the stability zones the free gas or gas-saturated water has to be sealed by a relatively impermeable layer of sediments, permafrost, or hydrate as it is less dense than water. Therefore the hydrate will form in the sediments and it can attain layers with a thickness of up to several 100 m [78].

The methane gas needed for the formation of gas hydrates may be either thermogenic or biogenic. Deep in the sediments, thermogenic gas is produced at temperatures above 100°C. It then has to diffuse upwards through channels and rifts to the hydrate stability zone. The biogenic gas which is thought to dominate in hydrates, can be formed *in situ* in sediments in the hydrate stability zone through low temperature chemical or biogenic conversion of organic matter into methane [129]. A high rate of sedimentation ($> 30 \text{ m}/10^6 \text{ yr}$) is required in order to provide the organic matter necessary for the hydrate formation. Biogenic hydrates thus occur on oceanic continental margins rich in organic matter, whereas thermogenic hydrates are common in tectonic active areas. Thermogenic and biogenic hydrates can be distinguished by the mass and the ratio of ^{13}C to ^{12}C isotopes of the included gas. Thermogenic gases contain a relative large amount of higher hydrocarbons, e.g. ethane or propane, whereas biogenic hydrates contain a higher fraction of the ^{12}C isotope as the CO_2 formed during the organic matter decomposition is enriched

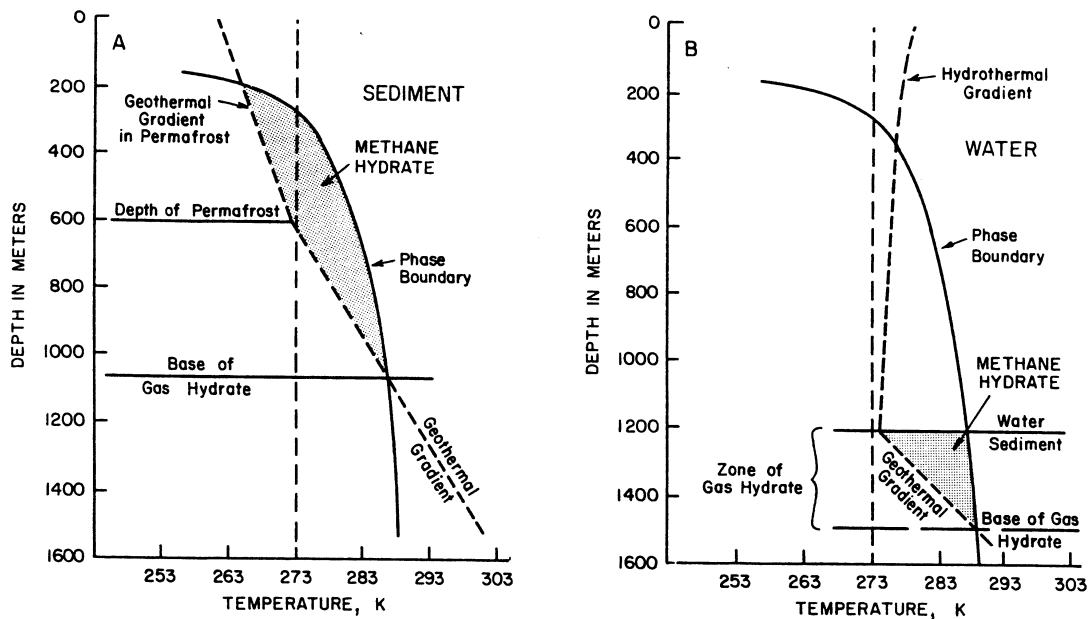


Figure 2.8: Methane hydrate stability zones in (A) permafrost and (B) in ocean sediments. The stability zones are limited by the geothermal gradient in the sediment or permafrost and the presence of sediments [129].

in ^{13}C .

Natural deposits of gas hydrates are identified either by sampling for both deep sea and continental hydrates or more indirectly by sonic seismic reflection methods for deep sea or continental margin hydrates. The seismic reflection methods use bottom simulating reflectors (BSRs) to identify possible locations of gas hydrates. The BSR is characterized by a strong decrease of the seismic impedance (velocity multiplied by density), pointing towards a decrease in velocity. The negative impedance at a BSR might be interpreted as a partial replacement of the sediment pore water by hydrates. As hydrates may also lead to an impermeability of the sediments, they can act as traps for free gas below the hydrate layers. The contrast between the higher velocity in hydrated sediments and the low velocity of free gas significantly contributes to the occurrence of a BSR.

The difficulties in hydrate detection lead to a relatively poor knowledge about the hydrate distributions on Earth. Figure 2.9 shows known and derived locations of gas hydrates. As the occurrence of oceanic hydrate exceeds the continental hydrates by more than two orders of magnitude, most of the economic interest is directed towards the hydrates found in oceanic reservoirs. Conservative estimates of the gas contained in hydrates are of the order of 10^{16} m^3 , which exceeds the conventional deposits of fossil fuels by a factor of two, leading to a potentially large economic significance of hydrates [79]. The recovery of the energy contained in gas hydrates is rather difficult, as they are

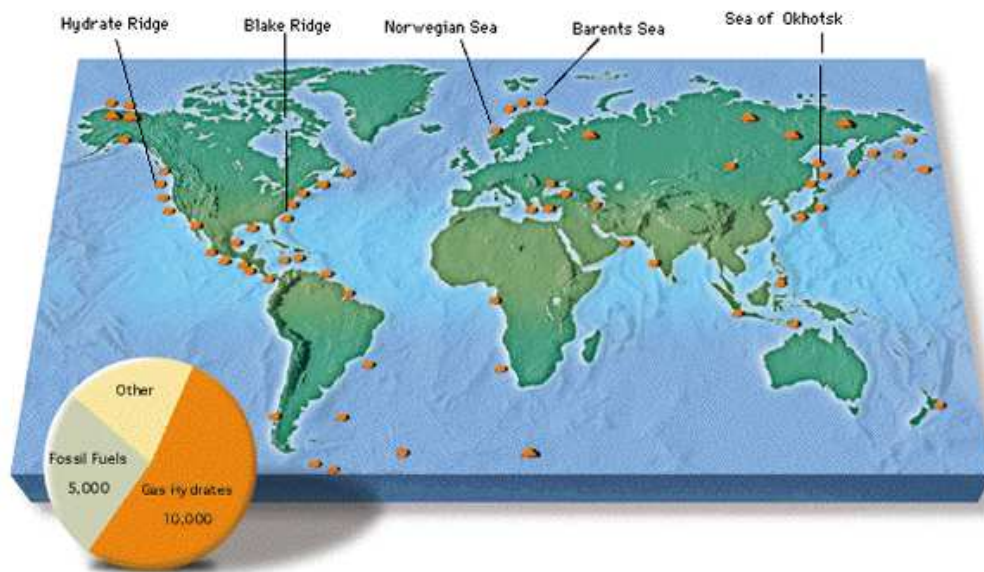


Figure 2.9: Map of known continental and oceanic gas hydrate deposits. Most of the hydrate deposits were found on the oceanic continental margins. The hydrocarbon contained in gas hydrates are thought to exceed the deposits of conventional fossil fuels by a factor of two.

dispersed in the sediments on the ocean floor in contrast to natural gas and oil reservoirs. The economic interest in gas hydrates can nevertheless be illustrated by first production tests of methane gas from continental hydrates at the Mallik field in Canada [1].

There is also a large geological interest in natural gas hydrates as large amounts of oceanic hydrates were recovered by the GEOMAR Institute of the University Kiel [141] (Figure 2.10). The natural hydrates recovered from GEOMAR did not only contain methane but were mixed hydrates of CH_4 , H_2S , and traces of higher hydrocarbons [13]. Hydrates in sediments are suggested to occur in nodular, layered, or massive form. The stability of the hydrates may therefore be important for slope failures [12], where the dissociation of hydrates may lead to a weakness in the sediment column. The methane released during decomposition is thought to contribute to the global carbon budget [93] and thus might play a role in the global warming. Recently, it was also discovered that both natural and synthetic hydrates have a mesoporous structures [76]. This porosity may influence the estimations of the amount of hydrocarbons in gas hydrates and may have other consequences, e.g. implications on the mechanical properties of gas hydrates.



Figure 2.10: Natural methane hydrate sample collected by GEOMAR from the *Hydrate Ridge* in the north Pacific Ocean. The white methane hydrate is covered with a layer of sediment.

Chapter 3

Lattice Dynamics Calculations

In the previous chapter the static crystal lattice of gas hydrates have been described in detail. However, at non-zero temperatures every atom in the crystal has some thermal energy and therefore performs small motions around its equilibrium position. These lattice vibrations affect equilibrium properties, e.g. specific heat, thermal expansion, thermal conductivity, or transmission of sound, and can be observed in inelastic scattering experiments with light, x-rays, or neutrons. The theory of lattice dynamics or *phonons* was developed to understand these phenomena [5, 41, 132]. In the following sections a short introduction into lattice dynamics calculations will be given in order to link the theory to experimental quantities and to develop lattice dynamical models for clathrate hydrates.

3.1 Force Constants and Dynamical Matrix

In the static model an atom is found at its equilibrium position in a general lattice. The general equilibrium atomic positions are given by

$$\bar{\mathbf{R}}(m\mu) = \bar{\mathbf{A}}(m) + \bar{\mathbf{R}}(\mu), \quad (3.1)$$

where $\bar{\mathbf{R}}(\mu)$ is the position of atom μ in the unit cell m with position $\bar{\mathbf{A}}(m)$. The atom is now assumed to oscillate about this position. In the *harmonic approximation* the displacements of the atom relative to its neighbors are assumed to be small compared to the interatomic distances in the lattice. The instantaneous position of an atom is thus given by

$$\mathbf{R}(m\mu) = \bar{\mathbf{R}}(m\mu) + \mathbf{s}(m\mu), \quad (3.2)$$

where $\mathbf{s}(m\mu)$ is the small displacement of the atom μ in the unit cell m from its equilibrium position. For small displacements the potential energy of the crystal lattice may be expanded around its minimum:

$$\begin{aligned} U &= U_0 + \sum_{m\mu i} \Phi_i(m\mu) s_i(m\mu) + \frac{1}{2} \sum_{m\mu i, n\nu k} \Phi_{ik}(m\mu; n\nu) s_i(m\mu) s_k(n\nu) + \dots \\ &= U_0 + U_1 + U_2 + \dots, \end{aligned} \quad (3.3)$$

where $i, k = 1, 2, 3$ denote the directions in Cartesian coordinates. The coefficients in the expansion (3.3) are the derivatives of the potential energy U at the equilibrium positions

$$\Phi_i(m\mu) = \left. \frac{\partial U}{\partial s_i(m\mu)} \right|_0 \quad (3.4)$$

$$\Phi_{ik}(m\mu; n\nu) = \left. \frac{\partial^2 U}{\partial s_i(m\mu) \partial s_k(n\nu)} \right|_0. \quad (3.5)$$

In the dynamical problem U_0 is not important and can be set to zero with an according normalization. U_1 vanishes in the equilibrium configuration, leading to the following expression for the harmonic potential energy of the crystal:

$$U_{harm} = \frac{1}{2} \sum_{m\mu i, n\nu k} \Phi_{ik}(m\mu; n\nu) s_i(m\mu) s_k(n\nu). \quad (3.6)$$

The equations of motion can now be expressed in terms of the harmonic potential U_{harm}

$$M_\mu \ddot{s}_i(m\mu) = - \frac{\partial U_{harm}}{\partial s_i(m\mu)} = - \sum_{n\nu k} \Phi_{ik}(m\mu; n\nu) s_k(n\nu) \quad (3.7)$$

with M_μ the mass of the atom, $\mu, \nu = 1, 2, \dots, p$ (p : number of atoms per unit cell), and Φ the *force constant matrix* defined by equation (3.5). The force constant can be understood as the force acting on the atom ($m\mu$) in the direction i if the atom ($n\nu$) is displaced a distance s in direction k , while all the other atoms stay in their equilibrium position. The force constants have two important symmetry properties. As every crystal lattice has a *lattice translational symmetry* the force constants do not depend on the unit cells m and n , but only on the difference between the unit cells m and n . Therefore the force constants can be written as

$$\Phi_{ik}(m\mu; n\nu) = \Phi_{ik}((m-n)\mu; (n-n)\nu) = \Phi_{ik}((m-n)\mu; 0\nu) = \Phi_{ik}^h(\mu; \nu), \quad (3.8)$$

with $h = m - n$. This means that a reference unit cell may be chosen arbitrarily when calculating the force constant matrix. Additionally, an infinitesimal translation or rotation does not change the force constants, i.e. if all the atoms are displaced equally, there is no force acting on any atom. This leads to the *infinitesimal translational invariance*

$$\sum_{h\mu} \Phi_{ik}^h(\mu; \nu) = 0. \quad (3.9)$$

Within the harmonic approximation the lattice dynamics of a crystal with p atoms is analyzed in term of the $3p$ equations of motion (3.7) or $3p$ *normal modes*. The quantum of energy associated with such a normal mode is called *phonon*. The aim of lattice dynamics is to find the normal modes of a crystal. The set of differential equations (3.7) can be solved with a plain wave ansatz of the form

$$s_i(m\mu) = \epsilon_i^\mu(\mathbf{q}) e^{i(\mathbf{q} \cdot \bar{\mathbf{R}}(m\mu) - \omega t)} \quad (3.10)$$

where \mathbf{q} is the direction of propagation, $\epsilon^\mu(\mathbf{q})$ is a vector that describes both the direction and the amplitude of the atomic movements. Substituting (3.10) into (3.7) leads to

$$M_\mu \omega^2 \epsilon_i^\mu(\mathbf{q}) = \sum_{\nu k} D_{ik}(\mu\nu; \mathbf{q}) \epsilon_k^\nu(\mathbf{q}), \quad (3.11)$$

for which non-trivial solutions are found by solving the secular equation

$$\det |D_{ik}(\mu\nu; \mathbf{q}) - \omega^2 \delta(ik) \delta(\mu\nu)| = 0. \quad (3.12)$$

The matrix $D_{ik}(\mu\nu; \mathbf{q})$ is given by

$$D_{ik}(\mu\nu; \mathbf{q}) = \frac{1}{M_\mu} \sum_h \Phi_{ik}^h(\mu; \nu) e^{-i\mathbf{q} \cdot [\bar{\mathbf{A}}(h) + \bar{\mathbf{R}}(\mu) - \bar{\mathbf{R}}(\nu)]}, \quad (3.13)$$

where $\bar{\mathbf{A}}(h) = \bar{\mathbf{A}}(m) - \bar{\mathbf{A}}(n)$. The hereby defined $(3p \times 3p)$ matrix is called the *dynamical matrix* of the system. As $\Phi_{ik}^h(\mu; \nu) = \Phi_{ki}^{-h}(\nu; \mu)$ the dynamical matrix is hermitian:

$$D_{ik}^*(\mu\nu; \mathbf{q}) = D_{ki}(\nu\mu; \mathbf{q}), \quad (3.14)$$

with $3p$ real eigenvalues $\omega^2(\mathbf{q}s)$, $s = 1, 2, \dots, 3p$. The eigenvalues are also assumed to be positive in order to satisfy the condition of a stable crystal. For each eigenvalue at a given \mathbf{q} an eigenvector $\mathbf{e}^\mu(\mathbf{q}s)$ exists. These eigenvectors satisfy ortho-normality and completeness relations [132]. Equation (3.11) can thus be expressed in term of eigenvalues and eigenvectors as

$$\omega^2(\mathbf{q}s) e_i^\mu(\mathbf{q}s) = \sum_{\nu k} D_{ik}(\mu\nu; \mathbf{q}) e_k^\nu(\mathbf{q}s). \quad (3.15)$$

A complete solution of the eigenproblem leads to the *phonon dispersion relation* that is presented as the eigenfrequencies ω of the normal modes as a function of their wave vector \mathbf{q} , namely $\omega = \omega(\mathbf{q}s)$. The index s denotes a branch in the phonon dispersion. The eigenvectors $\mathbf{e}^\mu(\mathbf{q}s)$ of each branch s are called the polarization vectors as they define the direction of the motion of each atom μ with respect to the propagation direction \mathbf{q} of the phonon. The $3p$ phonon branches of a crystal can be divided into 3 acoustic branches whose eigenfrequencies ω vanish linearly with \mathbf{q} in the long wavelength limit ($\mathbf{q} \rightarrow 0$) and $(3p - 3)$ optic branches whose eigenfrequencies approach constant values in the long wavelength limit.

In an isotropic crystal or isotropic elastic medium it is always possible to find solutions for a given wave vector such that the atomic displacements for both acoustic and optic branches are either in the direction of propagation ($\mathbf{e} \parallel \mathbf{q}$) or perpendicular to it ($\mathbf{e} \perp \mathbf{q}$). These branches are called *longitudinal* and *transverse*, respectively. In an anisotropic crystal this is not true in general. Only in the long wavelength limit, or for the propagation along high symmetry directions of the crystal, it is possible to construct solutions with three polarization vectors that are either parallel or perpendicular to the propagation direction. In the case of a cubic crystal for example the concept of pure longitudinal and transverse polarization is only valid for $|\mathbf{q}| \rightarrow 0$ or when \mathbf{q} is along the [001], [011], or [111] symmetry directions. In general directions the atomic displacements will be a mixture of both longitudinal and transverse contributions.

3.2 Density of States – DOS

Macroscopic properties like the specific heat depend upon the density of the normal modes or *density of states* [5]. The density of states is defined as the number of normal modes within an infinitesimal frequency interval $[\omega, \omega + d\omega]$ ($g(\omega)$), or between wave vectors \mathbf{q} and $\mathbf{q} + d\mathbf{q}$ ($\tilde{g}(\mathbf{q})$). By using periodic boundary conditions on a cube with a side length L containing N^3 primitive unit cells the number of allowed \mathbf{q} -values per unit volume is found to be

$$\left(\frac{L}{2\pi}\right)^3 = \frac{N_0\Omega}{(2\pi)^3} \quad (3.16)$$

with $N_0\Omega$ being the volume of N_0 unit cells. To find an expression for $g(\omega)$ the volume of a cylinder between two surfaces of constant frequencies ω and $\omega + d\omega$ is considered. The volume of such a cylinder with an area dS_ω on the constant frequency surface and a height dq_\perp is given by

$$\int dS_\omega dq_\perp = \int dS_\omega \frac{d\omega}{|\nabla_{\mathbf{q}}\omega|}, \quad (3.17)$$

as $\nabla_{\mathbf{q}}\omega$ is perpendicular to the constant frequency surface. As the density of momentum space is $N_0\Omega/8\pi^3$ (3.16), the number of \mathbf{q} -values in the cylindrical volume is given by

$$\begin{aligned} g(\omega)d\omega &= \frac{N_0\Omega}{(2\pi)^3} \times \text{volume of cylinder} \\ &= \frac{N_0\Omega}{(2\pi)^3} \int dS_\omega \frac{d\omega}{|\nabla_{\mathbf{q}}\omega|}. \end{aligned} \quad (3.18)$$

Thus, if the dispersion relation $\omega(\mathbf{q}s)$ in a crystal is known, the density of states can be represented in the form

$$g(\omega) = \frac{N_0\Omega}{(2\pi)^3} \sum_s \int \frac{dS_\omega}{|\nabla_{\mathbf{q}}\omega(\mathbf{q}s)|}, \quad (3.19)$$

where s is the branch index and the integration is over surfaces of constant energy $\omega = \omega(\mathbf{q}s)$. As $\omega(\mathbf{q}s)$ is periodic, there must be \mathbf{q} -values for each branch s in each primitive unit cell where $|\nabla_{\mathbf{q}}\omega(\mathbf{q}s)| = 0$. Such \mathbf{q} -points are called critical points and the according singularities in the density of states are called *van Hove* singularities.

In general, the density of states $g(\omega)$ of a crystal is calculated numerically. In such a calculation a realistic integration over the Brillouin zone of the crystal is important, requiring the knowledge of phonon frequencies for wave vectors over the entire Brillouin zone. The size of the Brillouin zone might be reduced by point symmetry operations but the integration still remains laborious. A simple approximation was made by *Debye*. All normal modes lying within a sphere of radius q_D that is centered at the Brillouin zone center, are assumed to have a linear dispersion $\omega(\mathbf{q}s) = v_s q$, where v_s is the constant sound velocity. The density of states can then be calculated from (3.19)

$$g(\omega) = \frac{N_0\Omega}{(2\pi)^3} \sum_s \frac{1}{v_s} \int dS_\omega = \frac{3N_0\Omega}{2\pi^2} \cdot \frac{\omega^2}{v^3}, \quad (3.20)$$

where $\sum_s 1/v_s^3 = 3/v$. The Debye radius q_D was determined such that the volume of the sphere contains $3N$ for N unit cells. It is therefore given by

$$k_B\theta = \hbar\omega_D = \hbar v q_D = \hbar v \left(\frac{6\pi^2 N}{N_0\Omega} \right)^{1/3} \quad (3.21)$$

with ω_D denoting the Debye frequency and θ_D the Debye temperature (k_B : Boltzmann's constant) of the crystal. The Debye density of states is a function of the phonon frequency $g(\omega) \propto \omega^2$. For energies below the first maximum of acoustic phonons it is often a good approximation of experimental densities of states.

A more realistic density of states can be calculated based on the following expression of equation (3.19)

$$g(\omega) = \frac{N_0\Omega}{(2\pi)^3} \sum_s \int d\mathbf{q} \delta(\omega - \omega(\mathbf{q}s)). \quad (3.22)$$

By sampling the eigenfrequencies at a large set of \mathbf{q} -points in the irreducible part of the Brillouin zone the density of states can be obtained as a histogram with

$$g(\omega) = \text{const.} \cdot \sum_{\mathbf{q}s} \delta_{\Delta\omega}(\omega - \omega(\mathbf{q}s)) \quad (3.23)$$

and

$$\delta_{\Delta\omega}(x) = \begin{cases} 1, & -\frac{\Delta}{2} < x < \frac{\Delta}{2} \\ 0, & \text{otherwise} \end{cases}.$$

Here, $\Delta\omega$ is the frequency interval in the histogram. It should be set to an appropriately small energy depending on the energy range of the density of states (usually, $\Delta\omega \sim 0.1$ meV). In order to obtain reliable results the number of sampling wave vectors should be in the range of 10^3 – 10^5 for complex or simple crystals, respectively. This high number of points can render this method somewhat time consuming for bigger crystal system. The calculated mode density is usually normalized

$$\int d\omega g(\omega) = 1, \quad (3.24)$$

by choosing the constant accordingly. Additionally, the notion of a *partial density of states* is of interest. It describes the contribution of an atom μ vibrating along a Cartesian coordinate i to the mode density and is defined as [99]

$$g_i^\mu(\omega) = \text{const.} \cdot \sum_{\mathbf{q}s} |e_i^\mu(\mathbf{q}s)|^2 \delta_{\Delta\omega}(\omega - \omega(\mathbf{q}s)). \quad (3.25)$$

As the eigenvectors are normalized as well the sum of the partial densities of states leads to the total density of states. The *off-diagonal partial density of states* is defined as

$$g_{ik}^\mu(\omega) = \text{const.} \cdot \sum_{\mathbf{q}s} e_i^\mu(\mathbf{q}s) e_k^{*\mu}(\mathbf{q}s) \delta_{\Delta\omega}(\omega - \omega(\mathbf{q}s)). \quad (3.26)$$

Both diagonal and off-diagonal density of states can be used to calculate thermodynamic properties of a crystal. Properties like the free energy, the entropy, or the heat capacity depend on the diagonal mode density. The thermal displacements of an atom can be expressed by the off-diagonal terms and thus Debye–Waller factors may be calculated.

3.3 Phenomenological Models for a Clathrate Hydrate

A basic problem of the lattice dynamics of a crystal is to find a model for the interatomic forces. One of the first models proposed by *Born* in 1914 [14] was an interatomic potential with nearest-neighbor central and non-central force constants. This model generally failed for calculating the frequencies and dispersion of transverse acoustic phonons away from the zone center. This is mainly due to the neglect of long-range interactions.

In the Born-von Karman model [15] the interatomic potential was expressed by central force constants $\Phi_{ik}(m\mu; n\nu)$ between atoms ($m\mu$) and ($n\nu$). The number of force constants for a given structure could be reduced due to symmetry operations of the potential and of the space group of the crystal. There is always a lowest number of force constants necessary to stabilize the crystal structure. In order to describe dispersion curves the number of force constants can be increased to include interactions between more distant atoms. The force constant could be determined from fits to experimental data. But the physical relevance of the chosen set of force constants was not always clear.

A more general description of interatomic force fields is to express the potential energy of a crystal in terms of internal displacements. Such a potential may be written as a function of empirical interaction functions [130]:

$$\begin{aligned}
 U(\mathbf{r}_1, \mathbf{r}_2, \dots, \mathbf{r}_N) = & \sum_i U_{bond}(i, \mathbf{r}_a, \mathbf{r}_b) \\
 & + \sum_i U_{angle}(i, \mathbf{r}_a, \mathbf{r}_b, \mathbf{r}_c) \\
 & + \sum_i U_{dihed}(i, \mathbf{r}_a, \mathbf{r}_b, \mathbf{r}_c, \mathbf{r}_d) \\
 & + \sum_i U_{inv}(i, \mathbf{r}_a, \mathbf{r}_b, \mathbf{r}_c, \mathbf{r}_d) \\
 & + \sum_{i,j} U_{pair}(i, j, |\mathbf{r}_i - \mathbf{r}_j|) \\
 & + \sum_{i,j,k} U_{3-body}(i, j, k, \mathbf{r}_i, \mathbf{r}_j, \mathbf{k}_k) \\
 & + \sum_{i,j,k,l} U_{4-body}(i, j, k, l, \mathbf{r}_i, \mathbf{r}_j, \mathbf{k}_k, \mathbf{r}_l)
 \end{aligned} \tag{3.27}$$

where U_{bond} , U_{angle} , U_{dihed} , U_{inv} , U_{pair} , U_{3-body} , U_{4-body} are the interaction functions for the bonds, valence angles, dihedral angles, inversion angles, 2-body, three-body, and four-body forces, respectively. Additionally, the long ranged electrostatic (Coulomb) potentials has to be included.

In the following a simplified model for clathrates hydrates based on central harmonic forces will be developed. A more realistic description of the lattice dynamics of gas hydrates is then introduced using interatomic forcefields based on empirical potential functions.

3.3.1 Central Harmonic Forces and Rigid Cages

In proton disordered structures symmetries are always related to the averaged crystallographic structure. In the dynamical problem the time-averaged crystallographic structure can no longer be used, instead single realizations of a unit cell have to be considered. For these “snap-shots” the crystal symmetries are no longer valid. Therefore every atom in the unit cell contributes to the dynamical problem. In the case of a structure type I hydrate with spherical guest molecules or atoms this leads 146 atoms in the unit cell. Due to this number of atoms the resulting dispersion relation contains a large number of branches, which become difficult to interpret. The task of analyzing the $3p$ -dimensional polarization vectors for p atoms in the unit cell may be even more tedious. In a first instance it is therefore attempted to simplify the problem as much as possible and to approximate the distinct characteristics of the hydrate structure in order to obtain a dynamical problem that is simple to handle but that may yet help to understand the complex dynamics of a regular hydrate structure.

The first simplification is to assume central harmonic forces between all the masses in the structure. It is assumed that the water cages are not distorted by the guest molecules (s. Section 2.3), the cages will therefore be considered as rigid boxes in the simplified model. This “box-clathrate” is assumed to have a simple cubic crystal structure with cubic boxes of mass M_c situated on the corners of the unit cell with lattice parameter a (Fig. 3.1). To describe a simple cubic structure with central harmonic forces, interactions up to the third neighbor have to be included. The guest molecules will be approximated by point masses M_g inside the boxes interacting only with the six box walls by a central harmonic force.

A central force $\mathbf{F}(m\mu; n\nu)$ with force constant α acting between two masses ($m\mu$) and ($n\nu$) can be expressed in terms of their displacements $\mathbf{s}(m\mu)$ and $\mathbf{s}(n\nu)$ from their equilibrium positions $\bar{\mathbf{R}}(m\mu)$ and $\bar{\mathbf{R}}(n\nu)$, respectively. Let $\varepsilon(n\nu)$ be the unit vector pointing along the line between the two equilibrium positions then in the limit of small displacements the force can be expressed as follows:

$$F_i(m\mu; n\nu) = \alpha \varepsilon_i(n\nu) \sum_k \varepsilon_k(n\nu) (s_k(n\nu) - s_k(m\mu)). \quad (3.28)$$

In the box-clathrate let α_1 , α_2 , and α_3 denote the force constants of the first, second, and third neighbor interaction between the cages, respectively. The force constant of the guest-cage interaction will be labeled α_4 . Let $\mu = 0$ be the lattice of the cages and $\mu = 1$ the lattice of the guest masses. In order to construct the force constant matrix Φ , the restoring forces between a reference cage and its first, second, and third neighbors and the restoring force between a reference guest and its cage have to be calculated. The reference cage is denoted with $(h\mu) = (00)$, the guest inside it with $(h\mu) = (01)$. For convenience the origin of the coordinate system is set to the position of the reference cage and guest. The neighbors of cage (00) are labeled as $(h0)$ with $h \in \{1, 2, \dots, 6\}$ for the six next neighbors, $h \in \{7, 8, \dots, 18\}$ for the twelve second neighbors, and $h \in \{19, 20, \dots, 26\}$

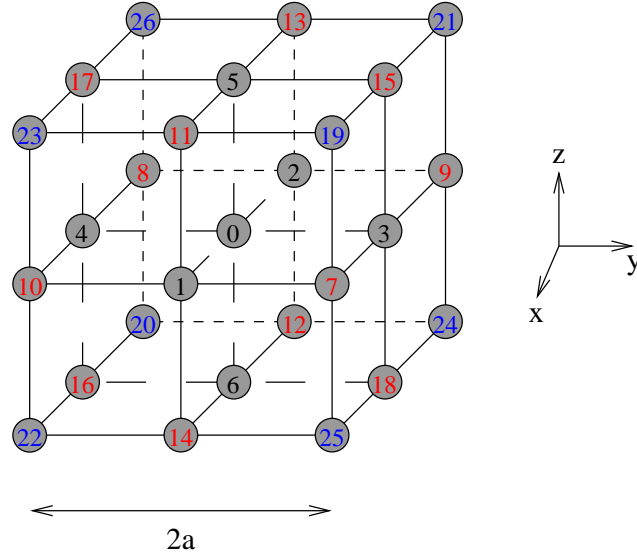


Figure 3.1: Schematics of the simple cubic structure (lattice constant a) of the box-clathrate model. The cages labeled with 0 is the reference cage, $h \in \{1, 2, \dots, 6\}$ are the first neighbors, $h \in \{7, 8, \dots, 18\}$ the second neighbors and $h \in \{19, 20, \dots, 26\}$ the third neighbors. The displayed cages are thus all interconnected by central harmonic forces.

for the eight third neighbors (Fig. 3.1). The guest within each of these cages is $(h1)$, $h \in \{1, 2, \dots, 26\}$. The resulting restoring forces $\mathbf{F}^h(\mu = 0; \nu = 0)$ between the reference cages and its neighbors are summarized in Table 3.1.

The restoring forces between the reference guest and the reference cage are displayed in Table 3.2. Only an interaction with the cage is assumed, the forces correspond therefore to the restoring force when either the guest or host is displaced by $\mathbf{s}(01)$ or $\mathbf{s}(00)$, respectively.

With equation (3.7) the force constant matrix can now be calculated:

$$M_\mu \ddot{s}_i(0\mu) = \sum_{h\nu} F_i^h(\mu; \nu) = - \sum_{h\nu k} \Phi_{ik}^h(\mu; \nu) s_k(h\nu). \quad (3.29)$$

The coefficients for $i = k = 1$ are for example:

$$\Phi_{11}^h(00) = \begin{cases} -\alpha_1, & h = 1, 2 \\ 0, & h = 3, 4, \dots, 6 \\ -\alpha_2/2, & h = 7, 8, \dots, 14 \\ 0, & h = 15, 16, \dots, 18 \\ -\alpha_3/3, & h = 19, 20, \dots, 26 \end{cases}$$

$$\Phi_{11}^0(01) = -2\alpha_4$$

$$\Phi_{11}^0(10) = -2\alpha_4.$$

$(h,0)$	$\mathbf{R}(h,0)$	$\tilde{\varepsilon}(h,0)$	$F_1^h(0;0)$	$F_2^h(0;0)$	$F_3^h(0;0)$
1	$(a,0,0)$	$(1,0,0)$	$\alpha_1[s_1(1) - s_1(0)]$	0	0
2	$(-a,0,0)$	$(-1,0,0)$	$\alpha_1[s_1(2) - s_1(0)]$	0	0
3	$(0,a,0)$	$(0,1,0)$	0	$\alpha_1[s_2(3) - s_2(0)]$	0
4	$(0,-a,0)$	$(0,-1,0)$	0	$\alpha_1[s_2(4) - s_2(0)]$	0
5	$(0,0,a)$	$(0,0,1)$	0	0	$\alpha_1[s_3(5) - s_3(0)]$
6	$(0,0,-a)$	$(0,0,-1)$	0	0	$\alpha_1[s_3(6) - s_3(0)]$
7	$(a,a,0)$	$(\frac{1}{\sqrt{2}}, \frac{1}{\sqrt{2}}, 0)$	$\frac{\alpha_1}{2}[s_1(7) - s_1(0) + s_2(7) - s_2(0)]$	$\frac{\alpha_2}{2}[s_1(7) - s_1(0) + s_2(7) - s_2(0)]$	0
8	$(-a,-a,0)$	$(-\frac{1}{\sqrt{2}}, -\frac{1}{\sqrt{2}}, 0)$	$\frac{\alpha_1}{2}[s_1(8) - s_1(0) + s_2(8) - s_2(0)]$	$\frac{\alpha_2}{2}[s_1(8) - s_1(0) + s_2(8) - s_2(0)]$	0
9	$(-a,a,0)$	$(-\frac{1}{\sqrt{2}}, \frac{1}{\sqrt{2}}, 0)$	$\frac{\alpha_1}{2}[s_1(9) - s_1(0) - s_2(9) + s_2(0)]$	$\frac{\alpha_2}{2}[-s_1(9) + s_1(0) + s_2(9) - s_2(0)]$	0
10	$(a,-a,0)$	$(\frac{1}{\sqrt{2}}, -\frac{1}{\sqrt{2}}, 0)$	$\frac{\alpha_1}{2}[s_1(10) - s_1(0) - s_2(10) + s_2(0)]$	$\frac{\alpha_2}{2}[-s_1(10) + s_1(0) + s_2(10) - s_2(0)]$	0
11	$(a,0,a)$	$(\frac{1}{\sqrt{2}}, 0, \frac{1}{\sqrt{2}})$	$\frac{\alpha_1}{2}[s_1(11) - s_1(0) + s_3(11) - s_3(0)]$	0	$\frac{\alpha_3}{2}[s_1(11) - s_1(0) + s_3(11) - s_3(0)]$
12	$(-a,0,-a)$	$(-\frac{1}{\sqrt{2}}, 0, -\frac{1}{\sqrt{2}})$	$\frac{\alpha_1}{2}[s_1(12) - s_1(0) + s_3(12) - s_3(0)]$	0	$\frac{\alpha_3}{2}[s_1(12) - s_1(0) + s_3(12) - s_3(0)]$
13	$(-a,0,a)$	$(-\frac{1}{\sqrt{2}}, 0, \frac{1}{\sqrt{2}})$	$\frac{\alpha_1}{2}[s_1(13) - s_1(0) - s_3(13) + s_3(0)]$	0	$\frac{\alpha_3}{2}[-s_1(13) + s_1(0) + s_3(13) - s_3(0)]$
14	$(a,0,-a)$	$(\frac{1}{\sqrt{2}}, 0, -\frac{1}{\sqrt{2}})$	$\frac{\alpha_1}{2}[s_1(14) - s_1(0) - s_3(14) + s_3(0)]$	0	$\frac{\alpha_3}{2}[-s_1(14) + s_1(0) + s_3(14) - s_3(0)]$
15	$(0,a,a)$	$(0, \frac{1}{\sqrt{2}}, \frac{1}{\sqrt{2}})$	0	$\frac{\alpha_2}{2}[s_2(15) - s_2(0) + s_3(15) - s_3(0)]$	$\frac{\alpha_3}{2}[s_2(15) - s_2(0) + s_3(15) - s_3(0)]$
16	$(0,-a,-a)$	$(0, -\frac{1}{\sqrt{2}}, -\frac{1}{\sqrt{2}})$	0	$\frac{\alpha_2}{2}[s_2(16) - s_2(0) + s_3(16) - s_3(0)]$	$\frac{\alpha_3}{2}[s_2(16) - s_2(0) + s_3(16) - s_3(0)]$
17	$(0,-a,a)$	$(0, -\frac{1}{\sqrt{2}}, \frac{1}{\sqrt{2}})$	0	$\frac{\alpha_2}{2}[s_2(17) - s_2(0) - s_3(17) + s_3(0)]$	$\frac{\alpha_3}{2}[-s_2(17) + s_2(0) + s_3(15) - s_3(0)]$
18	$(0,a,-a)$	$(0, \frac{1}{\sqrt{2}}, -\frac{1}{\sqrt{2}})$	0	$\frac{\alpha_2}{2}[s_2(18) - s_2(0) - s_3(18) + s_3(0)]$	$\frac{\alpha_3}{2}[-s_2(18) + s_2(0) + s_3(18) - s_3(0)]$
19	(a,a,a)	$(\frac{1}{\sqrt{3}}, \frac{1}{\sqrt{3}}, \frac{1}{\sqrt{3}})$	$\frac{\alpha_1}{3}[s_1(19) - s_1(0) + s_2(19) - s_2(0) + s_3(19) - s_3(0)]$	$\frac{\alpha_2}{3}[s_1(19) - s_1(0) + s_2(19) - s_2(0) + s_3(19) - s_3(0)]$	$\frac{\alpha_3}{3}[s_1(19) - s_1(0) + s_2(19) - s_2(0) + s_3(19) - s_3(0)]$
20	$(-a,-a,-a)$	$(-\frac{1}{\sqrt{3}}, -\frac{1}{\sqrt{3}}, -\frac{1}{\sqrt{3}})$	$\frac{\alpha_1}{3}[s_1(20) - s_1(0) + s_2(20) - s_2(0) + s_3(20) - s_3(0)]$	$\frac{\alpha_2}{3}[s_1(20) - s_1(0) + s_2(20) - s_2(0) + s_3(20) - s_3(0)]$	$\frac{\alpha_3}{3}[s_1(20) - s_1(0) + s_2(20) - s_2(0) + s_3(20) - s_3(0)]$
21	$(-a,a,a)$	$(-\frac{1}{\sqrt{3}}, \frac{1}{\sqrt{3}}, \frac{1}{\sqrt{3}})$	$\frac{\alpha_1}{3}[s_1(21) - s_1(0) - s_2(21) + s_2(0) - s_3(21) + s_3(0)]$	$\frac{\alpha_2}{3}[-s_1(21) + s_1(0) + s_2(21) - s_2(0) + s_3(21) - s_3(0)]$	$\frac{\alpha_3}{3}[-s_1(21) + s_1(0) + s_2(21) - s_2(0) + s_3(21) - s_3(0)]$
22	$(a,-a,-a)$	$(\frac{1}{\sqrt{3}}, -\frac{1}{\sqrt{3}}, -\frac{1}{\sqrt{3}})$	$\frac{\alpha_1}{3}[s_1(22) - s_1(0) - s_2(22) + s_2(0) - s_3(22) + s_3(0)]$	$\frac{\alpha_2}{3}[-s_1(22) + s_1(0) + s_2(22) - s_2(0) + s_3(22) - s_3(0)]$	$\frac{\alpha_3}{3}[-s_1(22) + s_1(0) + s_2(22) - s_2(0) + s_3(22) - s_3(0)]$
23	$(a,-a,a)$	$(\frac{1}{\sqrt{3}}, -\frac{1}{\sqrt{3}}, \frac{1}{\sqrt{3}})$	$\frac{\alpha_1}{3}[s_1(23) - s_1(0) - s_2(23) + s_2(0) + s_3(23) - s_3(0)]$	$\frac{\alpha_2}{3}[-s_1(23) + s_1(0) + s_2(23) - s_2(0) - s_3(23) + s_3(0)]$	$\frac{\alpha_3}{3}[s_1(23) + s_1(0) - s_2(23) + s_2(0) + s_3(23) - s_3(0)]$
24	$(-a,a,-a)$	$(-\frac{1}{\sqrt{3}}, \frac{1}{\sqrt{3}}, -\frac{1}{\sqrt{3}})$	$\frac{\alpha_1}{3}[s_1(24) - s_1(0) - s_2(24) + s_2(0) + s_3(24) - s_3(0)]$	$\frac{\alpha_2}{3}[-s_1(24) + s_1(0) + s_2(24) - s_2(0) - s_3(24) + s_3(0)]$	$\frac{\alpha_3}{3}[s_1(24) + s_1(0) - s_2(24) + s_2(0) + s_3(24) - s_3(0)]$
25	$(a,a,-a)$	$(\frac{1}{\sqrt{3}}, \frac{1}{\sqrt{3}}, -\frac{1}{\sqrt{3}})$	$\frac{\alpha_1}{3}[s_1(25) - s_1(0) + s_2(25) - s_2(0) - s_3(25) + s_3(0)]$	$\frac{\alpha_2}{3}[s_1(25) - s_1(0) + s_2(25) - s_2(0) - s_3(25) + s_3(0)]$	$\frac{\alpha_3}{3}[-s_1(25) + s_1(0) - s_2(25) + s_2(0) + s_3(25) - s_3(0)]$
26	$(-a,-a,a)$	$(-\frac{1}{\sqrt{3}}, -\frac{1}{\sqrt{3}}, \frac{1}{\sqrt{3}})$	$\frac{\alpha_1}{3}[s_1(26) - s_1(0) + s_2(26) - s_2(0) - s_3(26) + s_3(0)]$	$\frac{\alpha_2}{3}[s_1(26) - s_1(0) + s_2(26) - s_2(0) - s_3(26) + s_3(0)]$	$\frac{\alpha_3}{3}[-s_1(26) + s_1(0) - s_2(26) + s_2(0) + s_3(26) - s_3(0)]$

Table 3.1: Restoring forces between the cages in the box-clathrate model. For a stable simple cubic structure harmonic interactions up to the third neighbor have to be considered. The cages are labeled with $h \in \{1, 2, \dots, 26\}$ as shown in Figure 3.1.

h	μ	ν	$F_1^h(\mu; \nu)$	$F_2^h(\mu; \nu)$	$F_3^h(\mu; \nu)$
0	0	1	$2\alpha_4 [s_1(0\ 1) - s_1(0\ 0)]$	$2\alpha_4 [s_2(0\ 1) - s_2(0\ 0)]$	$2\alpha_4 [s_2(0\ 1) - s_2(0\ 0)]$
0	1	0	$2\alpha_4 [s_1(0\ 0) - s_1(0\ 1)]$	$2\alpha_4 [s_2(0\ 0) - s_2(0\ 1)]$	$2\alpha_4 [s_2(0\ 0) - s_2(0\ 1)]$

Table 3.2: Restoring forces between the guest mass and its cage. The guest masses are assumed not to interact with other guest masses or cages. Therefore, only two terms have to be taken into account.

The self-terms can then be determined from the infinitesimal translational invariance equation (3.9)

$$\begin{aligned}
\Phi_{11}^0(0\ 0) &= - \sum_{h=1}^{26} \sum_{\mu=0}^1 \Phi_{11}(0\ \mu) \\
&= 2\alpha_1 + 4\alpha_2 + 8/3\alpha_3 + 2\alpha_4 \\
\Phi_{11}^0(1\ 1) &= 2\alpha_4.
\end{aligned}$$

The other coefficients of the force constant matrix Φ can be calculated the same way. The dynamical matrix is then obtained by substituting the coefficients of the force constant matrix into equation (3.13).

The six dimensional dynamical matrix for the model system was then diagonalized for the three high symmetry \mathbf{q} -directions of the system, i.e. the [001], [011], and [111] direction. The six eigenvalues ω^2 were calculated and sorted in ascending order for 15 q -values $0 < q_i < \pi/a$ along each direction. Thus, the dispersion relation $\omega(\mathbf{q}s)$, $s = 1, 2, \dots, 6$ of the system could be obtained. In Figure 3.2 the dispersion curve along the [001]-direction is shown. The guest mass was chosen to be 20% of the cage mass ($M_g = 0.2 \cdot M_c$), corresponding roughly to the mass ratio between methane and water molecules in structure type I. The interaction between the guest mass and the cage was chosen to be weaker than the interactions between the cages ($\alpha_4 < \alpha_3 < \alpha_2 < \alpha_1$) in order to correspond qualitatively to the forces in gas hydrates and to obtain a guest mode whose frequency is below the frequency maximum of the transverse and longitudinal acoustic cage modes. At the zone center two kinds of excitations are visible: a longitudinal and a transverse optic mode with a frequency $\omega > 0$ at $q = 0$ and a longitudinal and a transverse acoustic mode. For the simple cubic structure the transverse phonons are degenerate in the [001]-direction, therefore only one pair of transverse modes is visible. In the [011] the degeneracy is lifted and all six modes would be observable.

The contribution of the guest and cage to these modes can be seen from the eigenvectors of these modes. The eigenvectors were therefore separated into guest $\mathbf{e}^g(\mathbf{q}s) = \mathbf{e}^1(\mathbf{q}s)$ and cage $\mathbf{e}^c(\mathbf{q}s) = \mathbf{e}^0(\mathbf{q}s)$ contributions. The absolute values of these components are displayed in Figure 3.3 for the [001]-direction. As required, the guest and host masses are vibrating equally in phase in the long wavelength limit for the acoustic modes. But the optic modes are not simply a vibration of both guest and cage masses in anti-phase, but

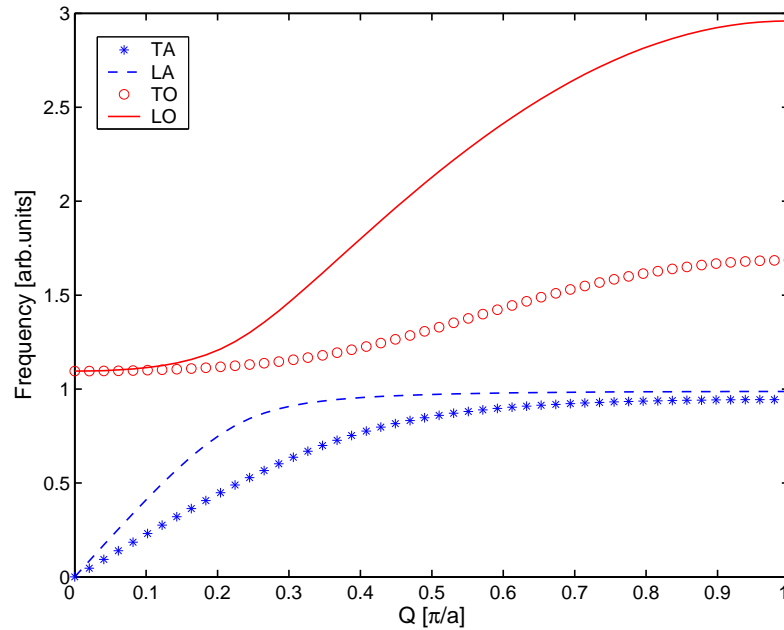


Figure 3.2: Dispersion curve in the [001]-direction of the cage-guest model. As the transverse modes are degenerate in this Q -direction, a transverse and a longitudinal acoustic mode ($\omega = 0$ at $Q = 0$) as well as a transverse and a longitudinal ($\omega = \omega_g > 0$ at $Q = 0$) optic mode can be observed at the zone center. An avoided crossing can be observed between the acoustic and the optic modes at $Q \simeq 0.25$ and $Q \simeq 0.5$ for the longitudinal and transverse modes, respectively. After the avoided crossing the acoustic modes assume a flat non-dispersive character whereas the optic modes obtain an acoustic behavior.

from the eigenvector-squares it can be seen that the optic modes are about 96% guest mass vibrations. As the guest mass is only 20% of the cages mass, the guest vibration does not have a significant impact on the host lattice at the zone center and the optic vibrations are almost pure guest modes. The optic modes therefore correspond at this point to a localized vibration of the guest masses with a frequency $\omega_g \propto \sqrt{\alpha_4/M_g}$.

As the acoustic modes disperse from the zone center a strong bending of both the transverse acoustic (TA) and the longitudinal acoustic (LA) modes becomes apparent in Figure 3.2. As the energy of the acoustic modes comes close to that of the optic guest modes, the acoustic branches bend to flat dispersion branches, whereas the optic modes assume dispersive character. This hybridization is due to an avoided crossing between the guest and host vibrations, promoted by the interaction between the guest mass and the cage. Similar behaviors can be observed in metals with point defects, where heavy substitutional defects perform resonant vibrations [34]. This avoided crossing can be related to a general behavior of eigenvalues of hermitian matrices: only eigenvalues with three independent parameters can be identical [97]. The eigenvalues of phonon dispersion

curves $\omega(\mathbf{q}_s)$ depend on the wave vector \mathbf{q} , the branch index s , and their symmetry representation. This leads to the consequence that branches with the same symmetry representation may not cross. The avoided crossings leads to a drastic change in the phonon dispersion curve and in the modes eigenvectors. As the acoustic modes propagate from the zone center and bend to become flat modes after the avoided crossing, the eigenvector change as well. The contribution of the guest masses to the acoustic modes increases and becomes dominant at the zone boundary. The modes that showed an optic behavior at the zone center and were almost pure guest modes, obtain an increasingly strong host lattice contribution. At the zone boundary these modes are almost pure lattice vibrations. Thus, a mixing of the eigenvectors can be observed, which eventually leads to an exchange of the eigenvectors of the optic modes at the avoided crossing. The inclusion of a guest mass that exhibits a resonant vibration with a frequency ω_g lower than the maximum frequency ω_{max} of the acoustic cage modes, has therefore a strong influence on the low energy and long wave length behavior of the dispersion relation. When ω_g increases the mode mixing is reduced until the influence of the guest mass on the acoustic modes becomes negligible for $\omega_g \gg \omega_{max}$.

As the density of states (DOS) can also be influenced by the guest masses inside the cages, the DOS and the partial DOS for the cage and the guest were calculated. Equation (3.22) was used to calculate the density of states for a $30 \times 30 \times 30$ grid of wave vectors. The results are displayed in Figure 3.4. The density of states shows a strong peak in the low frequency region and a broader distributions of intensities at higher frequencies. From the partial DOS it can be seen that the low frequency peak is mainly due to the guest vibrations, whereas the broad distribution corresponds mostly to the DOS of the cages. It is however interesting that the frequency of the guest peak does not correspond to the frequency ω_g as seen at the zone center in the dispersion relation. Instead the frequency of the peak is somewhat lower and corresponds to the frequencies of the flat acoustic modes after the avoided crossing. The optic guest modes at the zone center lead to a second peak at ω_g in the guest-DOS that is separated from the first by a small frequency gap, which corresponds to the minimal separation of the guest and host modes in the dispersion curve. The contribution of the guest vibrations to the DOS then decreases with increasing frequency.

The partial DOS of the cage vibrations is almost undisturbed by the guest modes at frequencies larger than ω_g . At frequencies below the first maximum of the acoustic lattice modes the cage DOS should follow a Debye behavior. But the intensity, instead of purely increasing with ω^2 , shows a weak but distinct peak at the frequency of the large guest peak. This excitation corresponds to contributions of the guest modes to the cage vibrations. The frequency of the guest vibration can therefore be observed in the density of states of the cages. However, the guest vibration at the zone center does not show in the cage-DOS. The guest mass is too small to affect the lattice to a visible degree when the frequencies of the cage and guest vibrations are still very different at the zone center. As the frequencies of the cage modes approach the ones of the guest modes, the avoided

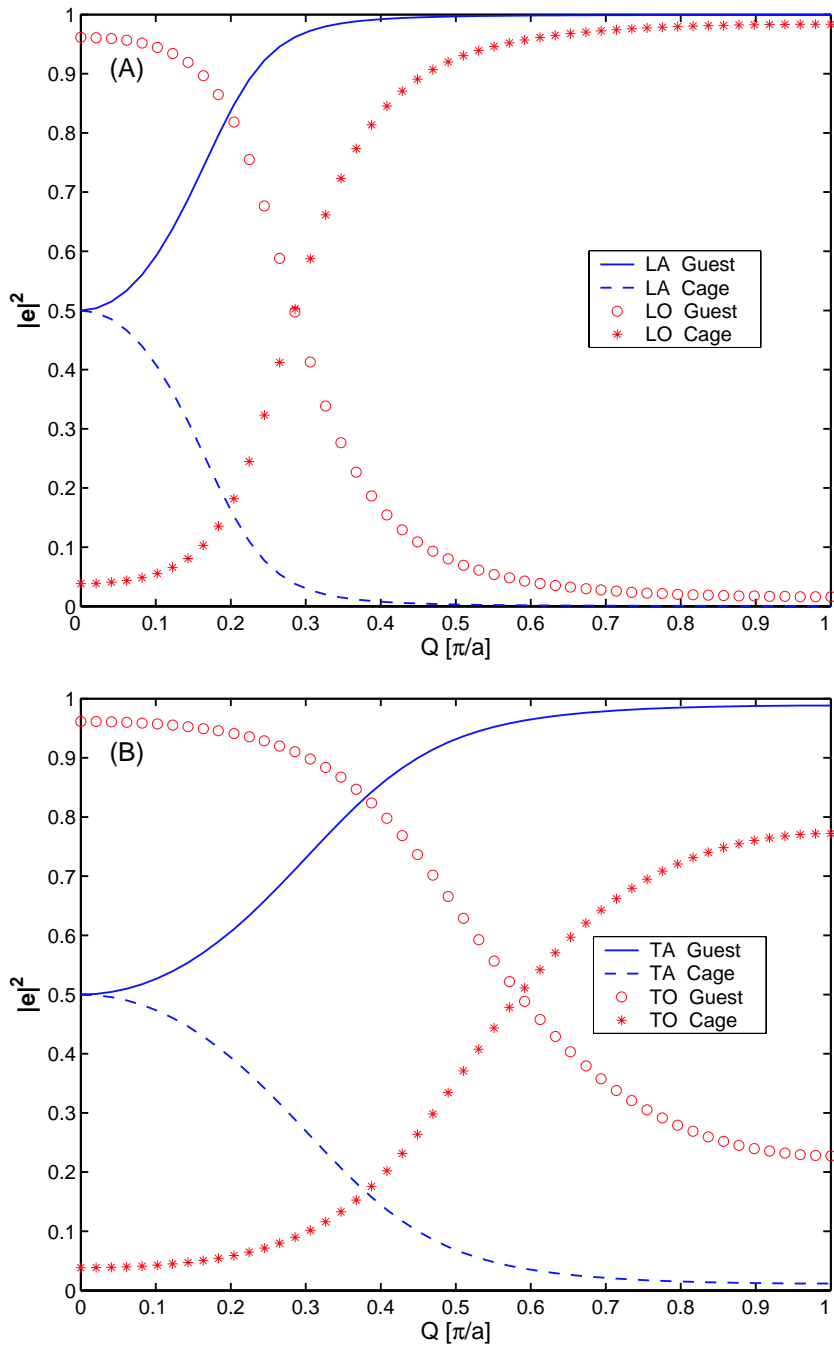


Figure 3.3: The absolute squares of the eigenvectors of (A) the longitudinal and (B) the transverse modes are shown. They were separated into the guest and cage contributions. Both the LA and the TA modes have equal guest (—) and cage (---) contributions at the zone center. As these modes propagate from the zone center the guest contributions increase significantly until after the avoided crossing the modes are almost pure guest modes. The LO and TO modes display an opposite behavior of their guest (ooo) and cage (***) contributions. The guest contributions to the optic modes are dominant at the zone center and diminish with increasing Q , until the optic modes are mostly cage modes.

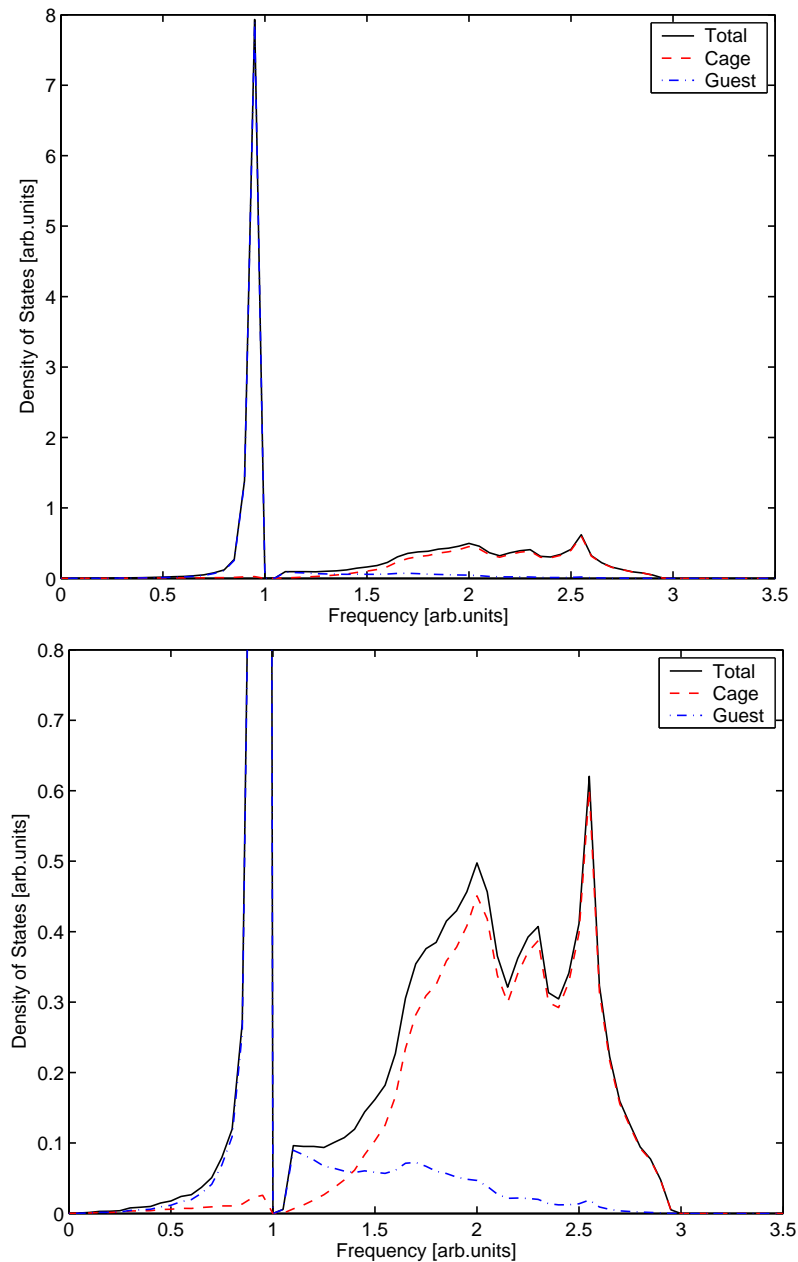


Figure 3.4: The DOS (—) and partial DOS of the cage (---) and of the guest mass (- · - ·) are shown. The overview is dominated by the peak of the guest-DOS. The broad distribution of intensity at higher frequencies corresponds mainly to the cage-DOS. In the close-up view ($\times 10$) it can be seen that the guest-DOS has a second smaller peak at ω_g and that the guest contributions to the DOS decrease at higher frequencies. The cage-DOS has a distinct peak at low frequencies corresponding to the coupling between the cage and guest vibrations. At higher frequencies it corresponds to the cage modes that become flat near the zone boundary.

crossing leads to a resonance between the guest and cage vibrations, which can then be observed in the cage-DOS. The peak in the cage-DOS can at this point be understood as a coupling between the guest and host vibrations: as a guest atom approaches the cage wall, both the guest and the cage get pushed back. If the guest mass or the interaction strength is increased a second peak eventually appears in the cage-DOS at ω_g when the guest mass or the interaction strength becomes important enough to counterbalance the resonance of the avoided crossing.

3.3.2 Lattice Dynamical Clathrate Model

The “box-clathrate” model allowed to study the general influence of the inclusion of guest masses on the lattice dynamics of a crystal. It allowed to gain a first understanding of the dispersion relation and of the density of states of an inclusion compound. However, to obtain results of physical relevance from such a calculation a more sophisticated model is necessary. A more realistic crystal potential will therefore be developed in this section.

In molecular crystals like gas hydrates, it is important to note that the molecules are held together by forces, e.g. van der Waal forces, hydrogen bonds, that are weak compared to the forces which bind the atoms in each molecule. In order to develop a crystal potential for a clathrate hydrate it is convenient to separate the potential in several terms that can be treated independently. It is therefore useful to separate the crystal potential into inter- and intramolecular contributions [20]

$$V = V_M + V_I, \quad (3.30)$$

where V_M and V_I represent the intermolecular and the internal potential of a molecule, respectively. In the case of clathrate hydrates the intermolecular interactions can additionally be separated into relatively strong hydrogen bonds between the water molecules inside the cages (~ 0.1 eV) and the weaker van der Waals interaction (\sim meV) between the guest molecules and the surrounding water molecules.

Normally the internal and external vibrations are well separated in frequency and uncoupled; at low temperatures, or for low frequencies processes, the internal vibrations of the molecules will generally not be excited. Therefore the separation of the potentials has a real physical meaning, corresponding to the separation of internal molecular excitations and external lattice vibrations. The internal potential dominates the internal vibrations of the molecules in a crystal, the intermolecular potential only acts as a small perturbation in this case. On the other hand, the lattice vibrations are completely controlled by the intermolecular potential. The approach of treating the lattice dynamics of the crystal while neglecting the internal molecular vibrations is called the *rigid body* approximation as it corresponds to assuming that the molecules behave as rigid bodies with no degree of internal freedom.

For gas hydrates the lattice dynamics of the water host lattice may be approximated by the lattice dynamics of hexagonal ice I_h that has been the subject of both experimental and theoretical investigations [107, 16]. The internal vibrations of the water molecules in ice I_h

are found at around 375 meV [157], whereas the intermolecular vibrations are found in the energy region of 0–40 meV and 60–140 meV for the translational and librational motions, respectively [83]. The inter- and intramolecular vibrations can therefore be assumed to be independent. With the rigid body approximation a series of intermolecular potentials have since been proposed for liquid water and regular ices, such as the *Stillinger* ST2 [139], the MCY [96], the SPC/E [10], or the TIPS potentials [67]. The SPC/E and TIPS potentials are today the most popular potentials for water molecules.

As the internal vibrations of guest and water molecules in gas hydrates are also well separated from their translational modes [142, 59], the rigid body approximation may also be used in this case. The energy of the crystal can thus be based on pairwise additive, classical potentials for the rigid molecules. Several water and guest potentials have been used to calculate the stability, elastic or dynamic properties of structure type I gas hydrates [38, 124, 143]. It was found that, of the simple water potentials, the TIP4P, which is originally parameterized for liquid water, describes the physical properties to an acceptable degree. The results could be further improved for various ice phases and hydrates by a slightly modified TIP4P potential [125]. This potential was therefore chosen as a model for the interatomic forces between the water molecules in the gas hydrates. The interactions between the guest molecules or atoms were described by Lennard–Jones 12-6 potentials where the potential parameters can be taken from the gas or liquid phase of the atom or molecule.

The TIP4P potential involves a rigid water monomer that is represented by four interaction sites: three on the nuclei and one on a point M located on the HOH bisector 0.15 Å from the oxygen towards the hydrogens. There is a charge of 0.52 e on the hydrogens and $-1.04 e$ on M. The intermolecular interaction between two water molecules consists of the Coulomb interaction and a Lennard–Jones 12-6 potential function:

$$V(r) = \sum_{ik} \frac{q_i q_k e^2}{r_{ik}} + 4\epsilon \left(\frac{\sigma^{12}}{r_{oo}^{12}} - \frac{\sigma^6}{r_{oo}^6} \right), \quad (3.31)$$

where q_i is the charge, r_{ik} the distance between two charged sites, ϵ , and σ potential parameters of the Lennard–Jones potential and r_{oo} the distance between two oxygens. In the TIP4P these parameters are chosen so that the potential reproduces the structural, thermodynamic, and dynamical properties of ice I_h . The values for the O–H bond length and the HOH angle are fixed at the experimental values for the water molecule (s. Table 3.3). The Lennard–Jones term describes the short–range van der Waals interaction between the water molecules. It has the advantage of being a pairwise additive atom–atom potential and the total potential energy can therefore easily be evaluated. The TIP4P potential can be improved by scaling the interactions parameters by a constant $k = 1.0066$. Effective charges are scaled by k^2 , Lennard–Jones parameter σ and ϵ by k and k^3 , respectively, and all distances between the interaction sites on the water molecules are scaled by k . The slightly modified TIP4P potential improves the calculated cell parameters for various phases of ice without deteriorating other calculated quantities [125].

Interaction Site	Model	σ [Å]	ϵ [kJ/mol]	Charge [e]
O	TIP4P	3.1533	0.6487	
H	TIP4P			0.52
M	TIP4P			-1.04
CH ₄	OPLS	3.73	1.2305	
Xe	LJ	4.047	1.9205	
TIP4P	O–H bond	0.957 Å	$\widehat{\text{HOH}}$ angle	104.52°
TIP4P	O–M bond	0.15 Å	$\widehat{\text{HOM}}$ angle	52.26°

Table 3.3: Parameters for the intermolecular potentials used in the lattice dynamical calculations. The water–water interactions are represented by three interaction sites. The oxygen is the site for the van der Waals interaction, the charges for the Coulomb interaction are localized on the hydrogens and the additional site M. For the guest molecules only van der Waals interactions are taken into account. Additionally, the parameters for the geometry of the water monomer are given.

Since the short–range interaction for both water and guest molecules or atoms are described by a Lennard–Jones type potential, the potential describing the guest–water interaction is of Lennard–Jones type again. The potential parameters for the short–range interaction between different types of molecules can then be deduced from combination rules. The *Lorentz–Berthelot* mixing rules [3] were chosen to calculate the potential parameters for the guest–water interaction:

$$\begin{aligned}\sigma_{gw} &= \frac{\sigma_{ww} + \sigma_{gg}}{2} \\ \epsilon_{gw} &= (\epsilon_{ww} \cdot \epsilon_{gg})^{1/2}.\end{aligned}\tag{3.32}$$

These mixing rules lead to zero interaction between the hydrogen atoms of the water molecules and the guest molecules or atoms as the oxygen atom is the only interaction site for van der Waals forces in the water molecules.

The electrostatic interaction between the molecules is described by the *effective charges* on the hydrogens and the interaction site M of the water molecules. The electrostatic potential can therefore be separated into atom–atom interactions like the short–range potential. But in contrast to the short–range potentials where the potential depends on very high powers of the intermolecular separation and the lattice sum can easily be truncated after 8 – 10 Å, the electrostatic has a long–range character. It is therefore necessary to consider a summation method that converges fast enough yet includes all the effects of the long–range interactions. The Ewald summation was used to compute these long–range interactions [3].

In the present work the lattice dynamics of methane and xenon hydrate is of interest. A xenon atom as guest species consists of a single interaction site. The Xe–Xe interac-

tion can thus be described by a Lennard–Jones potential. The potential parameters ϵ and σ are taken from the literature from previous calculations on xenon hydrate [151]. The methane molecules are assumed to be spherical symmetric Lennard–Jones particles [38] and the OPLS potential parameters were used to describe the methane–methane interactions. With potential parameters for both guest atoms or molecules and water molecules specified (Table 3.3), the guest–host interaction parameters can be deduced from the Lorentz–Berthelot mixing rules and the force constant matrix can be calculated. The lattice dynamical problem was solved with periodic boundary conditions for one proton–disordered unit cell of a structure I clathrate hydrate containing 46 water molecules and eight methane molecules or xenon atoms. The orientations of the water molecules in the unit cell are chosen such that the *Bernal–Fowler* ice–rules are satisfied [11] and that the dipole moment of the whole system has a vanishing value [106]. The lattice parameter of the unit cell was fixed at $a = 11.83 \text{ \AA}$. The atomic structure was optimized by minimizing the energy of the system prior to the calculation of the dynamic matrix. The dynamical matrix could then be diagonalized for any wave–vector direction leading to a full description of the lattice dynamics of methane and xenon hydrate.

To perform the calculations a Fortran based program was used. The core of the code was provided by *V.P. Shpakov* [126]. It was modified within the scope of the present work to match the requirements of the study, i.e. perform orientational averaged calculations and compute neutron and x-ray intensities.

Chapter 4

Theory of Neutron and X-ray Scattering

In this chapter a short overview of the scattering theory of neutrons and x-rays will be given. The section on neutron scattering will give a short overview of the scattering theory in general and then introduce the theoretical expressions needed to analyze the neutron experiments. The second section introduces the theory of inelastic x-ray scattering and the expressions needed for the interpretation of the experiments will be derived. A thorough introduction into scattering theory can be found in several text books, e.g. [131, 90, 9].

4.1 Neutron Scattering

In a scattering process of neutrons both their particle and wave characteristics have to be considered. The de Broglie wavelength gives the connection between the wavelength λ or wave vector \mathbf{k} and the velocity v or energy E of the neutron. In a scattering experiment the important variables are the change in neutron energy and the change in wave vector. If the initial and final energies and wave vectors are \mathbf{k} , E and \mathbf{k}' , E' , respectively, the energy and wave vector transfer are given by

$$\hbar\omega = E - E' = \frac{\hbar^2}{2m} (k^2 - k'^2) \quad (4.1)$$

$$\mathbf{Q} = \mathbf{k} - \mathbf{k}', \quad (4.2)$$

with m the mass of the neutron. The spectrum of the scattered neutrons is a function of \mathbf{Q} and $\hbar\omega$ as the scattering of low energy neutrons is a weak process. A perturbative calculation can thus be used to derive an expression for the scattering amplitude.

4.1.1 Scattering Cross Sections

A scattering process is in general described by the *double-differential scattering cross section* $\frac{d^2\sigma}{d\Omega dE}$. It gives the probability that an incident neutron with the energy E is scattered into a small solid angle $d\Omega$ with a final energy between E and $E + dE$.

The scattering process can be formulated in terms of initial and final states of the neutron and the scattering system, respectively. The neutron with incident wave vector \mathbf{k} interacts with the scattering system via an interaction potential \hat{V} . This interaction causes a transition of the neutron from its initial state $|\mathbf{k}\rangle$ to a final state $|\mathbf{k}'\rangle$, while the scattering system changes from an initial state $|i\rangle$ to a final state $|f\rangle$. The energy dependence is introduced taking into account the energy conservation. If E_i and E_f denote the initial and final energy of the scattering system, conservation of energy requires

$$\hbar\omega = E_f - E_i. \quad (4.3)$$

In the first Born approximation the double-differential scattering cross section may thus be written as

$$\frac{d^2\sigma}{d\Omega dE} = \frac{k'}{k} \left(\frac{m}{2\pi\hbar^2} \right)^2 \sum_{i,f} p_i \left| \langle \mathbf{k}' | \langle f | \hat{V} | i \rangle | \mathbf{k} \rangle \right|^2 \delta(\hbar\omega - (E_f - E_i)), \quad (4.4)$$

with m the mass of the neutrons and p_i is the statistical weight or occupation probability of the initial state $|i\rangle$ of the scattering system.

The interaction potential can be written separately for each nucleus in the scattering system and is described by the Fermi pseudo-potential:

$$\hat{V} = \frac{2\pi\hbar^2}{m} \sum_j b_j \delta(\mathbf{r} - \mathbf{R}_j), \quad (4.5)$$

where b_j is the spin and isotope dependent scattering length of the j th nucleus and \mathbf{r} and \mathbf{R}_j the coordinates of the neutron and the j th nucleus, respectively. Thus

$$\langle \mathbf{k}' | \hat{V} | \mathbf{k} \rangle = \sum_j b_j e^{i\mathbf{Q}\cdot\mathbf{R}_j}, \quad (4.6)$$

where \mathbf{Q} is the wave vector transfer. The δ -function for the energy can be written in terms of the Hamiltonian of the scattering system. Under the assumption of independent nuclear spin distributions the sum over the final and initial states of the scattering system leads to [131]

$$\frac{d^2\sigma}{d\Omega dE} = \frac{k'}{k} \frac{1}{2\pi\hbar} \int dt \sum_{j,j'} \overline{b_{j'}^* b_j} \langle e^{-i\mathbf{Q}\cdot\mathbf{R}_{j'}(0)} e^{i\mathbf{Q}\cdot\mathbf{R}_j(t)} \rangle e^{-i\omega t}. \quad (4.7)$$

The quantity $\overline{b_{j'}^* b_j}$ is the value of $b_{j'}^* b_j$ averaged over random nuclear spin orientations and random isotope distributions. For a monoatomic scattering system it follows that

$$\begin{aligned} \overline{b_{j'}^* b_j} &= |\bar{b}|^2, & \text{for } j' \neq j, \\ \overline{b_{j'}^* b_j} &= \overline{|b|^2}, & \text{for } j' = j, \end{aligned}$$

so that in general

$$\overline{b_{j'}^* b_j} = |\bar{b}|^2 + \delta_{j'j} \left(\overline{|b|^2} - |\bar{b}|^2 \right). \quad (4.8)$$

The scattering length of a nucleus can therefore be separated into a spin independent b_{si} and a spin dependent b_{sd} contribution:

$$b_{si} = |\bar{b}|, \quad (4.9)$$

$$b_{sd} = \left(|\bar{b}|^2 - |\bar{b}|^2 \right)^{1/2}. \quad (4.10)$$

If a scattering system with a single element with nuclear spin I interacts with a neutron, the spin of the nucleus–neutron system has the values $I + \frac{1}{2}$ or $I - \frac{1}{2}$. The scattering lengths of the two spin states are denoted with b_+ and b_- , respectively. Thus the values for \bar{b} and $|\bar{b}|^2$ can be calculated and the spin independent and dependent scattering lengths are

$$b_{si} = \frac{I+1}{2I+1}b_+ + \frac{I}{2I+1}b_- \quad (4.11)$$

$$b_{sd} = \frac{\sqrt{I(I+1)}}{2I+1}(b_+ - b_-). \quad (4.12)$$

With the Born approximation the double–differential scattering cross section (4.7) can thus be expressed in the *van Hove* representation [57]

$$\left(\frac{d^2\sigma}{d\Omega dE} \right)_{coh} = \frac{\sigma_{coh}}{4\pi} \frac{k'}{k} S_{coh}(\mathbf{Q}, \omega) \quad (4.13)$$

and

$$\left(\frac{d^2\sigma}{d\Omega dE} \right)_{inc} = \frac{\sigma_{inc}}{4\pi} \frac{k'}{k} S_{inc}(\mathbf{Q}, \omega), \quad (4.14)$$

where $\sigma_{coh} = 4\pi b_{si}^2$, $\sigma_{inc} = 4\pi b_{sd}^2$ are the *coherent* and *incoherent* scattering cross sections, respectively. The response functions

$$S_{coh}(\mathbf{Q}, \omega) = \frac{1}{2\pi\hbar} \int dt \sum_{j,j'} \langle e^{-i\mathbf{Q}\cdot\mathbf{R}_{j'}(0)} e^{i\mathbf{Q}\cdot\mathbf{R}_j(t)} \rangle e^{-i\omega t}, \quad (4.15)$$

$$S_{inc}(\mathbf{Q}, \omega) = \frac{1}{2\pi\hbar} \int dt \sum_j \langle e^{-i\mathbf{Q}\cdot\mathbf{R}_j(0)} e^{i\mathbf{Q}\cdot\mathbf{R}_j(t)} \rangle e^{-i\omega t} \quad (4.16)$$

are called *scattering function* or *dynamic structure factor*, respectively. The coherent scattering depends on the mean value of the scattering lengths in the scattering system, whereas the incoherent scattering arises from the deviations from this mean value. In general, the scattering lengths are not only a function of the spin but also of the isotope distribution of the scattering system. Therefore in addition to spin–incoherence an isotope–incoherence has to be considered. In the investigated systems the isotope–incoherence was negligible compared to the spin–incoherence as the components were 99% isotope pure. From the equations (4.15) and (4.16) it can be seen that the coherent scattering depends on the correlation between the positions of the same nucleus at different times and of different nuclei at different times. It thus leads to interference effects. The incoherent scattering depends only on the correlation between the positions

of the same nucleus at different times and therefore does not give interference effects. In the theory of neutron scattering the distinction between the coherent and the incoherent scattering cross section is therefore a central feature. The information that can be gained from the scattered neutrons is different for either case: the coherent scattering leads to informations on the collective properties of the sample, e.g. crystallographic structure, phonons, whereas the incoherent scattering reflects the single particle dynamics of the sample.

4.1.2 Coherent Scattering

In a general lattice the equilibrium position of an atom is given by $\bar{\mathbf{R}}(m\mu) = \bar{\mathbf{A}}(m) + \bar{\mathbf{R}}(\mu)$ and its instantaneous position by $\mathbf{R}(m\mu) = \bar{\mathbf{R}}(m\mu) + \mathbf{s}(m\mu)$. Here, $\bar{\mathbf{R}}(\mu)$ is the position of the atom μ in the unit cell m , which has the position $\bar{\mathbf{A}}(m)$. $\mathbf{s}(m\mu)$ is a small displacement of the atom μ in the unit cell m from its equilibrium position (s. Chapter 3). The coherent scattering length of the atom is denoted with $b_{si,\mu}$. In the harmonic approximation the atomic vibrations can be described by harmonic oscillations. The coherent scattering cross section (4.13) can then be written as [131]

$$\left(\frac{d^2\sigma}{d\Omega dE} \right)_{coh} = \frac{k'}{k} \frac{1}{2\pi\hbar} \sum_{m\mu, n\nu} b_{si,\mu} b_{si,\nu} e^{i\mathbf{Q} \cdot (\bar{\mathbf{R}}(m\mu) - \bar{\mathbf{R}}(n\nu))} \int dt e^{\langle U_\mu^2 \rangle} e^{\langle U_\mu V_\nu \rangle} e^{-i\omega t}, \quad (4.17)$$

with $U_\mu = -i\mathbf{Q} \cdot \mathbf{s}(m\mu; 0)$ and $V_\nu = i\mathbf{Q} \cdot \mathbf{s}(n\nu; t)$. The exponential term $e^{\langle U_\mu^2 \rangle} = e^{-W_\mu}$ is known as *Debye-Waller* factor. It is the mean square displacement of an atom multiplied by Q^2 :

$$W_\mu(\mathbf{Q}) = \frac{1}{2} \mathbf{Q}^T \cdot \mathbf{B}(\mu) \cdot \mathbf{Q}. \quad (4.18)$$

$\mathbf{B}(\mu)$ is a 3×3 matrix representing the static correlation function of the displacements $\mathbf{s}(m\mu)$ of atom $(m\mu)$ from its equilibrium position $\bar{\mathbf{R}}(m\mu)$. It can be related to the diagonal and off-diagonal densities of states $g_{ik}^\mu(\omega)$ of the atom

$$B_{ik}(\mu) = \frac{\hbar}{2M_\mu N} \int d\omega g_{ik}^\mu(\omega) \frac{1}{\omega} \coth \left(\frac{\hbar\omega}{2k_B T} \right). \quad (4.19)$$

For a cubic Bravais lattice the mean square displacements of an atom are independent of the lattice site and the expression (4.18) simplifies to $W = \frac{1}{3} Q^2 \langle s^2 \rangle$. Even for non-cubic lattices this may be a correct approximation. By expanding the correlation function $e^{\langle UV \rangle} = 1 + \langle UV \rangle + \frac{1}{2!} \langle UV \rangle^2 + \dots$ both elastic and inelastic coherent scattering cross sections can be derived from the expression (4.17).

Elastic Scattering

Diffraction experiments with neutrons or x-rays allow the determination of crystal structures. For x-rays the scattering cross sections is proportional to the atomic form factor $f(Q)$, which corresponds in the limit $Q \rightarrow 0$ to the number of electrons of the scatterer.

The sensitivity to light elements, e.g. hydrogen atoms, is therefore rather limited. In neutron diffraction experiments samples with large amounts of hydrogen are also difficult to handle due to the large incoherent scattering cross section. To solve this problem the sample can be deuterated, i.e. the hydrogen is replaced by deuterium. The scattering cross section of deuterium is more favorable as the rather large value of the coherent scattering length $b_{coh} = b_{si} = 6.67$ barn allows for a more precise determination of atomic positions and parameters.

The scattering cross section of x-rays decreases strongly with increasing wave vector transfer due to the atomic form factor. Details of the crystallographic structure, e.g. thermal vibrations or orientational distributions, only contribute to diffraction patterns at higher wave vector transfers. It is therefore an advantage of neutron scattering that the scattering length b_{si} does not depend on the wave vector transfer.

The diffraction experiments were performed on neutron diffractometers that measure the energy integrated angle dependence of the double-differential scattering cross section. Only the coherent part of the cross section contains structural information, the incoherent part appears only as a smooth background in the diffraction patterns. Additionally, diffuse scattering was not taken into account, as its intensity is normally negligible compared to the elastic intensity. The expansion of the correlation function $e^{\langle U_\mu V_\nu \rangle}$ in eq. (4.17) can thus be truncated after the first expansion term and the measured differential cross section can be expressed as

$$\left(\frac{d\sigma}{d\Omega}\right)_{coh,el} = \int \left(\frac{d\sigma^2}{d\Omega dE}\right)_{coh,el} dE = N \sum_m e^{i\mathbf{Q}\cdot\bar{\mathbf{A}}(m)} |F(\mathbf{Q})|^2, \quad (4.20)$$

where

$$F(\mathbf{Q}) = \sum_\mu b_{si,\mu} e^{i\mathbf{Q}\cdot\bar{\mathbf{R}}(\mu)} e^{-W_\mu} \quad (4.21)$$

is the *unit cell structure factor*. The summation in (4.21) extends over all atoms in the unit cell. $b_{si,\mu}$ is respective scattering length and e^{-W_μ} the respective Debye–Waller factor that takes account of the thermal motion of the atom concerned. The Debye–Waller factor leads to decreasing intensity with increasing wave vector transfer or with increasing thermal motions of the atoms. In simple models the Debye–Waller factor of an atom is assumed to be isotropic, although more elaborate models might take anisotropies into account.

The lattice sum $\sum_m e^{i\mathbf{Q}\cdot\bar{\mathbf{A}}(m)}$ in eq. (4.20) can be replaced by a sum over the reciprocal lattice vectors \mathbf{G} , thus leading to

$$\left(\frac{d\sigma}{d\Omega}\right)_{coh,el} = N \sum_{\mathbf{G}} \delta(\mathbf{Q} - \mathbf{G}) |F(\mathbf{Q})|^2. \quad (4.22)$$

From this expression for the differential cross section it can be seen that there is no scattering unless *Bragg's law* $\mathbf{Q} = \mathbf{k}' - \mathbf{k} = \mathbf{G}$ is fulfilled, i.e. the wave vector transfer \mathbf{Q} equals a vector \mathbf{G} of the reciprocal lattice. So coherent elastic neutron scattering is Bragg scattering.

In molecular crystals thermal excitations and reorientations of the molecules are common due to the weak intermolecular interaction. The description of the large amplitude vibrations is difficult if the atoms do not assume well defined equilibrium positions. This is the case for methane hydrate, where the methane molecules perform almost free rotations at low temperatures [42]. Symmetry adapted functions can be used to model the orientational disorder in these systems. This method has already been successfully applied in diffraction studies of methane hydrate [43]. The procedure is based on a model developed by *Press* and *Hüller* [103] and is presented in detail for methane hydrate in [45].

Inelastic Scattering

At non-zero temperatures the atoms in a crystal perform small translational motions around their equilibrium positions. These thermal excitations are already noticeable in diffraction experiments via the Debye–Waller factor. The displacements of the atoms from their equilibrium positions can be described by normal modes or phonons as introduced in chapter 3. In inelastic coherent neutron scattering experiments these collective lattice vibrations can be observed directly by the energy gain or loss and the wave vector transfer of the neutrons. The energy transfer of the neutron and the sample results in an emission or adsorption of one or more phonons. The phonon wave vector can be related to the wave vector transfer of the neutron. Thus, one of the important applications of neutron spectroscopy is the determination of the dispersion relation and density of states of a crystal. The width of the spectral lines contains furthermore information on the lifetime of the phonons.

In coherent inelastic neutron scattering experiments, incoherent scattering leads to a background in the spectra. Samples with large amounts of hydrogen are therefore difficult to investigate and deuterated samples or samples containing a coherent scatterer can be used only. Additionally, in order to interpret recorded dispersion relation, the experimental intensities have to be assigned to the correct phonon modes. It is therefore necessary to extract information about the polarization of the phonons from the experimental spectra as well. In general, this is only possible for phonon branches along the high symmetry directions of a crystal. This leads to the requirement of large single crystals in coherent inelastic neutron scattering experiments in order to achieve a sufficient count rate and to be able to select well defined directions in the crystal. Unfortunately, large single crystals of clathrate hydrates do not exist. Recently however, very high-resolution inelastic x-ray instruments have allowed the use of small crystals or powder samples.

The expression for the coherent phonon cross section can be obtained by taking the higher order terms of the expansion of $e^{\langle U_\mu V_\nu \rangle}$ in eq. (4.17) into account. The second term $\langle U_\mu V_\nu \rangle$ gives the expression for the coherent *one-phonon* scattering cross section, i.e. the scattered neutron leads to emission or adsorption of exactly one phonon. If the neutron is scattered, creating or annihilating two or more phonons simultaneously, the scattering is called *multi-phonon* scattering and is given by the third order or higher order terms of the expansion.

In order to find an expression for the coherent one-phonon scattering cross section the atomic vibrations are considered to be harmonic oscillators and the displacement $\mathbf{s}(m\mu)$ of an atom ($m\mu$) is given by

$$\mathbf{s}(m\mu) = \left(\frac{\hbar}{2M_\mu N} \right)^{1/2} \sum_{\mathbf{q},s} \frac{\mathbf{e}_s^\mu}{\sqrt{\omega_s}} \left(a_s e^{i(\mathbf{q}\cdot\bar{\mathbf{A}}(m)-\omega_s t)} + a_s^* e^{-i(\mathbf{q}\cdot\bar{\mathbf{A}}(m\mu)-\omega_s t)} \right), \quad (4.23)$$

where N is the number of unit cells, s the branch index and \mathbf{q} is the phonon wave vector, $\omega_s = \omega(\mathbf{q}s)$ the eigenfrequency, and $\mathbf{e}_s^\mu = \mathbf{e}^\mu(\mathbf{q}s)$ the eigenvector of the normal mode. a_s and a_s^* are the annihilation and creation operators of the mode, respectively. This expression of the atomic displacements is called *phonon expansion*. With the properties $\langle n | a a^* | n \rangle = n + 1$ and $\langle n | a^* a | n \rangle = n$ of the ladder operators it follows

$$\begin{aligned} \langle U_\mu V_\nu \rangle &= \frac{\hbar}{2N} \sum_{\mathbf{q},s} \frac{1}{\omega_s} \frac{(\mathbf{q} \cdot \mathbf{e}_s^\mu)(\mathbf{q} \cdot \mathbf{e}_s^\nu)}{\sqrt{M_\mu M_\nu}} \times \\ &\times \left(e^{i(\mathbf{q}\cdot(\bar{\mathbf{A}}(m)-\bar{\mathbf{A}}(n))+\omega_s t)} [\langle n_s \rangle + 1] + e^{-i(\mathbf{q}\cdot(\bar{\mathbf{A}}(m)-\bar{\mathbf{A}}(n))+\omega_s t)} \langle n_s \rangle \right). \end{aligned} \quad (4.24)$$

Substituting (4.24) in (4.17) leads to the double-differential coherent one-phonon scattering cross section, which can be split into a term for the phonon emission $[\langle n \rangle + 1]$ and for the phonon absorption $\langle n \rangle$. The term for a creation of one phonon is

$$\left(\frac{d^2\sigma}{d\Omega dE} \right)_{coh}^{+1} = \frac{k'}{k} \sum_{\mathbf{q},s} \sum_{\mathbf{G}} \frac{1}{2\omega_s} |G_s(\mathbf{q}, \mathbf{Q})|^2 \delta(\omega - \omega_s) \delta(\mathbf{Q} - \mathbf{q} - \mathbf{G}) [\langle n_s \rangle + 1], \quad (4.25)$$

where the integration with respect to t is $\delta(\omega - \omega_s)$ and the lattice sum with respect to m is $\sum_{\mathbf{G}} \delta(\mathbf{Q} - \mathbf{q} - \mathbf{G})$. $G_s(\mathbf{q}, \mathbf{Q})$ is called the *inelastic dynamic structure factor* and is given by

$$G_s(\mathbf{q}, \mathbf{Q}) = \sum_{\mu} b_{si,\mu} \frac{1}{\sqrt{M_\mu}} (\mathbf{Q} \cdot \mathbf{e}^\mu(\mathbf{q}s)) e^{i\mathbf{Q}\cdot\bar{\mathbf{R}}(\mu)} e^{-W_\mu}. \quad (4.26)$$

The summation in (4.26) is over all the atoms in the unit cell with $b_{si,\mu}$ their respective coherent scattering length. Similar to the result for elastic coherent scattering the Debye-Waller factor e^{-W_μ} leads to decreasing intensity with increasing wave vector transfer. For scattering to occur two conditions have to be satisfied:

$$\begin{aligned} \hbar\omega_s &= \hbar\omega = E - E' = \frac{\hbar^2}{2m}(k^2 - k'^2), \\ \mathbf{Q} &= \mathbf{k} - \mathbf{k}' = \mathbf{G} + \mathbf{q}. \end{aligned} \quad (4.27)$$

Therefore the energy transfer of the neutron to the crystal must be equal to the energy of the normal mode s , whereas the wave vector transfer of the neutron must correspond to the phonon wave vector \mathbf{q} plus a lattice vector \mathbf{G} . The term for phonon absorption is similar and the scattering conditions are:

$$\begin{aligned} \hbar\omega_s &= E' - E, \\ \mathbf{k} - \mathbf{k}' &= \mathbf{G} - \mathbf{q}. \end{aligned} \quad (4.28)$$

Here the neutron annihilates a phonon taking its energy and angular momentum.

By varying the wave vector transfer $\mathbf{Q} = \mathbf{k} - \mathbf{k}'$ and the energy transfer $\hbar\omega$ of the neutron the dispersion relation of a crystal $\omega(\mathbf{q}_s)$ can thus be determined. If the wave vector of the incident neutron is fixed ($\mathbf{k} = \text{const.}$), the cross section (4.25) is measured as a function of \mathbf{k}' . As \mathbf{k}' has to fulfill both conditions in (4.27) or (4.28), coherent one-phonon scattering occurs for discrete values of \mathbf{k}' only. A phonon spectrum at a given wave vector transfer consists therefore of a series of peaks as function of the energy transfer $\hbar\omega$.

For two-phonon scattering the two δ -functions in the scattering cross section lead to following scattering conditions

$$\begin{aligned} E - E' &= \hbar(\pm\omega_{s_1} \pm \omega_{s_2}) \\ \mathbf{k} - \mathbf{k}' &= \mathbf{G} \pm \mathbf{q}_1 \pm \mathbf{q}_2. \end{aligned} \quad (4.29)$$

In this case the scattering no longer occurs at discrete wave vectors as a combination of two normal modes satisfying (4.29) can always be found. Multi-phonon scattering can thus be assumed to contribute to the background of the spectra as the scattering occurs for a continuum of energy transfers at a given wave vector transfer [131]. The information about the dispersion relation of a crystal is thus only contained in the peaks of the coherent one-phonon scattering.

4.1.3 Incoherent Scattering

For a general lattice where the equilibrium and instantaneous position of an atom ($m\mu$) are given by eq. (3.1) and (3.2), respectively, the incoherent scattering cross section (4.14) can be written as

$$\left(\frac{d^2\sigma}{d\Omega dE} \right)_{inc} = \frac{k'}{k} \frac{1}{2\pi\hbar} \sum_{m\mu} b_{sd,\mu}^2 \int dt e^{\langle U_\mu^2 \rangle} e^{\langle U_\mu V_\mu \rangle} e^{i\omega t}, \quad (4.30)$$

where $U_\mu = -i\mathbf{Q} \cdot \mathbf{s}(m\mu; 0)$, $V_\mu = i\mathbf{Q} \cdot \mathbf{s}(m\mu; t)$, and $e^{\langle U_\mu^2 \rangle} = e^{-W_\mu}$ the Debye-Waller factor. The expansion of $e^{\langle U_\mu V_\mu \rangle}$ yields the elastic and inelastic scattering cross sections again.

The incoherent elastic cross-section is obtained truncating the expansion after the first constant term. The differential cross section is thus

$$\left(\frac{d\sigma}{d\Omega} \right)_{inc,el} = N \sum_{\mu} b_{sd,\mu}^2 e^{-W_\mu}. \quad (4.31)$$

Only the Debye-Waller factor in the expression for the incoherent elastic scattering cross section is dependent on the wave vector transfer. At low-temperatures the Debye-Waller factor is close to unity, and the incoherent elastic scattering is almost isotropic. In diffraction experiments the incoherent scattering is therefore a smooth background.

The incoherent inelastic one-phonon scattering can be obtained when truncating the expansion after the linear term. The atomic displacements can again be described by

the phonon expansion eq. (4.23) if the atomic vibrations are assumed to be harmonic oscillators. It follows then

$$\langle U_\mu V_\mu \rangle = \frac{\hbar}{2M_\mu N} \sum_{\mathbf{q},s} \frac{1}{\omega_s} (\mathbf{Q} \cdot \mathbf{e}_s^\mu)^2 (e^{i\omega_s t} [\langle n_s \rangle + 1] + e^{-i\omega_s t} \langle n_s \rangle), \quad (4.32)$$

where the expansion can be divided into phonon emission $[\langle n_s \rangle + 1]$ and phonon absorption $\langle n_s \rangle$, similar to the expression for the coherent one-phonon scattering. Substituting (4.32) into (4.30) thus leads to the incoherent one-phonon scattering cross section for phonon emission and absorption:

$$\left(\frac{d^2\sigma}{d\Omega dE} \right)_{inc} = \frac{k'}{k} \sum_{\mu} \frac{b_{sd,\mu}^2}{2M_\mu} e^{-W_\mu} \sum_{\mathbf{q},s} \frac{|\mathbf{Q} \cdot \mathbf{e}_s^\mu|^2}{\omega_s} (\delta(\omega - \omega_s) [\langle n_s \rangle + 1] + \delta(\omega + \omega_s) \langle n_s \rangle). \quad (4.33)$$

For a phonon emission to occur, only one scattering condition, the energy conservation

$$\hbar\omega_s = \hbar\omega = E - E' \quad (4.34)$$

has to be fulfilled. An interference condition similar to the conservation of the wave vector transfer in the coherent case does not have to be respected. The scattering therefore occurs for a continuum of wave vector transfers \mathbf{Q} , and for a given \mathbf{Q} it depends on the number of modes satisfying (4.34). Thus, one-phonon incoherent scattering cannot give the detailed information that coherent scattering can give. Nevertheless, the incoherent inelastic scattering cross section can be used to determine the vibrational density of states. For a Bravais lattice it is directly proportional to the density of states $g(\omega)$.

For a powder sample the orientationally average leads to the double-differential scattering cross section of [99]

$$\begin{aligned} \left(\frac{d^2\sigma}{d\Omega dE} \right)_{inc} &= \frac{k'}{k} \sum_{\mu} \frac{b_{sd,\mu}^2}{2M_\mu} e^{-W_\mu^{av}} \int d\omega' \frac{Q^2}{\omega'} (g_1^\mu(\omega) + g_2^\mu(\omega) + g_3^\mu(\omega)) \times \\ &\times ([\langle n \rangle + 1] \delta(\omega - \omega') + \langle n \rangle \delta(\omega + \omega')), \end{aligned} \quad (4.35)$$

where $[\langle n \rangle + 1]$ and $\langle n \rangle$ are the Bose thermal population factors

$$\begin{aligned} [\langle n \rangle + 1] &= \frac{1}{1 - e^{\hbar\omega/k_B T}}, & \text{for } \hbar\omega > 0 \\ \langle n \rangle &= \frac{1}{e^{\hbar\omega/k_B T} - 1}, & \text{for } \hbar\omega < 0. \end{aligned} \quad (4.36)$$

The orientationally averaged Debye-Waller factor is given by the trace of the static correlation function of the atoms displacement

$$W_\mu^{av} = \frac{1}{6} Q^2 \text{Tr} (\mathbf{B}(\mu)). \quad (4.37)$$

By measuring the incoherent one-phonon scattering as a function of the energy transfer, the phonon density of states may be determined. As every partial density of states is

weighted by the total scattering cross section $b_{sd,\mu}^2$ and the inverse mass $1/M_\mu$, hydrogen rich samples, e.g. water, ice, hydrates, lead to a signal that is dominated by the density of states of the hydrogen atoms. Incoherent inelastic neutron scattering can therefore be a useful tool to determine the dynamics of a hydrogenated sample or if large single crystals are not available. The estimation of the contributions from multi-phonon scattering is not as easy as for coherent scattering, as both one-phonon and multi-phonon processes contribute over a continuous range of wave vectors to the scattering signal. But in the limit of low sample temperatures and a low incident neutron energy the contributions from multi-phonon processes may be neglected.

4.2 Inelastic x-ray Scattering

An inelastic x-ray scattering (IXS) experiment is based on a similar arrangement as a neutron scattering experiment: the incident beam with wave vector \mathbf{k} , energy E , and polarization unit vector ε is scattered by a sample into the solid angle $d\Omega$. The scattered intensity can be described by the double-differential scattering cross section $\frac{d^2\sigma}{d\Omega dE}$. The scattering process contains information on the energy and momentum transfer:

$$\begin{aligned}\hbar\omega &= E - E' \\ \mathbf{Q} &= \mathbf{k} - \mathbf{k}' \\ Q^2 &= k^2 + k'^2 - 2kk' \cos \theta,\end{aligned}$$

where θ is the scattering angle between the incident (E, \mathbf{k}) and scattered (E', \mathbf{k}') photons. The energy losses or gains associated to phonon-like excitations are always much smaller than the energy of the incident photon ($\hbar\omega \ll E$), therefore the wave vector transfer can be written as

$$Q = 2k \cdot \sin(\theta/2). \quad (4.38)$$

The wave vector transfer is thus completely determined by the incident photon wave and the scattering angle and decoupled from the energy transfer. Therefore, IXS has no limitation in the energy transfer at a given momentum transfer for phonon-like excitations (kinematic limitations), in contrast to inelastic neutron scattering (INS) where a coupling between energy- and momentum transfer exists.

The double-differential scattering cross section can in Born approximation be expressed in the *van Hove* representation

$$\frac{d^2\sigma}{d\Omega dE} = \left(\frac{d\sigma}{d\Omega} \right)_0 S(\mathbf{Q}, \omega). \quad (4.39)$$

The double-differential scattering cross section can thus be separated into the coupling of the beam to the scattering system $(d\sigma/d\Omega)_0$ and the properties of the sample given by the scattering function $S(\mathbf{Q}, \omega)$. Within the first-order perturbation theory, resonance effects close to x-ray absorption thresholds of the scattering system and the much weaker

magnetic couplings can be neglected [127]. The coupling of the beam with the scattering cross section can thus be described by the Thomson scattering cross section [18]

$$\left(\frac{d\sigma}{d\Omega}\right)_0 = \left(\frac{d\sigma}{d\Omega}\right)_{Th} = r_0^2 \cdot (\varepsilon \cdot \varepsilon') \frac{k'}{k}, \quad (4.40)$$

where $r_0 = e^2/mc^2 = 2.818 \cdot 10^{-13}$ cm is the classical electron radius. The Thomson scattering cross section is of the order of 10^{-25} cm², i.e. comparable with the neutron-nucleus scattering cross section σ . The total absorption cross section of x-rays above 10 keV energy is limited in almost all cases ($Z > 4$) by the photoelectric absorption process, and not by the Thomson scattering. The sample size along the beam is thus determined by the photoelectric absorption, whose cross section is roughly proportional to Z^4 , and not by the Thomson scattering with a Z^2 dependence. Therefore multiple scattering processes can in general be neglected.

For a monoatomic scattering system a similar expression as in the case of neutron scattering can be found for the scattering function

$$S(\mathbf{Q}, \omega) = \frac{1}{2\pi} |f(Q)|^2 \int dt \sum_{j,j'} \langle e^{-i\mathbf{Q}\cdot\mathbf{R}_{j'}(0)} e^{i\mathbf{Q}\cdot\mathbf{R}_j(t)} \rangle e^{i\omega t}, \quad (4.41)$$

where $f(Q)$ is the atomic form factor. From this expression it can be seen that the inelastic scattering of photons is entirely coherent. It can therefore be used for the determination of phonon dispersion. The expression for the inelastic dynamic structure factor $G_s(\mathbf{q}, \mathbf{Q})$ for inelastic x-ray scattering can be obtained from eq. (4.26) by replacing the coherent scattering length with the atomic form factor $f(Q)$.

The study of phonon dispersion by inelastic scattering requires a probe with a wavelength comparable to interatomic distances and a energy resolution in the meV region. Due to these requirements neutrons can easily be used. X-rays in contrast have a very high incident energy and therefore have to be highly monochromated ($\Delta E/E \approx 10^{-7}$). This resolution with reasonable photon intensity could only be reached in recent years with the advance of third generation synchrotron sources. Even though IXS does not quite approach the energy resolution of inelastic neutron scattering it has some distinct advantages [6]:

- No kinematic limitation, e.g. high velocities of sound can be determined at low wave vector transfers and Raman scattering is feasible.
- The scattering is coherent and independent of the isotopes in the sample, e.g. hydrogenated samples can be investigated.
- The high brilliance of the beam allows the study of very small samples, e.g. small single crystals or high pressure sample environments can be used.

Inelastic x-ray scattering has therefore become a tool to determine the phonon dispersion of samples, where coherent inelastic neutron scattering is not feasible.

Chapter 5

Experimental Details

The neutron scattering experiments were performed at the high-flux research reactor of the Institute Laue-Langevin (ILL) in Grenoble (France) and at the spallation neutron-source SINQ of the Paul-Scherrer-Institute (PSI) in Villigen (Switzerland). The experiments with synchrotron radiation were carried out at the European Synchrotron Radiation Facility (ESRF) in Grenoble.

Full descriptions of the neutron time-of-flight spectrometers, the neutron powder diffractometer and the inelastic x-ray scattering beamline may be found in the published instrument description's of the respective institutes. In the following sections a short overview of the instruments is presented as well as a description of the sample environment used and developed for the experiments under ambient and high pressure conditions.

5.1 Time-of-Flight Spectrometers FOCUS and IN6

The inelastic neutron scattering experiments were conducted at the time-focusing time-of-flight (TOF) spectrometers FOCUS and IN6 at the PSI and the ILL, respectively. The important parameters for the choice of a spectrometer are the energy resolution of the instrument and the neutron flux. Both FOCUS and IN6 achieve a flexible and good energy resolution of $\Delta E \simeq 50\text{--}1000 \mu\text{eV}$ depending on the incident wavelength and the energy transfer of the detected neutron. Both instruments also have the possibility to choose the energy transfer at which the best resolution is reached via the time-focusing option. FOCUS has additionally the possibility to use monochromatic focusing conditions to obtain an energy resolution, which is almost independent of the energy transfer [64]. In the experiments the time-focusing option was chosen for both IN6 and FOCUS. The incident neutron wavelengths and energies used for the experiments are listed in table 5.1.

A description of FOCUS will be given to illustrate the two instruments. FOCUS is a direct geometry time-of-flight spectrometer for cold neutrons at the SINQ. It is located at the end position of the curved guide RNR 11. This guide collects neutrons from the cold source, which is a cold moderator of about 20 liters of liquid deuterium at a temperature of 20 K. The maximum flux of the moderated neutrons is reached at a wavelength of 4.5 Å.

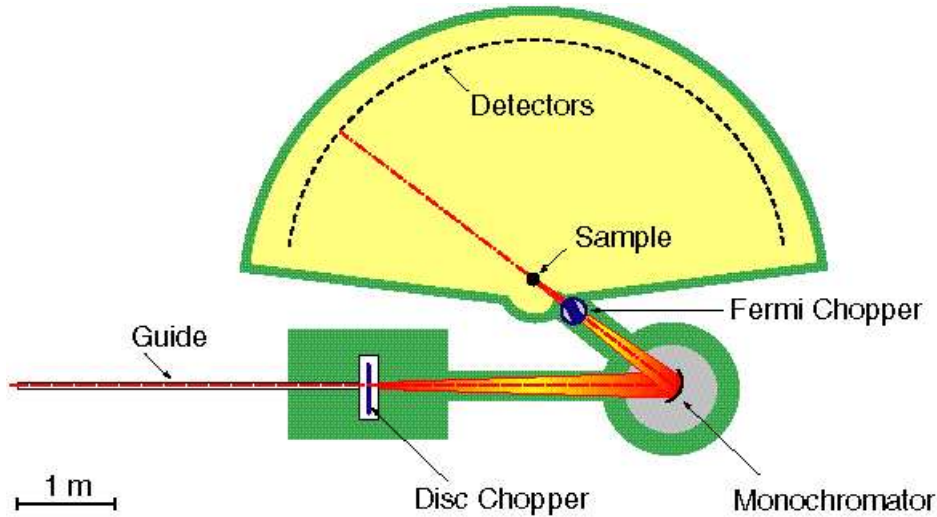


Figure 5.1: Schematics of the cold-neutron time-of-flight spectrometer FOCUS. The incoming neutrons are pulsed by the disc chopper; then the wavelength is selected by a Bragg-reflection from the monochromator that focuses the neutron in both directions through a Fermi chopper onto the sample. The scattered neutrons are then detected by 3 banks of ^3He -detectors.

Spectrometer	Wavelength λ [\AA]	Incident Energy E_0 [meV]	Resolution $\Delta E_{elastic}$ [μeV]
FOCUS	5.0	3.27	90
IN6	5.1	3.15	100

Table 5.1: Instrument parameters of FOCUS and IN6. Only the settings used for the experiments are given.

In Fig. 5.1 the schematics of the instrument are shown. The incident beam reduced by the vertically converging neutron guide is chopped by a pre-selection disc chopper. The incident wavelength can be selected by the (0,0,2) reflection order of a double-focusing pyrolytic graphite monochromator by varying the Bragg angle of the monochromator continuously from 17.5° to 70° . In the case of IN6 the wavelength is selected by the (0,0,2) reflection order of three pyrolytic graphite monochromators. Four different wavelength (4.1 \AA , 4.6 \AA , 5.1 \AA , and 5.9 \AA) can be chosen for IN6, whereas on FOCUS wavelengths from about 2 \AA to 6 \AA can be selected continuously. Contaminations from higher reflection orders are suppressed by a beryllium filter that scatters neutrons with energies higher than 5.2 meV (beryllium cut-off). The neutron beam then passes through a Fermi chopper onto the sample. The scattered neutrons pass a 2.5 m argon filled flight path before being detected by the 500 ^3He counter tubes covering a scattering angle of 10° to 130° . For smaller scattering angles a position sensitive multi-detector is also available. The energy

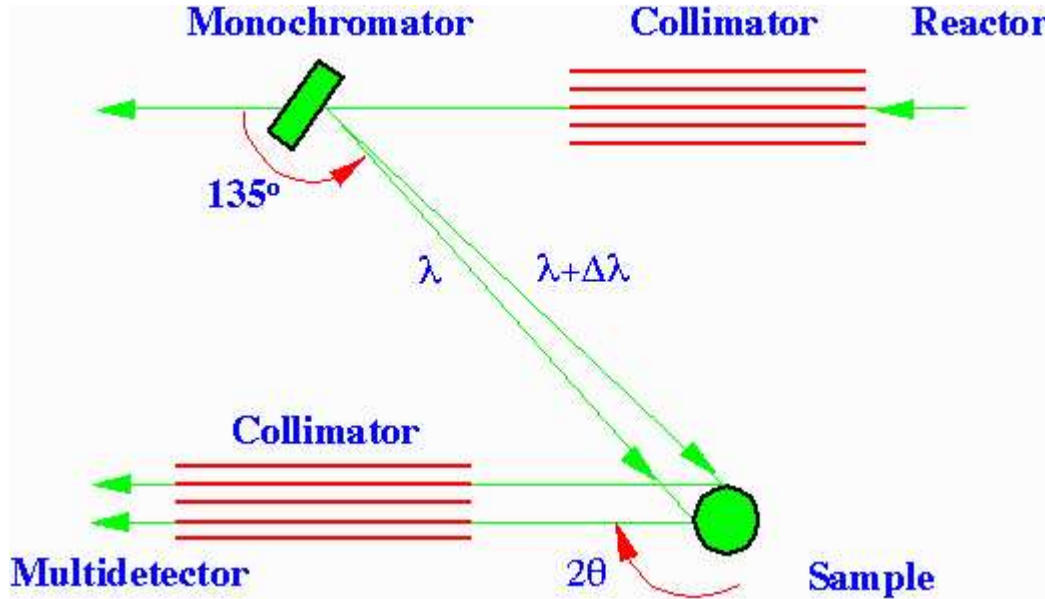


Figure 5.2: Schematics of the high-resolution powder diffractometer D2B. The monochromatic neutrons are scattered by the sample, then collimated and detected by a position sensitive array of ^3He detector tubes.

of the detected neutrons is determined by the time of flight of the neutrons from the disc chopper to the detectors. As the flight distances and the incident energy (wavelength) are known the energy transfer can thus be determined. The scattering angle together with the energy transfer give the wave vector transfer \mathbf{Q} of the detected neutrons. The energy resolution and the maximal wave vector transfer depend on the wavelength of the incident neutrons ($\Delta E \sim \Delta\lambda/\lambda^3$).

5.2 Diffractometer D2B

The diffraction experiments were performed at the high-resolution neutron diffractometer D2B at the ILL in Grenoble. Being at the thermal beam tube H11 in the reactor hall a range of incident wavelengths between 1.051 \AA and 3.152 \AA can be selected from the incoming neutrons by a monochromator consisting of 28 Ge[115] crystals. The high takeoff angle of the monochromator ($2\theta = 135^\circ$) guarantees the high-resolution of the instrument (s. Fig. 5.2). The neutrons are then detected by a 2D array of 128 ^3He detectors. The array is moved in steps of 0.05° in order to cover a scattering angle 2θ from 5° to 165° and to eliminate detector efficiency effects to the recorded patterns.

The required angle resolution of the instrument can be adjusted with the help of the collimators. In order to obtain a maximum flux a collimation of $10'$ together with a wavelength $\lambda=1.594 \text{ \AA}$ was chosen for the high-pressure diffraction experiments. At ambient pressure vanadium sample cells are optimal for diffraction experiments due to the very small coherent scattering cross-section. Vanadium sample holders contribute

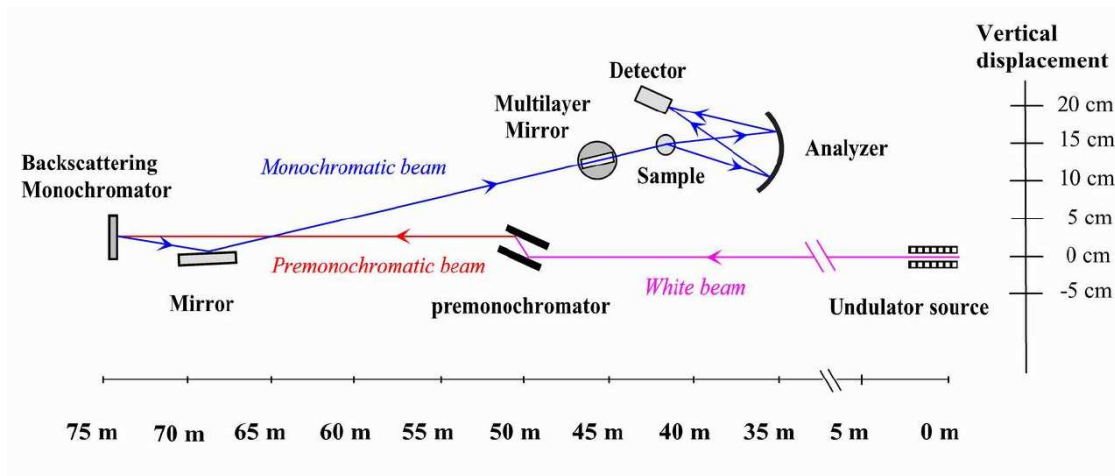


Figure 5.3: Schematics of the optics and the distances of the high-resolution inelastic beamline ID28 at the ESRF. Due to the backscattering geometry the beamline provides long distances in order to acquire a sufficient offset between the incident photon beam from the undulators and the focused very high-energy resolution beam at the sample position.

a smooth background with only very weak Bragg-peaks. The standard temperature control is ensured by the ILL orange helium cryostat for temperatures $1.5 \text{ K} < T < 300 \text{ K}$. A disadvantage of these cryostats is a parasitic aluminum Bragg-peak at about $2\theta = 150^\circ$, which has to be excluded in the data analysis.

5.3 Inelastic Scattering Beamline ID28

The collective dynamics of methane and xenon hydrate were determined with the help of synchrotron radiation at the high-resolution inelastic scattering beamline ID28 at the ESRF in Grenoble. The beamline is equipped with three undulators of 32 mm magnetic period. The undulators are the source of the synchrotron radiation, providing x-rays in the energy range between 13.8 keV and 25.7 keV, while maximizing the flux due to the reduced undulator period.

The lay-out of the instrument ID 28 is based on the triple-axis principle (s. Fig. 5.3), composed of the very high energy resolution monochromator (first axis), the sample goniometer (second axis) and the crystal analyzer (third axis). The x-ray beam provided by the undulators is pre-monochromatized by a silicon (1,1,1) crystal to a relative bandwidth of $\Delta E/E = 2 \cdot 10^{-4}$. The monochromator crystal is cooled to temperatures of about 100 K by a closed-cycle liquid nitrogen cryostat, in order to minimize thermal deformations due to the high heat load produced by the very intense undulator beam.

The main monochromator consists of a flat perfect single crystal, operating in backscattering geometry at a Bragg angle of 89.98° and using the silicon (n,n,n) reflection orders

Reflection Order	Energy [keV]	Resolution ΔE [meV]	$\Delta E/E$	Flux [photons/sec/200 mA]
Si(9,9,9)	17.794	3.0	$1.7 \cdot 10^{-7}$	$2.7 \cdot 10^{10}$
Si(11,11,11)	21.747	1.5	$6.9 \cdot 10^{-8}$	$6.6 \cdot 10^9$

Table 5.2: Instrument parameters for the high energy resolution beamline ID28.

(s. Table 5.2). This almost perfect backscattering configuration guarantees the very high energy resolution together with a maximal incident flux at the sample position. The crystal's temperature is controlled with an accuracy of mK by a high precision platinum Pt100 thermometer. Energy scans are performed by varying the temperature of the monochromator while keeping the temperature of the analyzer fixed. With the choice of the monochromator's reflection order the energy resolution and flux at the sample are determined. See Table 5.2 for relevant settings.

After backscattering from the monochromator the x-ray beam is impinging on the mirror, which focalizes the beam and deflects it upwards towards the sample. At the sample the focal spot size is thus $250 \mu\text{m} \times 80 \mu\text{m}$. If both the focalizing and the multilayer mirrors are used together the beam spot at the sample is further reduced to $25 \mu\text{m} \times 60 \mu\text{m}$.

At the end of a 7 m long rotating arm the five spherical crystal analyzers are mounted. The analyzers thus allow to record spectra at five different momentum transfers simultaneously. The difference in momentum transfer between the different analyzers is 2.43 nm^{-1} for the Si(9,9,9) monochromator reflection and 3.0 nm^{-1} for the Si(11,11,11) reflection, respectively. The momentum transfer resolution is set by slits in front of the crystal analyzers. Analyzers 1,3,4 and 5 are equipped with fixed slits of $20 \times 60 \text{ mm}^2$, whereas analyzer 2 is equipped with motorized slits.

5.4 Sample Handling and Sample Environments

The hydrate samples were synthesized at the National Research Council in Ottawa, Canada. They are made from 99% isotopically pure gas and water in a high pressure vessel by condensing the gas on a very fine ice powder at liquid nitrogen temperatures [48]. After the synthesis the pressure was released and the hydrate samples were recovered at liquid nitrogen temperatures. The "recovered" samples had to be stored and transported in liquid nitrogen making the handling more delicate. Cryogenic temperatures between 80 and 150 K have to be guaranteed during the whole process of the sample preparation for both the ambient pressure and the high pressure sample environments.

For the sample preparation liquid nitrogen is filled into a high polystyrene box. The powder samples were then prepared on massive copper cylindrical blocks, which were cooled down in the liquid nitrogen bath (s. Fig. 5.4). About 2 cm of liquid nitrogen

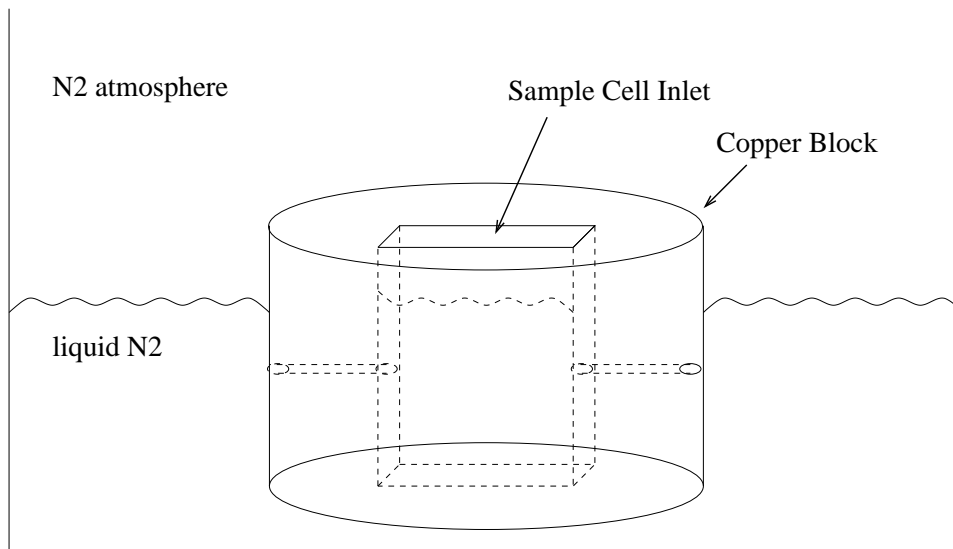


Figure 5.4: Schematics of a copper block standing in liquid nitrogen inside a polystyrene box. The box is high enough to allow a nitrogen atmosphere to form above the block. This prevents precipitation from humidity of the surrounding air onto the cold block. The inlet in the copper block is exemplary and is adapted to the respective sample cells that have to be loaded with hydrate powder.

were kept in the box in order to provide cooling and to supply the nitrogen atmosphere inside the box. This way the condensation of water from the surrounding air could be minimized, the ice contamination of the samples could always be held beneath 2%. The nitrogen condensation onto the hydrate powder proved to be more problematic. In order to prevent it, the liquid nitrogen level inside the box was kept as low as possible. In addition, before sealing any sample cell, it was held above the liquid nitrogen for some time thus warming above the condensation temperature of nitrogen.

5.4.1 Ambient Pressure Sample Cell

The inelastic neutron scattering experiments were all performed at atmospheric pressures. A standard flat aluminum sample cell was used [45] for these experiments. Before loading, the sample cell was cooled down to liquid nitrogen temperatures. It was set into an adapted inlay in one of the copper blocks (s. Fig. 5.4), holding it upright while it was still being cooled to the necessary temperatures. For the inelastic neutron experiments the very fine hydrate powder was filled into the flat sample holder. After preparing a sample with a thickness of about 0.5 mm, the sample holder was closed by a lid, though not sealed. It was then attached to a sample stick and transferred into a standard liquid helium cryostat that was precooled to a temperature of $T \simeq 100$ K. At this temperature any liquid nitrogen that might still be in the sample cell can evaporate.



Figure 5.5: Piston type diamond anvil cell as used in the high pressure inelastic x-ray scattering experiment. The pressure is driven by a membrane that forces the two pistons that contain the diamonds on to each other. The capillary supplying the membrane gas pressure is also visible.

For the inelastic x-ray experiments cylindrical sample cells of 15 mm diameter for methane hydrate and of 1 mm diameter for xenon hydrate were used. The sample preparation was identical to the inelastic neutron experiments. Once the powder was filled into the holder, it was attached to the pre-cooled cold finger of a closed-cycle helium cryostat by a strong permanent magnet. The preset temperature was around $T \simeq 100$ K.

5.4.2 High Pressure Sample Cells

Diamond Anvil Cell

For the high-pressure inelastic x-ray experiments pressures in the range of 10-20 kbar were needed. These pressures cannot be obtained with regular large volume or gas pressure sample cells. Therefore a diamond anvil cell (DAC) was used in the experiments (Figure 5.5). A diamond anvil cell is a small mechanical press where the flat faces of two diamonds are forced together on the sample to create very high pressures. It uses diamonds as they do not break or deform under the pressure and in addition are transparent to x-rays and light. In order to obtain hydrostatic pressures the faces of the diamonds are aligned perfectly parallel. A gasket (circular metal disk) is placed between the anvils of the diamonds (Figure 5.6) to hold the sample between the faces of the diamonds and to maintain the pressure. In the center of the gasket a hole is drilled by electro erosion that can hold the sample. The diameter and depth of the hole depends on the size of the diamonds, the sample and the pressure range. In general, the smaller the hole, the higher the pressures that can be reached.

As methane hydrate scatters x-rays rather weakly a DAC with very large diamonds was used. The anvils had a diameter of $600 \mu\text{m}$, therefore gaskets with a $350\text{-}400 \mu\text{m}$ hole could be used in order to take advantage of the whole beam size available at ID28. Several

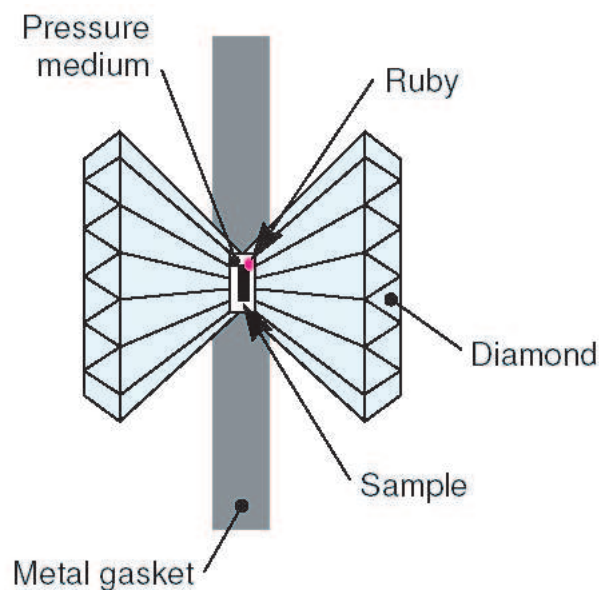


Figure 5.6: Schematics of the diamond anvils with the gasket in between. The sample and the ruby are contained within the hole in the gasket. If a single crystal is used a pressure medium has to be added. (Figure from [2])

INOX-gaskets were prepared prior to the experiment. The gaskets were first indented in the diamond anvil cell, in order to reach a sample thickness of $50\ \mu\text{m}$. The gaskets were fixed on top of one diamond by metal pins. Before loading the sample a small ruby chip was placed on both of the diamond anvils. The ruby chip is used to measure the pressure *in situ* as it emits a fluorescent light with characteristic frequencies when illuminated with a laser. The frequencies of the spectral lines are calibrated as a function of pressure.

Once the gasket and the rubies were in place, the parts of the DAC were cooled to liquid nitrogen temperatures in a polystyrene box. When the equilibrium temperature was reached, they were kept on top of copper blocks inside the nitrogen atmosphere. The hole in the gasket was then filled with as much powder as possible. The sample was compacted with the help of a needle with a $100\ \mu\text{m}$ tip. After loading the gasket with the sample the DAC was assembled in the liquid nitrogen atmosphere and a small pressure was applied to seal the cell. The sealed DAC was warmed to room temperature leading to an initial pressure of about 11 kbar. The pressure could then be adjusted reliably on the beamline with the help of *in situ* ruby fluorescence pressure measurements.

Gas Pressure Cell

To study the crystallographic parameters of methane hydrate under geological conditions pressures of $40\ \text{bar} < p < 100\ \text{bar}$ and temperatures of $T \simeq 4^\circ\text{C}$ are required. As methane hydrate is a very hydrogen-rich compound, it produces a high incoherent background in neutron diffraction experiments. The sample was therefore prepared from 99% isotopically

pure deuterated methane (CD_4) and heavy water (D_2O). The crystallographic parameters of the sample are well known from previous neutron diffraction experiments at very low temperatures. The sample stoichiometry is $\text{CD}_4 \cdot 5.75\text{D}_2\text{O}$ and an intrinsic amount of 2%–3% of hexagonal ice I_h is present in the sample [43]. To keep the hydrate sample stable at this temperature, not only the respective pressure is required, but the sample has to be pressurized with the same gas as encaged in the hydrate. Otherwise the gas hydrate will decompose or if stable under present conditions form a hydrate structure containing the pressure medium as guests [47, 85]. Therefore deuterated methane had to be used as pressure medium.

As standard high pressure equipment is not well adapted for expensive gases, a special low volume sample cell and low volume gas compressor were used. Regular high pressure cells, designed for pressure up to about 7 kbar, are made from high strength aluminum and therefore contribute a number of high intensity Bragg-peaks to the diffraction pattern. These parasitic peaks have to be excluded from the data refinement and reduce the quality of the diffractograms at higher diffraction angles considerably. As the pressure range in the present experiment was limited to 100 bar, it was possible to make the sample cell from pure vanadium. With a coherent and incoherent scattering cross section of $\sigma_{coh}=0.0184$ barn and $\sigma_{inc}=5.08$ barn, respectively, the vanadium mostly contributes to the incoherent background. The cylindrical cell is 60 mm long with a diameter of 12 mm (Figure 5.7). The walls of the cell have a thickness of 1 mm in order to keep the incoherent background to a minimum. The cell is screwed to a cryostat stick with a high pressure capillary, which can be linked to the gas handling system. The pressure was supplied by a Haskel 500 bar gas compressor, which guarantees a minimal gas consumption. The pressure could be measured with both a mechanical manometer and a electronic pressure gauge.

The hydrate powder is filled into a vanadium cylinder with a diameter of 5 mm under liquid nitrogen conditions prior to the experiment. The high pressure sample cell was cooled to $T=80$ K as well. The sample cylinder was transferred into the cold high pressure sample cell (Figure 5.7) that was then sealed. The procedure was carried out under liquid nitrogen condition in order to keep the sample stable. Once the cell was loaded and sealed, it was mounted in a liquid helium cryostat, which was precooled to $T=150$ K. A gas pressure of a few bar was then applied. The pressure was raised slowly together with the temperature in order to keep the methane condensation to a minimum. Nevertheless, measurements at $T=220$ K and $p=100$ bar showed a broad peak in the range of $10^\circ < 2\theta < 25^\circ$ that originates from liquid methane still present in the sample. The methane could be evaporated when the temperature was raised to $T=275$ K. The excess gas was released in order to keep the pressure stable at $p=100$ bar.

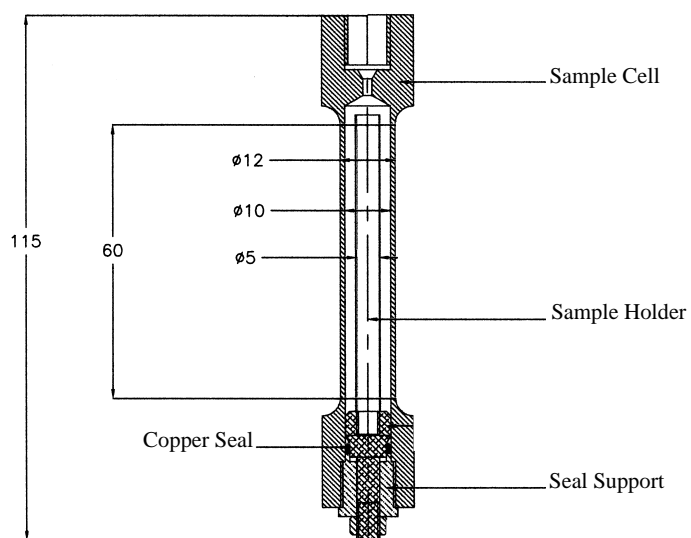


Figure 5.7: Schematics of the vanadium high pressure sample cell. It can be fixed to a standard high pressure cryostat stick and is sealed with a copper seal. A 60 mm long cylindrical sample holder fits inside the cell, taking full advantage of the height of the neutron beam.

Chapter 6

Methane Hydrate – Results and Discussion

The purpose of this chapter is to present the results on the structure and dynamics of methane hydrate. The experimental and theoretical findings will be compared and discussed.

The structural details were obtained for methane hydrate under geological conditions. Here the thermal vibrations of the guest and host molecules and geometry changes of the cage structures near the stability limit have been determined. The investigations of the dynamics focused on the guest molecule and host lattice vibrations and their interactions for methane hydrate structure type I. A combination of results from inelastic neutron and inelastic x-ray experiments allowed the density of states and phonon dispersion curves to be determined. A consistent interpretation of the lattice dynamics of methane hydrate was possible with the addition of lattice dynamical calculations. At higher pressure of a few kilobars the elastic properties of two new methane hydrate structures could be determined by inelastic x-ray spectroscopy.

6.1 Structure of Methane Hydrate under Geological Conditions

In 1984 methane hydrate was identified as hydrate structure type I (space group Pm3n) with a lattice constant $a_0=11.77 \text{ \AA}$ at $T=100 \text{ K}$ [31]. Precise crystallographic parameters of both the host lattice and the encaged methane molecules have been reported recently from a high resolution neutron diffraction study of fully deuterated methane hydrate at low temperature and ambient pressure [43].

Geological conditions are of interest for a determination of details of the cage filling as a function of guest species and gas pressure [21]. Here statistical thermodynamic theories for the cage fillings can be verified experimentally. However, large displacements are to be expected for all molecules at elevated temperatures and high pressures. This is especially true close to the decomposition of solid hydrate to liquid water and gaseous methane,

where high order terms in the crystal potentials are expected to become relevant. These large thermal vibrations make a precise determination of cage occupancies from Rietveld refinements very difficult as both parameters are often strongly correlated [69]. Thus a precise determination of the structure of methane hydrate at high temperatures and high pressures is desirable, but not a simple task. For the neutron diffraction experiments under geological temperature and pressure conditions a specially adapted sample environment together with a fully deuterated methane hydrate sample were used (Chapter 5). The goal of the diffraction experiments was to determine both the structural changes and the thermal parameters of guest and host molecules as close as possible to the decomposition limit of methane hydrate under geological conditions. Therefore, diffraction patterns have been recorded at temperatures of $T=220$ K, 275 K, and 280 K at a pressure of $p=100$ bar at the high-resolution powder diffractometer D2B at the ILL ($\lambda=1.594$ Å). At this pressure the decomposition temperature of the fully deuterated methane hydrate sample was found to be $T\approx 290$ K. The diffractogram at $T=280$ K and $p=100$ bar is thus of special interest.

6.1.1 Structure Refinement

The numerical description of the background in the diffraction patterns is necessary to analyze the data. The density of methane gas at a pressure of 100 bar corresponds to $\sim \frac{1}{10}$ of the density of solid methane. The strong background in the diffractograms arises therefore mainly from the incoherent scattering from the vanadium sample cell and the CD_4 gas atmosphere. The background has been modeled by selecting 90 points between the Bragg peaks and interpolating between those points. The program *Fullprof* was used for this task.

The sample, which was used for the experiments, had a very good powder quality, so no corrections for preferred orientations were needed. As standard method for the refinement of powder diffraction data the Rietveld method was used [109, 110]. To achieve a better description of the diffraction patterns at high temperatures, Rietveld refinement was combined with a maximum entropy analysis, which was performed with the program of *K. Burger* [17] based on the original maximum entropy electron density (MEED) algorithm by *S. Kumazawa et. al.* [114, 77].

Within the 2θ range from 10° to 148° ($\lambda=1.594$ Å) space group Pm3n yields 314 reflections. However, due to the powder sample and the finite resolution of the instrument only 65 non-overlapping reflections were observed in the diffractogram. Figure 6.1 shows the diffractogram of deuterated methane hydrate at $T=280$ K and $p=100$ bar. The high background at small scattering angles stems from the gaseous CD_4 . A detailed section of the pattern is displayed in Fig. 6.2, showing the good quality of the data despite the low Bragg intensities and a high background at the high temperature and gas pressure. Unfortunately, the standard cryostat produces a parasitic reflection at $2\theta=150^\circ$ that had to be excluded from the refinement. Additionally, six reflection, which cannot be indexed by the Pm3n space group of hydrate structure type I, are found in the diffraction patterns. They can be identified with the Im3m space group and arise from the vanadium

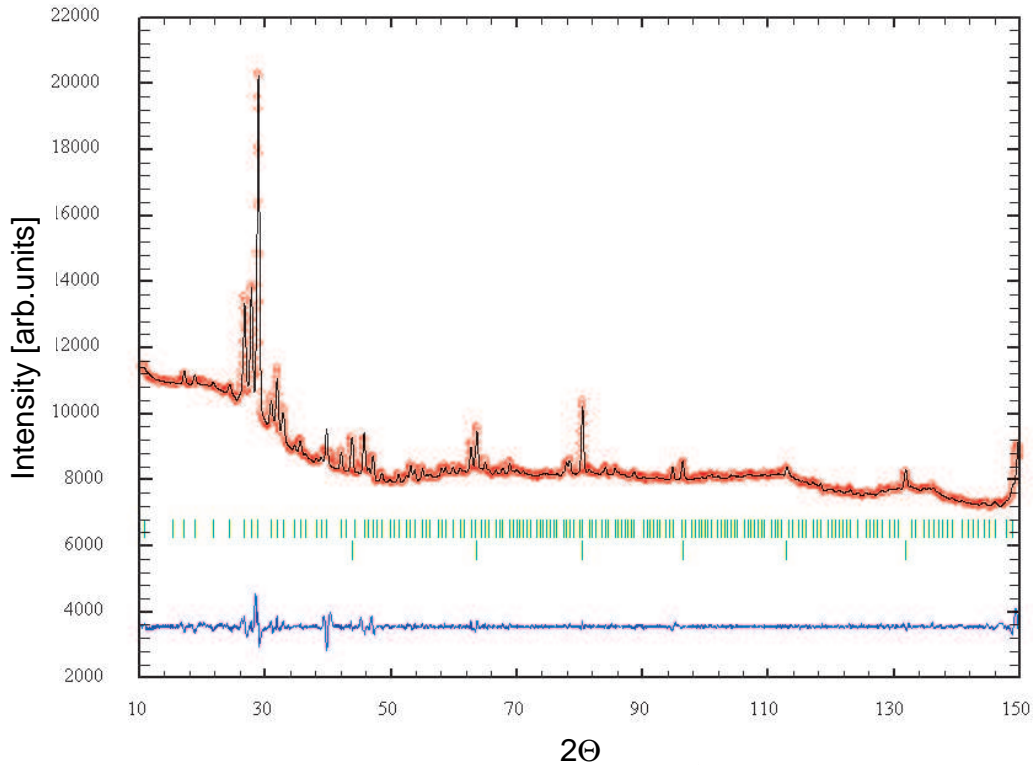


Figure 6.1: Diffraction pattern and profile matching of deuterated methane hydrate ($\text{CD}_4 \cdot 5.75\text{D}_2\text{O}$) at $T=280\text{ K}$ and $p=100\text{ bar}$. The pattern was collected on the diffractometer D2B at $\lambda=1.594\text{ \AA}$ at the ILL. The tick marks refer to the reflections of the hydrate structure I (upper set) and of vanadium (lower set). The difference between the observed and calculated pattern is shown beneath the tick marks.

pressure cell (lower tick set). Due to the small coherent scattering cross section of vanadium these peaks are of low intensity and do not mask large parts of the diffractogram. The structure refinement can be done by excluding a small range around the vanadium peaks. Four hydrate peaks, i.e. the 7 3 2, 9 3 2, 11 2 0, and 11 6 0 peak, are masked by the vanadium reflections. D2B is an angle-dispersive instrument and its resolution Γ (FWHM) is angle-dependent. The profile function of the peak shape is usually well described by [19]

$$\Gamma = \sqrt{U \tan^2 \theta + V \tan \theta + W}, \quad (6.1)$$

where U , V , W are refinable parameters. These parameters depend on characteristics of the diffractometer, e.g. mosaicity of the monochromator, the collimation, or the sample size. Hexagonal D_2O ice melts at 277 K and is therefore present in the diffractograms at

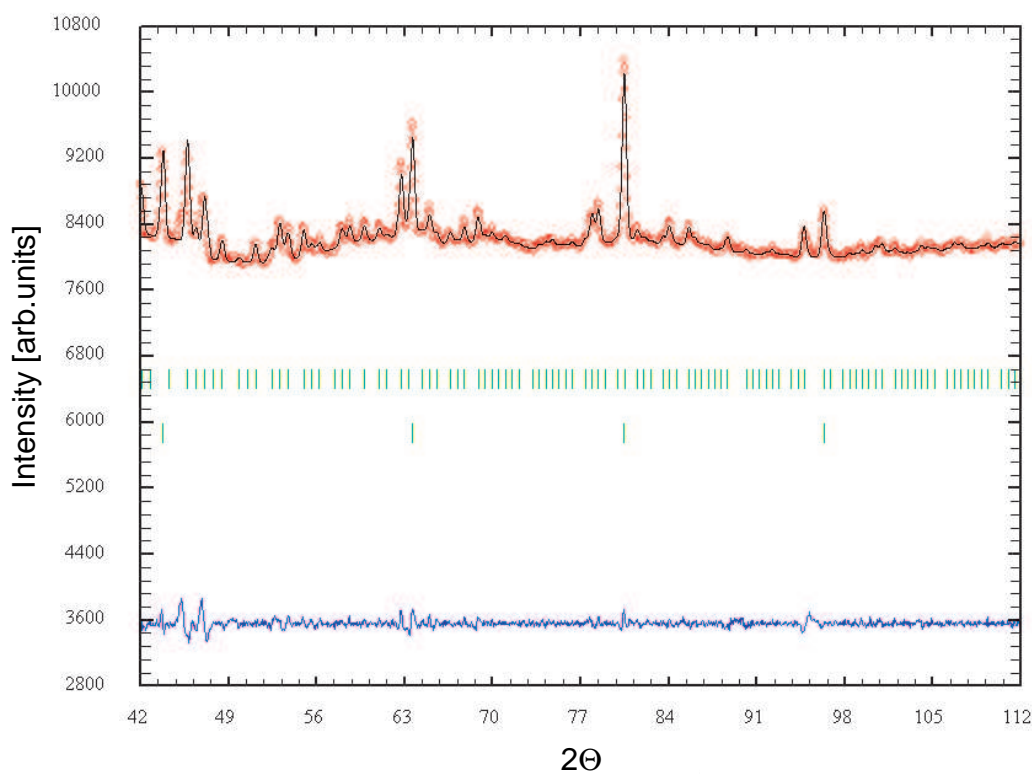


Figure 6.2: A more detailed section (42° – 112°) of the diffraction pattern of deuterated methane hydrate ($\text{CD}_4 \cdot 5.75\text{D}_2\text{O}$) at $T=280$ K and $p=100$ bar. Four vanadium reflections are observed at $2\theta=43.7^{\circ}$, 63.5° , 80.3° , and 96.2° (lower tick set).

220 K and 275 K. The ice reflections were included in the refinement using the precisely determined crystallographic parameters [74, 43].

Rietveld Refinement

The Rietveld refinement was started with initial atomic positions obtained from the previous low temperature study [43]. As the host lattice is disordered with respect to the deuterium positions, the deuterium atoms follow the ice rules with a site occupancy of 0.5. In view of the low count rate at higher scattering angles, a single isotropic Debye–Waller factor U has been refined for all six deuterium positions and one for all three oxygen positions. However, it will be seen from the maximum entropy analysis that this assumption may be too restrictive. Lattice constant, zero point of the scattering angle and angle dependent resolution were included in the refinement procedure.

Regarding the modeling of the methane molecules, the formalism described by *Press*

and *Hüller* was used [103, 104] (see also [102]). In this formalism the CD₄ molecules are treated as rigid units resulting in a structure factor

$$F(Q) = \exp(iQR_0) \exp[-W(Q)]F_{Rot}(Q), \quad (6.2)$$

where R_0 denotes the equilibrium center-of-mass position, $W(Q)$ is the Debye-Waller factor for translational motion and F_{Rot} is the rotational form factor of the methane molecules. At low temperatures the molecules occupy positions in the cage centers [43]. The rotational structure factor can therefore be expanded into symmetry adapted functions (SAF), which belong to the irreducible representation of the group, that contains both the elements of the site and of the molecular symmetry. In the case of methane ($\bar{4}3m$) the cubic harmonics $K_{lm}(\theta\phi)$ [80] form the appropriate set of SAFs. The rotational structure factor of the CD₄ molecules reads

$$F_{Rot}(Q) = 4\pi \sum_{l=0}^{\infty} \sum_{m=1}^{2l+1} i^l j_l(Qr) c_{lm} K_{lm}(\Omega_Q), \quad (6.3)$$

where j_l denotes spherical Bessel functions of order l , Q the scattering vector, r the radius of the methane molecule ($r=1.09 \text{ \AA}$), c_{lm} the expansion coefficients and Ω_Q the polar coordinates of Q . The cubic crystal axes can be used as coordinate system for the expansion in the small cage, which has cubic $m\bar{3}$ site symmetry, whereas in the large cage with $\bar{4}2m$ site symmetry, the z axis is chosen to be parallel to the short $\bar{4}$ axis of the cage. The expansion coefficients c_{lm} are parameters of the Rietveld refinement program, in which the multipole expansion was included. A detailed description may be found in [45, 43].

In a first step a harmonic potential was assumed for the translational movements of the methane molecules. The Debye-Waller factor derived in eq. (4.18) can thus be applied to the data refinement. The static correlation function of the displacements of the methane molecules is

$$B_{ij} = \langle u_i u_j \rangle, \quad (6.4)$$

where u_i denote the displacement along the coordinate i . The site symmetry of the methane molecules dictates the terms of B_{ij} that are allowed. For the cubic site symmetry in the small cage it follows [62]

$$B_{11} = B_{22} = B_{33} = U_{iso} \quad (6.5)$$

and

$$B_{ij} = 0, \quad \text{for } i \neq j. \quad (6.6)$$

In the large cage the the mean square displacements are

$$B_{11} = B_{22} = U_{\perp\bar{4}} \neq B_{33} = U_{\parallel\bar{4}}, \quad (6.7)$$

$$B_{ij} = 0, \quad \text{for } i \neq j, \quad (6.8)$$

with u_1 , u_2 perpendicular the $\bar{4}$ axis of the cage and u_3 parallel to the $\bar{4}$ axis. Therefore one isotropic Debye–Waller factor for the methane molecules in the small cages and two Debye–Waller factors respecting the anisotropic geometry of the large cages have been refined. The inclusion of the first symmetry allowed anharmonic terms in the Debye–Waller factors did not result in an improvement of the refinement.

With the help of this model the Rietveld refinement was performed. The quality of the refinement is described by the R–factor that is given by

$$R = \sqrt{\frac{\sum_i w_i (I_{i,calc} - I_{i,obs})^2}{\sum_i w_i I_{i,obs}^2}}, \quad (6.9)$$

where I_{calc} is the calculated, I_{obs} the observed intensity, and w_i the weight of the data point i . The resulting quality of the Rietveld refinement was not satisfactory, which is attributed to an inadequate description of the methane molecules at higher temperature. Correct modeling of the encaged guest molecules in gas hydrates is often a very difficult task in the Rietveld refinement. The open cage structure leads to large rotational and translational amplitudes of the guests. The high symmetry of the methane molecule in combination with very low temperatures enabled a precise description in previous experiments [43]. Though, already in the case of structure II hydrate formed by small rare gas atoms, e.g. argon or krypton, the occurrence of double occupancies and static disorder may render the situation more complex. The same is true for guest molecules of low symmetry. In the past, a priori models or more sophisticated models based on MD calculations [21] have been used to further improve the Rietveld refinement.

While no unique solution to this problem exists, Maximum Entropy Methods (MEM) have often demonstrated their power in extracting weak signals from noisy background, a situation similar to that encountered at high temperature high pressure diffraction. It has been shown that MEM can provide useful information about thermal displacements and orientational scattering length densities even in the case of powder samples. Therefore MEM has been applied to obtain further information about the scattering length density of methane hydrate.

Maximum Entropy Refinement

The maximum entropy method is based on the expression

$$S = - \sum_r \rho'(r) \log(\rho'(r)/\tau'(r)). \quad (6.10)$$

The probability $\rho'(r)$ and prior probability $\tau'(r)$ are connected with the actual nuclear scattering length density by

$$\rho'(r) = \rho(r) / \sum_r \rho(r) \quad (6.11)$$

and

$$\tau'(r) = \tau(r) / \sum_r \tau(r), \quad (6.12)$$

where $\rho(r)$ is the scattering length density at pixel r and $\tau(r)$ is the prior density for $\rho(r)$.

In the algorithm the expression eq. (6.10) is maximized under the constraints

$$C_1 = (1/N_1) \sum_k |F_{cal}(k) - F_{obs}(k)|^2 / \sigma^2(k) \quad (6.13)$$

and

$$C_2 = (1/N_2) \sum_k ||F_{cal}(k)| - |F_{obs}(k)||^2 / \sigma^2(k), \quad (6.14)$$

where N_1 and N_2 are the numbers of reflections for the phase-known and phase-unknown structure factors, respectively. k denotes the reflection, F_{obs} the observed and F_{cal} the calculated structure factor, $\sigma(k)$ is the standard deviation of F_{obs} . F_{cal} is given as

$$F_{cal} = V \sum_r \rho(r) \exp(-2\pi i r \cdot k), \quad (6.15)$$

with V denoting the unit cell volume. *Collins* [26] used Lagrange's method to obtain an expression of the scattering length density $\rho(r)$ resulting from maximizing S under the constraints C_1 and C_2 .

The quality on the MEM analysis is also described by an R-factor, that is calculated according to

$$R = \sum_k |F_{obs}(k) - F_{calc}(k)|^2 / F_{obs}(k)^2, \quad (6.16)$$

where $F_{i,obs}$ and $F_{i,calc}$ denote the observed and calculated structure factors of the k th data point, respectively [114]. This R-factor is not the same as the one defined in the Rietveld refinement. In general, the R-factor from a MEM analysis is found to be smaller than the one in the Rietveld refinement.

It has to be emphasized that the procedure of applying MEM is not a model free refinement of the data set. Instead all the prior knowledge about the hydrate structure is used to extract further details of the scattering length density of both the host water lattice and the guest molecules. For this purpose Rietveld refinement and MEM have been combined. From the Rietveld refinement, phases have been generated according to the refined model (note that the cubic space group with central symmetry restricts the phases to values of 0 and π only). Then peak intensities have been determined by profile matching the pattern within the space group Pm3n, i.e. the peak intensities were free parameters in the fit.

6.1.2 Results and Discussion

The Host Lattice

Lattice constants, fractional coordinates, and isotropic Debye-Waller factors were determined from the Rietveld refinement.

The diffractograms that were recorded could all be indexed with the space group Pm3n and thus identified with the hydrate structure type I. The lattice constant of fully

Atom	Wyckhoff letter	Multi-plicity	Site Occupancy	x	y	z	Temperature factor U [10^{-2} \AA^2]
1 O	(i)	16	1	0.183(1)	0.183(1)	0.183(1)	4.3(5)
2 O	(k)	24	1	0.0000	0.310(1)	0.123(1)	4.3(5)
3 O	(c)	6	1	0.0000	0.5000	0.2500	4.3(5)
7 D	(i)	16	0.5	0.226(1)	0.226(1)	0.226(1)	5(1)
8 D	(k)	24	0.5	0.0000	0.437(1)	0.200(1)	5(1)
9 D	(k)	24	0.5	0.0000	0.387(1)	0.155(1)	5(1)
10 D	(k)	24	0.5	0.0000	0.327(1)	0.030(1)	5(1)
11 D	(l)	48	0.5	0.064(1)	0.260(1)	0.136(1)	5(1)
12 D	(l)	48	0.5	0.125(1)	0.230(1)	0.161(1)	5(1)

Table 6.1: Fractional coordinates and Debye–Waller factors of the water molecules of the host lattice of methane hydrate at T=280 K and p=100 bar.

deuterated methane hydrate at a gas pressure of p=100 bar was found to increase from $a_0=11.910(1) \text{ \AA}$ at T=220 K, to $11.958(1) \text{ \AA}$ at T=275 K, and $11.964(1) \text{ \AA}$ at T=280 K. For a fully deuterated sample at ambient pressure a lattice constant $a_0=11.821 \text{ \AA}$ at T=2 K was determined [43]. For a partially deuterated $\text{CH}_4\text{-D}_2\text{O}$ hydrate a lattice constant of $a_0=11.97 \text{ \AA}$ has been reported at T=273.15 K and p=100 bar gas pressure [69]. Even though the partially deuterated sample appears to have a larger lattice constant than the fully deuterated sample, the difference is probably within the errors. The lattice constants of $\text{CH}_4\text{-D}_2\text{O}$ hydrate have been found to be larger than those $\text{CH}_4\text{-H}_2\text{O}$ hydrate in agreement with the normal isotope effect [69].

Table 6.1 displays the fractional coordinates of the host lattice at T=280 K and p=100 bar. Most of the values differ by around 3–4% from the corresponding low temperature results, while some of them show a difference of up to 7% in comparison with the low temperature data. The differences in the host lattice become more visible by an inspection of the geometry of the corresponding cage building polygons: three kinds of polygons are present in the structure: two non-planar pentagons (called A and B) and a planar hexagon [55, 94]. The small dodecahedral cages (5^{12}) are formed by twelve pentagons of type A, while the large cages ($5^{12}6^2$) are formed by four pentagons of type A, eight pentagons of type B and two hexagons.

Table 6.2 contains the bond angles and lengths of the hexagon and pentagon A and B. Comparing the three polygon types with the low temperature results, considerably larger deviations of the bond angles from the ideal polygon angles can be observed at geological conditions. For instance, the D–O–D bond angles in pentagon A deviate up to 6.4° from the ideal geometry, in comparison to a difference of 0.5° at T=2 K and

Hexagon			
	bond	angle [°]	length[Å]
D-O-D	8-3-8	101.6	0.96, 0.96
D-O-D	10-2-9	101.6	0.99, 1.04
O-O-O	3-2-2	123.7	2.73, 2.94
O-O-O	2-3-2	112.5	2.73, 2.73
Pentagon B			
	bond	angle [°]	length[Å]
D-O-D	8-3-8	113.5	0.96, 0.96
D-O-D	9-2-10	119.3	0.99, 0.99
D-O-D	12-1-7	103.9	0.93, 0.89
O-O-O	2-3-2	107.9	2.73, 2.73
O-O-O	1-2-3	108.2	2.73, 2.76
O-O-O	2-1-1	106.9	2.76, 2.76
Pentagon A			
	bond	angle [°]	length[Å]
D-O-D	12-1-12	114.2	0.93, 0.93
D-O-D	11-2-10	105.9	0.98, 1.04
D-O-D	11-2-11	103.2	0.98, 0.98
O-O-O	2-2-1	105.0	2.95, 2.76
O-O-O	2-1-2	112.0	2.76, 2.76
O-O-O	1-2-1	105.0	2.76, 2.76

Table 6.2: Bond angles and lengths in deuterated methane hydrate as obtained from the Rietveld refinement of the diffraction pattern recorded at $T=280$ K and $p=100$ bar. The bond labels are referring to the atom numbering in Table 6.1. The errors of the bond angles are about 0.1° , the ones of the bond lengths about 0.005 Å.

	T=220K	T=280K
Dodecahedral Cage		
m3		
U_{iso} [10^{-2} \AA^2]	6(1)	7(1)
Tetracaidecahedral Cage		
$\bar{4}2m$		
$U_{\parallel\bar{4}}$ [10^{-2} \AA^2]	10(2)	39(5)
$U_{\perp\bar{4}}$ [10^{-2} \AA^2]	22(3)	14(3)

Table 6.3: Structure parameters of the CD_4 molecules in methane hydrate.

ambient pressure. In case of pentagon B, the difference is even larger with deviations of the bond angles of up to 11.3° . The D–O–D bond lengths vary between 0.89 \AA and 1.04 \AA , which may be compared with 0.96 \AA and 1.00 \AA at $T=2 \text{ K}$. In the hexagon O–O–O bond angles of $123.7(1)^\circ$ and $112.5(1)^\circ$ are found. Considerable deviations from the low temperature structure can also be found in the D–O–D bonds in the hexagons. Here bond angles of $101.6(1)^\circ$ have been found in comparison to values of 109.3° and 116.5° at low temperature. Thus the differences in the fractional coordinates result from a distortion of the cage geometries. This distortion becomes more visible in the MEM analysis. A similar trend, though with a weaker impact, has been observed previously, comparing data at $T=2 \text{ K}$ with data at $T=150 \text{ K}$ [43].

Concerning the thermal vibrations of the atoms in the host network, isotropic Debye–Waller factors of $U = 4.3(5) \cdot 10^{-2} \text{ \AA}^2$ for the oxygen atoms and $U = 5(1) \cdot 10^{-2} \text{ \AA}^2$ for the deuterium atoms have been determined from the Rietveld refinement at $T=280 \text{ K}$. At $T=220 \text{ K}$ the values are somewhat lower with $U = 3.1(2) \cdot 10^{-2} \text{ \AA}^2$ for the oxygen atoms and $U=4.5(5) \cdot 10^{-2} \text{ \AA}^2$ for the deuterium atoms.

The Guest Molecules

In general, clathrate hydrates are non–stoichiometric compounds. The occupation of the cages depends on the size of the guest molecules and on the gas pressure applied during the synthesis. Methane hydrate is, however, known to be nearly stoichiometric [27, 43]. From the refinement the occupancy was found to be 90–100% for both cage types, reflecting the same synthesis procedure as for the deuterated methane hydrate used for the low temperature diffraction studies. The temperature and pressure conditions do not seem to change the hydrate composition, unless the conditions leave the stability limits of the hydrate sample.

For the methane molecules in the small cages, a single expansion coefficient c_{41} of the orientational scattering length density and one isotropic Debye–Waller factor was

refined. Values of $c_{41}=0.2(1)$ have been determined for all three temperature sets. Higher order coefficients did not contribute significantly and were thus omitted. Comparing these findings to the value of $c_{41}=0.14(7)$ at $T=2$ K, it can be concluded that the orientational scattering length density of the methane molecules in the small cages does not change significantly with increasing temperature or pressure. The thermal motion of the methane molecules increases with increasing temperature as can be seen from the Debye–Waller factor, which increases from $U_{iso} = 2.7(5) \cdot 10^{-2} \text{ \AA}^2$ at $T=2$ K to $U_{iso} = 6(1) \cdot 10^{-2} \text{ \AA}^2$ at $T=220$ K, and $U_{iso} = 7(1) \cdot 10^{-2} \text{ \AA}^2$ at $T=280$ K (see Table 6.3). These values are about twice as large as the thermal displacements of the oxygen atoms of the host lattice and correspond to the findings of $U_{iso} = 7 \cdot 10^{-2} \text{ \AA}^2$ at $T=150$ K [45]. The thermal displacements thus seem to be limited by the cage geometry, pointing towards large excursions of the methane molecules, though sampling the cage potential more rigorously.

The Rietveld refinement of the host lattice and the CD_4 molecules in the small cages resulted at all temperatures and pressures in good convergence and small correlations of the refined parameters. This, however, was not the case for the guest molecules in the large cages. The expansion coefficients of the orientational scattering length density in the large cages were therefore fixed to their initial values and only the two Debye–Waller factors were refined. This improved the convergence at $T=220$ K considerably and values of $U_{\parallel\bar{4}} = 10(2) \cdot 10^{-2} \text{ \AA}^2$ along the short $\bar{4}$ axis of the cage and $U_{\perp\bar{4}} = 22(3) \cdot 10^{-2} \text{ \AA}^2$ along the long axis perpendicular to the $\bar{4}$ axis could be determined. These values indicate large thermal vibrations of the methane molecules in the large cages. Compared to the values found at $T=150$ K and ambient pressure [45], the thermal displacements along the short $\bar{4}$ axis do not increase significantly. However, the Debye–Waller factor $U_{\perp\bar{4}}$ almost doubles. This evolution of the Debye–Waller factors reflects the geometry of the large cages. At $T=275$ K and $T=280$ K the convergence was considerably slower and correlations between the refined parameters increased. The refinement of the Debye–Waller factors resulted in $U_{\parallel\bar{4}} = 39(5) \cdot 10^{-2} \text{ \AA}^2$ along the short axis of the cage and $U_{\perp\bar{4}} = 14(3) \cdot 10^{-2} \text{ \AA}^2$ along the long axis. It is intriguing that the thermal vibrations of the methane molecules in the large cage seem to be more important along the short axis of the cage for temperatures close to the stability limit. This may point towards activated vibrational modes, which become populated due to the high temperature. The cage deformations paired with a translational–rotational coupling in motion of the methane molecule may also allow for a larger excursion of the guest molecule from its equilibrium position along the short axis of the large cage. Anharmonic terms of the Debye–Waller factors were tentatively included to account for these large amplitude motions, but they did not lead to a better refinement: The precision of the large $Q(\text{hkl})$ -data is limited and hence there is a serious restriction to the number of parameters, which can be used in the fit. The final R-factors of the refinement were varying around 5–8%, indicating that details of the scattering length density of methane hydrate are only poorly described by this model.

The MEM Analysis

Implementing a more complex model for both the CD_4 guest molecules and the D_2O molecules forming the host lattice would lead to a large number of parameters to refine. With regard to the low intensity of the hydrate peaks at high scattering angles such a procedure is not promising. Instead a less biased method based on the maximum entropy algorithm was used. For this purpose the intensities of all but the already mentioned four masked hydrate peaks have been determined by profile matching within the space group $\text{Pm}\bar{3}\text{n}$. Profile parameters of the peak shape function and angle dependent resolution have been included. In this way, the intensities of 65 non-overlapping reflections were obtained, providing the first set of constraints according to eq. (6.13). The other 249 reflections can be grouped in 89 overlapping reflections, which enter the second set of constraints according to eq. (6.14).

Using the MEM algorithm without phases, i.e. using constraint eq. (6.14) only, did not result in meaningful results. Therefore the phases of the 65 non-overlapping reflections were determined from a Rietveld refinement of the respective data set, where only a spherically symmetric scattering length density was assumed for the CD_4 molecules in both types of cages (i.e. only the expansion coefficient c_{01} is nonzero). The result of the MEM should thus be as unbiased as possible. In addition the Debye–Waller factors of the guest molecules were set to small isotropic values in both types of cages. A uniform scattering length density with 80 pixels per unit cell axis was used as the starting point for the MEM analysis. The MEED algorithm generates maps of the scattering length densities by maximizing the entropy function S (eq. (6.10)) within the constraints given by the structure factors and within the given space group $\text{Pm}\bar{3}\text{n}$. Thus the resulting scattering length density maps provide the symmetry properties of the corresponding space group.

For reasons of comparison, the same MEM procedure was applied to the low temperature, ambient pressure data set. The MEM based analysis leads to values of the corresponding R-factors of 1.5%.

Figure 6.3 displays the resulting scattering length densities in the (001) plane at $T=2\text{ K}$ and ambient pressure and $T=280\text{ K}$ and $p=100\text{ bar}$. Only values of the scattering length densities between 3 and 18 barn/ \AA^3 are shown. The background of 0–3 barn/ \AA^3 has been omitted for reasons of clarity. The scattering length density of the host lattice is labeled in the maps according to the atomic labels from Table 6.1. In the plane the corners are occupied by the CD_4 molecules in the small cages, while the CD_4 molecules in the large cages occupy the positions $(1/4, 1/2)$ and $(3/4, 1/2)$. Two parts of the hexagonal rings belonging to the large cages can be seen in the lower and upper part of the plane. This structure is formed by the oxygen atom $\text{O}(3)$ at $(1/2, 1/4)$ and two oxygen atoms $\text{O}(2)$ at $(1/4, 1/8)$ and $(3/4, 1/8)$, respectively. The hydrogen bonds between the oxygen atoms are also visible. The low temperature map reveals that the orientational scattering length density of the CD_4 molecules in both types of cages obtained from previous Rietveld refinements [43, 45], is correctly reconstructed in the MEM map. This points towards the

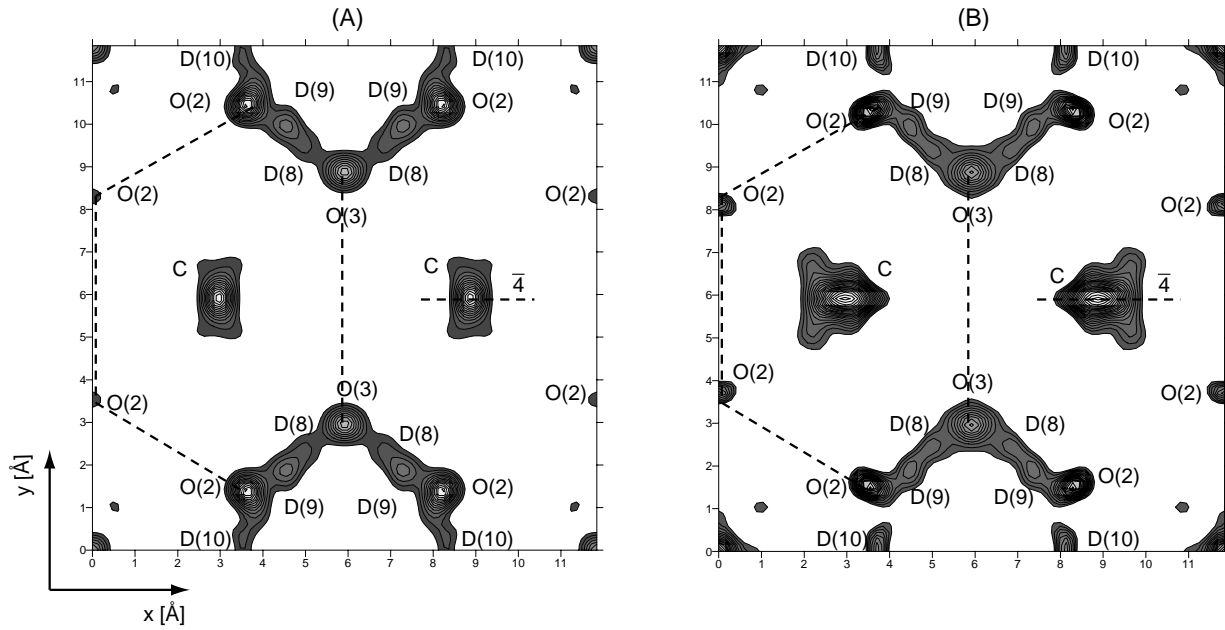


Figure 6.3: Scattering length density map of the (001) plane obtained from maximum entropy analysis at (A) $T=2$ K and ambient pressure and (B) $T=280$ K and $p=100$ bar. Scattering length densities from 3 to 18 barn/ \AA^3 are shown. The axes correspond to the x and y axes of the unit cell. The density of the host lattice is labeled corresponding to the atom labels in Table 6.1. The CD_4 molecules in the small cages can be observed in the corners of the plane, whereas the CD_4 molecules in the large cages occupy the positions $(1/4, 1/2)$ and $(3/4, 1/2)$. The dashed lines show the limits of the cage and the $\bar{4}$ axis.

equivalence of the results of both Rietveld refinement and MEM analysis.

When comparing the MEM maps of the two different temperatures ($T=2$ K and $T=280$ K), differences in the cage structures and the scattering length density of the guest molecules become apparent. At high temperature ($T=280$ K) and pressure ($p=100$ bar) the distortions of the cage structure as already found in the Rietveld refinement can also be observed in the MEM analysis. While the positions of the oxygen atoms $\text{O}(3)$ are fixed by symmetry, the positions of the oxygen atoms $\text{O}(2)$ are found to move outwards from the low temperature positions. This leads to the larger deviations in bond angles from the ideal polygon values. At low temperature the scattering length density of the oxygen atoms is close to spherically symmetric. This is, however, not the case at geological conditions. Here the direction of the thermal displacement of the oxygen atoms $\text{O}(2)$ is almost perpendicular to the hydrogen bonds of the hexagons. In this plane the thermal displacements of the oxygen atoms $\text{O}(3)$ look symmetric, however for maps at different positions in the unit cell larger displacements of tetrahedral symmetry are also found. This is the reason why the peak value of the scattering length density of the oxygen atoms $\text{O}(3)$ is somewhat lower than the peak values of the other oxygen atoms. These thermal

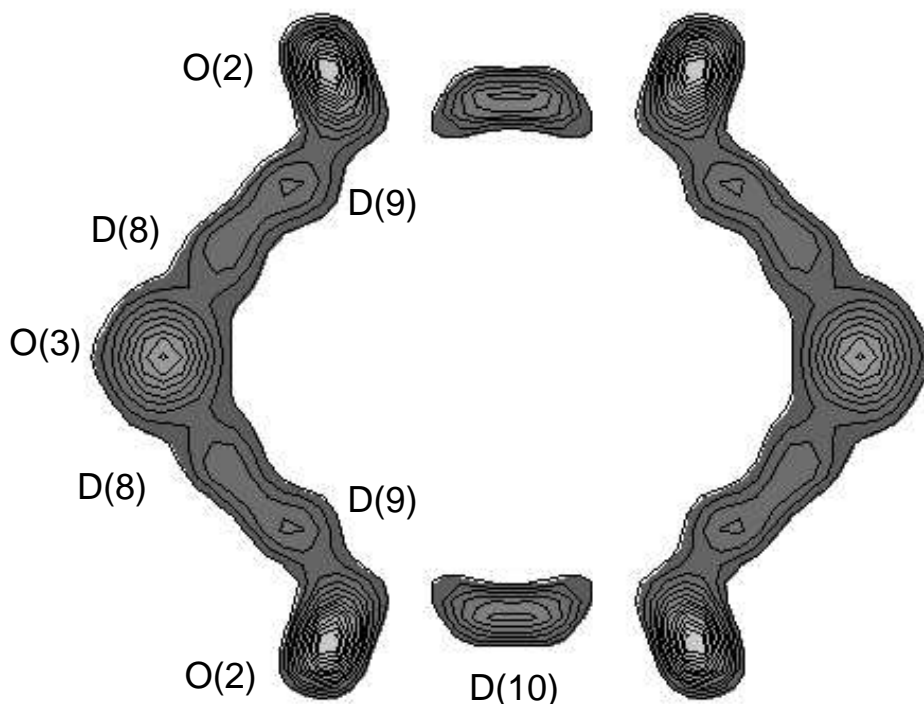


Figure 6.4: Scattering length density of the hexagonal ring of the large cages in the (001) plane in more detail. The scattering length density was obtained from maximum entropy analysis at $T=280$ K and $p=100$ bar.

displacements show that the model using isotropic Debye–Waller factors in the Rietveld refinement is a good description at low temperatures but an inadequate approximation at geological temperature and pressure conditions. The larger thermal displacements are reproduced in both the Rietveld and the MEM analysis, though the assumption of isotropic Debye–Waller factor in Rietveld refinement is too restrictive. Figure 6.4 displays the hexagonal ring in more detail.

Of special interest are the encaged methane molecules. At $T=280$ K and $p=100$ bar large amplitude motions are observed in the scattering length density of the methane molecules. The scattering length density of the CD_4 molecules in the small cage displays in addition the cubic site symmetry of the cage. By far the largest thermal amplitudes in the hydrate structure is provided by the CD_4 molecules in the large cages. From Fig. 6.3 it can be seen that the scattering density distribution is highly elongated along the short axis of the large cage. This finding, originating from a prior with spherical scattering length distribution, is in agreement with the Debye–Waller factors determined in the Rietveld refinement. Weaker features of the scattering length density show up parallel to the y axis

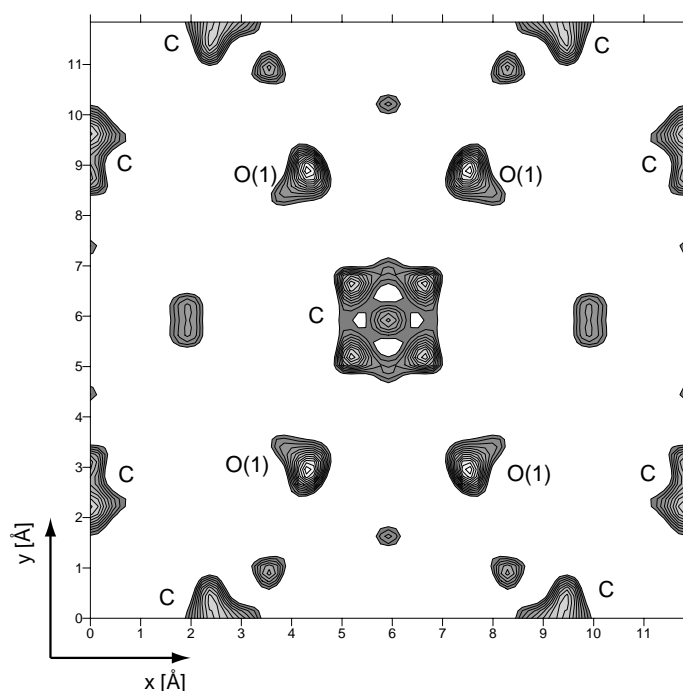


Figure 6.5: Scattering length density map $\sim 1 \text{ \AA}$ above the $(\frac{1}{2}01)$ plane obtained from maximum entropy analysis at $T=280 \text{ K}$ and $p=100 \text{ bar}$. The plane contains the upper half of the small cage, cutting through the scattering length density of the deuterium atoms of the methane molecule at position $(1/2, 1/2)$.

of the unit cell. This may be caused by the rotational motion of the CD_4 molecules. It seems reasonable that this more complicated form of the scattering length density caused the problems of parameter correlation in the Rietveld refinement. This picture suggests an additional term in the displacement function to be relevant. Obviously, a description of the thermal displacements by simple isotropic Debye–Waller factors is not adequate.

In Figure 6.5 a MEM map of the CD_4 molecules in the small cage is displayed. The scattering length density map is showing a cut $\sim 1 \text{ \AA}$ above the $(\frac{1}{2}01)$ plane. The CD_4 molecule in the small cage can be observed at $(1/2, 1/2)$. A trailer of the scattering length density of the central carbon atom is still visible, surrounded by a fourfold coordinated scattering length density. As the deuterium atoms of the methane molecules should be found at a distance of $\sim 1 \text{ \AA}$ from the carbon atom, this scattering length density is attributed to the orientational scattering length density of the deuterium atoms and thus shows the c_{41} term of the multipole expansion of the orientational scattering length density. The MEM analysis leads therefore to the same details of the scattering length density as the Rietveld refinement, from a prior containing only a spherical symmetric scattering length density. At the edges of the unit cell the asymmetric shape of the CD_4 molecules in the large cages is also visible.

6.1.3 Summary and Conclusions

With the help of an adapted high pressure sample cell it was possible to record diffractograms of a fully deuterated methane hydrate sample at temperatures of 220 K, 275 K and 280 K and a pressure of 100 bar of CD₄ gas. These conditions correspond to the geological conditions as present at typical gas hydrate deposits in the world's oceans. The data were analyzed with a combination of Rietveld refinement and maximum entropy methods.

From the Rietveld refinement, precise fractional coordinates of the ice-like host lattice have been obtained. A comparison of the host lattice of methane hydrate with the lattice of other hydrates at low temperatures shows that size and shape of the guest molecule seem to have only minor influence on the structure of the host lattice. However, at elevated temperatures and pressures, distortions of the cages can be observed. The bond angles show considerable deviations from ideal polygon values pointing towards more deformed cages at geological conditions. The MEM analysis provides further insight into the scattering length density. The thermal displacement of both the oxygen atoms of the ice lattice and of the encaged CD₄ molecules show deviations from the simple isotropic models used in the Rietveld refinement. In particular for the guests in the large cages, a more complicated form of the scattering length density is found. Overall, the MEM analysis could not only provide details of the scattering length density, it also reproduced the findings of the Rietveld refinement although only isotropic Debye–Waller factors and spherical scattering length densities were assumed as a prior.

The results of the analysis show that large amplitude motions of methane and water molecules are present under geological conditions, close to the decomposition limit of the clathrate. At some point the amplitude of the vibration should become so large that the atoms start to disturb their nearest neighbors, thus initiating the melting process. Here, the *Lindemann criterion* provides a simple relation [84]: melting might be expected when root mean vibration amplitude $\sqrt{\langle u^2 \rangle}$ reaches at least 10% of the nearest neighbor distance. If the mean O–O distance (~ 2.77 Å) is considered to be the nearest neighbor distance between the water molecules in the host lattice, then the root mean vibration amplitude of the oxygen atoms at T=280 K and p=100 bar ($\sqrt{U} \simeq 0.21$ Å) is 7.5% of the nearest neighbor distance. The large amplitude motions of the water molecules thus reflect the proximity to the decomposition. However, it should be stressed that the Lindemann model for vibrational melting refers only to a crystal with the simplest possible structure, i.e. assemblies of closed packed atoms. It can therefore only be a simple approximation of the melting conditions of a complex inclusion compound like methane hydrate. Deviations from this model can already be observed when applying the Lindemann criterion to the methane molecules. While the mean root vibration amplitude of the methane molecules in the small cages is about 7% of the nearest neighbor distance (~ 3.89 Å), the vibration amplitude of the methane molecules in the large cages can exceed the 10%. In the large cage the nearest neighbor distance along the short $\bar{4}$ axis is ~ 4.0 Å and ~ 4.6 Å along the long axis, resulting in root mean vibration amplitudes of 8% of the next neighbor distance

for the long axis and 16% for the short axis. These deviations from the Lindemann criterion illustrate the inclusion character of methane hydrate: The methane molecules are free to explore the potential surface inside the ice cages and do not seem to influence the bonds between the water molecules in the crystalline host lattice.

Overall, the dissociation of methane hydrate can probably not be considered as a simple process, e.g. unusual behaviors like the metastable hydrate preservation have still to be explained in detail [138]. However, understanding the decomposition process is clearly important with respect to recovering methane from the clathrates and measurements close to the stability limit of the sample give vital reference points and information in this context. For example, if molecular dynamics simulations are to be used to study the decomposition process, then the simulations should reproduce this diffraction data close to the stability limit.

6.2 Dynamics of Methane Hydrate

As it is known that the guest molecules perform sizeable translational motions inside the cages at elevated temperatures, a study of this dynamics is of interest. Dynamical processes in methane hydrate structure I have been investigated to some extent both experimentally and theoretically. The experiments focused mainly on the rotational dynamics of the methane molecules in the cages at very low temperatures [149, 42], whereas the lattice dynamics was the subject of theoretical studies only [143, 38]. The anomalous behavior of the thermal conductivity in clathrate compounds is thought to be connected to their lattice dynamical properties: It is attributed to a resonant scattering of the acoustic phonons by the localized guest vibrations in the cages. In the resonant scattering model [147] it is hypothesized that an *avoided crossing* between acoustic (host)-lattice phonons and localized guest modes of the same symmetry leads to a mixing of guest and host modes with an energy exchange as a consequence. Results of recent inelastic neutron scattering experiments pointed towards a coupling between guest and host vibrations. Examples are found in the phonon density of states of xenon hydrate [151, 46] as well as in various silicon clathrates [95, 108].

The full information about the lattice dynamical properties is given by the complete phonon dispersion of a sample. As methane hydrate is only available in polycrystalline form, only an orientationally averaged information can be gained from the measurements of the phonons. A combination of inelastic neutron scattering (INS), inelastic x-ray scattering (IXS), and lattice dynamical (LD) calculations was therefore used to study the lattice dynamics of methane hydrate in a temperature range of 50 K to 150 K at pressures of a few *mbar* as found in cryogenic sample environments. The combined results can give detailed insight into the lattice dynamical properties, as the methods can supplement each other. The goal was to find experimental evidence for both the guest–host coupling and the avoided crossing between the guest and host modes.

Atom / Molecule	σ [barn]	m [u]	σ/m [barn/u]
H	82.0	1.0	82.0
D	7.6	2.0	3.8
C	5.6	12.0	0.5
O	4.2	16.0	0.3
H ₂ O	168.3	18.0	9.4
D ₂ O	19.5	20.0	1.0
CH ₄	333.7	16.0	20.9
CD ₄	36.1	20.0	1.8

Table 6.4: Total scattering cross section and atomic mass of the atoms and molecules in the different methane hydrate samples. The scattering power σ/m is also given.

6.2.1 Neutron Spectroscopy

The INS experiments on methane hydrate were performed at the time-focusing time-of-flight spectrometer FOCUS at the PSI, Switzerland. The incoming wavelength was $\lambda = 5 \text{ \AA}$ and the time-focusing was set to the elastic line. This resulted in an elastic energy resolution of about $90 \mu\text{eV}$ (FWHM). The raw spectra were corrected for empty container signal and detector efficiency. The average counting time for a spectrum was about eight hours.

To obtain a description as complete as possible of the translational excitations of both the methane guest molecules and the ice-like host lattice, different partially deuterated and protonated methane hydrate samples were used. The INS spectra were recorded for synthesized CH₄-D₂O, and CD₄-H₂O samples in a temperature range of $50 \text{ K} < T < 150 \text{ K}$. At temperatures below $T=50 \text{ K}$ the inelastic neutron spectra are dominated by the rotational excitations of the methane molecules. This is due to their higher scattering cross section [45]. The translational excitations can thus be observed at higher temperatures $T > 50 \text{ K}$, where the damped rotational excitations of the methane molecules can be described by a classical rotational diffusion motion. The rotational diffusion leads to a broad quasielastic signal. It is thus possible to separate the inelastic signal of the translational motion of the water and methane molecules from the quasielastic signal.

Neutron scattering from a polycrystal is usually considered to consist of both the incoherent and the coherent contributions. However, due to the orientational averaging the coherent scattering disregards the wave vector conservation law. Within the “incoherent approximation” [117] the total scattering cross section can there be used in the double-differential scattering cross section eq. (4.35). This approximation has already been tested to be reliable for clathrate hydrate and ice measurements on time-of-flight type instru-

ments [22]. The inelastic scattering is thus a function of the vibrational densities of states of the different atoms weighted by their total scattering cross section σ and inverse mass $1/m$. It is therefore useful to consider the ratio σ/m (scattering power), when comparing the INS spectra of the different samples. This ratio is given in Table 6.4 for the atoms composing the different methane hydrate samples. As the experiments focus on the low frequency lattice dynamics of methane hydrate, translational vibrations are considered only. The individual atoms are therefore assumed to display a similar density of states (DOS) as the molecule that they form. In the observed energy range the inelastic part of the spectra thus consists of the partial densities of states of the host lattice molecules and of the guest molecules.

CH₄-D₂O Sample

In the case of the CH₄-D₂O the deuteration of the water molecules implies a ratio of 20:1 between the scattering power of the methane molecules and the water molecules. Hence, the deuteration of the host lattice strongly suppresses the contribution of the host lattice phonons to the spectra. The spectra should therefore predominantly yield informations about the partial density of states of the methane guest molecules. Figure 6.6 shows the experimental INS spectrum of the partially deuterated methane hydrate (CH₄ · 5.75 D₂O) at T=150 K in the energy region of -15 meV to 0 meV (neutron energy gain). For intensity reasons the signal from all detectors in the accessible Q-range from 0.4 Å⁻¹ to 3.2 Å⁻¹ was summed up. In the spectra a broad quasielastic background is observed. It can be described by a single broad Lorentzian excitation and is thus attributed to the damped rotational diffusion of the methane molecules inside the water cages. Furthermore broad inelastic excitations in an energy region from 4 meV to 13 meV can be observed, with the peak at ~5 meV being the most distinct feature. The detailed balance condition was included in order to emphasize the inelastic contributions in the range of energy transfers from 6 meV to 13 meV in the spectrum.

To attribute these excitations, results from early molecular dynamics (MD) simulations can be used. From these it is known that motion of the encaged methane molecules can be partitioned into the translational center of mass motion and the rotational motion about this center [145]. These two contributions were found to be almost independent. Additionally, the translational power spectrum was determined. Three distinct vibrational frequencies were found. The highest frequency of 8.75 meV was assigned to the vibration of the methane molecules in the small spherical cages. The ellipsoidal shape of the large cage was leading to two lower vibrational frequencies of 6.5 meV and 4 meV, corresponding to the motions along the short and the long axes, respectively.

The inelastic excitations observed in the energy range from 5 meV to 13 meV are thus assigned to the vibrational density of states of the methane molecules. While the peak at ~5 meV can be clearly identified, it is not clear how many excitations contribute to the broad shoulder, which is observed from 7–13 meV. On the basis of the results from the MD simulations three excitations are favored. The inelastic excitations were therefore

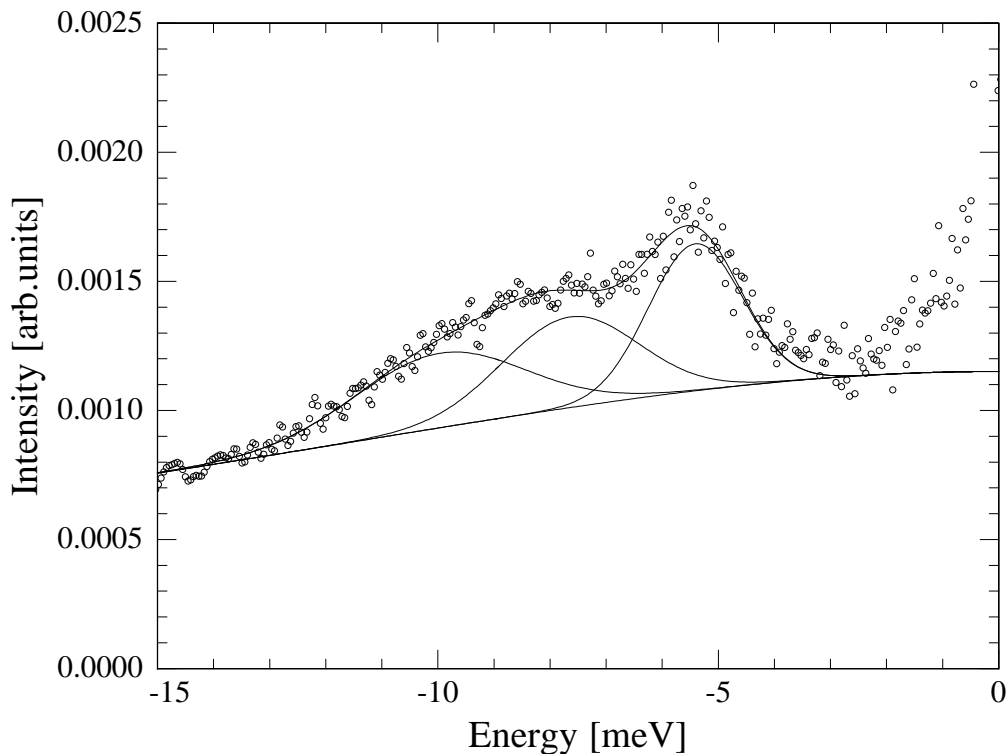


Figure 6.6: Inelastic neutron spectrum of $\text{CH}_4\text{-D}_2\text{O}$ hydrate at $T=150$ K. It was recorded at $\lambda=5$ Å at the FOCUS spectrometer at the PSI, Switzerland. In the region from 4 meV to 13 meV broad inelastic contributions from the translational vibrations of the methane molecules inside the water cages are observable. The broad quasielastic background is attributed to the damped rotational excitations of the methane guest molecules.

fitted with three Gaussian functions. From the fit the energy positions of the peaks are found to be 5.4 meV, 7.6 meV, and 10.0 meV in good agreement with the those from the MD simulations. The peak widths were found to be 1.6 meV, 2.4 meV, and 3 meV (FWHM), respectively. The ratio between the peak intensities is 2:1.7:1.7. A simplistic single particle consideration yields an intensity ratio of about 2:1:1, as there are six large and two small cages in the unit cell. The deviations of the intensity ratios between the fitted peaks from the expected values may point towards a contribution of the water lattice vibrations to the density of states of the methane molecules through a coupling of the guest and host modes. This idea is also supported by the rather broad widths of the observed excitations, ranging from 2 meV to 3 meV.

In the case of xenon hydrate a small frequency increase for the guest modes was observed when raising the temperature from 50 K to 180 K. The peak positions shifted by about $\Delta E \sim 100 \mu\text{eV}$ over this temperature range [46]. The temperature behavior of the vibrations of the methane guest molecules is therefore of interest, as such a behavior may also be observable. INS spectra of $\text{CH}_4 \cdot 5.75 \text{D}_2\text{O}$ in a temperature interval from

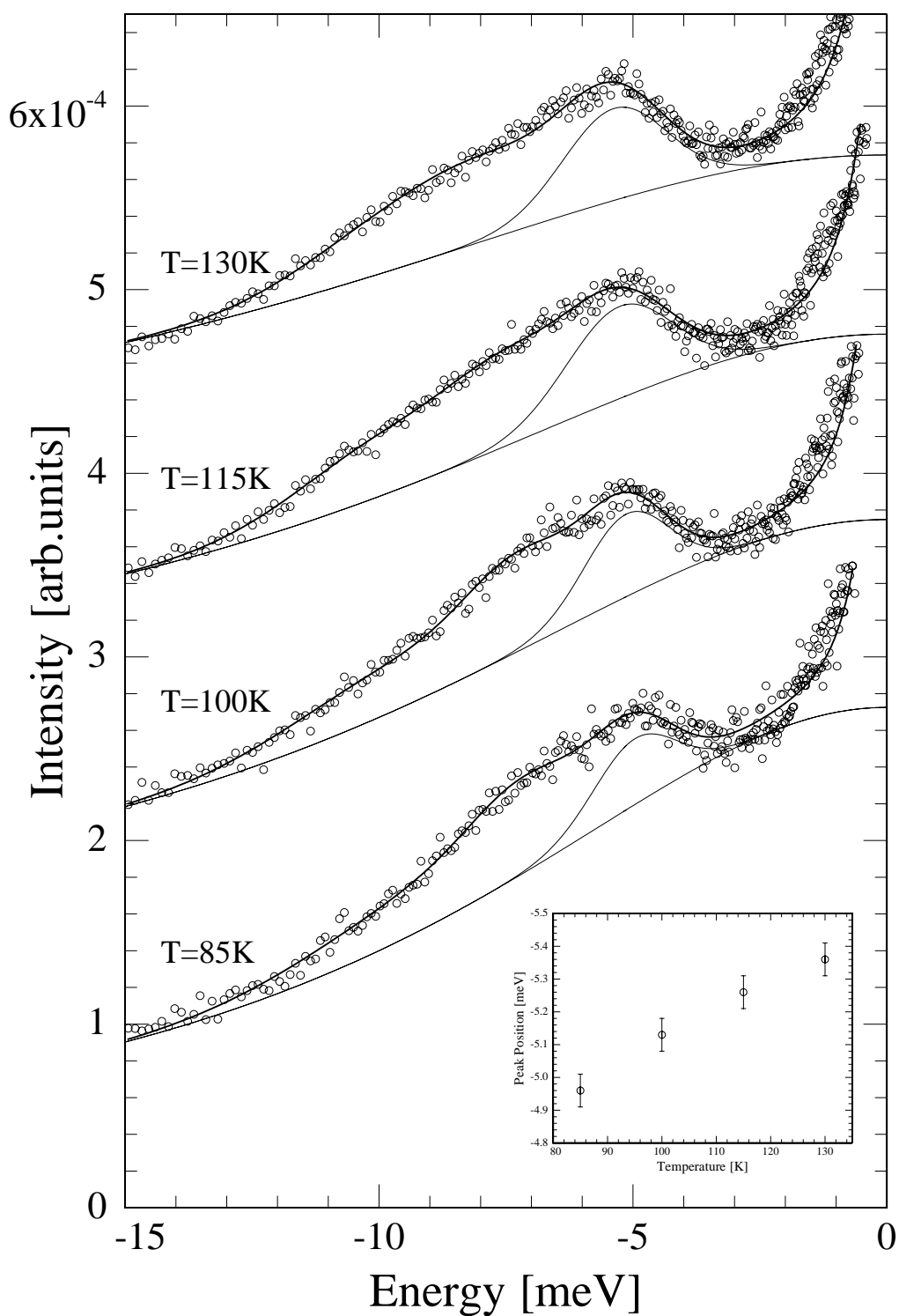


Figure 6.7: INS spectra of CH₄-D₂O hydrate at temperatures of 85 K, 100 K, 115 K, and 130 K. The energy position of the excitation at ~ 5 meV is found to increase with increasing temperature. Its temperature dependence is displayed in the inset.

T [K]	E ₁ [meV]	ΔE ₁ [meV]	E ₂ [meV]	ΔE ₂ [meV]	E ₃ [meV]	ΔE ₃ [meV]
150	5.4	1.6	7.6	2.4	10.0	3.0
130	5.4	2.0	7.5	3.0	9.8	3.4
115	5.3	2.0	7.4	2.4	9.7	3.6
100	5.1	1.6	7.1	2.2	9.6	4.2
85	5.0	1.6	7.0	2.2	8.8	4.6

Table 6.5: Peak positions and peak widths (FWHM) of the three inelastic excitations observed in the INS spectra of CH₄-D₂O hydrate. The peaks were attributed to the vibrations of the methane molecules inside the hydrate cages.

85 K to 130 K were thus recorded in steps of $\Delta T=15$ K. They are displayed in Figure 6.7. Broad inelastic excitations are observed in the energy region of 4 meV to 13 meV at all temperatures. The intensity of the inelastic excitations increases with temperature, as the vibrational modes are more populated, according to the Bose thermal occupation factor. The temperature dependence of the peak positions attributed to the guest molecule vibrations is given in Table 6.5. The peak positions of all three excitations are displayed, even though the values determined for the separation of the excitations at ~ 7 meV and ~ 10 meV were increasingly arbitrary for the INS spectra at lower temperatures. Due to the loss of intensity at lower temperatures, the width of the inelastic excitation at the highest frequency was difficult to determine. Therefore only the well defined energy position of the excitation at ~ 5 meV is considered. For this peak an increase in frequency is, however, found. When increasing the temperature from 85 K to 150 K the guest mode shifts $400 \mu\text{eV}$ towards higher frequencies. In the harmonic approximation of the lattice vibrations the expansion of the crystal with increasing temperature should lead to a lower potential. The vibrational modes are therefore expected to soften with increasing temperature, i.e. to lead to decreasing frequencies with increasing temperature. The increase in frequency with increasing temperature thus points towards the importance of anharmonic terms in the interaction potentials between the water cage and the guest molecule. The influence of anharmonic terms on the frequencies of the lattice dynamics can be treated within perturbation theory [56]

$$\omega' = \omega + \frac{\partial^4 U / \partial x^4}{2\sqrt{m_1 m_2}} \langle x^2 \rangle, \quad (6.17)$$

with $\langle x^2 \rangle$ the squared vibrational amplitude, U the interaction potential, and m_1 , m_2 the masses of the water and methane molecule, respectively. From diffraction experiments it is known that the guest molecules perform large amplitude vibrations at temperatures $T > 100$ K [43]. It is therefore assumed that the repulsive part of the guest–water interaction

potential is thoroughly probed by the large excursions of the guest molecules from their equilibrium positions. As a consequence the interaction potential is dominated by a repulsive interaction, and it follows that $\partial^4 U / \partial x^4 > 0$. The vibrational frequencies thus increase with increasing temperature, as $\langle x^2 \rangle \sim T$. This situation is similar to that found in rare gas solids [156].

A lattice dynamical analysis of methane hydrate showed that the methane molecules would perform localized vibrations with the same symmetry as the acoustic host lattice vibrations [150]. As a consequence, a symmetry avoided crossing between the methane vibrational modes and the acoustic lattice modes was predicted, leading to a mixing of the guest and framework vibrations. This mixing should be observable in either the guest molecule or host lattice density of states. It is therefore of interest to determine the vibrational density of states of the water molecule framework as well. This may be obtained in a first step from the difference of INS spectra of $\text{CH}_4 \cdot 5.75 \text{H}_2\text{O}$ and $\text{CH}_4 \cdot 5.75 \text{D}_2\text{O}$ hydrates. An INS of spectrum of a $\text{CH}_4\text{-D}_2\text{O}$ hydrate sample was therefore additionally recorded at $T=100 \text{ K}$. For both samples measurements at $T=4 \text{ K}$ were additionally performed, recording the inelastic lines from the transition between the first rotational levels of almost free methane rotors (see also [42, 44]). The integral intensities of these lines were used to calibrate the sample quantity, in order to evaluate difference spectra between the protonated and the partially deuterated methane hydrate. Hence the difference spectra should yield the signal from the host lattice.

The difference spectrum was obtained for $T=100 \text{ K}$ (s. Fig. 6.8) in the energy region from -15 meV to 0 meV . In this energy region two relatively broad peaks are observable. A fit with two Gaussian functions leads to energy positions of 7.0 meV and 10.6 meV and peak widths of 1.7 meV and 3.0 meV (FWHM), respectively. The peak at 7.0 meV can be attributed to the transverse acoustic phonons of the host lattice near the zone boundary in good agreement with experimental findings for different clathrate hydrates [151, 46, 22]. The peak at 10.6 meV is assigned to the fold-back of the TA modes towards the zone center. These spectral features may additionally be compared to the INS spectrum of ice I_h , which was recorded for this purpose at $T=100 \text{ K}$ at the time-of-flight spectrometer IN6 at the ILL and is displayed in Figure 6.9. The spectrum was scaled with the Bose occupation factor to obtain the vibrational density of states of the water molecules. In contrast to the difference spectrum of methane hydrate, the INS spectrum of ice I_h displays only one well defined peak at 7.0 meV . This excitation is known to correspond to the maximum of the TA modes [83]. It can therefore be concluded that the two excitations, which are observable in the case of hydrates, are a fingerprint of the open cage structure of the host lattice of water molecules. The statistics of the inelastic features below 6 meV in the difference spectrum of methane hydrate is not sufficient to draw any conclusions, as inelastic excitations and statistical artefacts from the spectra subtraction cannot be distinguished. In this region of the spectrum the relative error of the data points is about 60%. From the comparison of the difference spectrum with the $\text{CH}_4\text{-D}_2\text{O}$ spectrum it is therefore not clear if the strongest translational mode at 5.4 meV in the $\text{CH}_4\text{-D}_2\text{O}$

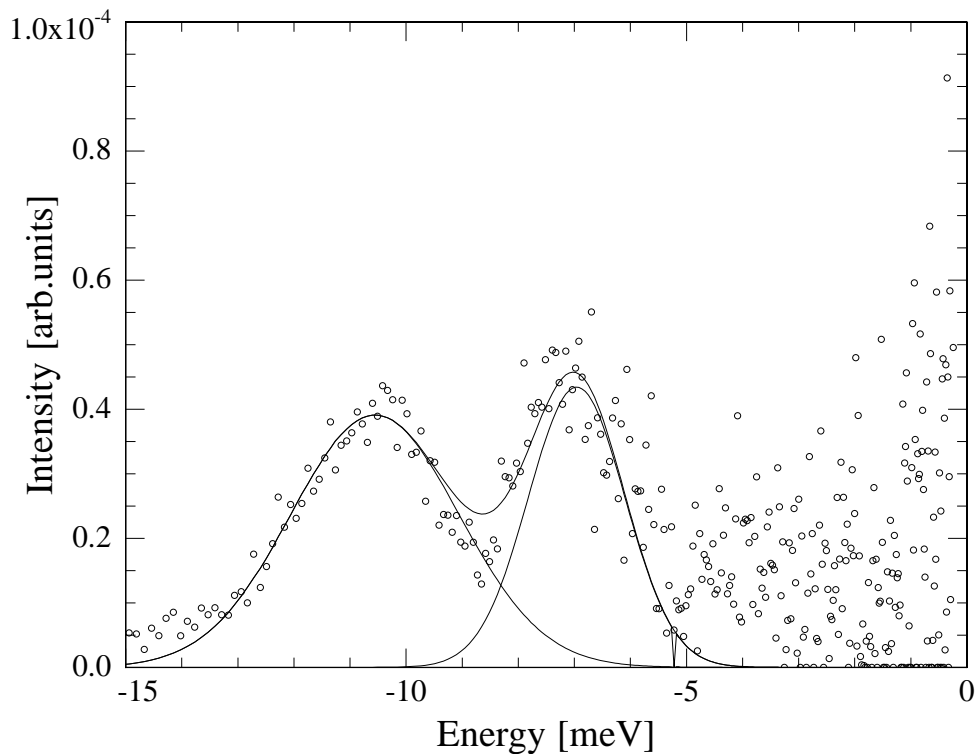


Figure 6.8: The INS difference spectrum of $\text{CH}_4\text{-H}_2\text{O}$ and $\text{CH}_4\text{-D}_2\text{O}$ hydrate at $T=100\text{ K}$ is displayed. Before subtraction of one from the other, the intensity of both was corrected for the sample amount. The resulting difference spectrum shows the DOS of the host lattice. The peaks at 7.0 meV and 10.6 meV are assigned to the TA modes near the zone boundary and the fold back of the TA modes towards the zone center, respectively.

spectrum leads to a distinct excitation in the vibrational density of states of the host lattice. This would have been a clear sign of a coupling of the guest and host vibrations. The guest–host coupling can, however, be too weak to be observed in a “brute force” subtraction of the spectra. Additional information could be gained by INS spectra of $\text{CD}_4\text{-H}_2\text{O}$ hydrate.

$\text{CD}_4\text{-H}_2\text{O}$ Sample

The deuteration of the methane molecules masks their contribution to the INS spectra. The scattering power of the water molecules is 5 times larger than that of the deuterated methane molecules. The intensity of the rotational diffusion of the methane molecules, which was very strong in the case of the $\text{CH}_4\text{-D}_2\text{O}$ sample, should be weaker than the intensity from the vibrational DOS of the host lattice. It is therefore possible to scale the measured scattering functions by the Bose thermal population factor $n(\omega) = (e^{\hbar\omega/k_B T} -$

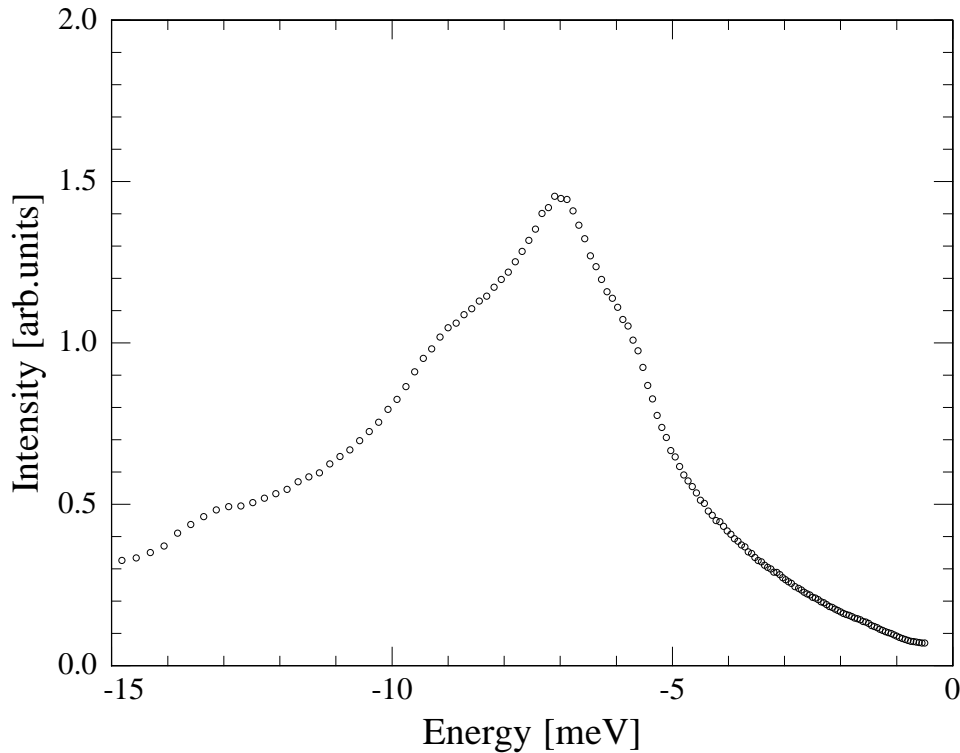


Figure 6.9: INS spectrum of ice I_h at $T=100$ K and $\lambda=5.1$ Å. It was recorded at the time-of-flight spectrometer IN6 at the ILL, France. The peak at 7 meV is attributed to the maximum of the TA lattice modes at the Brillouin zone boundary.

$1)^{-1}$, yielding the generalized susceptibility $\chi''(Q, \omega)$

$$S(Q, \omega) = \frac{1}{\pi} [1 + n(\omega)] \chi''(Q, \omega). \quad (6.18)$$

The generalized susceptibility $\chi''(Q, \omega)$ is proportional to the vibrational density of states of the host and guest molecules weighted by their scattering powers. Additionally, $\chi''(Q, \omega)$ is independent of the temperature for a harmonic lattice.

In order to obtain the generalized susceptibility it is necessary to carefully extract the scattering function $S(Q, \omega)$ from the measured double-differential scattering cross section. For intensity reasons the signal was summed over the available Q -range. The spectrum of the empty container that was recorded at $T=150$ K, was scaled to the respective sample temperatures, assuming a Bose population of the phonons in the aluminum sample cell. The raw spectra were furthermore corrected for background scattering. The scattering function was then obtained after normalizing with k'/k for the incoming flux.

Figure 6.10 shows the obtained INS spectrum of the $\text{CD}_4 \cdot 5.75 \text{H}_2\text{O}$ sample at $T=100$ K in the energy region of -15 meV to 0 meV. Three distinct peaks are the most prominent features of the spectrum. The two peaks at 7.3 meV and 11.0 meV correspond well to the

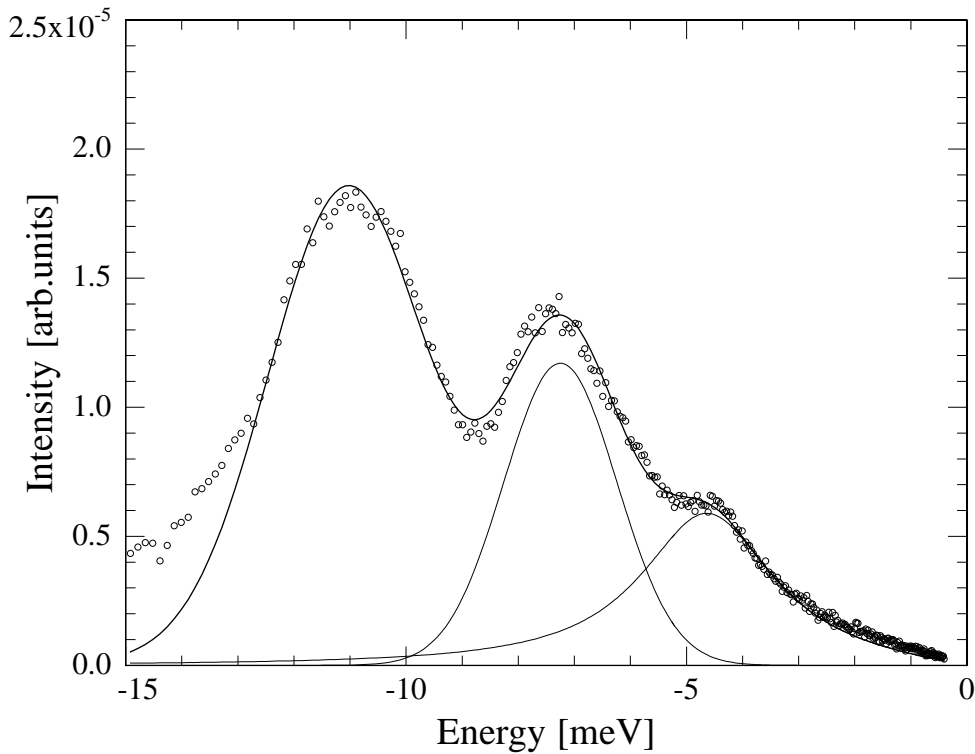


Figure 6.10: Generalized susceptibility $\chi''(Q, \omega)$ of partially deuterated methane hydrate ($\text{CD}_4 \cdot 5.75 \text{H}_2\text{O}$) at $T=100 \text{ K}$ and $\lambda=5.1 \text{ \AA}$. It was recorded at the spectrometer FOCUS at the PSI. A coupling between the localized vibrations of the methane molecules and the host lattice modes is thought to contribute to the intensity of the peak at 4.7 meV .

excitations found in the difference spectrum (s. Fig. 6.8). They can thus be assigned to the TA lattice modes near the Brillouin zone boundary and to the fold-back of the TA lattice modes towards the center of the Brillouin zone. A fit with Gaussian functions leads to peak positions of 7.3 meV and 11.0 meV , and FWHMs of 2.0 meV and 2.8 meV , respectively. These values are also in good agreement with those deduced from the difference spectrum and with values found for xenon hydrate [46]. The two excitations therefore not only seem to be a fingerprint of the open cage structure of the host lattice, but also to be relatively independent of the guest species trapped in the ice cages.

The low energy region of the hydrate spectrum, however, is of particular interest. Instead of observing a pure Debye ω^2 -behavior at energies below 6 meV as found in ice I_h (s. Fig. 6.9), a well defined peak is found in the spectrum of $\text{CD}_4\text{-H}_2\text{O}$ hydrate. Its energy position was determined from the fit with a damped harmonic oscillator function (DHO)

$$\chi''(\omega) = I \frac{4\omega E \Delta E}{(\omega^2 - E^2)^2 + 4\omega^2 \Delta E^2}, \quad (6.19)$$

where I , E , ΔE denote the intensity, the energy position, and the peak width (HWHM),

respectively. The energy position of the excitation was thus determined to be $E=4.85$ meV. This energy can be compared to the findings for $\text{CH}_4\text{-D}_2\text{O}$ hydrate (s. Table 6.5) if the increased mass of the deuterated methane molecules is taken into consideration. Assuming equal potentials for the deuterated and the protonated methane molecules, the peak positions for the translational vibrations of the CD_4 molecules are approximated with

$$\hbar\omega_{\text{CD}_4} \simeq \sqrt{\frac{m_{\text{CH}_4}}{m_{\text{CD}_4}}} \hbar\omega_{\text{CH}_4}. \quad (6.20)$$

A peak at 4.6 meV is thus expected at $T=100$ K. This energy is somewhat lower than the energy position of the observed excitation. However, considering the simple approximation, the peak is still attributed to the localized methane vibrations along the long axes in the large cage. The methane molecule vibrations along the short $\bar{4}$ axis of the large cage and in the small cage found at 7.2 meV and 9.6 meV at $T=100$ K in the case of $\text{CH}_4\text{-D}_2\text{O}$ hydrate are not observed in the spectrum of $\text{CD}_4\text{-H}_2\text{O}$. At energies below 3 meV the fit cannot reproduce the observed intensity. In this energy region the observed intensity strongly depends on the treatment of the raw data. As the spectrum from the empty container was originally recorded at $T=150$ K and then scaled to 100 K, this probably introduced an error. The rotational diffusion of the methane molecules, may also contribute to this part of the spectrum.

The assignment of the guest and host contributions to the peak at 4.85 meV holds information about a possible coupling between the guest and host molecule vibrations. As the intensity depends on the partial densities of states weighted by the respective scattering power, both the partial density of states and the scattering power of the water and methane molecules have to be considered. The scattering power of the guest molecules is substantially lower than the one of the host lattice in the case of $\text{CD}_4 \cdot 5.75 \text{H}_2\text{O}$. However, the partial density of states, which depends on the amplitudes of the vibrational motions, may counterbalance the difference in scattering power. It is therefore difficult to determine if the scattering intensity below 6 meV is due to the partial density of states of the methane or water molecules. In the latter case the peak at 4.7 meV would show the coupling between the guest and host lattice vibrations. Even though it is not possible to quantitatively determine the contribution of either guest molecule or host lattice vibrations to the observed experimental intensities, it is probably valid to assume that both methane and host lattice modes contribute to the energy region below 6 meV of the INS spectra. As a consequence a coupling between the guest vibrations and the host lattice modes would be visible in the spectrum. To determine the strength of the coupling lattice dynamical calculations are necessary in order to separate the contribution of the partial densities of states of the water and methane molecules.

The energy positions of the peaks in the INS spectra of $\text{CH}_4\text{-D}_2\text{O}$ hydrate attributed to the methane vibrations were found to increase with increasing temperature. A similar characteristic is expected in $\text{CD}_4\text{-H}_2\text{O}$ hydrate. INS spectra of the $\text{CD}_4 \cdot 5.75 \text{H}_2\text{O}$ sample were therefore additionally recorded at temperatures of 50 K, 70 K, 85 K, 115 K, and 150 K. These temperatures were chosen in order to compare the spectra with the previous

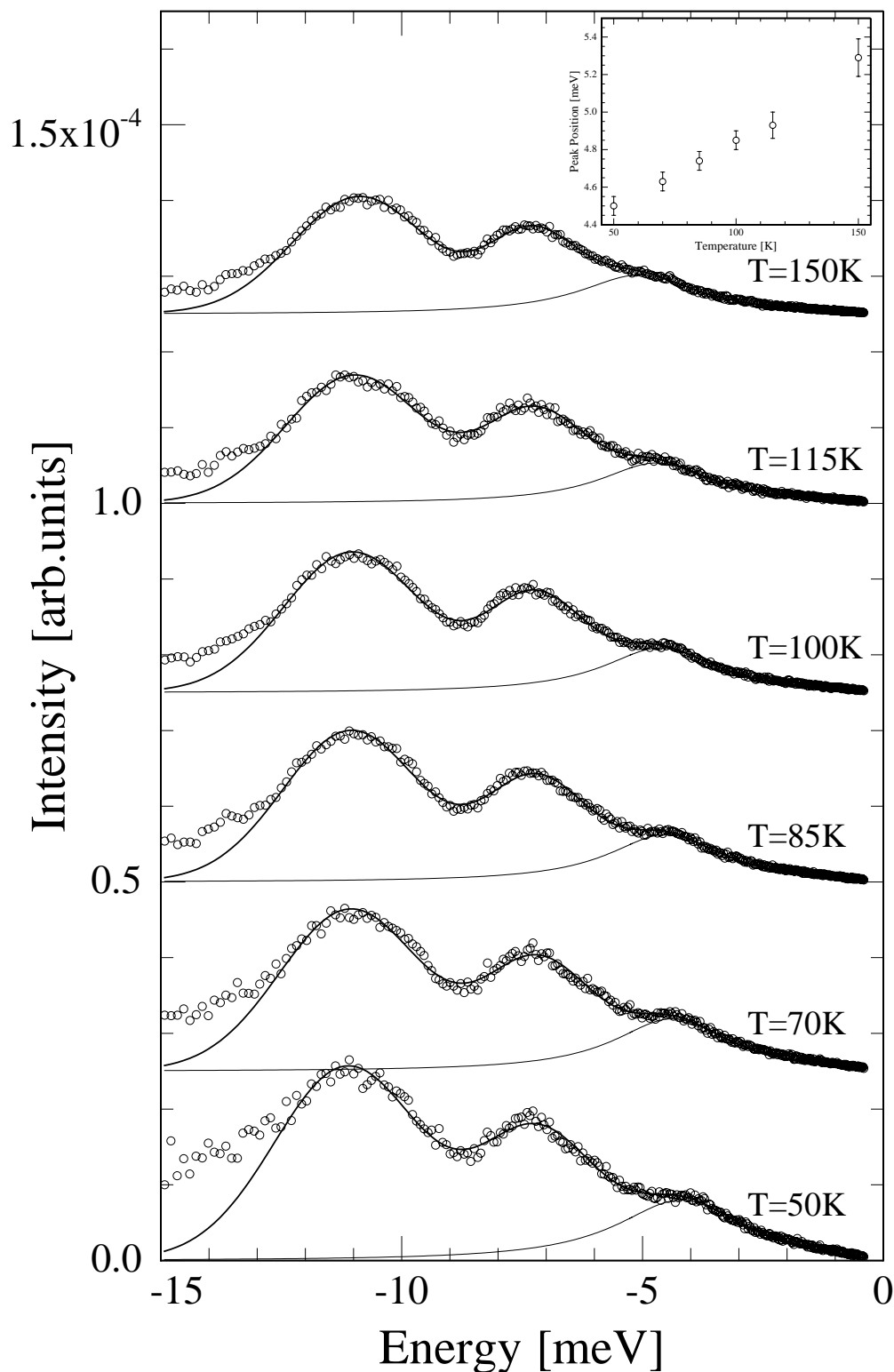


Figure 6.11: INS spectra of CD₄-H₂O hydrate at temperatures of 50 K, 70 K, 85 K, 100 K, 115 K, and 150 K. The energy position of the excitation at 4.5 meV at T=50 K is found to increase with increasing temperature to 5.3 meV at T=150 K.

T [K]	E ₁	ΔE ₁	I ₁ [a.u.]	E ₂	ΔE ₂	I ₂ [a.u.]	E ₃	ΔE ₃	I ₃ [a.u.]
150	5.30	3.0	0.05	7.30	1.8	0.15	10.90	3.0	0.37
115	4.90	2.8	0.04	7.25	2.0	0.16	11.00	2.8	0.34
100	4.85	2.8	0.04	7.25	2.0	0.16	11.00	2.8	0.35
85	4.75	3.0	0.04	7.20	2.0	0.15	11.05	2.8	0.33
70	4.60	3.0	0.04	7.20	2.2	0.14	11.05	2.8	0.30
50	4.50	3.4	0.04	7.20	2.4	0.13	11.15	3.0	0.28

Table 6.6: Peak positions E [meV], peak widths (FWHM) ΔE [meV] and peak intensities I [arb.units] of the three inelastic excitations observed in the INS spectra of CD₄-H₂O hydrate. The excitation at the lowest energy was fitted with a DHO function, whereas Gaussian functions were used for the two excitations at higher energy.

findings from the CH₄-D₂O hydrate sample and to extend the range of measurements towards lower temperatures. The recorded spectra are displayed in Figure 6.11. They were obtained from the raw data as described above. The excitations assigned to the TA host lattice modes were fitted with Gaussian function, whereas a DHO function (eq. (6.19)) was used for the peak in the acoustic region of the spectra below 6 meV. The parameters of the fit are given in Table 6.6.

The excitation at ~7 meV attributed to the maximum of the TA host lattice modes near the zone boundary shows only very little temperature dependence. The peak at ~11 meV is assigned to the fold back of the TA lattice modes towards the zone center. Its energy position slightly increases with decreasing temperature. However, the peak position may have been influenced by contributions from the guest vibrations inside the small cages at around 9–10 meV. It is therefore assumed that the energy positions of the excitations assigned to the transverse acoustic host lattice dynamics are constant within the experimental error.

The peak position of the excitation associated with both coupled and uncoupled guest vibrations along the long axes in the large cage is found to increase with increasing temperature. In the temperature range from 50 K to 115 K the peak at the lowest energy shifts about 400 μeV. At 150 K the peak positions of the excitations at ~5 meV and ~7 meV are strongly correlated in the fit, leading to the strong increase in the energy position from 115 K to 150 K. The anharmonicity that was observed in CH₄-D₂O hydrate, is thus also found for CD₄-H₂O hydrate. The peak shift seems to be somewhat higher in the latter hydrate sample. The peak positions are also found at slightly higher energies than deduced with eq. (6.20) from the respective peak positions in CH₄-D₂O. This can be understood assuming a stronger interaction between the deuterated methane molecules and the protonated lattice. As the potential is thought to be dominated by a repulsive

interaction between the guest and host molecules, an increase in the interaction strength would lead to a more important frequency shift of the modes (s. eq. (6.17)). Both the deviations from eq. (6.20) and the stronger anharmonicity in $\text{CD}_4\text{-H}_2\text{O}$ hydrate may thus be understood assuming an increase in the guest–host interaction strength from $\text{CH}_4\text{-D}_2\text{O}$ to $\text{CD}_4\text{-H}_2\text{O}$ hydrate.

6.2.2 X–ray Spectroscopy

The results of the INS experiments on the various methane hydrate samples have led to some experimental evidence that a coupling between the guest and host vibrations exists. However, the coupling was found to be rather weak corresponding to the findings from early MD simulations on methane hydrate [143]. Comparing these results to the findings from the “box–clathrate”, the weak coupling can be explained by the guest mass, which is only $\sim 16\%$ of that of the surrounding water molecules. The density of states is therefore only little affected by the localized guest vibrations inside the water cages. It is, however, of particular interest if experimental evidence for the avoided crossing between the optic guest modes and the acoustic host lattice can be found. This avoided crossing was also found in the simple “box–clathrate” model, and it was predicted from a lattice dynamical analysis of methane hydrate [149, 150]. It was found that both the acoustic host lattice modes and the localized guest vibrations in the small and large cages have the same symmetry. It was argued that the subsequent avoided crossing leads to strong mixing of the guest molecule and lattice vibrations and to collective motions between the guests and the water framework.

In order to investigate these phenomena, the collective dynamics of methane hydrate has to be determined experimentally. As methane hydrate only exists in polycrystalline form, an unambiguous assignment of observed phonon modes is not possible in general. The direction of the momentum transfer \mathbf{Q} is not defined for the randomly oriented single crystals, which constitute the powder. This means the intensity is measured as a function of $|\mathbf{Q}| = Q$ and the scattering process takes place on a spherical shell in reciprocal space. For a chosen momentum transfer Q a variety of phonon modes can therefore be excited. Only in the first Brillouin zone where the reciprocal lattice $\mathbf{G} = 0$ is it possible to reliably assign the observed modes, as the selection rule for the momentum transfer in the one–phonon approximation leads to $\mathbf{Q} = \mathbf{q}$. Inspecting the inelastic dynamic structure factor (eq. (4.26))

$$G_s(\mathbf{q}, \mathbf{Q}) = \sum_{\mu} f_{\mu}(Q) \frac{1}{\sqrt{M_{\mu}}} (\mathbf{Q} \cdot \mathbf{e}^{\mu}(\mathbf{q}_s)) e^{i\mathbf{Q} \cdot \bar{\mathbf{R}}(\mu)} e^{-W_{\mu}},$$

it can be seen that only components of the atomic displacements parallel to \mathbf{Q} are visible in the spectra. That is only components of atomic displacements with $\mathbf{q} \parallel \mathbf{e}^{\mu}$ are observable within the first Brillouin zone, limiting the contributions to the spectra to longitudinal modes. Momentum transfers beyond the first Brillouin zone can excite several longitudinal and transverse phonons, thus giving information on the density of states of these modes [18]. The use of neutrons to determine the collective excitations is virtually ruled out

due to restrictions in Q - ω space at Q -values within the first Brillouin zone (simultaneous conservation of energy and momentum transfer), and due to the incoherent contribution of the hydrogen atoms to the spectrum. As IXS can access the small Q -values needed and provide the necessary energy resolution at the same time, the experiments were performed at the beamline ID28 at the European Synchrotron Radiation Facility in Grenoble. By using the Silicon (11,11,11) reflection order for both the monochromator and the analyzer an overall energy resolution (FWHM) of 1.5 meV at 21.747 keV was achieved. For the experiment a methane hydrate sample ($\text{CH}_4 \cdot 5.75 \text{H}_2\text{O}$) with a thickness of 15 mm was prepared and loaded onto the precooled cold finger of a closed-cycle helium cryostat. The purity and quality of the sample were assured prior to the inelastic scans by measuring the static structure factors. The contamination with ice I_h of the hydrate sample was less than 2% and it displayed a very good polycrystallinity without preferred orientations. Inelastic scans were then recorded at $T=100$ K in the energy region of -20 meV to 20 meV at momentum transfers of $1.5 \text{ nm}^{-1} < Q < 11.0 \text{ nm}^{-1}$. At lower momentum transfers the contributions from the incident beam were too important. These momentum transfers were chosen in order to cover and extend the measurements beyond the first Brillouin zone. This should give the possibility to assign the observed phonon modes as well as to compare the results with the density of states obtained from the INS experiments.

In Figure 6.12 a selection of inelastic x-ray spectra of methane hydrate is shown at several momentum transfers between 1.5 nm^{-1} and 5.0 nm^{-1} . The elastic line at $E=0$ meV can be attributed to small angle scattering and to scattering from residual disorder in the powder as well as from the sample container. The spectra display a well defined dispersive mode and, from 3 nm^{-1} on, a second non-dispersive peak. In order to extract the energy positions $\Omega(Q)$ of the excitations, the peaks were fitted using Lorentzian functions convoluted with the instrument's resolution. From these fits the energy position of the non-dispersive peak is found to be $\Omega_G=5.0 \pm 0.1$ meV over the whole observed Q -range. The position of the dispersive mode is found to scale linearly with the momentum transfer in the Q -range of $Q < 6.0 \text{ nm}^{-1}$ (inset Fig. 6.12). This dispersive excitation can be identified with the longitudinal acoustic (LA) host-lattice phonon branch. From the slope of the dispersion of the longitudinal acoustic mode an orientationally averaged sound velocity of $c=3950 \pm 50$ m/s can be deduced. The value found is very close to that of ice I_h and in agreement with very recent results obtained by Brillouin light scattering [122] and pulse-transmission wave speed measurements [50].

Additional information can be obtained from spectra at higher momentum transfers (Fig. 6.13). Due to the better contrast – the LA mode moves out of the energy window – additional broad features can be observed at around 7-10 meV. The broad excitations were fitted with an additional Lorentzian function. The energy position of this peak displays a slight dispersion, it ranges from 6.9 ± 0.2 meV at $Q=8.0 \text{ nm}^{-1}$ to 9.5 ± 0.3 meV at $Q=11.0 \text{ nm}^{-1}$. As the smallest diameter of the first Brillouin zone, determined from the first allowed (110) Bragg-peak [55], is $Q_{min}=\pi/d=3.8 \text{ nm}^{-1}$, the spectra in the Q -region from 5 to 11 nm^{-1} reflect both longitudinal and transverse phonons. If the Q -value is

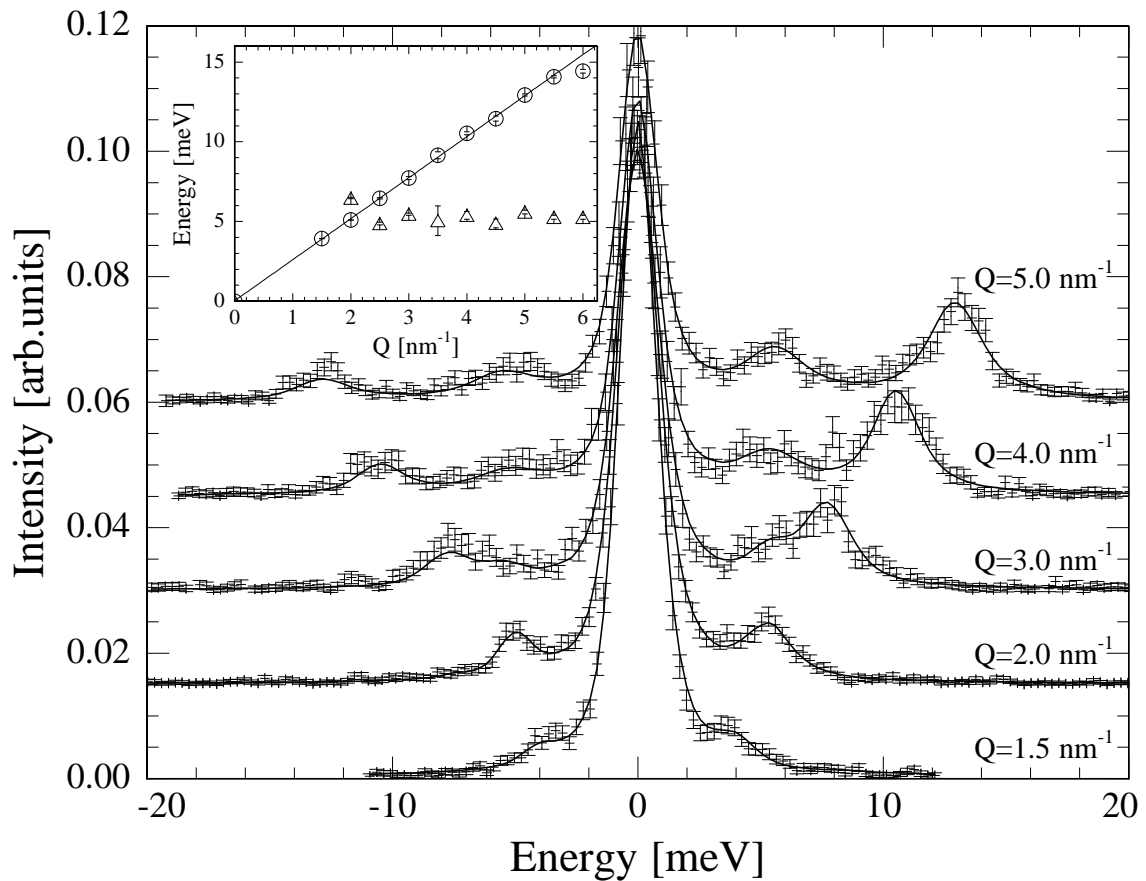


Figure 6.12: Inelastic x-ray spectra of methane hydrate at several Q -values at $T=100$ K. The spectra were recorded at the beamline ID28 at the ESRF. The lines are fits to the spectra using Lorentzian functions convoluted with the experimental resolution. The spectra were normalized to their integrated intensity. The dispersive excitation visible in the spectra is attributed to the longitudinal acoustic lattice mode, whereas the optic-like mode ($\Omega_G=5.0$ meV) is attributed to the localized guest vibrations inside the large cage. The inset shows the respective dispersion relations.

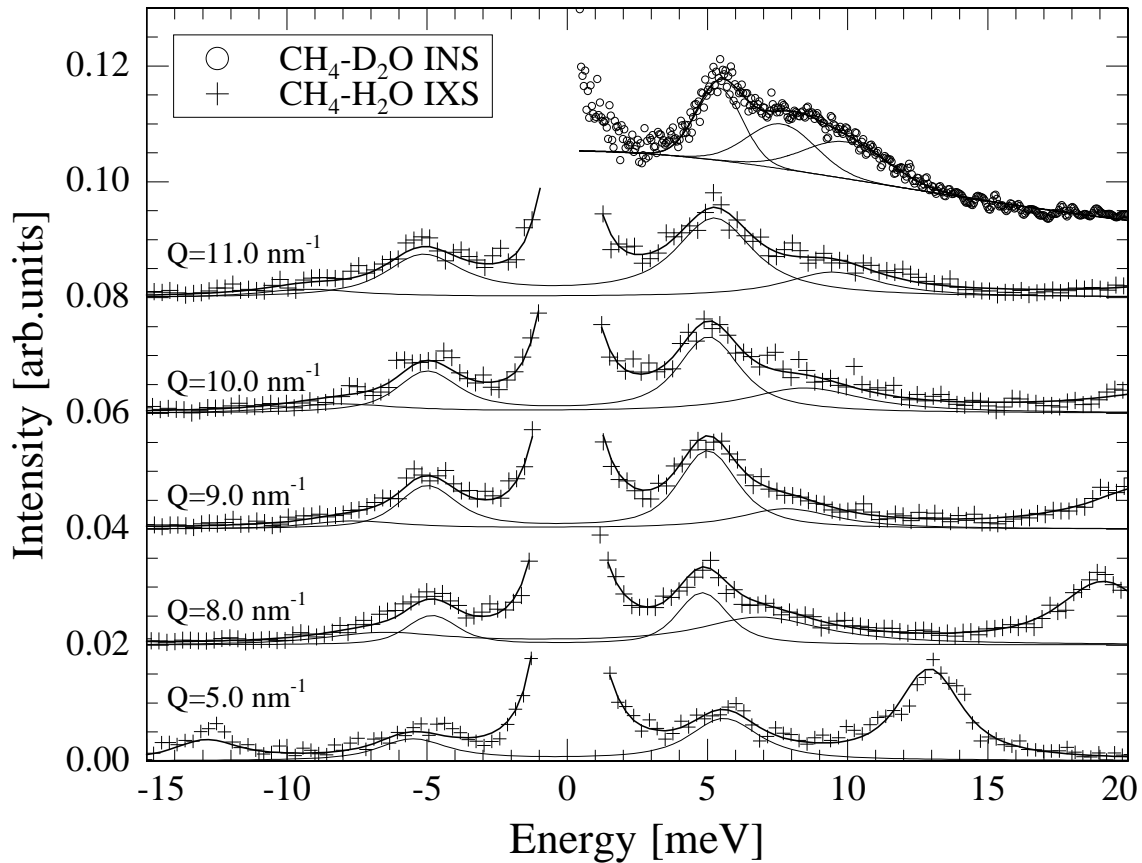


Figure 6.13: Inelastic x-ray spectra of methane hydrate at several Q -values beyond the first Brillouin zone and an inelastic neutron spectrum of $\text{CH}_4\text{-D}_2\text{O}$ hydrate are shown. The excitation at 5.4 meV in the INS spectrum and the optic mode at 5 meV in the IXS spectra are assigned to the localized vibrations of methane molecules along the long axes of the large cage. The peaks fitted to the broad shoulder in the INS spectrum (7.6 meV and 10.0 meV) arise from the guest vibrations along the short axis of the large cage and inside the small cage. The broad slightly dispersive excitation at 7–10 meV in the IXS spectra is thus attributed to both the TA host lattice phonons and additional guest molecule vibrations.

large enough to excite many phonons of different symmetry, than the specific features of the density of states (DOS) should be reproduced. A comparison of the IXS spectra with INS data can therefore help to attribute the observed modes.

The INS spectrum of the $\text{CH}_4\text{-D}_2\text{O}$ sample at $T=150\text{ K}$ is shown in Fig.6.13 for comparison. As the host lattice is deuterated the spectrum reflects the dynamics of the methane guest molecules. The broad background in the INS was fitted with a Lorentzian, reflecting the damped rotational excitations of the methane molecules. These molecular rotations are not visible in the IXS experiments, as they are not sensitive to single particle dynamics. Additionally, a peak at 5.4 meV with a broad shoulder centered at 8 meV are observed in the INS spectrum. This peak and the broad shoulder were fitted with three Gaussian functions, assigned to the methane vibrations inside the small cages (10.0 meV), along the short $\bar{4}$ axis of the large cages (7.6 meV), and along the long axes of the large cages (5.4 meV).

In the IXS spectra the peak at 5 meV appears at $Q \simeq 3\text{ nm}^{-1}$, which is close to the “smallest size” of the Brillouin zone in structure type I clathrate ($Q_{min}=3.8\text{ nm}^{-1}$). It might be attributed to the transverse acoustic lattice modes near the zone edge, in analogy to findings in ice I_h [119]. But contrary to our results, the peak assigned to the transverse modes in ice I_h only appears at the zone boundary on increasing Q and its intensity increases significantly with increasing Q and quickly dominates the experimental spectra. This intensity behavior indicates a strongly transverse symmetry. However, in the IXS spectra of methane hydrate the intensity of the peak at 5 meV does not show a strong increase in intensity with increasing wave vector transfer. From previous INS experiments on $\text{CD}_4\text{-H}_2\text{O}$ and from the difference spectrum of $\text{CH}_4\text{-D}_2\text{O}$ and $\text{CH}_4\text{-H}_2\text{O}$ it is known that the maximum of the transverse acoustic modes is at about 7 meV [7]. The open cage structure also leads to a “fold-back” of the transverse acoustic (TA)-modes, its maximum is located at about 10 meV in the experimental density of states. The energy region below the contributions of the host lattice was found to exhibit the translational vibrations of the guest molecules inside the water cages. The peak at 5.4 meV in the INS spectrum was therefore attributed to the methane molecule vibrations inside the large cage. Hence, an energy position of 5 meV in the IXS for the first maximum of the TA lattice modes would disagree with the DOS of the host lattice as determined from INS experiments. The TA lattice modes would also have to display a slight dispersion from the maximum at the zone boundary towards the maximum of the fold-back. Considering the optic character of the observed mode, it is very unlikely that the peak at 5 meV is linked to transverse acoustic lattice modes. The resemblance of the IXS spectra at higher Q -values with the INS spectrum of $\text{CH}_4\text{-D}_2\text{O}$ points to a different explanation of the observed spectral features: The excitation at 5 meV in the IXS spectra, in analogy to the interpretation of the INS spectrum, is attributed to the guest vibrations inside the large cage. These vibrations become visible in the spectrum after the intersection with the longitudinal acoustic (LA) lattice mode at $Q \simeq 2.5\text{ nm}^{-1}$, which is still within the first Brillouin zone. This behavior supports the assumption of a coupling between the localized guest vibrations and the

acoustic host lattice modes. The shoulder at 7–10 meV, which becomes visible at Q -values beyond the first Brillouin zone, cannot be assigned unambiguously. It appears in the same energy region as the maxima of the TA host lattice modes and in the same energy region as the additional guest vibrations. As a discrimination between transverse and longitudinal phonons is not possible, the shoulder is assumed to contain contributions from both lattice and guest vibrations.

It is of special interest that the guest mode is only observed after the crossing with the LA host lattice mode. This supports the idea of a resonant scattering, which promotes a transfer of scattered intensity from one phonon branch to the other. This behavior may be a sign of a scattering of the lattice phonons through the excitations of localized guest molecule vibrations. It is also intriguing that only a single distinct guest mode is visible in the IXS spectra. Although this corresponds to the findings from the INS experiments, it is only a speculation that it is due to the frequency of the guest vibrations being in the same region as the first maxima of the TA host lattice modes. To investigate these questions in detail, lattice dynamical calculations yielding eigenvectors and eigenfrequencies can be a powerful tools. They allow to determine both theoretical INS and IXS intensities and, hence, a more profound understanding of the experimental data.

6.2.3 Lattice Dynamical Calculations

The correctness of the interpretation of the results of both the inelastic neutron and x-ray scattering experiments should be validated on the basis of lattice dynamical (LD) calculations for methane hydrate. With the calculation of the INS and IXS intensities the following questions should also be addressed:

- Are only guest modes visible in the INS spectra of $\text{CH}_4\text{-D}_2\text{O}$?
- How strong is the coupling that is thought to be visible in the INS spectra of $\text{CD}_4\text{-D}_2\text{O}$ and why are the guest modes expected at ~ 7 meV and ~ 10 meV not observed?
- Why is the optic guest mode in the IXS spectra only observable after the crossing with the longitudinal acoustic host lattice mode?
- Why is only one distinct guest mode visible in the IXS spectra?

The starting point for the LD calculations was one proton-disordered unit cell of structure I clathrate hydrate containing 46 water and 8 methane molecules. The orientations of the rigid water molecules were chosen such that the ice-rules are satisfied and that the total dipole moment of this unit cell has a vanishing value. The cubic unit cell had a lattice parameter of $a=11.83$ Å. The interactions between the water molecules were described by the slightly modified TIP4P potential [125] (s. Chapter 3). The methane molecules were assumed to be situated at the center of the cages. The methane molecules are additionally approximated by spherical symmetric Lennard-Jones particles [38] and the simple OPLS

potential, whose parameters are based on the physical properties of methane gas, was used in the calculations. This is a valid assumption as orientational scattering length density of the methane molecules was found to be almost spherical [43]. The rotations of the methane that were already treated as a background in the INS spectra. They are not observed in the IXS spectra and are thus not calculated at all. The short-range interactions between the methane and water molecules were defined by the Lorentz–Berthelot mixing rules (s. eq. (3.32)).

In a first step the theoretical density of states (DOS) was calculated. The partial densities of states of the guest and host molecules of methane hydrate are obtained for a cubic grid of $\sim 10^5$ phonon wave vectors. As the DOS is obtained, sampling the eigenfrequencies and eigenvectors at a large number of \mathbf{q} -points, it is intrinsically orientationally averaged and can be used to calculate directly the measured INS intensities.

In Figure 6.14 the partial densities of states of the water and methane molecules are shown. In the calculated DOS of the guest molecules three peaks at about 3 meV, 5.5 meV, and 9 meV can be observed. They correspond to the characteristic guest molecule vibrations inside the large cage (3 meV and 5.5 meV) and the small cage (9 meV), respectively. The calculated energies of the guest modes are thus shifted towards lower frequencies with respect to the measured energy positions of 5.1 meV, 7.1 meV, and 9.6 meV, respectively. The difference between the calculated and the experimental energy positions of the guest modes points towards an underestimation of the repulsive methane–water potentials. This is not very surprising as the methane–water interactions parameters were gained from the combination of the potential parameters of two potentials, which were optimized with regard to the structures of ice (TIP4P) and with regard to the physical properties of gaseous methane (OPLS). However, the peak positions of the guest vibrations reproduce qualitatively the findings from the INS experiments: The peak at the lowest energy is found below the first maximum of the TA lattice modes, whereas the other two peaks coincide with the maxima of the lattice modes. The similarity of the calculated and experimental DOS should thus be close enough to draw conclusions on the coupling between the guest and host lattice modes.

The calculated DOS of the host lattice displays the maximum of the TA modes at 6 meV and of its "fold-back" at 10 meV. These values correspond well to the findings from the INS experiments on $\text{CD}_4\text{-H}_2\text{O}$ and from the difference spectrum of $\text{CH}_4\text{-D}_2\text{O}$ and $\text{CH}_4\text{-H}_2\text{O}$. The coupling between the guest and host lattice vibrations can also be observed. The partial DOS of the host lattice, instead of increasing with ω^2 , shows a very weak but distinct peak at 3 meV. This excitation corresponds to contributions of the guest modes to the cage vibrations. At about 5.5 meV a shoulder is observed in the host lattice DOS, which coincides with the second strong peak in the guest DOS. While the coupled modes are found to contribute only weakly to the total DOS, their contributions to the INS intensities will be amplified by ratio of the scattering powers when calculating the INS spectra of $\text{CD}_4\text{-H}_2\text{O}$.

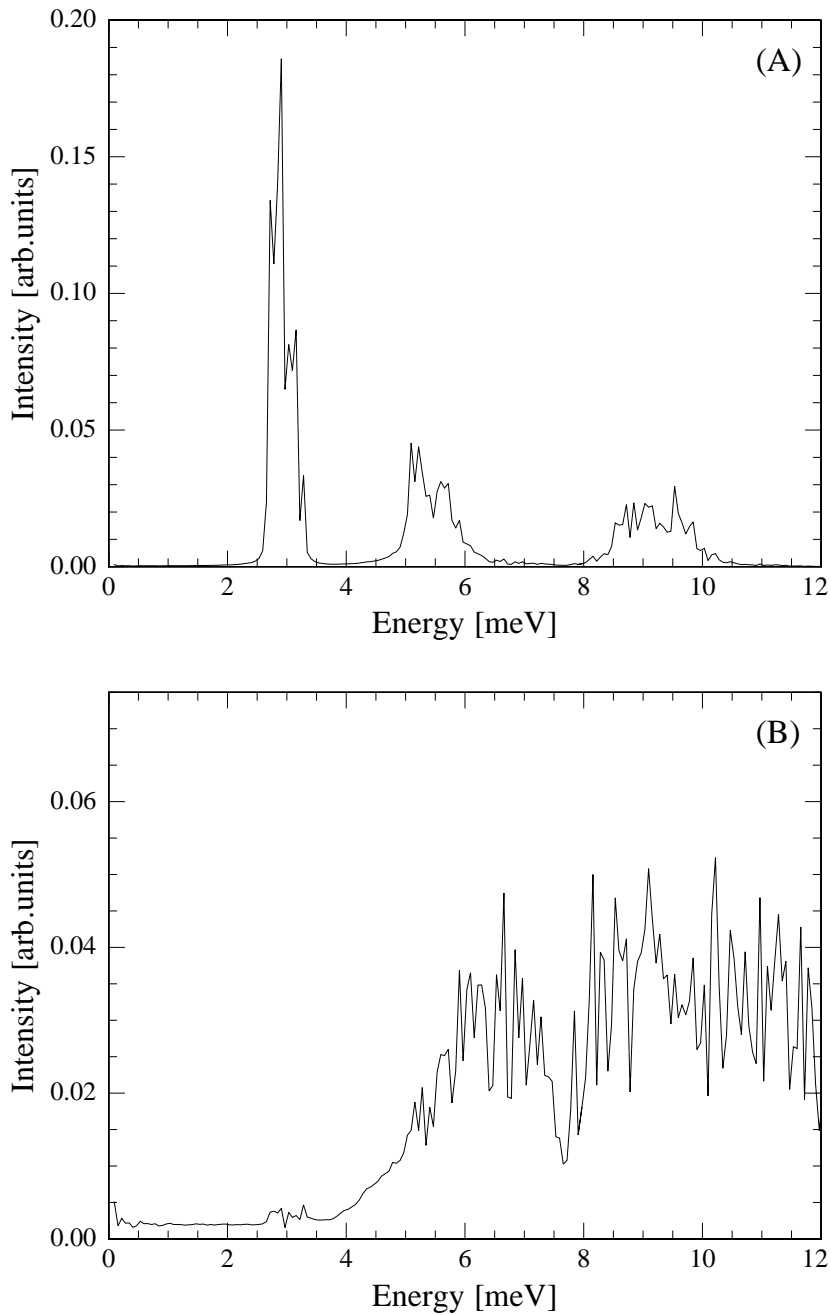


Figure 6.14: (A) The calculated partial DOS of the methane molecules is shown. The characteristic vibrations of the guest molecules are found at about 3 meV, 5.5 meV, and 9 meV. The peaks at 3 meV and 5.5 meV correspond to the methane vibrations inside the large cage, the peak at 9 meV to the guest vibrations inside the small cage. (B) The partial DOS of the host lattice is shown. The first maxima of the transverse acoustic lattice modes are found at about 6.5 and 10 meV. The peak at 6.5 meV corresponds to the TA modes near the zone boundary, the peak at 10 meV to the fold-back of the TA modes towards the zone center. Below 4 meV an additional small peak corresponding to the coupling between the cage and guest vibrations is observed.

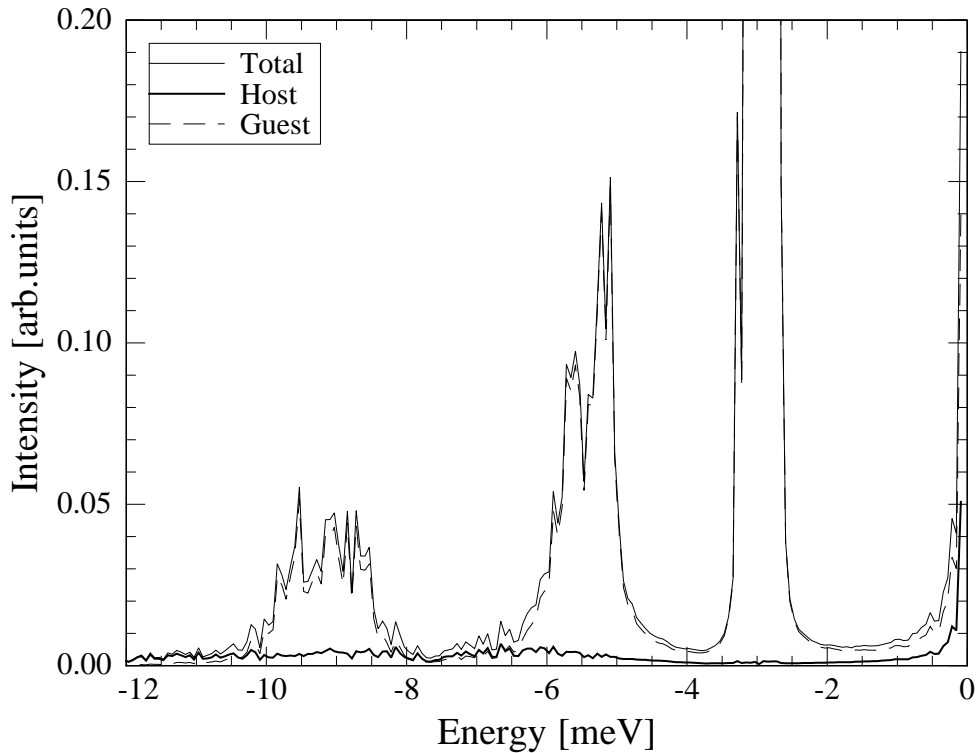


Figure 6.15: The calculated scattering function, corresponding to the INS spectra of $\text{CH}_4\text{-D}_2\text{O}$ hydrate is shown in a close-up view. The spectrum is dominated by the guest vibrations, which lead to the peaks at 3 meV, 5.5 meV, and 9 meV (the maximum of the peak at 3 meV is at 1.1).

From the calculated density of states the intensities of the INS spectra can be calculated from (s. Chapter 4)

$$S_{inc}(Q, \omega) = \sum_{\mu=1}^N \frac{Q^2}{2} \frac{\sigma_{\mu}}{M_{\mu}} e^{-W_{\mu}^{av}} \frac{g^{\mu}(\omega)}{\omega}, \quad (6.21)$$

where g^{μ} is the partial density of states of atom (μ), weighted by its scattering power σ_{μ}/M_{μ} . The spectrum of $\text{CH}_4\text{-D}_2\text{O}$ hydrate was obtained with the scattering powers of the CH_4 and D_2O molecules (s Table 6.4). A close-up view of the calculated spectrum is shown in Fig. 6.15. The three guest modes dominate the calculated spectrum. It can therefore be concluded that the experimental intensities in the case of $\text{CH}_4\text{-D}_2\text{O}$ hydrate are almost entirely due to the partial density of states and the rotational diffusion of the methane molecules. The convolution of the broad quasielastic scattering from the rotational diffusion with the inelastic excitations would contribute to peak widths. At 6–8 meV a weak coupling between the guest and host vibrations can be observed. In this range the guest vibrations are modulated by the host lattice modes.

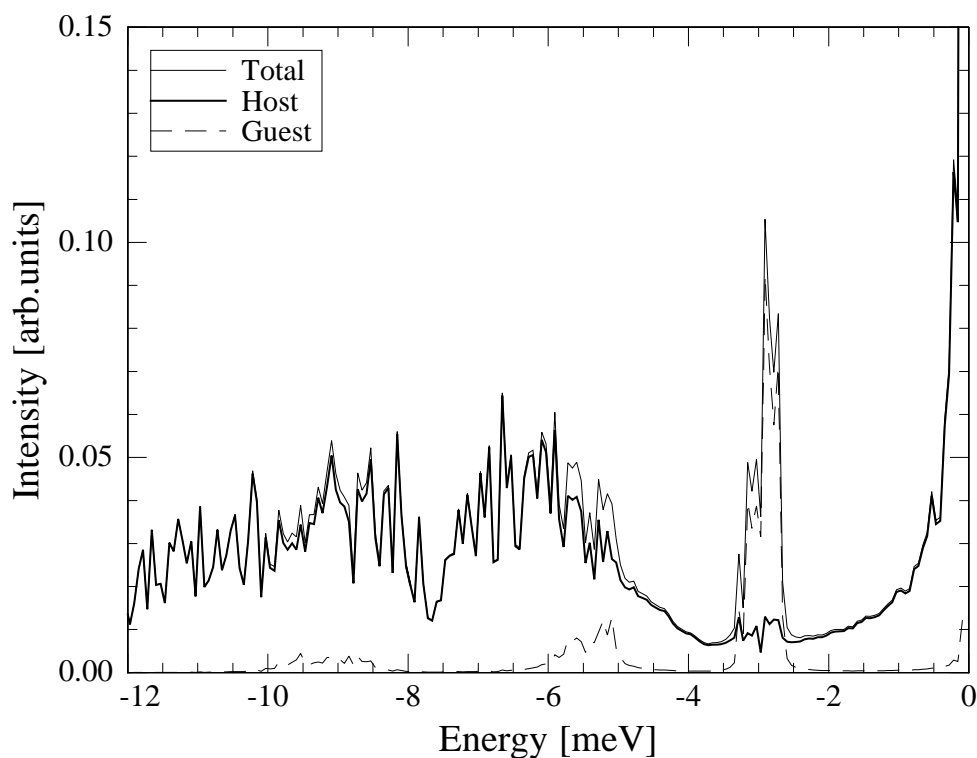


Figure 6.16: The calculated INS spectrum of $\text{CD}_4\text{-H}_2\text{O}$ is shown. The intensity of the peak at 3 meV is to 75% directly due to the guest vibrations, the guest–host coupling contributes roughly 20% to the intensity.

Figure 6.16 shows the calculated INS intensities as derived from the DOS using the scattering power for CD_4 and H_2O molecules. In this case, the scattering power of the protonated lattice is about five times that of the deuterated methane molecules. However, the contributions of the guest molecule vibrations to the spectrum are important below 4 meV. At energies above 4 meV the contributions of the guest modes decrease rapidly. An analysis of the contributions to the peak at 3 meV shows that $\sim 20\%$ of the integrated intensity of the peak comes from host lattice modes. The guest molecule vibrations contribute $\sim 75\%$ of the intensity. Unfortunately, due to the difference between the calculated and observed peak positions, a quantitative assignment of the observed peak composition is not possible from the calculations. However, the qualitative interpretation of the experimental spectra in terms of guest modes and coupled guest modes is confirmed by the theoretical results. Overall, it is found that indeed a guest–host coupling contributes to the low frequency spectrum of $\text{CD}_4\text{-H}_2\text{O}$. The guest modes, which coincide with the maxima of the TA lattice modes, are broader, pointing to less localized modes and thus leading to a weaker contribution in the theoretical INS spectrum. As a consequence, these modes cannot be separated from the host lattice peaks in the experimental INS spectra.

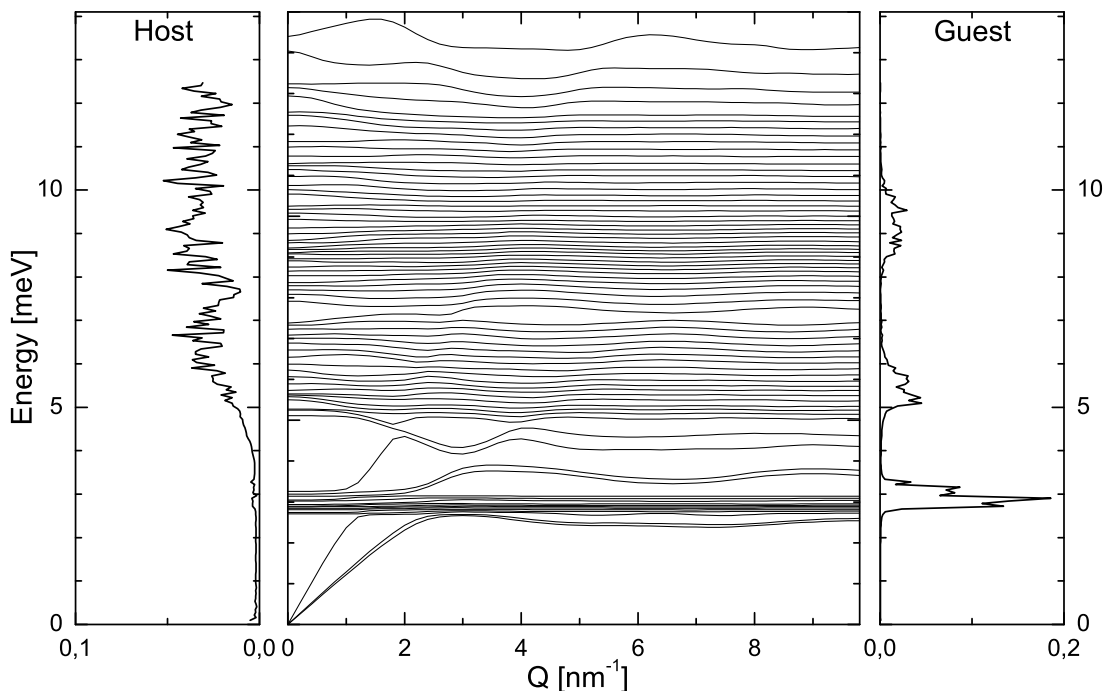


Figure 6.17: Calculated powder averaged phonon dispersion of methane hydrate as deduced from 239 randomly chosen Q -directions. The partial densities of states of the host lattice and the guest molecules are displayed on the left and right side of the dispersion curve, respectively.

Additional information on the coupling mechanism can be obtained by calculating the phonon dispersion curve of methane hydrate. In order to calculate phonon intensities, which can be compared with the experimental ones, the polycrystallinity of the sample has to be accounted for. Therefore, the phonon dispersion of a powder has to be calculated by averaging phonon dispersions for Q -values along many random wave vector directions. In order to match the experiments, Q -values from $Q=0 \text{ nm}^{-1}$ to $Q=10 \text{ nm}^{-1}$ were chosen along each direction. The relation $\mathbf{q} = \mathbf{Q}$ valid within the first Brillouin zone ($\mathbf{G} = 0$) becomes $\mathbf{q} = \mathbf{Q} - \mathbf{G}$ for Q -values beyond the first Brillouin zone. For each direction of the wave vector transfer \mathbf{Q} the phonon wave vector \mathbf{q} was thus chosen to be the vector to the nearest Γ -point and \mathbf{G} the appropriate reciprocal lattice vector. With this method the orientationally averaged phonon dispersion of methane hydrate was deduced from 239 randomly chosen Q -directions.

In Fig. 6.17 the powder averaged dispersion relation of methane hydrate and the partial density of states for both the guest and the host vibrations are shown. The dispersive modes near the zone center are the transverse (TA) and longitudinal (LA) acoustic lattice

modes. The calculated orientationally averaged longitudinal sound velocity is 3800 m/s, in good agreement with the experimental value. A strong bending of the LA and TA modes can be observed at the crossing points with the guest branches at $Q \simeq 1.1 \text{ nm}^{-1}$ and $Q \simeq 2.2 \text{ nm}^{-1}$, respectively. This bending is due to an avoided crossing between the localized methane vibrations and the acoustic phonons of the same symmetry. More avoided crossings between guest and host phonon branches can be observed in the energy region of 5–12 meV. In the phonon dispersion it can also be seen that the methane vibrations at 3 meV lead to a very narrow band of optic modes, whereas the vibrations at 5.5 meV and 9 meV are spread out over a wider energy region and are almost indistinguishable from the lattice modes.

As the acoustic lattice modes bend to become optic modes, the guest component of the eigenfunctions increases. At the zone boundary these modes are thus almost pure guest modes. The water molecule component that remains in the eigenfunction leads to the coupling, which is observed in the partial DOS of the host lattice. The coupling observed in the INS spectra is thus attributed to a strong mixing of the eigenvectors caused by the resonant interaction between the guest and host modes at the avoided crossing.

In order to compare the calculated dispersion with the experimental IXS spectra it is important to take the intensity of the calculated modes into account. The scattering function $S(\mathbf{Q}, \omega)$ was therefore calculated from the LD results to allow a direct comparison with the experimental results. The scattering function was also convoluted with the Lorentzian-shaped resolution function of the instrument. In a one-phonon approach the scattering function in an IXS experiment can be written as

$$S(\mathbf{Q}, \omega) = G(\mathbf{Q}, \mathbf{q}, j) \cdot F(\omega, T, \mathbf{q}, j), \quad (6.22)$$

where \mathbf{q} denotes the phonon wave vector in branch j , $G(\mathbf{Q}, \mathbf{q}, j)$ is the dynamical structure factor and $F(\omega, T, \mathbf{q}, j)$ is the response function [18]. $G(\mathbf{Q}, \mathbf{q}, j)$ was calculated and averaged for the eigenvectors from the LD simulations for each of the 239 different directions within the Q -range of 0–10 nm^{-1} . Thus, the intensities of both the longitudinal and the transverse modes are calculated. In the harmonic approximation the response function $F(\omega, T, \mathbf{q}, j)$ of an undamped harmonic oscillator was chosen and on this basis a scattering function $S(\mathbf{Q}, \omega)$ could be calculated.

The resulting theoretical scattering function for methane is shown in Fig. 6.18. The calculated IXS spectra for methane hydrate display two distinct excitations, a dispersive mode, which is the LA host lattice mode, and an optic mode at $\Omega \simeq 3 \text{ meV}$, which becomes observable at the crossing with the LA ($Q > 1.0 \text{ nm}^{-1}$) mode and corresponds to the methane vibrations inside the large cage. The characteristic features of the experimental spectra of methane hydrate are thus reproduced by the calculations, supporting the interpretation of the spectra in terms of guest modes and host lattice phonons. The guest mode becomes only visible after the crossing with the LA lattice mode, showing the importance of the avoided crossing observed in the dispersion relation. This behavior can also be attributed to the mixing of the eigenfunctions at the avoided crossing: The mixing

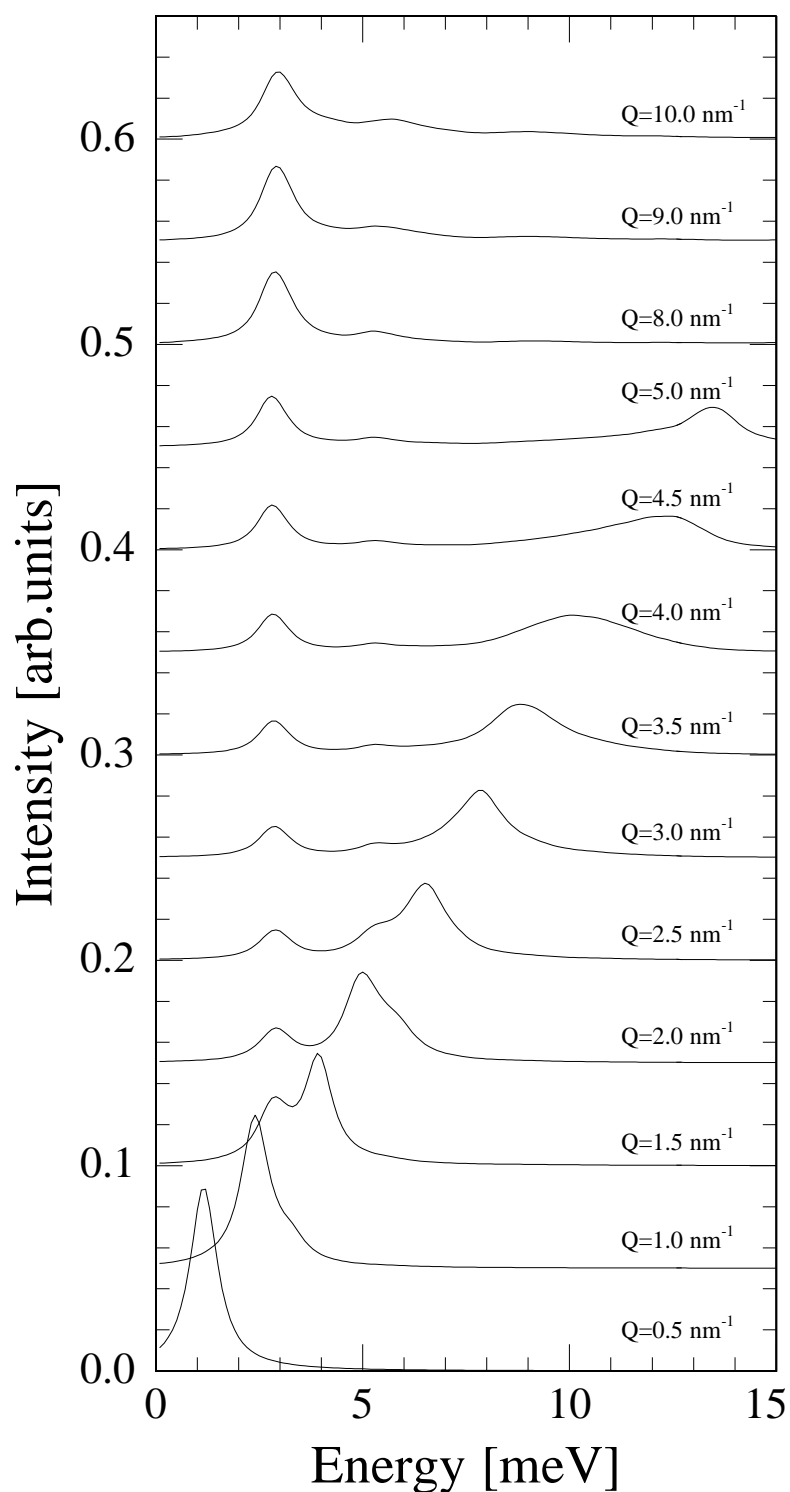


Figure 6.18: Theoretical orientationally averaged scattering function $S(Q, \omega)$ of methane hydrate. The spectra are shown for Q -values between 0.5 nm^{-1} and 10 nm^{-1} . The peak at 3 meV corresponds to the methane molecule vibrations and becomes visible after the avoided crossing due to a mixing of the guest and host modes.

of the eigenfunctions leads to a change in the polarization of the guest contributions. The resulting collective guest mode is then observed in the IXS spectra. At Q -values smaller than the wave vector transfer of the avoided crossing the guest molecules are independent oscillators and a collective guest mode could thus not be observed. The additional guest modes are not observed as their frequency is too high to lead to a noticeable mixing of the eigenvectors.

6.2.4 Discussion and Summary

The combination of INS and IXS experiments, together with LD calculations gave detailed insight into the lattice dynamics of methane hydrate.

With the help of the deuteration of the host lattice the energy of the localized guest modes could be determined. At $T=150$ K the methane molecules in the small dodecahedral cages were found to vibrate with the highest frequency of 10.0 meV, while the ellipsoidal shape of the large cage lead to two lower vibrational frequencies of 7.6 meV and 5.4 meV. Deviations from the relative intensities between the experimentally determined peaks and the expected theoretical ratio of 2:1:1 suggest the contribution of lattice phonons via a guest–host coupling.

When deuteration of the guest molecules the density of states of the host lattice could be determined. The first maximum and the fold–back of the transverse acoustic lattice modes were found at 7.3 meV and 11 meV, respectively. This was found to be in good agreement with the results from the LD calculations, where the peaks were predicted to be at 6.5 meV and 10 meV. An additional peak observed at ~ 4.8 meV included contribution from both guest molecule vibrations and host lattice modes. The host lattice displays oscillations at this energy through a coupling to the localized guest vibrations. From the LD calculation at least 20% of the peak intensity could be tentatively attributed to the coupled modes. This is, however, not an indication of a mode coupling as found in xenon hydrate, where the guest vibrations gave rise to distinct narrow peaks in the DOS of the host lattice [151, 46]. The narrow peaks point towards very localized rattling modes of the xenon atoms inside the hydrate cages. The modes of the methane molecules are less localized as could be seen from the broad inelastic excitation in the INS spectrum of $\text{CH}_4\text{-D}_2\text{O}$. The frequencies of the guest vibrations and the guest mass therefore play an important role for the coupling with the lattice vibrations. In the phenomenological model of the “box–clathrate” a similar dependence was found (s. Chapter 3). Two general “rules”:

- Only guest vibrations with a frequency below the maximum of the transverse acoustic host lattice modes are found to have a noticeable impact on the lattice dynamics of the hydrate.
- If the mass of the guest is smaller than that of the cage, then the density of states of the host lattice is only little disturbed by the guest vibration.

In the IXS spectra of methane hydrate a single optic mode, attributed to the guest vibrations along the long axes in the large cage, could be identified, the LA lattice mode was observed over a wide Q -range, and at higher Q -values contributions from the TA lattice modes appeared in the experimental spectra. The LD calculations reproduced these characteristic features of the spectra. Especially, the host lattice dynamics was found to be well reproduced by the TIP4P potential. Additionally from an inspection of the theoretical dynamical structure factor the coupling mechanism can be identified. At the zone center, before the crossing of the guest and host modes, the guest molecules behave like independent Einstein oscillators in the cages, leading to a negligible intensity of the guest modes compared to that of the collective acoustic lattice mode in the IXS spectra. It is at the avoided crossing with the LA host lattice branch that the independent localized vibrations of the guest molecules or atoms receive a strong longitudinal polarization through a mixing of the eigenvectors of the guest and host modes. At these Q -values the guest vibrations are no longer independent rattlers in the cages. Instead their vibrations are modulated by the host lattice, leading to a transfer of scattered intensity from the acoustic lattice mode to the guest vibrations and thus to the observed optic modes. The strength of this coupling is dependent on the localization of the guest modes. Therefore only the lowest guest mode leads to a distinct optic mode in the experimental and calculated spectra. The guest–host interaction is thus responsible for a decrease of the intensity of the dispersive lattice phonons in the region of the avoided crossings in the Brillouin zone.

In conclusion, the combination of inelastic scattering experiments and lattice dynamical calculations allowed to assign the excitations observed in the measured INS and IXS spectra. With the theoretical results the lattice dynamics of methane hydrate was characterized in detail. The existence of a guest–host coupling and of an avoided crossing between the acoustic lattice phonons and the localized guest modes could be deduced. The avoided crossing was found to lead to a decrease of the intensity of the acoustic lattice phonons, which are related to the thermal conductivity of a material. To gain insight into the influence of this avoided crossing on the thermal conductivity an experimental determination of the phonon lifetime in clathrate hydrates would, however, be necessary.

6.3 Elastic Properties of High Pressure Methane Hydrates

In the study of the dynamics of methane hydrate it was found that the repulsive interaction between the guest and host molecules is responsible for the anharmonic terms observed in the temperature behavior of the guest molecule vibrations. This hydrophobic interaction is therefore studied under high pressure, where the repulsive part of the guest–host interaction should be thoroughly probed.

Methane hydrate structure I (MH-sI) is a hydrogen bonded network of water molecules that forms host cages in which CH_4 guest molecules are contained. Recently, several new

hydrate phases were found in the pressure range between 1 kbar and 20 kbar [23, 24, 52, 88, 121]. In all of the studies two phases could be reproduced reliably. The phase transformations were found at $p \approx 9$ kbar and $p \approx 19$ kbar. At the first structural transition MH-sI transforms into the hexagonal structure MH-II and at the second transition MH-II transforms into the orthorhombic structure MH-III. MH-II was identified with a cage-like hydrate structure, which is thought to be similar to the structure type H, though it is not solved in detail. The structure of MH-III in contrast was found to be a “filled-ice”, where the ice lattice is related to the structure of ice I_h and the methane molecules are located between the ice sheets.

In high pressure Raman scattering experiments strong differences of the intramolecular modes in MH-II and MH-III could be linked to the differences of the crystallographic structures [123]. A similar effect might be observable in the elastic properties of these hydrate structures. To determine the elastic properties of these hydrates, high pressure inelastic x-ray scattering (IXS) experiments were performed. For the IXS measurements the samples were prepared from synthesized methane hydrate structure type I as initial sample material. The very fine powder was loaded into a membrane-type diamond anvil cell (DAC) as described in chapter 5. The rate of compression was kept low, with maximum values of about 1 kbar per minute. In this way a MH-II sample at a pressure of $p=17$ kbar and a MH-III sample at $p=21$ kbar were prepared. The loaded DAC was mounted onto the inelastic x-ray spectrometer ID28 at the ESRF in Grenoble, where the measurements were performed at room temperature ($T=298$ K). As the sample thickness was only about $50 \mu\text{m}$, the Si(9,9,9) reflection order was used for both the monochromator and the analyzer, leading to a energy resolution of ~ 3 meV (FWHM) at 17.794 keV and maximizing the flux at the sample position. Nevertheless, the counting times ranged between 770 s and 1440 s per data point, leading to 16–30 hours per energy scan.

The goal of the experiment was to determine the elastic properties of the ice lattice of the two hydrate structures. In order to gain some insight into the influence of the guest molecules on the elastic properties, the measured quantities will be compared to the ones of ice VI, which is the ice phase stable at the present experimental conditions. This approach is chosen in analogy to the approximation of the physical properties of MH-sI by the ones of ice I_h . It is also of interest if a guest–host coupling similar to the one found in the IXS spectra of MH-sI can be observed for the high pressure hydrates as well.

6.3.1 Methane Hydrate MH-II

The crystallographic structure of MH-II has yet to be solved in detail. However, from diffraction studies MH-II is estimated to have a 1:3.5 methane to water ratio ($\text{CH}_4 \cdot 3.5\text{H}_2\text{O}$) [88]. At the phase transition from MH-sI to MH-II 2.25 water molecules per unit cell per methane molecule are thus released. At $p=17$ kbar and $T=298$ K this leads to sample, which is composed of both MH-II and Ice VI. A diffraction pattern was recorded prior to the inelastic scans to confirm the composition of the sample. Figure 6.19

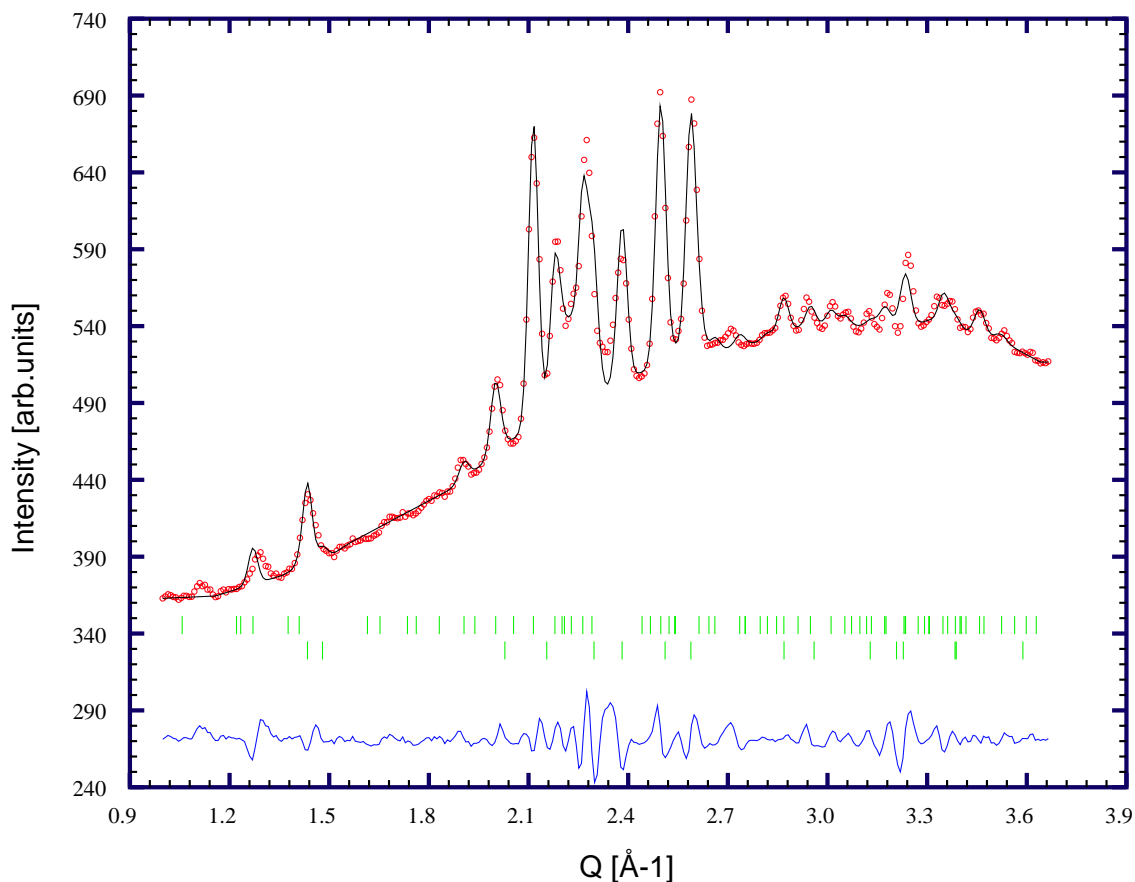


Figure 6.19: Diffraction pattern of MH-II and ice VI at $T=298$ K and $p=21$ kbar. The structure of MH-II has not been solved yet. As MH-II structure may be similar to hydrate structure type H, the pattern was tentatively indexed with the hydrate structure type H (upper tick set) and with ice VI (lower tick set). From the fit it can be seen that the structure of MH-II cannot be identified with structure type H in detail.

shows the x-ray diffraction pattern recorded with a CCD-detector. The diffractogram matches the experimental findings reported for samples prepared in a similar way [52, 89]. As hydrate structure type H was proposed as a possible crystal structure of MH-II [23, 52], the diffractogram was tentatively indexed with the tetragonal unit cell of ice VI with $a=6.1917$ Å, $c=5.8319$ Å and a hexagonal unit cell (space group P6/mmm) with $a=11.8849$ Å, $c=9.8905$ Å corresponding to structure type H. Although the diffraction pattern could be indexed by a hexagonal unit cell, it could not be identified with hydrate structure type H, e.g. deviations at $Q=1.2$ Å⁻¹ and $Q=2.7$ Å⁻¹. A solution of the structure, however, leaves the scope of this work. In the following the data analysis will therefore not rely on structural details. It will only be assumed that MH-II displays a cage-like structure with a 1:3.5 methane to water ratio, which is supported by all of the

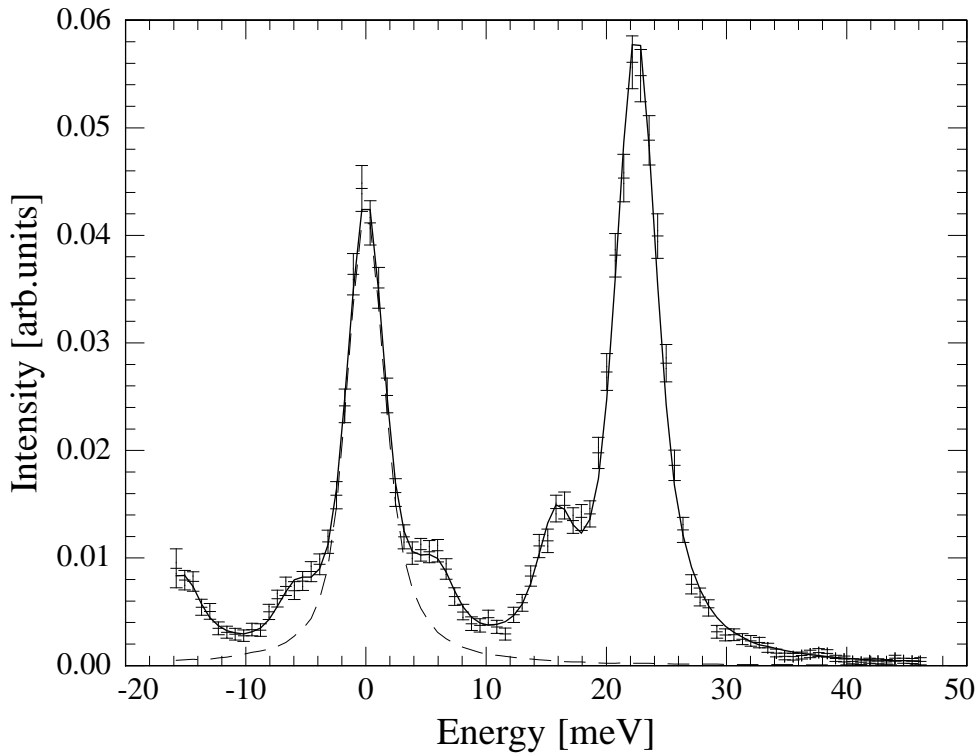


Figure 6.20: Inelastic x-ray spectrum of a sample containing ice VI and MH-II at $Q=2.0 \text{ nm}^{-1}$, $T=298 \text{ K}$ and $p=17 \text{ kbar}$. The measurement was performed at the beamline ID28 at 17.794 keV with a counting time of 1400 s per data point. The solid line (—) is a fit to the spectrum using Lorentzian functions convoluted with the experimental resolution (---). The excitations at 22.5 meV and 15.8 meV can be attributed to the acoustic phonons of the diamond anvils, whereas the peak at 5.9 meV corresponds to the longitudinal acoustic phonons of ice VI and MH-II.

structural and spectroscopic studies on MH-II [23, 52, 88, 89, 123].

From the relative intensities of the diffraction peaks it was concluded that the ice VI displayed preferred orientations, while the MH-II appeared to be a good powder. As the inelastic scans are performed at low wave vector transfers a ratio of the scattering power of MH-II and ice VI can also be estimated. In the limit $Q \rightarrow 0$, it is possible to approximate the measured intensity to be proportional to the atomic form factor $f(Q)$, which is close to the number of electrons at these Q -values. Therefore taking the stoichiometry of MH-II into account, a ratio of 2:1 between the scattered intensity of MH-II and ice VI can be expected. The phonons of MH-II and ice VI have thus to be separated in the measured IXS spectra. To solve this difficulty inelastic scans were recorded in the energy region of -15 to 45 meV over a wide range of momentum transfers of $2.0 \text{ nm}^{-1} < Q < 13.1 \text{ nm}^{-1}$.

Figure 6.20 shows an inelastic x-ray spectrum of the sample at a wave vector transfer of $Q=2 \text{ nm}^{-1}$. The experimental data are normalized to the integrated intensity and dis-

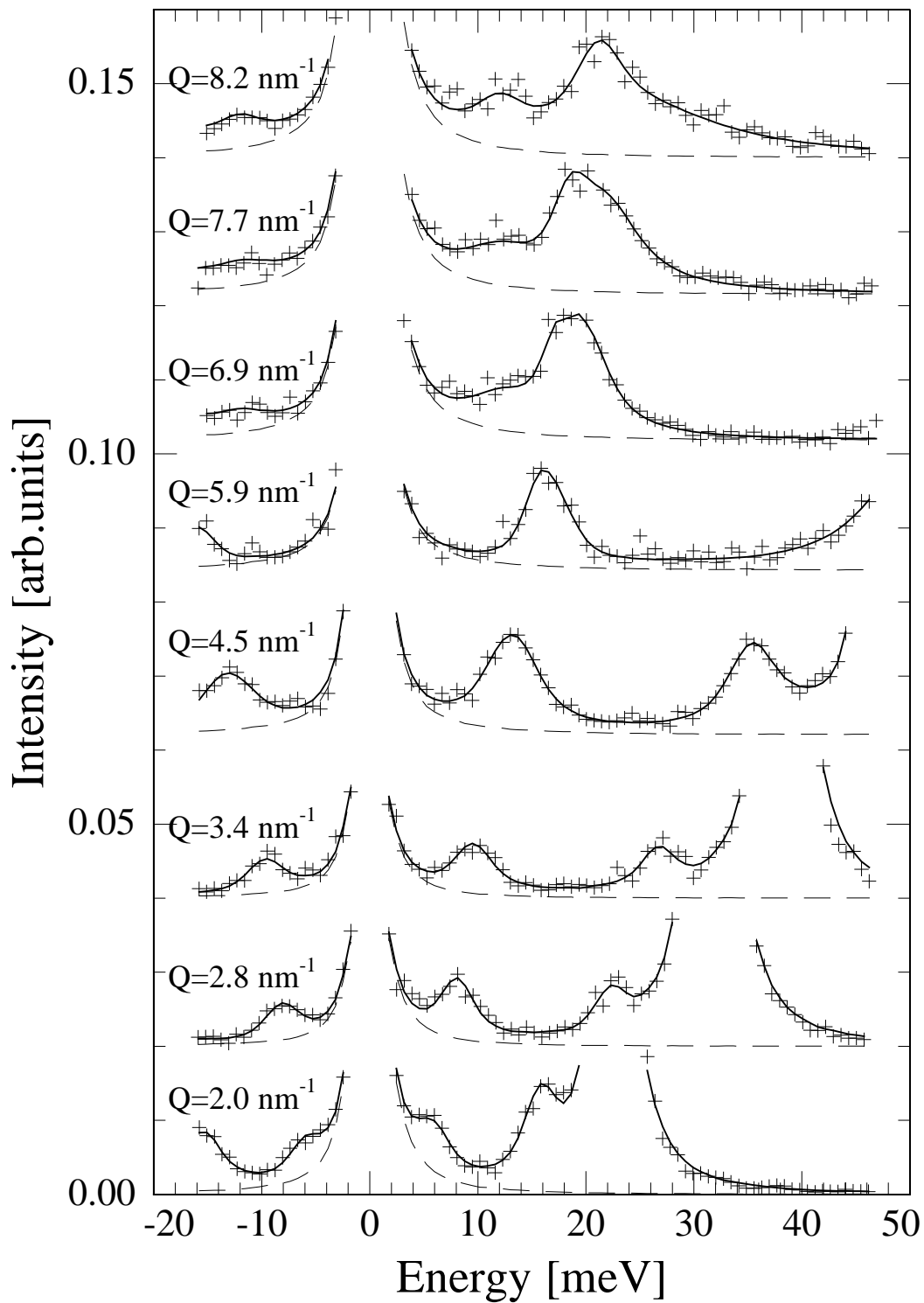


Figure 6.21: Inelastic x-ray spectra of the ice VI, MH-II sample are shown at several Q -values between 2.0 nm^{-1} and 8.2 nm^{-1} . The two highly dispersive excitations can be attributed to the acoustic phonons from the diamond anvils. The third dispersive excitation is assigned to the longitudinal acoustic phonons of MH-II and ice VI. The LA phonons of MH-II and ice VI are distinguishable for $Q > 5.9 \text{ nm}^{-1}$, as a growing asymmetry of the line shape of the peak is observed. The non-dispersive peak visible for $Q \geq 6.9 \text{ nm}^{-1}$ at $E \simeq 12 \text{ meV}$ is thought to correspond to transverse acoustic contributions.

played with their error bars. The elastic line at $E=0$ meV can be attributed to scattering from residual disorder in the powder and from the sample container. The count rate at the central line was ~ 0.3 counts/s. Additionally, the spectrum displays three inelastic excitations. In order to extract their energy positions $E(Q)$, the spectrum was fitted using a pair of Lorentzian functions for each excitation, convoluted with the experimentally determined instrument resolution. The intensity ratio between the Lorentzian functions for the energy-loss and for the energy-gain side is given by the Bose occupation factor. The instrument resolution is also shown in Fig. 6.20. The energy positions of the inelastic excitations were determined to be $E(Q)=5.9$ meV, $E(Q)=15.8$ meV, and $E(Q)=22.5$ meV at $Q=2$ nm $^{-1}$. These peaks are assigned to the inelastic signal from the sample and from the diamond anvils of the DAC. It is known that the longitudinal acoustic phonons of the diamond anvils yield very intense inelastic peaks. The velocity of sound of diamond is ≈ 13000 m/s [71] and thus much higher than the expectations for ice compounds in the present pressure and temperature range. The inelastic excitations of the anvils should therefore display a steeper dispersion than the ones of hydrate-ice sample.

In Figure 6.21 a selection of inelastic x-ray spectra at different wave vector transfers Q between 2.0 nm $^{-1}$ and 8.2 nm $^{-1}$ is shown. Three dispersive inelastic excitations can be observed at low momentum transfers. The two peaks at $E=15.8$ meV and $E=22.5$ meV at $Q=2$ nm $^{-1}$ display a very strong dispersion and cannot be observed any longer for wave vector transfers $Q>5$ nm $^{-1}$. From the Q -dependence of the energy positions of the two excitations sound velocities of ≈ 12000 m/s and ≈ 17000 m/s are determined. The excitations are therefore attributed to the acoustic modes of the diamond anvils. As a consequence, the third dispersive excitation at 5.9 meV at $Q=2.0$ nm $^{-1}$ can be identified with the orientationally averaged longitudinal acoustic (LA) phonon branches of ice VI and MH-II. For $Q\geq 6.9$ nm $^{-1}$ an additional non-dispersive excitation is observed. Its energy position is found to be $E=11.9\pm 0.2$ meV. It may be assigned to transverse modes near the zone boundary but it cannot be concluded for certain whether it is due to phonons of ice VI or MH-II.

In order to obtain informations about the lattice dynamical properties of MH-II, the ice and hydrate contributions to the peak assigned to the LA phonons have to be determined. It is therefore of special interest that the line shape of this excitation grows increasingly asymmetric with increasing wave vector transfer, indicating a contributions of two peaks. Fitting two Lorentzian functions convoluted with the experimental resolution to the excitation, the asymmetry is used to separate the LA phonons of ice VI and MH-II. The energy position of the peak corresponding to the LA phonon of ice VI was initially set to values derived from the orientationally averaged sound velocity as measured with Brillouin light scattering ($v\approx 4650$ m/s) [101] assuming a linear dispersion in the Q -range of the measurements. In this way, a stable fit could be obtained for wave vector transfers $Q\geq 4.5$ nm $^{-1}$. The peak widths and peak intensities, however, were found to be correlated. As a consequence only the peak positions will be considered in the discussion. In Fig. 6.22 the corresponding fit is shown for $Q=7.7$ nm $^{-1}$. The asymmetric peak is well described

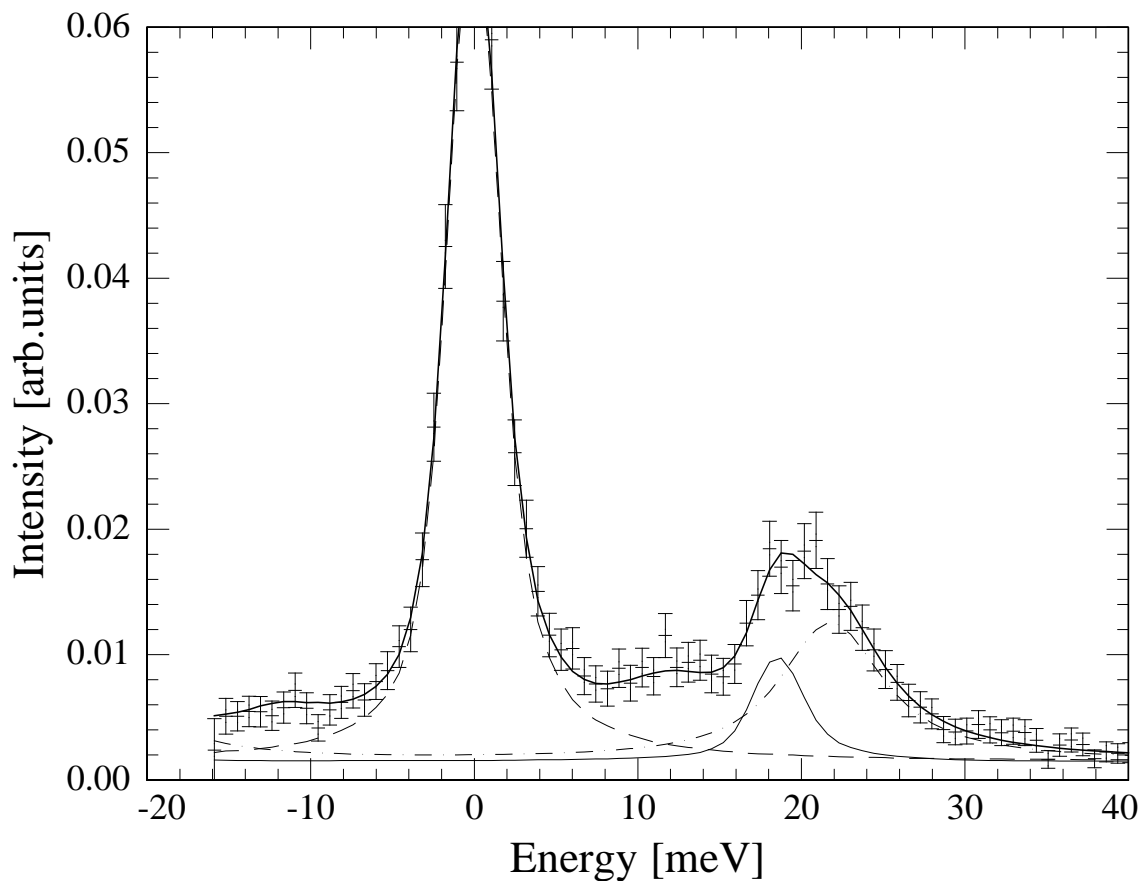


Figure 6.22: Inelastic x-ray spectrum of MH-II and ice VI at $Q=7.7 \text{ nm}^{-1}$. The asymmetric line shape of the excitation is attributed to the LA phonons of MH-II and ice VI. Fitting two Lorentzian functions, the peak was separated into the respective contributions of MH-II (—) and ice VI (- · - ·).

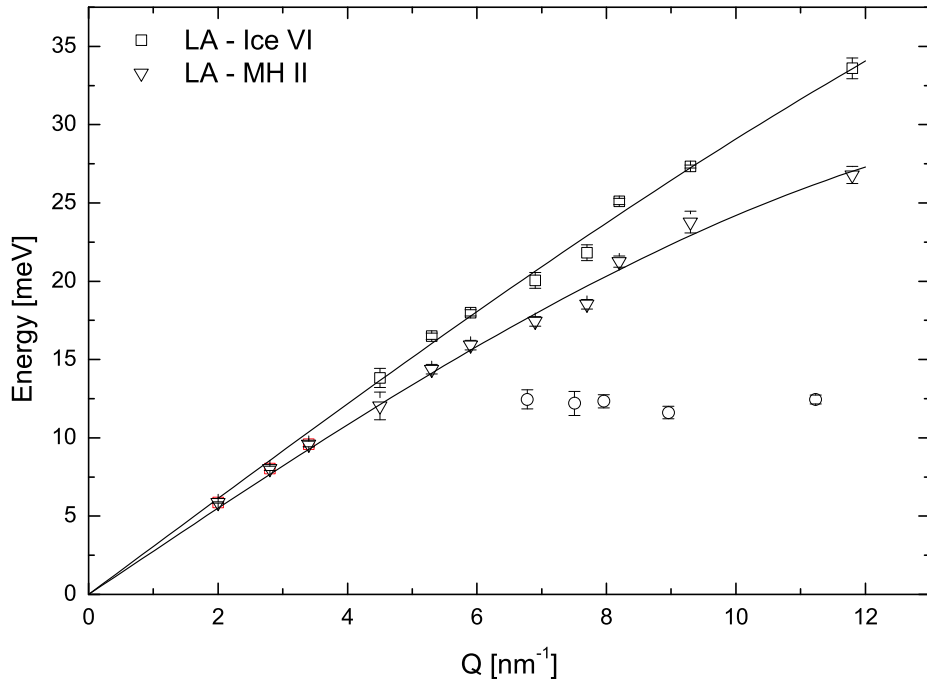


Figure 6.23: Dispersion curve of the MH-II sample at $p=17$ kbar and $T=298$ K. For $Q \geq 4.5 \text{ nm}^{-1}$ the longitudinal acoustic modes of MH-II and Ice-VI can be separated. From the dispersion relation orientationally averaged sound velocities of 4700 m/s and 4200 m/s could be deduced for ice-VI and MH-II, respectively. The non-dispersive mode at about 12 meV is attributed to transverse acoustic modes. It cannot be concluded if these TA modes belong to MH-II or ice VI.

by two Lorentzian functions, separating the excitation into the orientationally averaged LA modes of MH-II (solid line) and of ice VI (dashed-dotted line). The energy positions are found to be $E_{\text{MH-II}}(Q) = 18.5 \pm 0.3 \text{ meV}$ and $E_{\text{iceVI}}(Q) = 21.8 \pm 0.5 \text{ meV}$ at $Q = 7.7 \text{ nm}^{-1}$. The energy position of the peak attributed to the ice VI LA phonon is in agreement with values extrapolated from IXS experiments on ice VI at different pressures [72].

The resulting phonon dispersion curves of ice VI and MH-II are shown in Fig.6.23. From the dispersion relation the velocities of sound of MH-II and ice VI were estimated by fitting a sinus-law to the curves and determining the slopes in the $Q=0$ limit. The first three points at momentum transfers of 2.0 nm^{-1} , 2.8 nm^{-1} , and 3.4 nm^{-1} were excluded from the fit, as a separation of the ice VI and MH-II phonons was not possible at these low Q -values. An orientationally averaged compressional sound velocity of $v_{\text{iceVI}} = 4700 \pm 100 \text{ m/s}$ was determined for ice VI at $T=298 \text{ K}$ and $p=17 \text{ kbar}$. This value is in good agreement with values from Brillouin light scattering [101, 120]. For MH-II an orientationally averaged compressional sound velocity of $v_{\text{MH-II}} = 4200 \pm 100 \text{ m/s}$ was deduced from the phonon dispersion. The sound velocity of the hydrate is therefore about

10% smaller than that of the stable ice phase (ice VI).

The compressional velocity of sound of material is defined as [118]

$$v_p = \sqrt{\frac{C}{\rho}}, \quad (6.23)$$

where C is a combination of the elastic constants (eff. elastic modulus) and ρ the density of the material. Under the assumption that the compound is elastically isotropic the compressional and shear sound velocities can also be expressed by

$$v_p = \sqrt{\frac{1}{\rho} \left(B + \frac{4}{3}G \right)}, \quad (6.24)$$

$$v_s = \sqrt{\frac{G}{\rho}}, \quad (6.25)$$

where B is the *bulk modulus* and G the *shear modulus*. The bulk modulus can be estimated from diffraction data as a function of pressure. Thus, the shear modulus or the shear wave velocity can be determined from measurements of the compressional sound velocity if the bulk modulus and the density is known.

For MH-II the bulk modulus at $p=17$ kbar is $B=14.4$ GPa [52] and the density is $\rho=1.07$ g/cm³ [88]. The effective elastic modulus C for the longitudinal waves in MH-II can thus be determined from eq. (6.23) and is found to be $C \simeq 18.9$ GPa. Measured elastic constants of the polycrystalline samples are intrinsically orientationally averaged and can therefore be assumed to be isotropic, if the powder does not show preferred orientations and if enough crystallites are included in the scattering volume. In Brillouin light scattering experiments, single crystals of MH-sI were found to have a nearly isotropic elasticity, a feature that was related to the void-rich cage structure of the hydrate [122]. As the MH-II sample showed a good polycrystallinity and as it is assumed to have a cage-like structure, it may also be approximated by an elastic isotropic medium. Under this assumption, the shear modulus G can be determined with eq. (6.24) to be $G \simeq 3.4$ GPa. This leads to a shear wave velocity of $v_s \simeq 1800$ m/s.

6.3.2 Methane Hydrate MH-III

The MH-III sample was prepared from a synthesized MH-sI powder in a diamond anvil sample cell with the same procedure used for MH-II. The structure of MH-III was recently discovered and solved by *Loveday et. al.* [88, 87]. The structure was identified with the space group $Imcm$ and the stoichiometry of MH-III was found to be $CH_4 \cdot 2H_2O$. This leads to 3.75 free water molecules per unit cell per methane molecule when transforming MH-sI into MH-III. At $p=21$ kbar and $T=298$ K the sample is thus composed of both MH-III and ice VI. A diffraction pattern recorded with a CCD-detector prior to the inelastic scans confirmed this sample composition (Fig. 6.24). The MH-III was indexed

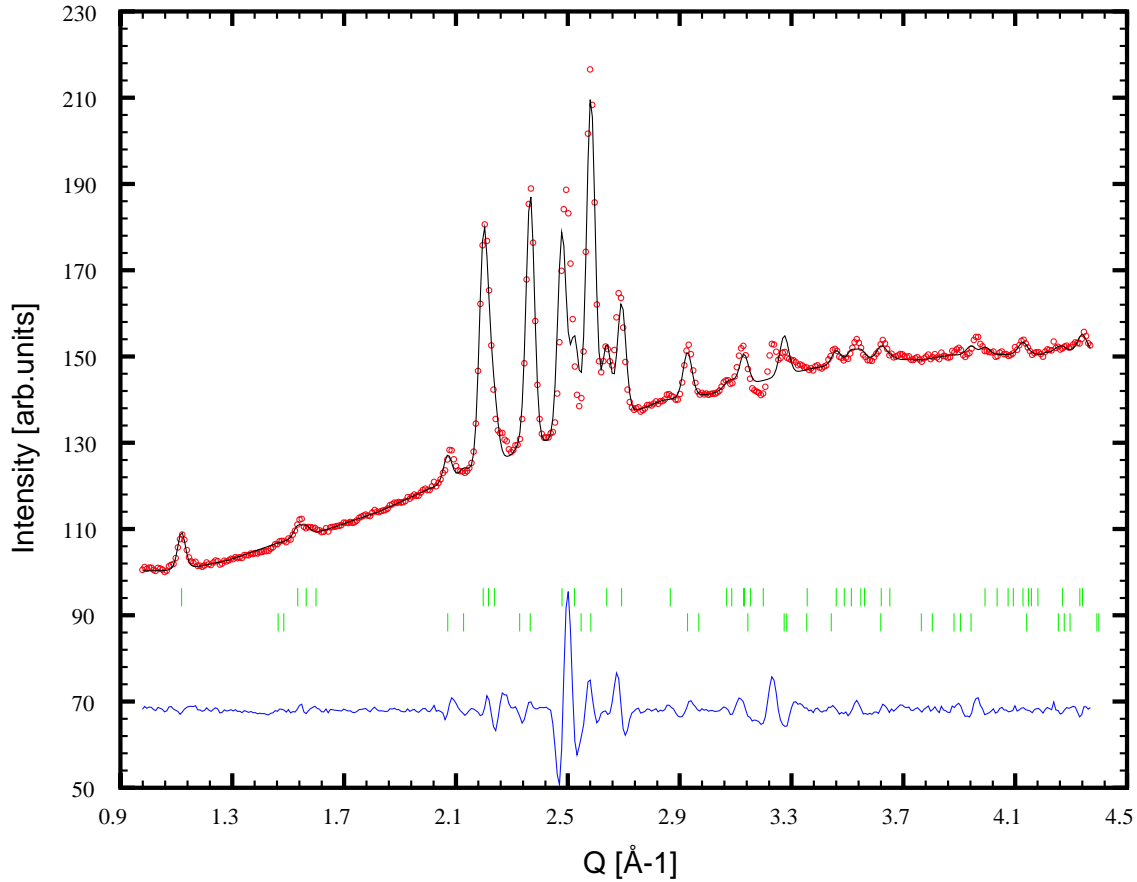


Figure 6.24: Diffraction pattern of the hydrate sample at $T=298$ K and $p=21$ kbar. The diffractogram is indexed with the space group $Im\bar{c}m$ of MH-III (upper tick set) and with ice VI (lower tick set). At $Q \simeq 2.5 \text{ \AA}^{-1}$ several Bragg peaks could not be separated, leading to the larger differences between the calculated and measured intensities.

with the space group $Im\bar{c}m$ with $a=4.7612 \text{ \AA}$, $b=8.0322 \text{ \AA}$, $c=7.8562 \text{ \AA}$, while the ice VI was identified with its corresponding $P4_2/nmc$ space group with $a=6.2411 \text{ \AA}$, $c=5.8066 \text{ \AA}$. These findings are in good agreement with the published values [87].

From the diffraction pattern it was concluded that the MH-III sample displayed a good powder quality, whereas the ice VI again showed some preferred orientations. In the limit of small wave transfers the ratio of scattered intensity of MH-III and ice VI is approximately 1:1.25. As before, it is therefore necessary to separate ice and hydrate phonons in the IXS spectra. The inelastic scans were thus recorded in the energy region of -15 to 45 meV and for wave vector transfers $2.8 \text{ nm}^{-1} < Q < 10.1 \text{ nm}^{-1}$. The counting rates were comparable to those of the MH-II sample with ~ 0.28 counts/s in the central line. The inelastic excitations were fitted with Lorentzian functions analogous to the treatment of the MH-II spectra.

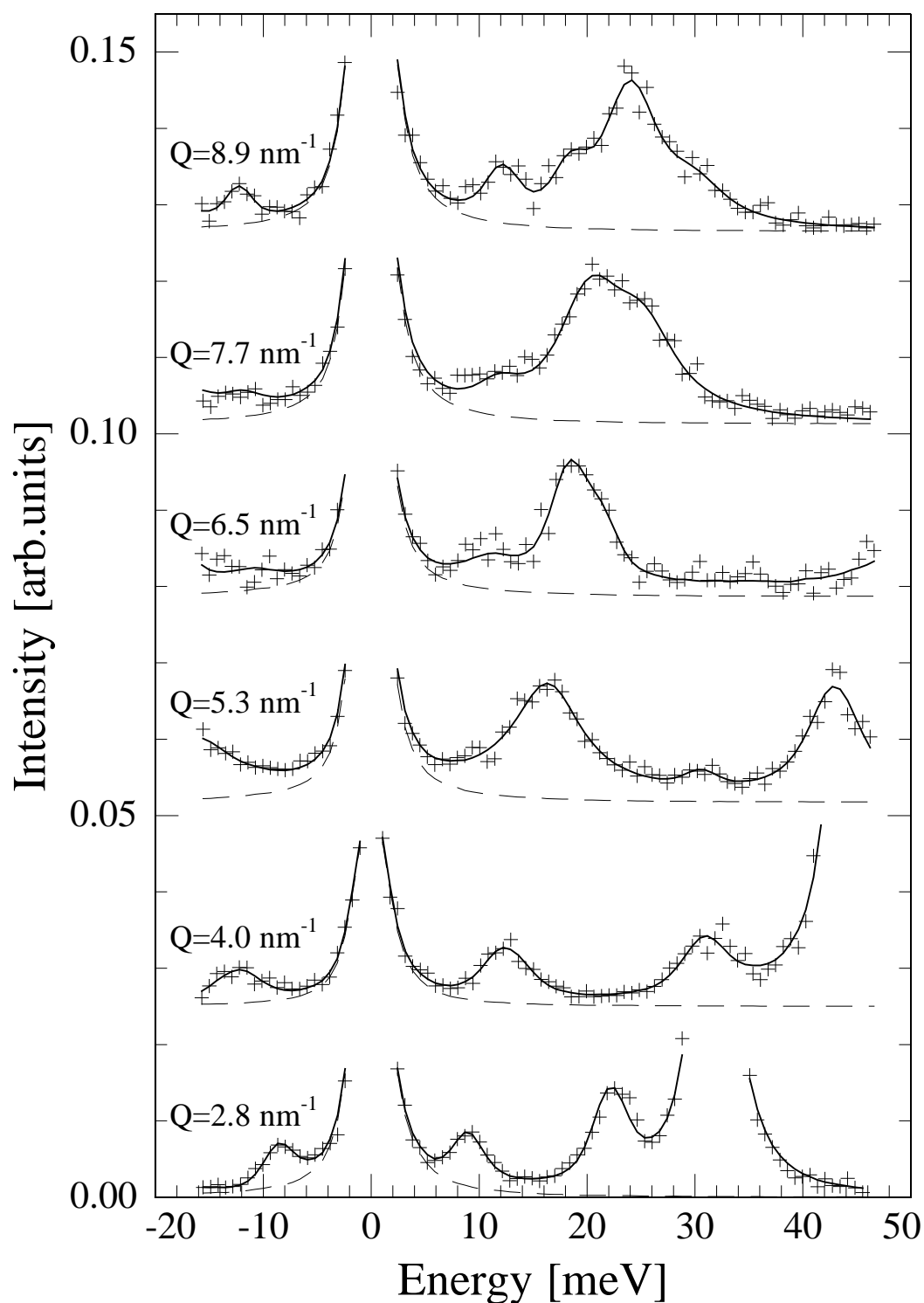


Figure 6.25: Inelastic x-ray spectra of the ice VI, MH-III sample, displayed for several Q -values between 2.8 nm^{-1} and 8.9 nm^{-1} . The LA phonons of ice and hydrate can be distinguished for $Q > 6.5 \text{ nm}^{-1}$, as growing asymmetry of the line shape of the peak observed.

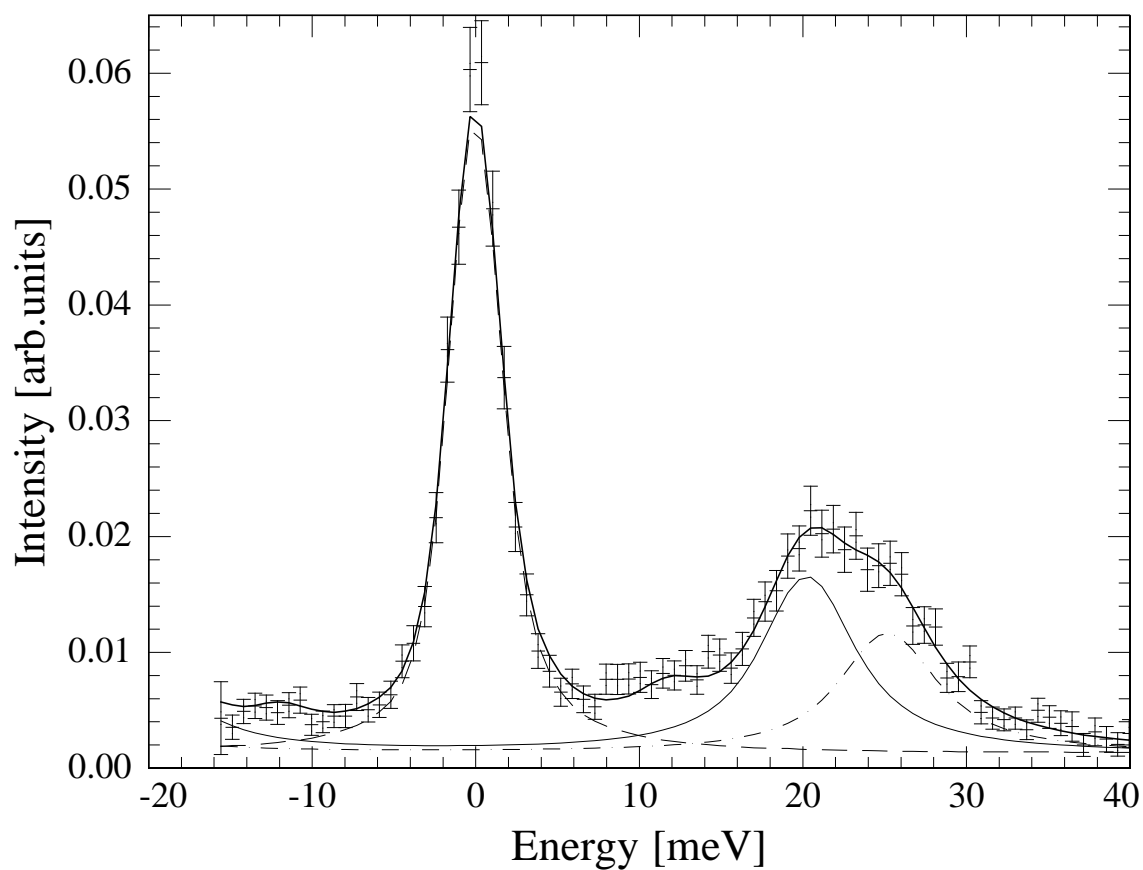


Figure 6.26: Inelastic x-ray spectrum of MH-III at $Q=7.7 \text{ nm}^{-1}$. The asymmetric line shape of the excitation suggest the contribution of two peaks. It was therefore fitted with two Lorentzian functions, separating the LA phonons of MH-III (—) and ice VI (-·-·).

In Fig. 6.25 a selection of IXS spectra of the MH-III sample is shown in the range of momentum transfers $2.8 \text{ nm}^{-1} < Q < 8.9 \text{ nm}^{-1}$. At $Q=2.8 \text{ nm}^{-1}$ three inelastic excitations can be observed. The energy positions of the inelastic peaks were determined as $E(Q)=8.9 \text{ meV}$, $E(Q)=22.2 \text{ meV}$, and $E(Q)=31.8 \text{ meV}$. The peak at 8.9 meV is assigned to the LA phonon branches of MH-III and ice VI, whereas the two intense excitations at higher energies are assumed to correspond to the acoustic phonons of the diamond anvils of the sample cell. This assignment of the observed modes is confirmed by the Q -dependence of energy positions of the excitations. The peaks attributed to the acoustic phonons of the diamond anvils show a steep dispersion, leading to sound velocities of $\approx 12000 \text{ m/s}$ and $\approx 17000 \text{ m/s}$, corresponding to the values found for the MH-II sample. The acoustic phonons of the diamond anvils are not observed any longer for $Q > 5.3 \text{ nm}^{-1}$. The third excitation ($E(Q)=8.9 \text{ meV}$ at $Q=2.8 \text{ nm}^{-1}$) thus corresponds to the orientationally averaged LA lattice vibrations of ice VI and MH-III. At $Q \geq 6.5 \text{ nm}^{-1}$ an additional excitation can be observed at $E \approx 12 \text{ meV}$. In the observed Q -range this mode displays only a very weak dispersion and it is thus assumed to have a constant energy ($E=11.7 \pm 0.2 \text{ meV}$) within the experimental error in the observed range of momentum transfers. Additionally, at the highest displayed wave vector ($Q=8.9 \text{ nm}^{-1}$) a shoulder at $E \approx 18 \text{ meV}$ can be observed. The origin of the two additional excitations cannot be assigned unambiguously. It can be speculated if they belong to ice VI or MH-III, but taking the relatively high momentum transfer into account, it is reasonable to assume that both are related to transverse phonons in either ice VI or MH-III.

As in the case of the MH-II spectra, the excitation corresponding to the ice VI and MH-III LA phonons shows an increasing asymmetric line shape with increasing momentum transfer. The asymmetry points to a contribution of two peaks to the observed excitation, which is therefore fitted with two Lorentzian functions in order to separate the LA phonons of ice and hydrate. The energy positions of line corresponding to the LA phonon of ice VI were deduced from the orientationally averaged sound velocity as measured by Brillouin light scattering ($v \approx 4900 \text{ m/s}$) [101]. A stable fit could thus be obtained for wave vector transfers $Q \geq 4.0 \text{ nm}^{-1}$. In Fig. 6.26 a fit of the two Lorentzian functions for the LA phonons of ice VI and of MH-III is shown for $Q=7.7 \text{ nm}^{-1}$. The energy positions are found to be $E_{\text{MH-III}}=20.3 \pm 0.7 \text{ meV}$ and $E_{\text{iceVI}}=25 \pm 0.9 \text{ meV}$ for MH-III and ice VI, respectively. With the separation it is possible to obtain the dispersion relation for MH-III and ice VI at $p=21 \text{ kbar}$ and $T=298 \text{ K}$ that is shown in Fig. 6.27. The results from the fits of the IXS spectra are displayed with their error bars. In the limit $Q \rightarrow 0$ the velocities of sound can be determined from the dispersion curve. The first point at $Q=2.8 \text{ nm}^{-1}$ was excluded, as the separation of ice and hydrate LA phonons was not possible at this small Q -value. The orientationally averaged compressional sound velocities at $p=17 \text{ kbar}$ and $T=298 \text{ K}$ are $v_{\text{iceVI}}=4950 \pm 100 \text{ m/s}$ and $v_{\text{MH-III}}=4600 \pm 100 \text{ m/s}$ for ice VI and methane hydrate MH-III, respectively. The deduced sound velocity of ice VI is in good agreement with values from Brillouin light scattering experiments [101, 120]. The sound speed of MH-III is thus found to be about 7% smaller than that of ice VI.

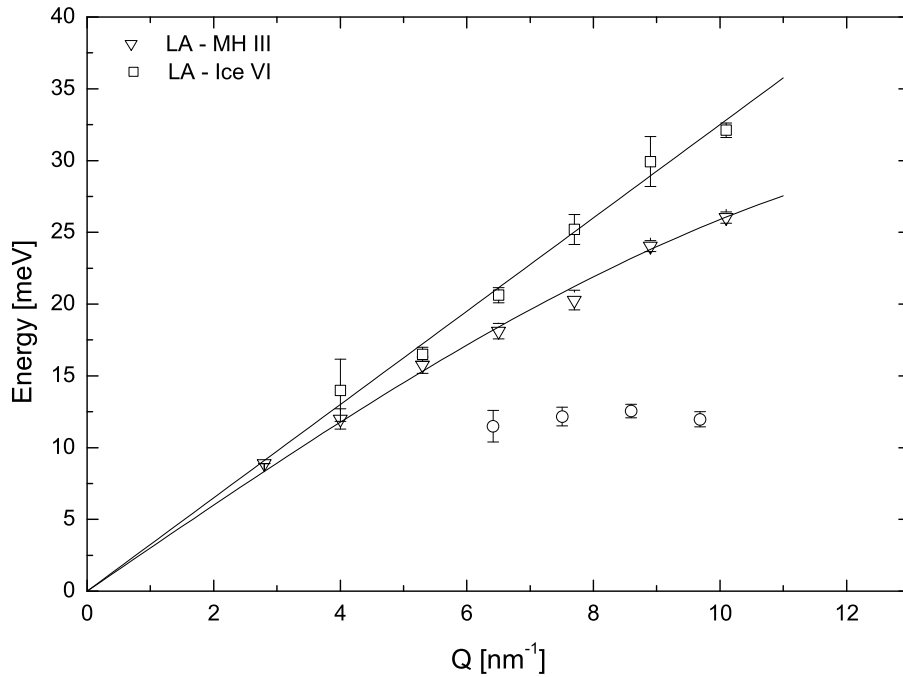


Figure 6.27: Dispersion curve of the MH-III sample at $p=21$ kbar and $T=298$ K. For $Q \geq 4.0 \text{ nm}^{-1}$ the longitudinal acoustic modes of MH-III and Ice-VI can be separated. From the dispersion relation orientationally averaged sound velocities of 4950 m/s and 4600 m/s could be deduced for ice VI and MH-III, respectively. The non-dispersive mode at about 12 meV is attributed to phonon modes with transverse symmetry in MH-III or ice VI.

The bulk modulus as well as the density of MH-III at $p=21$ kbar and $T=298$ K are known from x-ray diffraction to be $B=23.6 \text{ GPa}$ and $\rho=1.16 \text{ g/cm}^3$, respectively [88]. The effective elastic modulus C can thus be calculated from eq.(6.23), which yields $C \simeq 24.5 \text{ GPa}$. As the MH-III sample showed a good powder quality and in order to compare the deduced elastic properties of MH-II with MH-III, the MH-III sample is assumed to be an elastically isotropic medium as well. The shear modulus can then be approximated with $G = \frac{3}{4}(C - B) \simeq 0.75 \text{ GPa}$, which leads to a shear velocity $v_s \simeq 800 \text{ m/s}$.

6.3.3 Discussion and Conclusions

From the analysis of the high-pressure IXS spectra, the compressional velocities of sound of MH-II and MH-III could be determined, separating the contributions of the LA phonons of the corresponding hydrate and of ice VI.

The low frequency guest vibrations found in the IXS spectra of MH-sI and xenon hydrate [8] are absent in the case of the high pressure hydrate structures MH-II and MH-III. The frequencies of the methane molecule vibrations are probably higher than the maximum frequency of the acoustic host lattice modes. The guest modes are thus

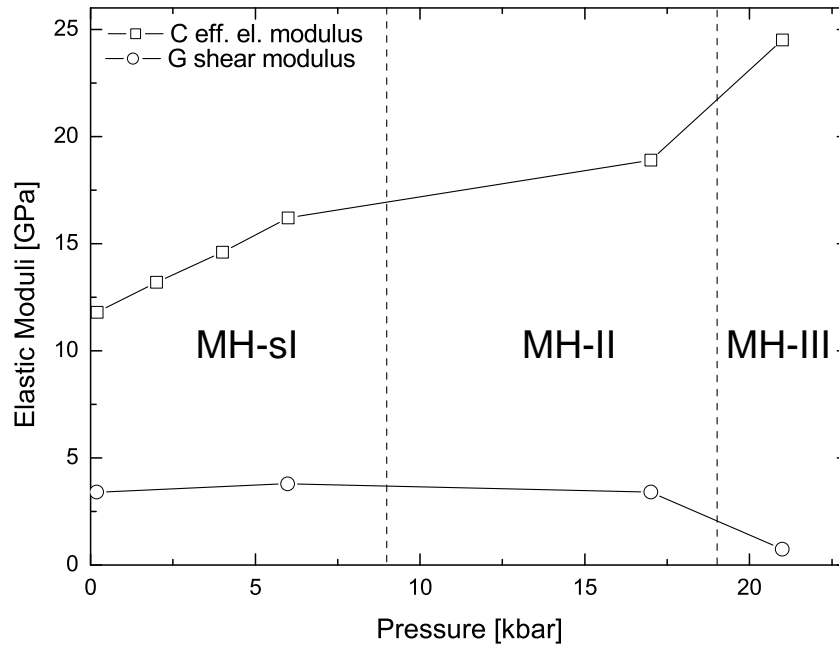


Figure 6.28: The effective elastic modulus C and the shear modulus G , determined from the IXS experiments on MH-II and MH-III, are shown together with the pressure dependence of the elastic constants of MH-sI [122]. The lines are guides to the eye only.

a part of the collective excitations of the crystal. This may originate from the repulsive guest–host interaction, which increases strongly with increasing pressure leading to high vibrational frequencies.

The elastic moduli C and G and the wave velocities v_p and v_s for MH-sI, MH-II, and MH-III are shown in Fig. 6.28. As MH-sI is known to display nearly isotropic elasticity, it can be assumed that $C=C_{11}$ and $G=C_{44}$ and based on this the moduli can be taken from *Shimizu et. al.* [122]. MH-sI and MH-II are found to have similar elastic properties. The effective elastic modulus C at 17 kbar is only slightly larger than the value of MH-sI at 6 kbar and lower than the value extrapolated from the linear pressure dependence of C in MH-sI. The shear modulus G , which is already nearly constant in MH-sI, does not show any change within the accuracy of the measurement. These results point towards the similar structural characteristics of MH-sI and MH-II. The void-rich arrangement of the hydrogen-bonded water molecules seems to lead to similar wave velocities. For MH-III the elastic properties change considerably. The effective elastic modulus is substantially higher than for MH-II, whereas the shear modulus decreases significantly. The transition from a cage clathrate to a filled ice can probably be observed in the elastic moduli: the effective elastic modulus shows a strong increase, that may be connected to the denser and more compact structure of MH-III. Furthermore, the layered structure of ice sheets and

Pressure	17 kbar		21 kbar		0.2 kbar	
Temperature	298 K		298 K		239 K	298 K
Property	Ice VI	MH-II	Ice VI	MH-III	Ice I _h	MH-sI
ρ [g/cm ³]	1.39 [101]	1.07 [88]	1.41 [101]	1.16 [88]	0.92	0.90
B [GPa]	22.0 [120]	14.4 [52]	24.0 [120]	23.5 [88]	9.3	8.0
v_p [km/s]	4.7	4.2	4.95	4.6	3.92	3.7
C [GPa]	30.7	18.9	34.5	24.5	14.1	12.3
G [GPa]	6.5	3.4	7.9	0.75	3.6	3.3
v_s [km/s]	2.2	1.8	2.4	0.8	2.0	1.9

Table 6.7: The compressional wave velocity v_p , the effective elastic modulus C, the shear modulus G, and the shear wave velocity v_s of ice VI, MH-II, and MH-III as deduced from the IXS measurements taking literature values for densities ρ and bulk moduli B. Additionally, elastic properties of ice I_h [39] and MH-sI [122, 115] are given for comparison.

hydrophobic guest molecules of MH-III may provide an instability against shear stress, which would result in the observed decrease of the shear modulus.

For the hydrate structure type I and II it was found that their elastic properties could be approximated by the ones of ice I_h. The influence of the guest molecules could be considered small in a first approximation. The elastic properties of MH-II and MH-III determined from the IXS experiments are hence compared to the values known for ice VI, which is the corresponding stable ice phase (s. Table 6.7). In the case of MH-II the effective elastic modulus and the shear modulus are both 40-50% smaller than the corresponding properties of ice VI. For MH-III the effective elastic modulus is about 30% smaller than the one of ice VI, whereas the shear modulus is found to be ten times smaller. These differences between the elastic properties of MH-II and MH-III and of ice VI can be explained by a growing importance of presence of the guest molecules on these properties. Whereas in the case of MH-sI and ice I_h the inclusion of a guest species does not lead to a significant change in density of the structure, this is not true for the high pressure hydrates MH-II and MH-III. In the case of MH-II the presence of the repulsive guest-host interaction seems to anticipate a dense structure, like the one of ice VI. The differences in the elastic constants of MH-II and ice VI may be mostly attributed to this effect. The density of the structure of MH-III is closer to the one of ice VI, however, the guest molecules may have induced an instability to shear stress in the structure.

Overall, the contribution of the guest molecules to the elastic properties of the hydrate can no longer be neglected for the high pressure structures of methane hydrate. Molecular dynamics and lattice dynamical calculations could provide further insight into the influence of the guest molecules on the elastic properties of MH-II and MH-III. The experimental results can therefore be potentially used as test cases for the repulsive part of the empirical water pair potentials in the calculations.

Chapter 7

Xenon Hydrate – Results and Discussion

The xenon atom is very similar to the methane molecule concerning the van der Waals radius and the interaction with water molecules. It also forms hydrate structure type I, as methane hydrate. The mass of the xenon atom is far more important than that of the methane molecule, allowing the influence of the guest mass to be studied in detail. A comparison between the dynamics of methane and xenon hydrate can therefore provide insight into the influence of the guest atom or molecule on the lattice dynamics of the host structure.

The dynamics of xenon hydrate has already been investigated in several experimental and theoretical studies. In the theoretical studies the lattice dynamics was studied with molecular dynamics (MD) simulations and lattice dynamical (LD) calculations [144, 149, 61]. In several inelastic neutron scattering studies xenon hydrate was considered to be a model system for the investigation of the low frequency dynamics of clathrate hydrate, due to the large difference between the scattering cross sections of xenon atoms and of water molecules [151, 46, 22].

Further investigations of the lattice dynamics of xenon hydrate are presented in this chapter. Combining inelastic neutron scattering (INS) and inelastic x-ray scattering (IXS) experiments, the density of states and the collective lattice dynamics of xenon hydrate could be determined and investigated in detail at a temperature of $T=100$ K and a pressure of a few *mbar* as found in cryogenic sample environments. The results are supported by lattice dynamical calculations.

7.1 Neutron Spectroscopy

For the INS experiment the xenon hydrate powder sample was filled into a flat aluminum sample cell of ~ 0.5 mm thickness. The measurements were performed on the time-focusing time-of-flight spectrometer FOCUS at the Paul-Scherrer-Institute in Switzerland. A neutron wavelength of $\lambda = 5$ Å from the 002 reflection of a PG-monochromator was used. With the time-focusing option an energy resolution of 0.1–0.4 meV (FWHM)

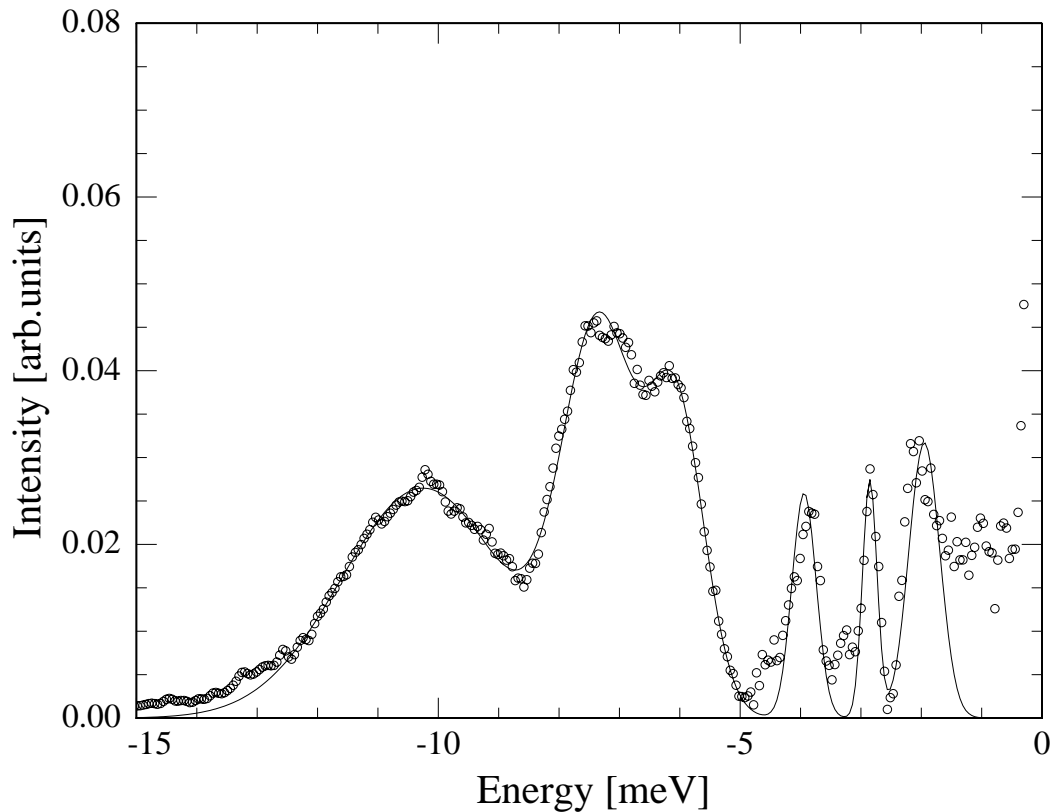


Figure 7.1: Inelastic incoherent neutron spectrum of xenon hydrate at $T=100$ K. It was recorded at $\lambda=5$ Å at the FOCUS spectrometer at the PSI, Switzerland. The peaks observable at 7.3 meV and 10.3 meV are attributed to the transverse acoustic (TA) lattice modes near the zone boundary and the fold-back of the TA modes towards the zone center. The three distinct peaks at 2.05 meV, 2.87 meV and 3.94 meV are assigned to the localized xenon vibrations, which are coupled to the host lattice vibrations.

in the range of neutron energy gain of 2–10 meV was obtained. A spectrum was recorded at a temperature of $T=100$ K.

In Figure 7.1 the INS spectrum of xenon hydrate at $T=100$ K is shown in the energy region of -15 meV to 0 meV. The signal from all detectors was summed in order to obtain better statistics for the spectrum. The signal from the empty aluminum sample container was subtracted and the spectra were treated for background corrections. In the xenon hydrate spectrum five distinct peaks can be identified. At 7.3 meV and 10.3 meV two relatively broad peaks can be observed, with an additional weaker feature at 5.9 meV. The fit with Gaussians leads to FWHMs of 1.6 meV and 2.8 meV, respectively (0.8 meV for the peak at 5.9 meV). The first maximum at 7.3 meV is assigned to the transverse acoustic (TA) modes near the zone boundary. The second peak at 10.3 meV is attributed to the fold-back of the transverse acoustic modes towards the center of the Brillouin

Atom / Molecule	σ [barn]	m [u]	σ/m [barn/u]
H	82.03	1.00	82.03
O	4.23	16.00	0.26
Xe	4.36	131.30	0.03
H ₂ O	168.29	18.00	9.35

Table 7.1: Total scattering cross section and atomic mass of the atoms and molecules in the xenon hydrate sample. The scattering power σ/m is also given.

zone, resulting in a high density of states [151, 46, 7]. In contrast to any known inelastic neutron spectrum of ice (s. Fig. 6.9) [83], three distinct excitations observed below the TA band in the case of xenon hydrate. The three sharp peaks at 2.05 meV, 2.87 meV and 3.94 meV display small line widths (FWHM of 0.2, 0.1 and 0.3 meV, respectively) and a lack of dispersion pointing towards a localized character of these excitations. These lines indirectly show the coupling of the guest and host vibrations [46]. Considering the scattering cross section and the mass of the xenon atoms and the water molecules (s. Tab. 7.1), a ratio between the scattering power of a xenon atom and a water molecule of about 1 : 300 is found. Furthermore, from diffraction experiments it is known that the amplitude of the translational vibrations of the xenon guest atoms is similar to that of the water molecules [60, 45]. The measured inelastic spectrum thus represents the partial density of states of the water molecules only.

It is known from lattice dynamical calculations that there is a symmetry avoided crossing between the flat optic guest modes and the dispersive acoustic lattice phonons [151]. This avoided crossing leads to a strong optic-like behavior of the acoustic lattice modes in the frequency range of the localized guest modes which results in a high density of states. It is this high density of states which is visible in the experimental spectrum. The three observed peaks thus correspond to the localized guest vibrations, which become visible through the guest–host coupling. The xenon atoms in the small spherical cage (site symmetry $m\bar{3}$) vibrate with the highest energy leading to a peak at 3.94 meV whereas the large ellipsoidal cage (site symmetry $\bar{4}2m$) gives raise to the two excitations at lower energy transfers, i.e. 2.87 meV and 2.05 meV, respectively. Regarding the relative intensities, a simplistic single particle consideration yields a theoretical ratio of 2:1:1 (three lines, order of increasing energy) as there are six large and two small cages in the unit cell. However, the intensity ratio is found to be close to 2:1:2, pointing towards a stronger guest–host coupling in the small cages. A similar behavior has also been found in MD simulations of xenon hydrate [148].

Compared with the INS results of methane hydrate (s. Chapter 6), xenon hydrate proved to be an ideal system for the investigation of the guest–host coupling. A direct

contribution of the partial density of states of the guest atoms can be neglected, allowing a clear identification of coupled modes in the measured DOS. Furthermore, the small line widths in the case of xenon hydrate point towards localized modes of the guest atoms. This is attributed to the large mass of the xenon atoms that leads to vibrations well below the maximum of the TA band of the framework vibrations at 7.3 meV. From a simple consideration of the masses of the methane guest molecules and the xenon guest atoms (s. eq. (6.20)), the xenon mode at the lowest energy position would have been expected at ~ 1.8 meV. The potential between the guest–water potential is therefore only slightly stronger in the case of xenon hydrate. The stronger disturbance of the host lattice of xenon hydrate is therefore attributed to effects of the increased guest mass and the stronger localization of the guest modes.

7.2 X–ray Spectroscopy

As the guest–host coupling in the INS spectrum of xenon hydrate was found to be much stronger than in the case of methane hydrate, the effect of the guest vibrations on the dispersion relation can also be expected to be more important. The orientationally averaged dispersion curve of xenon hydrate was determined at the beam line ID28 at the ESRF in Grenoble. The same experimental setup as for methane hydrate was chosen, i.e. Si(11,11,11) reflection with an energy resolution (FWHM) of 1.5 meV at 21.747 keV. As the atomic number of xenon is larger than that of the methane molecules, the sample thickness had to be reduced to 0.5 mm. The sample purity and quality were assured prior to the inelastic scans by measuring the static structure factor. The sample displayed a very good polycrystallinity and the ice I_h contamination was less than 2%. Inelastic spectra were recorded at $T=100$ K in the energy region of -10 meV to 15 meV with wave vector transfers of $1.5 \text{ nm}^{-1} < Q < 11.0 \text{ nm}^{-1}$, corresponding to the range of momentum transfers for methane hydrate. It was not possible to record inelastic spectra below 1.5 nm^{-1} as the contributions from the incident photon beam were too important.

In Figure 7.2 a selection of IXS spectra of xenon hydrate is shown for Q –values between 1.5 nm^{-1} and 11 nm^{-1} . Over this whole Q –range the spectra show a broad non–dispersive inelastic excitation near the elastic line. The energy position of this feature was determined by fitting it with a Lorentzian function, convoluted with the instrument’s resolution function. The energy positions vary between 2.2 meV and 3.1 meV, with an average of $\Omega_G=2.5\pm 0.3$ meV. Additionally, at several Q –values below 5 nm^{-1} a small dispersing feature is visible. The statistics did not allow for a consistent treatment, only at 2.0 nm^{-1} and 3.0 nm^{-1} a determination of the energy position was possible. At these two Q –values the energy position of the excitation was found to be 5.0 ± 0.1 meV and 9.1 ± 0.2 meV, respectively. These values correspond roughly to the values of the LA mode in methane hydrate (~ 5 meV and ~ 8 meV). The dispersive feature is therefore assigned to the LA host lattice modes in xenon hydrate. As there are only a few data points available, a reliable velocity of sound could not be determined for xenon hydrate. The optic–like excitation

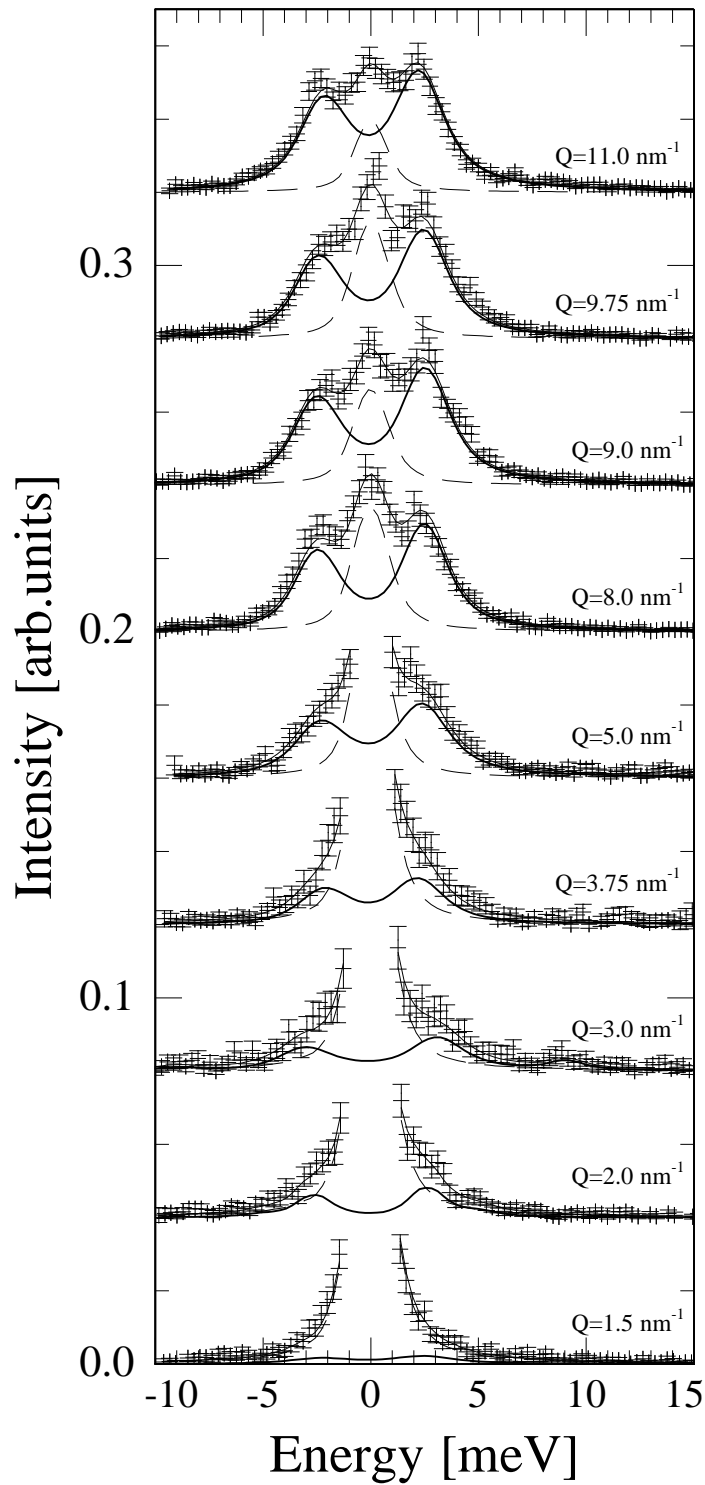


Figure 7.2: Inelastic x-ray spectra of xenon hydrate at several Q -values at $T=100$ K. The spectra were recorded at the ID28 beam line at 21.747 keV. The lines are fits to the spectra using Lorentzians convoluted with the experimental resolution. The spectra were normalized to their integrated intensity. The non-dispersive feature visible near the elastic line ($\Omega_G \simeq 2.5$ meV) is attributed to the localized xenon vibrations inside the water cages.

at 2.5 meV is already observable at the lowest Q -values and has therefore a longitudinal character. With the information from INS results on the dynamics of xenon hydrate it can be assigned to the localized guest vibrations. From the INS results it is known that the localized guest vibrations of the xenon atoms inside the water cages are found at 2.05 eV, 2.87 meV, and 3.94 meV at $T=100$ K. Considering the resolution of 1.5 meV (FWHM) in the present IXS experiment, it can be understood that these vibrations were not resolved. Instead, a single broad excitation is observed in the spectra, whose energy position matches the average energy position of 2.95 meV of the INS findings.

The intensity of the LA host lattice mode is almost negligible in the IXS spectra. This may point towards a stronger resonant scattering of phonons at the avoided crossing, leading to an almost complete decrease of the intensity of the acoustic host lattice phonons. In order to validate the mode assignment and the interpretation of the INS and IXS spectra, the intensities should be calculated from a lattice dynamical model.

7.3 Lattice Dynamical Calculations

The density of states, the dispersion relation and the theoretical INS and IXS intensities are calculated to understand the origin of the experimentally observed features. In analogy to the calculations on methane hydrate, the LD calculations on xenon hydrate were performed with periodic boundary conditions on one proton-disordered unit cell of structure I clathrate hydrate containing 46 water and 8 xenon atoms with a lattice parameter $a=11.83$ Å. The interactions between the water molecules were again described by the slightly modified TIP4P potential [125]. The xenon interactions were described by a Lennard-Jones type potential [144]. The potential parameters of the short-range interaction between the xenon atoms and the water molecules were obtained with the Lorentz-Berthelot mixing rules (s. also Chapter 3). The density of states was calculated for the guest atoms and the host molecules on a cubic grid of $\sim 10^5$ phonon wave vectors. The calculated phonon dispersion had to be orientationally averaged in order to reproduce the measured dispersion relation of the powder sample. It was therefore averaged over 239 randomly chosen wave vector directions in the Brillouin zone in order to simulate the powder sample. The powder averaged phonon dispersions of methane and xenon hydrate are thus directly comparable.

The calculated partial densities of states of xenon hydrate are shown in Figure 7.3. The partial DOS of the guest molecules displays four distinct peaks. They correspond to the xenon vibrations inside the large and small cages. The energy positions of the peaks are about 2 meV, 3 meV, 4.5 meV, and 6 meV. The DOS of the host lattice displays two strong excitations at about 7 meV and 10 meV. The first peak corresponds to the TA lattice modes near the Brillouin zone boundary. The second peak is due to the flat phonon bands associated with the fold-back of the TA modes towards the zone center. These values correspond well to the findings from the INS experiments (7.3 meV and 10.3 meV). Three excitations at about 2 meV, 3 meV, and 4 meV are also observed in the

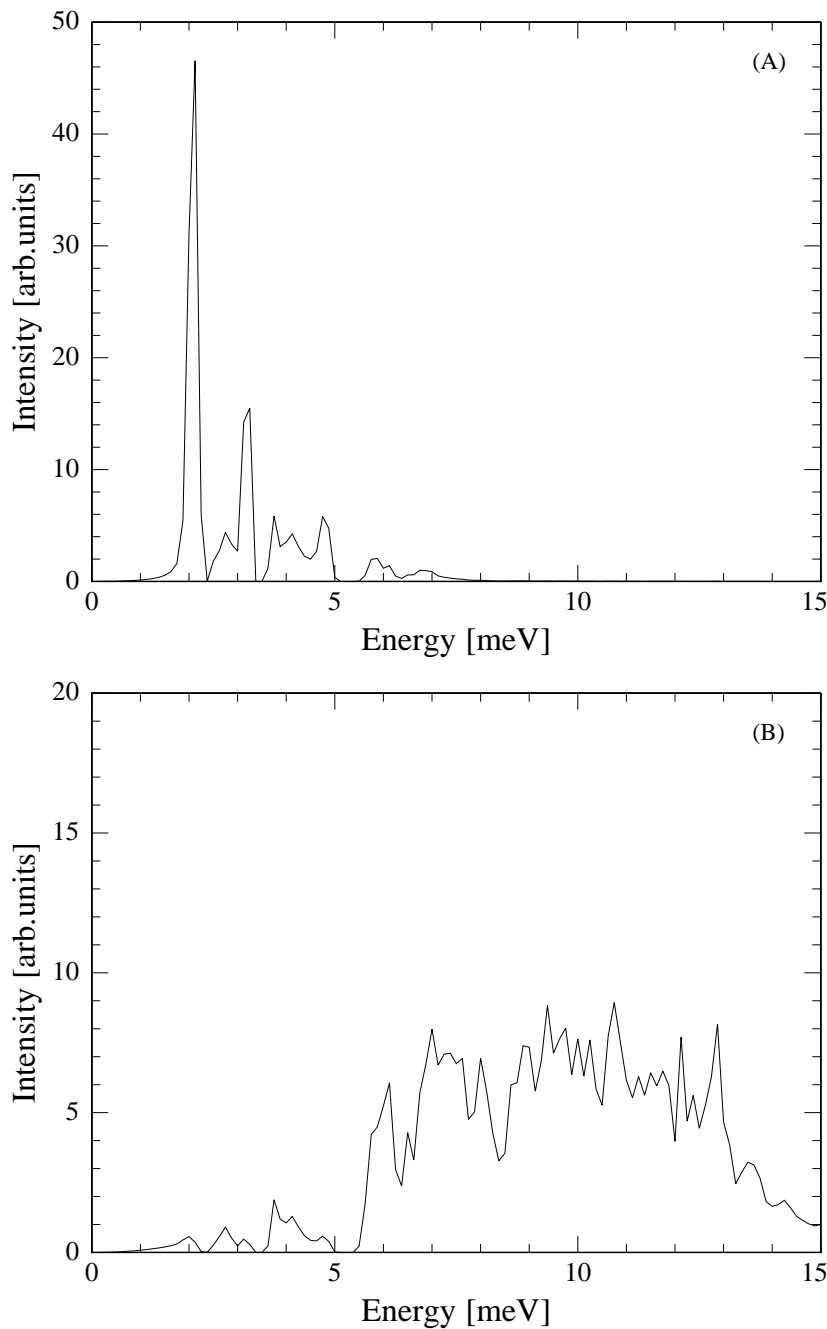


Figure 7.3: (A) The calculated partial DOS of the xenon molecules is shown. Characteristic vibrations of the guest molecules are found at about 2 meV, 3 meV, 4.5 meV, and 6 meV. The peaks at 2 meV and 3 meV correspond to xenon vibrations in the large cages, whereas the peaks at 4.5 meV and 6 meV are xenon vibrations in the small cage. (B) The calculated partial DOS of the host lattice is shown. The peaks at 7 meV and 10 meV are the TA modes near the zone boundary and the fold-back of the TA modes towards the zone center. Below 5 meV three distinct excitations are observed, which arise from a coupling between the cage and guest vibrations.

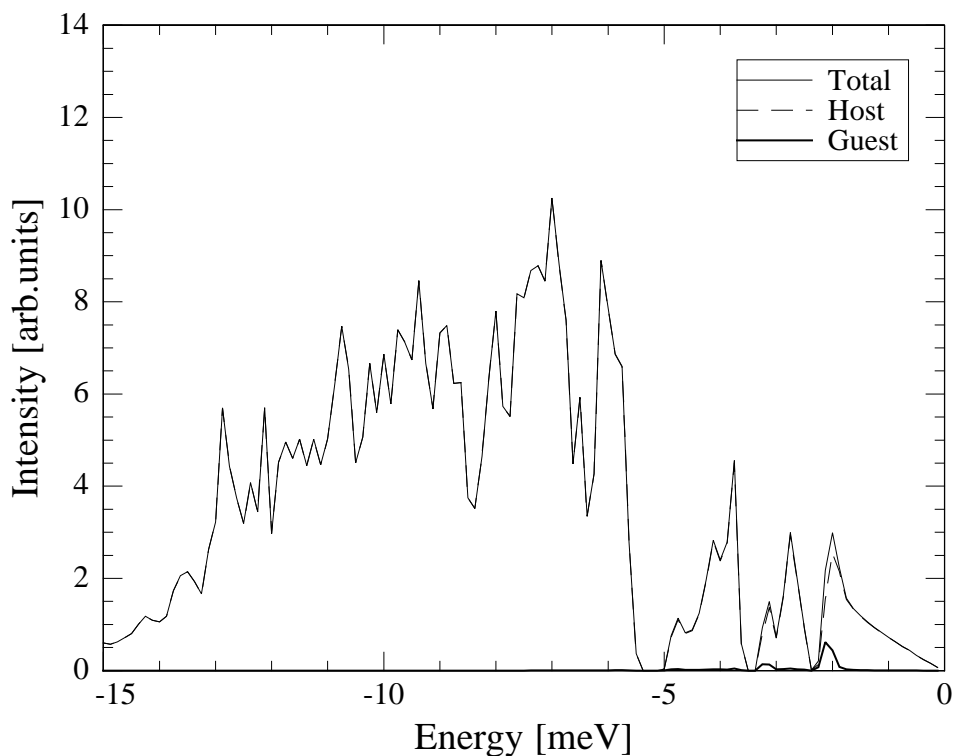


Figure 7.4: The calculated INS spectrum of Xe-H₂O is shown. The low frequency excitations are clearly visible below 5 meV. The contribution from the xenon partial DOS to the peaks is very small (<5%). The low frequency peaks therefore arise from a coupling between the vibrations of the xenon atoms and the host lattice.

partial density of states of the host lattice. The energy positions correspond to the ones of the first three peaks observed in the partial DOS of the guest molecules that has been obtained above. These modes in the vibrational DOS of the host lattice arise from a coupling between the guest and host vibrations.

To validate the assignment of the excitations observed in the experimental INS spectrum, intensities have to be calculated from the DOS of xenon hydrate. As the calculated energy positions of both the guest modes and the host lattice vibrations are in good agreement with the experimental findings, the calculated intensities (s. eq.(6.21)) are directly comparable to the experimental spectra. The theoretical INS spectrum of xenon hydrate is shown in Figure 7.4. Comparing the calculated and experimental spectrum a very good agreement is found. The peaks observed in the calculated spectrum at about 2 meV, 2.8 meV, and 4 meV correspond well to the experimental findings. From the calculations the peak intensity can be attributed almost entirely to host lattice vibrations (>95%). The interpretation of the experimental spectrum in terms of coupled vibrations is validated. Additionally, details of the experimental spectrum are also reproduced by the calculation. In the experimental spectrum weaker features at energy transfers of 3.2 meV

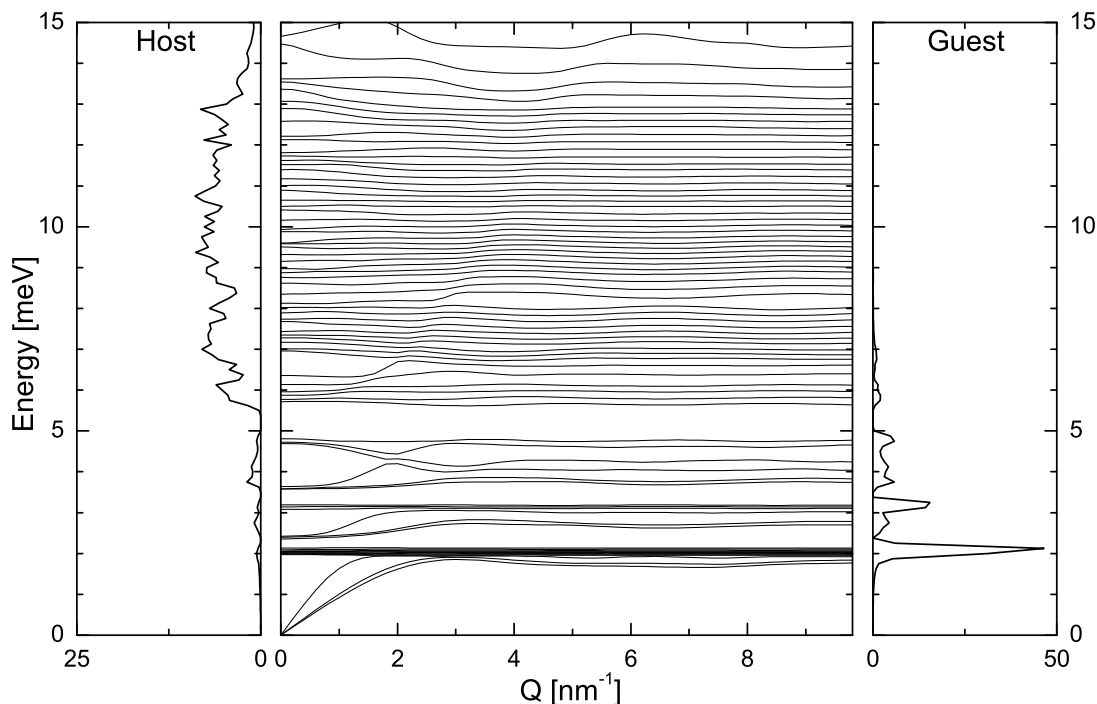


Figure 7.5: Calculated powder averaged phonon dispersion curves of xenon hydrate as deduced from 239 randomly chosen Q -directions. The partial densities of states of the host lattice and the guest molecules are displayed on the left and right side of the dispersion curve, respectively. The characteristic vibrations of the guest atoms are found at about 2 meV, 3 meV, and 4.5 meV. The first maximum of the host DOS is observed at 7 meV.

and 4.8 meV were observed. This asymmetric line shape of the peaks is observed in the theoretical spectrum as well. The mechanism behind the guest–host coupling and the origin of the weak features can be explained with the calculated dispersion relation and eigenvectors.

In Figure 7.5 the orientationally averaged dispersion relation of xenon hydrate is displayed together with the partial densities of states. In the phonon dispersion curves the TA and LA phonon branches of the host lattice are visible below 2 meV. The theoretical orientationally averaged longitudinal velocity of sound is found to be 3000 m/s. This value is in good agreement with experimental results from Brillouin light scattering [68], where an orientationally averaged compressional wave velocity of 2900 m/s was measured. As already observed in the calculated dispersion relation of methane hydrate, the LA and TA modes display a strong bending at the crossing points with the guest branches at 1.2 nm^{-1} and 2.4 nm^{-1} , respectively. But in contrast to methane hydrate the additional guest modes, which are found below the first maximum of the TA lattice modes, also lead

to a strong bending of the acoustic host lattice branches. Furthermore the guest modes are only found in a very narrow energy range. The three more localized xenon modes will probably have a stronger impact on the acoustic region of the dispersion relation of the hydrate lattice than the single guest mode that was found below the first TA maximum in the case of methane hydrate.

As the acoustic lattice modes bend to become optic modes, the guest contributions to the eigenfunctions increases. Here, the resonant interaction at the avoided crossing promotes the mixing of the eigenvectors of the xenon modes and of the host lattice modes. However, a host molecule component remains in the eigenfunctions. This component is observed in the experimental spectrum. The xenon vibrations are thus observed indirectly in the INS spectrum via the guest–host coupling. The origin of the weaker features can also be understood from the dispersion relation: Their energy positions correspond to those of the unperturbed flat xenon modes at the zone center (3.1 meV and 4.8 meV). The xenon mass is large enough to counterbalance the resonance effect of the avoided crossing, and thus the guest vibrations at the zone center already lead to coupled modes. These are observed in the theoretical INS spectrum at 3.1 meV and 4.8 meV.

From the dispersion relation a theoretical scattering function is calculated, as for methane hydrate. The resulting theoretical scattering functions for xenon hydrate is shown in Figure. 7.6. The optic guest modes also become observable at the crossing with the acoustic host lattice mode ($Q > 1.0 \text{ nm}^{-1}$). All of the guest modes are visible in the spectra due to the slightly better resolution that was chosen in the calculations. The mode corresponding to the xenon vibrations along the long axes inside the large cage, however, dominates the spectra. The LA lattice mode loses most of its intensity at the avoided crossing and disappears for $Q > 3.0 \text{ nm}^{-1}$. The theoretical spectra validate the assignment of the experimental IXS intensities. The negligible intensity of the LA lattice mode cannot be solely explained by the difference in the atomic form factor of the xenon atoms and the hydrate lattice. An additional decrease has to occur at the avoided crossing. Inspecting the calculated dynamical structure factor it is found that the mixing of the eigenvectors at the avoided crossing leads to a change in polarization of the modes. The LA lattice mode transfers intensity to the optic guest modes. The strong localization and the important mass of the xenon atoms subsequently lead to an almost complete disappearance of the LA lattice mode.

Overall, the TIP4P potential provided a good set of parameters for the simulation of the characteristics of the ice lattice of hydrates. The potential parameters of the guest molecules are the deciding factors for the correct determination of the guest dynamics and of eventual coupling effects between the guest and host dynamics. While the OPLS potential in methane hydrate was not optimized for hydrate calculations, the Lennard–Jones parameters for the xenon–xenon interactions were already tested in lattice dynamical calculations on xenon hydrate [151]. The calculation could thus not only verify the assignment of the peaks in the INS and IXS spectra, it could also provide details on the coupling mechanism and even reproduce the details of the INS spectrum.

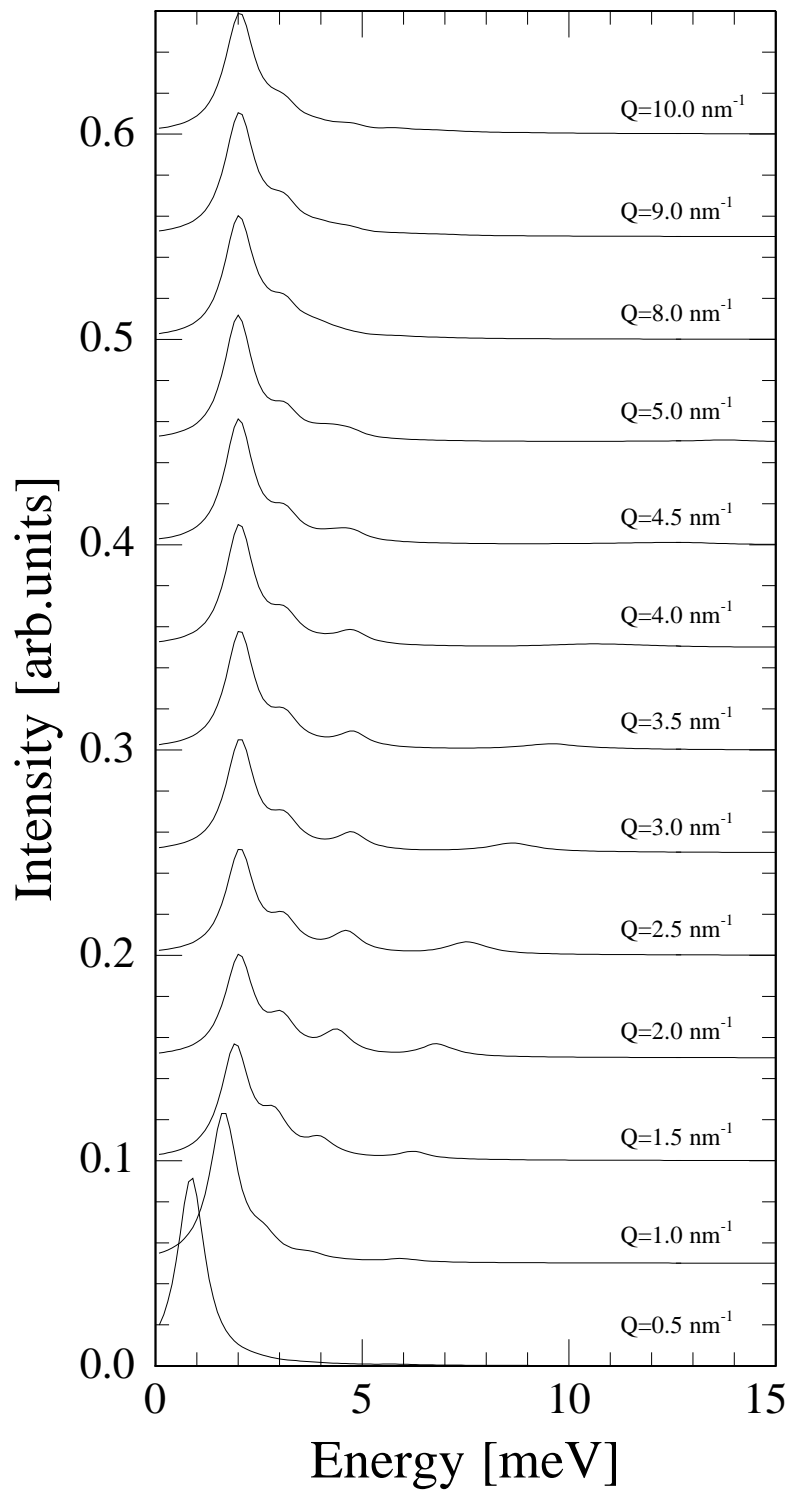


Figure 7.6: Theoretical orientationally averaged scattering function $S(Q, \omega)$ of xenon hydrate. The spectra are shown for Q -values between 0.5 nm^{-1} and 10 nm^{-1} . The peak at 2 meV corresponds to the xenon vibrations along the long axes of the large cage. It becomes visible after the avoided crossing due to a mixing of the eigenvectors of the guest and host modes.

7.4 Discussion and Summary

The combination of INS and IXS experiments with LD calculations gave detailed insight into the lattice dynamics of xenon hydrate.

In the INS experiments the guest–host coupling was confirmed by the observation of three sharp peaks at energy transfers of 2.05 meV, 2.87 meV, and 3.94 meV at $T=100$ K. These peaks were attributed to resonant cage vibrations of the host lattice at the energy of the encaged xenon atoms. Direct contributions of the xenon vibrations could be ruled out due to the large difference between the scattering powers (σ/m) of the xenon atoms and the water molecules. The LD calculations validated the mode assignment, yielding peaks in the partial density of states of the host lattice at energies of 2 meV, 2.8 meV, 4 meV. Furthermore the calculation of theoretical INS intensities could help to understand details of the experimental INS spectrum. The assumption that the direct contributions of the xenon vibrations are negligible in the spectrum is confirmed. Compared to methane hydrate, the increased mass of the xenon guest atoms was found to lead to a strong coupling between the guest and host vibrations. In the discussion of the “box–clathrate” it was already mentioned that an important guest mass could counterbalance the resonance at the avoided crossing and lead to a second coupled mode at an energy corresponding to the one of the guest modes at the zone center. In the case of xenon hydrate the dispersion relation showed very flat xenon modes at about 3.1 meV and 4.8 meV. The host lattice reflects these modes via additional weak features found in both the experimental and theoretical INS spectrum. In the experimental spectrum these excitations are found at 3.2 meV and 4.8 meV, which is in perfect agreement with the observation of peaks at 3.1 meV and 4.8 meV in the calculated INS spectrum. Overall, the INS spectrum provided information on the lattice dynamics of xenon hydrate integrated over the Brillouin zone.

The strong influence of the xenon guest atoms on the lattice dynamics of the hydrate are also found in the IXS spectra. Here, the intensity of the longitudinal acoustic lattice mode is found to be negligible in the spectra, whereas an optic–like mode ($E \approx 2.5$ meV), which was assigned to the xenon vibrations, dominated the spectra. This was attributed to the resonant scattering of the guest and host modes at the avoided crossing. This interpretation was supported by the LD calculations. In the calculated spectra a single non–dispersive mode ($E=2.1$ meV) corresponding to the xenon vibrations along the long axes in the large cage was found to dominate the spectra. The LA host lattice mode could only be observed at wave vector transfers below the avoided crossing. At Q –values beyond the avoided crossing the intensity of the LA lattice modes is almost entirely transferred to the xenon modes. The avoided crossing promotes a mixing of the eigenvectors of the phonon branches, leading to a collective vibration of the guest atoms and consequently to a high intensity mode. *Tse et. al.* [151] found in their lattice dynamical calculation of xenon hydrate reduced phonon lifetimes at the Q –values of the avoided crossings. The phonon relaxation time calculations also predicted a stronger effect for the TA lattice modes. This points towards a stronger coupling of the xenon vibrations with the TA lattice modes and may explain the complete absence of transverse lattice modes in the

IXS spectra of xenon hydrate. In contrast to the INS spectrum, the IXS spectra provided details on dynamics of xenon hydrate for distinct $Q-\omega$ regions in the Brillouin zone. Even though the dispersion relation was orientationally averaged, the results from the experimental and theoretical IXS spectra additionally showed that the strongest coupling between the guest and host vibrations is found in a narrow $Q-\omega$ range around the avoided crossings.

In comparison with methane hydrate, the change in the guest species in xenon hydrate leads to a shift in the vibrational frequencies that accounts for the difference in guest mass and a small change in guest–host interaction strength. As a consequence, the guest modes are found in a narrow energy range. While the INS and IXS spectra strongly depend on the guest species, the coupling mechanism remains the same: The guest–host coupling is promoted by the resonance effect at the avoided crossings between the acoustic host lattice modes and the flat guest branches. The most important criterion for the strong coupling between the guest and host vibrations is that the energy of the guest modes has to be lower than the first maximum of the TA lattice modes.

Chapter 8

Conclusions – Summary and Outlook

In the present work both the structure of methane hydrate under geological conditions and the dynamics of methane and xenon hydrate were investigated.

The structure of methane hydrate under geological conditions was studied in a high resolution neutron diffraction experiment. The use of a fully deuterated sample required a sample environment that was adapted for the use of expensive CD_4 gas as a pressure medium, of which only limited quantities are available. The high pressure sample cell was made from vanadium avoiding the parasitic Bragg peaks of standard aluminum high pressure sample cells. With the optimized equipment it was possible to determine the crystallographic parameters of both the methane molecules and the ice lattice in a temperature range of $T=220\text{ K}$ to $T=280\text{ K}$ and a pressure of $p=100\text{ bar}$. The data were analyzed with a combination of Rietveld refinements and maximum entropy methods. Comparing the host lattice determined at geological conditions with that obtained at low temperatures, one notes a considerable difference between the bond angles of the water molecules, pointing towards strong cage deformations at geological conditions. The thermal displacements of the methane molecules are considerably larger than those of the water molecules in the host lattice. This reflects the void rich character of methane hydrate, where the guest molecules are relatively free to explore the potential surface of the cage. Close to the limit of decomposition the Rietveld refinement was no longer satisfactory. Here, the maximum entropy analysis was needed to provide further insight. The scattering length density of the methane molecules displayed a more complicated form, deviating from the simple isotropic models used in the Rietveld refinement. Overall, large amplitude motions of the guest and host molecules are present under geological conditions, leading to deviations from simple harmonic and isotropic models that are valid at low temperatures and pressures.

The methane and water molecule vibrations were studied in detail over a wide temperature range from $T=50\text{ K}$ to $T=150\text{ K}$ at pressures of a few *mbar* with inelastic neutron scattering. Partially deuterated samples allowed to amplify the contributions of either the guest or the host vibrations to the spectra. The methane molecules were found to perform localized oscillations inside the cages. The data were analyzed, assuming the vibrational frequencies to reflect the size and geometry of the different cages in hydrate structure

type I. The dynamics of the host lattice displayed not only excitations corresponding to the acoustic lattice modes, it was also found to reflect the guest vibrations. This was interpreted as a coupling between the guest and host vibrations. To understand the mechanism of the guest–host coupling inelastic x–ray experiments were performed yielding the collective dynamics of methane hydrate. The coupling was found to be strong in specific regions in reciprocal space, where the frequency of the acoustic lattice vibrations approached the one of the guest vibrations. Lattice dynamical calculations showed that this is due to an avoided crossing between the optic–like guest modes and the acoustic host lattice modes of the same symmetry. At the avoided crossings an exchange in the eigenvector components promotes the observation of guest vibrations in the density of states of the water molecules and to the observation of collective guest vibrations. From the lattice dynamical calculations theoretical intensities for both the inelastic neutron scattering and the inelastic x–ray scattering experiments were calculated, reproducing the experimental results.

The isostructural xenon hydrate was also investigated by a combination of inelastic neutron scattering and inelastic x–ray scattering experiments to study the influence of the guest species on the lattice dynamical characteristics of a hydrate. The contribution of the guest atom vibrations to the inelastic neutron scattering spectra can be neglected for this sample. The three sharp excitations, which are observed in the acoustic region of the spectra ($E < 4$ meV), can thus directly be attributed to the coupling between the guest and host vibrations. The coupling seems to be more important than in the case of methane hydrate. The inelastic x–ray spectra support this assumption: In the case of xenon hydrate only the xenon modes are observed in the spectra, whereas the lattice vibrations have a negligible intensity. The lattice dynamical calculations of xenon hydrate could reproduce both the inelastic neutron and the inelastic x–ray spectra. The calculations showed that the increased guest mass leads to three optic–like guest branches, localized in a narrow energy range in the acoustic region of the lattice modes. As for methane hydrate the guest–host coupling is found to be promoted by the resonance effect at the avoided crossings between the flat guest branches and the acoustic lattice modes. The mixing of eigenvectors of the guest and host molecules at the avoided crossing is apparently determined by the guest species (mass, interaction strength), which can lead to considerably different intensities for the guest and lattice modes.

The results on the lattice dynamics of both methane and xenon hydrate support the idea that the heat carrying lattice waves are scattered by the localized guest vibrations via the resonant interaction. This may lead to a relaxation of the acoustic lattice phonons and thus contribute considerably to the glass–like thermal conductivity of the gas hydrates.

The measurements of the density of states showed also that the peak positions of the guest vibrations and the coupled modes display an unusual temperature dependence. When raising the temperature from $T=85$ K to $T=150$ K the peaks were found to shift by about $400\text{--}600$ μeV towards higher energies. The increase of the translational frequencies with increasing temperatures points towards the importance of anharmonic terms in

the guest and host molecule potentials. Regarding the large amplitude motions of the guest molecules, it is reasonable to assume the repulsive part of the guest–host potential contributes mainly to the anharmonic terms.

These hydrophobic interactions are thought to be even more important in the high pressure structures of methane hydrate. Here, the elastic properties of these recently discovered structures were determined with inelastic x–ray scattering. The absence of distinct guest modes in the spectra is pointing towards a strong increase of the vibrational frequencies of the guest molecules with increasing pressure. The guest modes may thus be considered to be a part of the collective excitations of the crystal. For both high pressure structures the compressional velocity of sound could be determined. Combining these results with the recent results from diffraction experiments, an orientationally averaged elastic modulus and a shear modulus could be determined. The structural transition from a “cage” clathrate (MH–II) to a “filled–ice” (MH–III) is reproduced by the change in the elastic constants. The denser structure of MH–III induces a considerably higher elastic modulus. However, the inclusion of hydrophobic methane molecules between the ice sheets in MH–III seems to lead to an instability against shear stress, which can be observed in a sudden decrease of the shear modulus.

Outlook

In the future gas hydrates will continue to be of interest due to their potentially large economical and geological impact. At present most of the experimental results are gained from synthesized samples at low temperatures and pressures. Under these conditions a precise determination of the structural and dynamical properties is possible. Under geological conditions the determination of precise physical parameters is more difficult but based on the knowledge from previous experiments at low temperatures and pressures it may yet help to understand the “in–situ” properties of gas hydrates. The influence of gases like H_2S , which are present at the ocean floors, on the stability of the gas hydrates is has to be considered in this context. The investigation of the dynamical properties of gas hydrates under geological conditions has still to be addressed. The large amplitude motions found in the diffraction experiments as well as the anharmonicities may have an impact on the lattice dynamics, e.g. if the frequency of the guest vibrations is found to increase beyond the first maximum of the acoustic lattice modes, it is possible that the strong guest–coupling does not exist any longer. With the recent successes in the preparation of a single crystal of methane in a diamond anvil cell, the precise determination of the lattice dynamics of methane hydrate under geological conditions should be possible by inelastic x–ray scattering experiments. Inelastic neutron scattering experiments should also be feasible to determine the vibrational density of states at high pressure and temperatures.

Additional questions concerning the physical properties of clathrate hydrates are connected to the formation and decomposition of gas hydrates. Here, the investigation of

the formation is limited to the study of the cage fillings at the beginning of the hydrate growth process. To date, hydrates are synthesized in a batch process and this process is difficult to use in industrial applications, e.g. gas storage. The parameters that drive the hydrate formation process are therefore of both industrial and geological interest, as a knowledge of these variables may contribute to the industrial use of hydrates and to an understanding of the formation of natural hydrate deposits. An investigation of the very first steps of the hydrate growth process, which should be observable at water–gas interfaces, may help to understand the fundamentals of hydrate formation. The porosity of synthetic and natural hydrates is probably also linked to the formation process of gas hydrates. The influence of this porosity on the properties of gas hydrates is still to be evaluated.

The hydrate decomposition has a direct environmental impact, as large quantities of green house gas are stored on the ocean sea floors. It is therefore necessary to understand the mechanism and the kinetics of the hydrate decomposition. The investigation of a controlled hydrate decomposition would also be of economic interest, as the results would be useful for the production of methane from natural deposits as well as for hydrate growth inhibition in gas pipelines.

Bibliography

- [1] D. Adam, *Nature* **415**, 913 (2002)
- [2] J. Akella, *Science & Technology Review*, March 1996
- [3] M.P. Allen and D.J. Tildesley, *Computer Simulation of Liquids*, Clarendon Press, Oxford, 1989
- [4] P. Andersson and R. Ross, *J. Phys. C: Solid State Phys.* **16**, 1423 (1983)
- [5] N.W. Ashcroft and N.D. Mermin, *Solid State Physics*, Harcourt Brace, Orlando, 1976
- [6] M. d’Astuto, P. Guira, M. Krisch, M. Lorenzen, A. Mermet, G. Monaco, H. Requardt, F. Sette, A. Shukla, and R. Verbeni, *Physica B* **316–317**, 150 (2002)
- [7] J. Baumert, C. Gutt, W. Press, J.S. Tse, and S. Janssen, in *Proceedings of the 4th International Conference on Gas Hydrates*, Yokohama, May 2002, p. 687
- [8] J. Baumert, C. Gutt, V.P. Shpakov, J.S. Tse, M. Krisch, M. Müller, H. Requardt, D.D. Klug, S. Janssen, and W. Press, *Phys. Rev. B* **68**, 174301 (2003)
- [9] M. Bee, *Quasielastic Neutron Scattering*, Adam Hilger, Bristol, 1985
- [10] H.J.C. Berendsen, J.R. Grigera, and T.P. Straatsma, *J. Phys. Chem.* **91**, 6269 (1987)
- [11] J.D. Bernal and R.H. Fowler, *J. Chem. Phys.* **1**, 515 (1933)
- [12] C. Berndt, J. Mienert, M. Vanneste, S. Bünz, and P. Bryn, *Proceedings of the Fourth International Conference on Gas Hydrates*, Yokohama, Vol. 1, p. 71 (2002)
- [13] G. Bohrmann, J. Greinert, E. Suess, and M. Torres, *Geology* **26**, 647 (1998)
- [14] M. Born, *Ann. Phys.* **44**, 605 (1914)
- [15] M. Born and K. Huang, *Dynamical Theory of Crystal Lattices*, Clarendon, Oxford, 1956

- [16] P. Bosi, R. Tubino, and G. Zerbi, in *Physics and Chemistry of Ice*, E. Whalley, S.J. Jones, L.W. Gold, eds., Royal Society of Canada, Ottawa, 1973
- [17] K. Burger, PhD Thesis, Universität Tübingen, Germany, 1997
- [18] E. Burkel, *J. Phys.: Condens. Matter* **13**, 7627 (2001)
- [19] G. Caglioti, A. Paoletti, and F.P. Ricci, *Nucl. Instrum. Methods* **35**, 223 (1958)
- [20] S. Califano, V. Schettino, and N. Neto, *Lattice Dynamics of Molecular Crystals in Lecture Notes in Chemistry*, Vol. 26, G. Berthier, M.J.S. Dewar, H. Fischer, K. Fukui, G.G. Hall, H. Hartmann, H.H. Jaffé, J. Jortner, W. Kutzelnigg, K. Ruedenberg, E. Scrocco, eds., Springer, Berlin, 1981
- [21] B. Chazallon and W.F. Kuhs, *J. Chem. Phys.* **117**, 308 (2002)
- [22] B. Chazallon, H. Itoh, M. Koza, W.F. Kuhs, and H. Schober, *Phys. Chem. Chem. Phys.* **4**, 4809 (2002)
- [23] I.M. Chou, A. Sharma, C. Burruss, J. Shu, H. Mao, R.J. Hemley, A.F. Goncharov, L.A. Stern, and S.H. Kirby, *Proc. Nat. Acad. Sci.* **97**, 13484 (2000)
- [24] I.M. Chou, A. Sharma, R.C. Burruss, R.J. Hemley, A.F. Goncharov, L.A. Stern, and S.H. Kirby, *J. Phys. Chem. A* **105**, 4664 (2001)
- [25] J.L. Cohn, G.S. Nolas, V. Fessatidis, T.H. Metcalf, and G.A. Slack, *Phys. Rev. Lett.* **82**, 779 (1999)
- [26] D.M. Collins, *Nature* **298**, 49 (1982)
- [27] M.I. Collins, C.I. Ratcliffe, and J.A. Ripmeester, *J. Phys. Chem.* **94**, 157 (1990)
- [28] J.G. Cook and D.G. Leaist, *Geophys. Res. Lett.* **10**, 397 (1983)
- [29] C. Cros, M. Pouchard, and P. Hagenmuller, *J. Solid State Chem.* **2**, 570 (1970)
- [30] D.W. Davidson, in *Water, a Comprehensive Treatise*, F. Franks, Ed., Plenum Press, New York (1973)
- [31] D.W. Davidson, Y.P. Handa, C.I. Ratcliffe, J.S. Tse, and B.M. Powell, *Nature* **311**, 142 (1984)
- [32] D.W. Davidson and J.A. Ripmeester, in *Inclusion Compounds*, Vol. 3, J.L. Atwood, J.E.D. Davies, D.D. MacNicol, eds., Acad. Press (1984)
- [33] H. Davy, *Phil. Trans. Roy. Soc. London* **101**, 1 (1811)

- [34] P.H. Dederichs, K. Schroeder, and R. Zeller, *Point defects in metals II. Dynamical properties and diffusion controlled reactions. Theory of diffusion controlled reactions of point defects in metals* in *Springer Tracts in Modern Physics*, Vol. 87, G. Hoehler, E.A. Niekisch, S. Fluegge, H. Haken, J. Hamilton, H. Lehmann, W. Paul, eds., Springer, Berlin, 1980
- [35] M.W.C. Dharma-Wardana, *J. Phys. Chem.* **87**, 4185 (1983)
- [36] J. Dong, O.F. Sankey, and C.W. Myles, *Phys. Rev. Lett.* **86**, 2361 (2001)
- [37] Y.A. Dyadin, E.G. Larionov, and A.Y. Manakov, *Proceedings of the Fourth International Conference on Gas Hydrates, Yokohama*, Vol. 2, p. 590 (2002)
- [38] O.K. Forrisdahl, B. Kvamme, and A.D.J. Haymet, *Mol. Phys.* **89**, 89 (1996)
- [39] R.E. Gagnon, H. Kiefte, M.J. Clouter, and E. Whalley, *J. Chem. Phys.* **89**, 4522 (1988)
- [40] H. Gerke and H. Gies, *Zeit. für Kristall.* **11**, 166 (1984)
- [41] A.K. Ghatak and L.S. Kothari, *an introduction to Lattice Dynamics*, Addison-Wesley, London, 1972
- [42] C. Gutt, B. Asmussen, W. Press, C. Merkl, H. Casalta, J. Greinert, G. Bohrmann, J.S. Tse, and A. Hüller, *Europhys. Lett.* **48**, 269 (1999)
- [43] C. Gutt, B. Asmussen, W. Press, J.S. Tse, Y.P. Handa, and M.R. Johnson, *J. Chem. Phys.* **113**, 4713 (2000)
- [44] C. Gutt, W. Press, A. Hüller, J.S. Tse, and H. Casalta, *J. Chem. Phys.* **114**, 4160 (2001).
- [45] C. Gutt, PhD Thesis, Universität Kiel, Germany, 2001
- [46] C. Gutt, J. Baumert, W. Press, J.S. Tse, and S. Janssen, *J. Chem. Phys.* **116**, 3795 (2002)
- [47] Y. Halpern, V. Thieu, R.W. Henning, X. Wang, and A.J. Schultz, *J. Am. Chem. Soc.* **123**, 12826 (2001)
- [48] Y.P. Handa, *J. Chem. Therm.* **18**, 915 (1986)
- [49] Y.P. Handa and J.G. Cook, *J. Phys. Chem.* **91**, 6327 (1987)
- [50] M.B. Helgerud, W.F. Waite, S.H. Kirby, and A. Nur, in *Proceedings of the 4th International Conference on Gas Hydrates, Yokohama, May 2002*, p. 711

- [51] H. Hirai, T. Kondo, M. Hasegawa, T. Yagi, Y. Yamamoto, T. Komai, K. Nagashima, M. Sakashita, H. Fujihisa, and K. Aoki, *J. Phys. Chem. B* **104**, 1429 (2000)
- [52] H. Hirai, Y. Uchihara, H. Fujihisa, M. Sakashita, E. Katoh, K. Aoki, K. Nagashima, Y. Yamamoto, and T. Yagi, *J. Chem. Phys.* **115**, 7066 (2001)
- [53] H. Hirai, Y. Uchihara, Y. Nichimura, T. Kawamura, Y. Yamamoto, and T. Yagi, *J. Phys. Chem. B* **106**, 11089 (2002)
- [54] G.D. Holder, G. Corbin, and K.D. Papadopoulos, *Ind. Eng. Chem. Fundam.* **19**, 282 (1980)
- [55] F. Hollander and G.A. Jeffrey, *J. Chem. Phys.* **66**, 4699 (1977)
- [56] D.J. Hooton, *Philos. Mag.* **46**, 422 (1955)
- [57] L. van Hove, *Phys. Rev.* **95**, 249 (1954)
- [58] G. Hummer, S. Garde, A.E. Garcia, M.E. Paulaitis, and L.R. Pratt, *Proc. Natl. Acad. Sci. U.S.A.* **95**, 1552 (1998)
- [59] T. Ikeda, S. Mae, and T. Uchida, *J. Chem. Phys.* **108**, 1352 (1998)
- [60] T. Ikeda, S. Mae, O. Yamamuro, T. Matsuo, S. Ikeda, and R.M. Ibberson, *J. Phys. Chem. A* **104**, 10623 (2000)
- [61] R. Inoue, H. Tanaka, and K. Nakanishi, *J. Chem. Phys.* **104**, 9569 (1996)
- [62] *International Tables for Crystallography*, Vol. C, A.J.C. Wilson, ed., Kluwer Academic Publishers, Dordrecht, 1992
- [63] H. Itoh, J.S. Tse, and K. Kawamura, *J. Chem. Phys.* **115**, 9414 (2001)
- [64] S. Janssen, D. Rubio-Temprano, and A. Furrer, *Physica B* **283**, 355 (2000)
- [65] G.A. Jeffrey and R.K. McMullan, *Prog. Inorg. Chem.* **8**, 43 (1967)-108
- [66] G.A. Jeffrey, in *Inclusion Compounds*, Vol. 1, J.L. Atwood, J.E.D. Davies, D.D. MacNicol, eds., Acad. Press, London (1984)
- [67] W.L. Jorgensen, J. Chandrasekhar, J.D. Madura, R.W. Impey, and M.L. Klein, *J. Chem. Phys.* **79**, 926 (1983)
- [68] H. Kiefte, M.J. Clouter, and R.E. Gagnon, *J. Phys. Chem.* **89**, 3103 (1985)
- [69] A. Klapproth, E. Goreshnik, D. Staykova, H. Klein, and W.F. Kuhs, *Can. J. Phys.* **81**, 503 (2003)

- [70] J. Klinger and G.J. Rochas, *J. Phys. Chem.* **87**, 4155 (1983)
- [71] M.H. Krisch, A. Mermet, A.S. Miguel, F. Sette, and C. Masciovecchio, *Phys. Rev. B* **56**, 8691 (1997)
- [72] M. Krisch, private communications, April (2002)
- [73] A. Krivchikov et. al., unpublished
- [74] W.F. Kuhs and M.S. Lehmann, *Water Sci. Rev.* **2**, 1 (1986)
- [75] W.F. Kuhs, B. Chazallon, P.G. Radaelli, and F. Pauer, *J. Incl. Phenom. Mol. Recognit. Chem.* **29**, 65 (1997)
- [76] W.F. Kuhs, A. Klapproth, F. Gotthardt, K. Techmer, and T. Heinrichs, *Geophys. Res. Lett.* **27**, 2929 (2000)
- [77] S. Kumazawa, Y. Kubota, M. Takata, and M. Sakata, *J. Appl. Cryst.* **26**, 453 (1993)
- [78] K.A. Kvenvolden, *Rev. Geophysics* **31**, 173 (1993)
- [79] K.A. Kvenvolden, *Chem. Geol.* **71**, 41 (1988)
- [80] F.C. van der Lage and H.A. Bethe, *Phys. Rev.* **71**, 61(1947)
- [81] J.E. Lennard–Jones, A.F. Devonshire, *Proc. Roy. Soc.* **A163**, 53 (1932)
- [82] J.E. Lennard–Jones, A.F. Devonshire, *Proc. Roy. Soc.* **A165**, 1 (1938)
- [83] J. Li, *J. Chem. Phys.* **105**, 6733 (1996)
- [84] F. Lindemann, *Z. Phys.* **11**, 609 (1910)
- [85] C. Lobban, J.L. Finney, and W.F. Kuhs, *J. Chem. Phys.* **117**, 3928 (2002)
- [86] D. Londono, J.L. Finney, and W.F. Kuhs, *J. Chem. Phys.* **97**, 547 (1992)
- [87] J.S. Loveday, R.J. Nelmes, M. Guthrie, D.D. Klug, and J.S. Tse, *Phys. Rev. Lett.* **87**, 215501 (2001)
- [88] J.S. Loveday, R.J. Nelmes, M. Guthrie, S.A. Belmonte, D.R. Allan, D.D. Klug, J.S. Tse, and Y.P. Handa, *Nature* **410**, 661 (2001)
- [89] J.S. Loveday, R.J. Nelmes, and M. Guthrie, *Chem. Phys. Lett.* **350**, 459 (2001)
- [90] S.W. Lovesey, *Theory of Neutron Scattering from Condensed Matter*, Vol. 1, Clarendon Press, Oxford, 1984
- [91] K. Lum, D. Chandler, and J.D. Weeks, *J. Phys. Chem. B* **103**, 4570 (1999)

- [92] T.C.W. Mak and R.K. MacMullan, *J. Chem. Phys.* **42**, 2732 (1965)
- [93] M.A. Maslin and E. Thomas, *Quaternary Sci. Rev.* **22**, 1729 (2003)
- [94] R.K. McMullan and G.A. Jeffrey, *J. Chem. Phys.* **42**, 2725 (1965)
- [95] P. Melinon, P. Keghelian, A. Perez, B. Champagnon, Y. Guyot, L. Saviot, E. Reny, C. Cros, M. Pouchard, and A.J. Dianoux, *Phys. Rev. B* **59**, 10099 (1999)
- [96] M. Mezei and D.L. Beveridge, *J. Chem. Phys.* **76**, 593 (1982)
- [97] J.v. Neumann and E. Wigner, *Physik. Zeitschr.* **30**, 467 (1929)
- [98] G.S. Nolas, J.L. Cohn, G.A. Slack, and S.B. Schujman, *Appl. Phys. Lett.* **73**, 178 (1998)
- [99] K. Parlinski, *PHONON* software manual, version 3.11, Cracow, Poland (2002)
- [100] W.R. Parrish and J.M. Prausnitz, *Ind. Eng. Chem. Process Des. Develop.* **11**, 26 (1972)
- [101] A. Polian and M. Grimsditch, *Phys. Rev. B* **27**, 6409 (1983)
- [102] W. Prandl, *Acta Cryst. A* **37**, 811 (1981)
- [103] W. Press and A. Hüller, *Acta Cryst. A* **29**, 252 (1972)
- [104] W. Press, *Acta Cryst. A* **29**, 257 (1972)
- [105] W. Press, H. Grimm, and A. Hüller, *Acta Cryst. A* **35**, 881 (1979)
- [106] A. Rahman and F.H. Stillinger, *J. Chem. Phys.* **57**, 4009 (1972)
- [107] B. Renker, in *Physics and Chemistry of Ice*, E. Whalley, S.J. Jones, L.W. Gold, eds., Royal Society of Canada, Ottawa, 1973
- [108] E. Reny, A. San-Miguel, Y. Guyot, B. Masenelli, P. Melinon, L. Saviot, S. Yamanaka, B. Champagnon, C. Cros, M. Pouchard, M. Borowski, and A.J. Dianoux, *Phys. Rev. B* **66**, 14532 (2002)
- [109] H.M. Rietveld, *Acta Cryst.* **22**, 151 (1967)
- [110] H.M. Rietveld, *J. Appl. Cryst.* **2**, 65 (1969)
- [111] J.A. Ripmeester, J.S. Tse, C.I. Ratcliffe, and B.M. Powell, *Nature* **325**, 135 (1987)
- [112] J.A. Ripmeester and C.I. Ratcliffe, *J. Phys. Chem.* **94**, 8773 (1990)
- [113] R.G. Ross, P. Andersson, G. Backström, *Nature* **290**, 322 (1981)

- [114] M. Sakata and M. Sato, *Acta Cryst. A* **46**, 263 (1990)
- [115] S. Sasaki, T. Kumazaki, T. Kume, and H. Shimizu, *J. Phys.: Condens. Matter* **14**, 10445 (2002)
- [116] R. Sassen, I.R. MacDonald, A.G. Requejo, N.L. Guinasso, I.I. Kennicutt, S.T. Sweet, and J.M. Brooks, *Geo-Marine Letters* **14**, 110 (1994)
- [117] H. Schober, A. Tölle, B. Renker, R. Heid, and F. Gompf, *Phys. Rev. B* **56**, 5937 (1997)
- [118] E. Schreiber, O. Anderson, and N. Soga, *Elastic constants and their measurement*, McGraw-Hill, New York, 1973
- [119] F. Sette, G. Ruocco, M. Krisch, C. Masciovecchio, R. Verbini, and U. Bergmann, *Phys. Rev. Lett.* **77**, 83 (1996)
- [120] H. Shimizu, T. Nabetani, T. Nishiba, and S. Sasaki, *Phys. Rev. B* **53**, 6107 (1996)
- [121] H. Shimizu, T. Kumazaki, T. Kume, and S. Sasaki, *J. Phys. Chem. B* **106**, 30 (2002)
- [122] H. Shimizu, T. Kumazaki, T. Kume, and S. Sasaki, *Phys. Rev. B* **65**, 212102 (2002)
- [123] H. Shimizu, T. Kumazaki, T. Kume, and S. Sasaki, *J. Phys. Chem. B* **106**, 30 (2002)
- [124] V.P. Shpakov, J.S. Tse, C.A. Tulk, B. Kvamme, and V.R. Belosludov, *Chem. Phys. Lett.* **282**, 107 (1998)
- [125] V.P. Shpakov, P.M. Rodger, J.S. Tse, D.D. Klug, and V.R. Belosludov, *Phys. Rev. Lett.* **88**, 1555021 (2002)
- [126] V.P. Shpakov, private communications, Mai (2002)
- [127] S.K. Sinha, *J. Phys.: Condens. Matter* **13**, 7511 (2001)
- [128] G.A. Slack, *Phys. Rev. B* **22**, 3065 (1980)
- [129] E.D. Sloan, jr., *Clathrate Hydrates of Natural Gases*, 2nd ed., Marcel Dekker Inc., New York (1998)
- [130] W. Smith and T.R. Forester, *The DL_POLY_2 User Manual*, Daresbury Laboratory, Warrington, 2001

- [131] G.L. Squires, *Introduction to the Theory of Thermal Neutron Scattering*, Cambridge University Press, Cambridge, 1978
- [132] G.P. Srivastava, *The Physics of Phonons*, Adam Hilger, Bristol, 1990
- [133] M. von Stackelberg, *Naturwissenschaften* **36**, 327 (1949)
- [134] M. von Stackelberg and H.R. Müller, *Naturwissenschaften* **38**, 327 (1951)
- [135] M. von Stackelberg and H.R. Müller, *J. Chem. Phys.* **19**, 1319 (1949)
- [136] M. von Stackelberg and W. Jahns, *Z. Elektrochem.* **58**, 99 (1954)
- [137] M. von Stackelberg and H.R. Müller, *Z. Elektrochem.* **58**, 25 (1954)
- [138] L.A. Stern, S. Circone, S.H. Kirby, and W.B. Durham, *J. Phys. Chem.* **105**, 1756 (2001)
- [139] F.H. Stillinger and A. Rahman, *J. Chem. Phys.* **60**, 1545 (1974)
- [140] R.D. Stoll and G.M. Bryan, *J. Geophys. Res.* **84**, 1629 (1979)
- [141] E. Suess, G. Bohrmann, J. Greinert, and E. Lausch, *Spektrum der Wissenschaften* **6**, 62 (1999)
- [142] A.K. Sum, R.C. Burruss, and E.D. Sloan, Jr., *J. Phys. Chem. B* **101**, 7371 (1997)
- [143] J.S. Tse, M.L. Klein, and I.R. McDonald, *J. Phys. Chem.* **87**, 4198 (1983)
- [144] J.S. Tse, M.L. Klein, and I.R. McDonald, *J. Chem. Phys.* **78**, 2096 (1983)
- [145] J.S. Tse, M.L. Klein, and I.R. McDonald, *J. Chem. Phys.* **810**, 6146 (1984)
- [146] J.S. Tse, W.R. McKinnon, and M. Marchi, *J. Phys. Chem.* **91**, 4188 (1987)
- [147] J.S. Tse and M.A. White, *J. Phys. Chem.* **92**, 5006 (1988)
- [148] J.S. Tse, B.M. Powell, V.J. Sears, and Y.P. Hande, *Chem. Phys. Lett.* **215**, 383 (1993)
- [149] J.S. Tse, C.I. Ratcliffe, B.M. Powell, V.F. Sears, and Y.P. Handa, *J. Phys. Chem.* **101**, 4491 (1997)
- [150] J.S. Tse, V.P. Shpakov, V.V. Murashov, and V.R. Belosludov, *J. Chem. Phys.* **107**, 9271 (1997)
- [151] J.S. Tse, V.P. Shpakov, V.R. Belosludov, F. Trouw, Y.P. Handa, and W. Press, *Europhys. Lett* **54**, 354 (2001)

- [152] K.A. Udachin, C.I. Ratcliffe, G.D. Enright, and J.A. Ripmeester, *Supramol. Chem.* **8**, 173 (1997)
- [153] K.A. Udachin, C.I. Ratcliffe, and J.A. Ripmeester, *Proceedings of the Fourth International Conference on Gas Hydrates, Yokohama, Vol. 2*, p. 604 (2002)
- [154] W.L. Vos, L.W. Finger, R.J. Hemley, and H.K. Mao, *Phys. Rev. Lett.* **71**, 3150 (1993)
- [155] J.H. van der Waals and J.C. PLatteuw, *Adv. Chem. Phys.* **2**, 1 (1959)
- [156] N.R. Werthamer, in *Rare Gas Solids*, Vol. 1, M.L. Klein, J.A. Venables, eds., Acad. Press, London, 1976
- [157] E. Whalley, *Can. J. Chem.* **55**, 3429 (1977)
- [158] E. Whalley, *J. Geophys. Res.* **85**, 2539 (1980)

Eidesstattliche Erklärung

Hiermit erkläre ich an Eides statt, dass die vorliegende Dissertation – abgesehen von der Beratung durch meine akademischen Lehrer – nach Inhalt und Form meine eigene Arbeit ist.

Diese Arbeit wurde weder ganz noch in Teilen an anderer Stelle im Rahmen eines Prüfungsverfahrens vorgelegt.

Frühere Promotionsversuche wurden von mir nicht vorgenommen.

Kiel, den 23.12.2003

Lebenslauf

Julian Baumert
33, rue Thiers
38000 Grenoble
Frankreich

Geburtsdatum 16.6.1975
Geburtsort Berlin
Eltern Ingrid und Jürgen Baumert
Staatsangehörigkeit Deutsch

1981 - 1985 Löcknitz Grundschule Berlin
1985 - 1991 College Francais Berlin
1991 - 1993 Max-Planck Gymnasium Kiel
1993 - 1994 Waukesha West High School, Wisconsin, USA
Okt. 1994 - Okt. 1995 Physikstudium (Diplom) an der
Christian-Albrechts-Universität zu Kiel
Okt. 1995 - Okt. 1996 Zivildienst
Okt. 1996 - Jul. 2000 Physikstudium (Diplom) an der
Christian-Albrechts-Universität zu Kiel
Nov. 1997 Vordiplomprüfung Physik mit Nebenfach Informatik
Jul. - Sep. 1998 Praktikum am Institut Laue-Langevin in Grenoble, Frankreich
Sep. 1998 - Feb. 2000 wissenschaftliche Hilfskraft am Institut für Theoretische Physik der
Christian-Albrechts-Universität zu Kiel
Okt. 1998 Mündliche Diplomprüfung im Nebenfach Informatik
Feb. 1999 - Apr. 1999 Mündliche Diplomprüfungen im Hauptfach Physik
Mai 1999 - Juni 2000 Anfertigung der Diplomarbeit
*Untersuchung der Rotations- und Translationsdynamik von Hexan
in porösen Materialien mit quasielastischer Neutronenstreuung*
am Institut für Experimentelle
und Angewandte Physik der Christian-Albrechts-Universität
zu Kiel in der Arbeitsgruppe von Prof. Dr. W. Press

- seit Okt. 2000 Wissenschaftlicher Mitarbeiter am Institut für Experimentelle und Angewandte Physik der Christian-Albrechts-Universität zu Kiel.
Anfertigung der vorliegenden Dissertation in der Arbeitsgruppe von Prof. Dr. W. Press
- Sept. 2003 Young Scientist Award der ECNS, Montpellier

Acknowledgments

I would like to thank Prof. Dr. Werner Press for the warm welcome in his workgroup and for the proposition of the interesting subject of the present work. I benefitted a lot from the discussions with him and from his encouragements.

I also express my thanks to Mark Johnson, who welcomed me in his workgroup at the ILL in Grenoble. His knowledge on numerical methods and his supply of computing hours on many machines stimulated much of the numerical work.

A special thanks to Christian Gutt, who helped me during most of the experiments, despite his new responsibilities for his first couple children. His interest in my work and the many discussions on the phone were extremely valuable during the preparation of this work. He also showed exceptional persistence in the corrections of the final manuscript.

The collaboration with John Tse at the NRC in Canada did not only provide me with all the samples I needed, his ideas also stimulated many of the questions that I tried to answer in this work. Especially, a three weeks visit to his work group that was partially financed by the NRC, helped a lot to advance the theoretical output for my work. For his supply of ideas, and financial aid I would like to thank. I would also like to thank Dennis Klug, who synthesized most of the samples, which always arrived on time for the experiments.

In Kiel I have to thank Klaas Kölln who signed all the papers that needed a signature and helped with purchases of equipment and with transports to Grenoble. At this point I also thank Monika Seeger, without her I could have never solved the administrative problems over the distance Kiel–Grenoble.

During all the neutron scattering and x-ray scattering experiments many people helped to make the experiments a success. For their assistance I would like to thank Christian Gutt, Herwig Requardt, Mark Johnson, Michael Krisch, Martin Müller, Stefan Janssen, and Fanni Juranyi. The high pressure experiments at the ESRF would have never been possible without Dean Gibson, who taught me the first steps and assisted me during all the critical phases. I would also like to thank Michael Hanfland, who helped with the diamond anvil cells. At the ILL Jean-Luc Laborier helped prepare the pressure equipment and the high pressure sample cell for the diffraction experiments.

I thank my parents for their support. A very special thanks to Maren Martens, who most of all had to bear my absence. A distance of 1336 km was far but yet not too far for her.

The research in this work was funded by the BMBF within the program GEOTECHNOLOGIEN (project no. 03GO551A).

Teile dieser Arbeit wurden bereits veröffentlicht:

- J. Baumert, C. Gutt, V.P. Shpakov, J.S. Tse, M. Krisch, M. Müller, H. Requardt, D.D. Klug, S. Janssen, and W. Press, *Phys. Rev. B* **68**, 174301 (2003)
- C. Gutt, J. Baumert, W. Press, J.S. Tse, and S. Janssen, *J. Chem. Phys.* **116**, 3795 (2002)
- J. Baumert, C. Gutt, W. Press, J.S. Tse, and S. Janssen, in *Proceedings of the 4th International Conference on Gas Hydrates*, Yokohama, May 2002, p. 687